UiO : University of Oslo

Hao Zhao

Improvements in seismic imaging and migration-velocity model building

Thesis submitted for the degree of Philosophiae Doctor

Department of Geosciences
Faculty of Mathematics and Natural Sciences

Group of petroleum geosciences
Group of digital signal processing and image analysis (DSB)

2019

Series of dissertations submitted to the
Faculty of Mathematics and Natural Sciences, University of Oslo
No. 2218

ISSN 1501-7710

Cover: Hanne Baadsgaard Utigard.
Print production: Reprosentralen, University of Oslo.

Preface

This thesis is submitted in partial fulfillment of the requirements for the degree of *Philosophiae Doctor* at the University of Oslo. The research presented here is conducted under the main supervision of Professor Leiv-J Gelius, Associate Professor Einar Iversen, and co-supervision of Professor Anne H. Schistad Solberg, Doctor Walter Söllner and Doctor Endrias Asgedom. This work is a part of a joint project, *improved seismic imaging based on resolution enhancement and pattern recognition*, which is cooperated between the Department of Geosciences and the Department of Informatics at the University of Oslo. The project is funded by the Norwegian Research Council under the Large program for petroleum research (PETROMAKS2) with the project number 234019.

The thesis is a collection of three papers, presented in chronological order. The common theme to them is in the methods to improve seismic imaging and migration-velocity model building. The papers are preceded by an introductory chapter that relates them together and provides background information and motivation for the work. One of the papers, I am the second author for the joint work. For the remaining papers, I am the first author.

Acknowledgements

I would like to thank my supervisors for their support through my Ph.D. study. I am especially grateful to Prof. Leiv-J Gelius and Assoc. Prof. Einar Iversen for their good guidance and advice for my studies and researches. I would also like to extend my gratitude to Prof. Martin Tygel, Prof. Anne H. Schistad Solberg., Dr. Walter Söllner and Dr. Endrias Asgedom for their co-supervision and discussions regarding my papers. I also specially thank Anders U. Waldeland for his good collaboration and valuable discussions in this project. I would also like to thank all the co-authors of the articles appended. During my Ph.D. study, I have worked at both the Department of Geosciences and the Digital Signal Processing and Image Analysis Group in Department of Informatics, where I have obtained the great support for my study and research. I especially thank professor Annik M Myhre, Professor Valerie Maupin, Michael Heeremans, Hans Peter Verne and Svein Bøe for your kind help of providing me the good environment for my study and arranging the necessary computing resource for conducting my work. Finally, I especially thank my parents and families for all the love and support for this journey.

Hao Zhao
Oslo, December 2019

List of Publications

This thesis is based on the following papers, referred to in the text by their romain numbers(I-III):

Paper I

Fast and robust common-reflection-surface parameter estimation.

Anders U. Waldeland, Hao Zhao, Jorge H. Faccipieri, Anne H. Schistad Solberg, and Leiv-J. Gelius.

Geophysics VOL.**83** NO.**1** (2018), O1-O13

Paper II

3D Prestack Fourier Mixed-Domain (FMD) depth migration for VTI media with large lateral contrasts.

Hao Zhao, Leiv-J. Gelius, Martin Tygel, Espen Harris Nilsen, and Andreas Kjelsrud Evensen.

Journal of Applied Geophysics VOL.**168** (2019), 118-127

Paper III

Time-migration velocity estimation using Fréchet derivatives based on nonlinear kinematic migration/demigration solvers.

Hao Zhao, Anders U. Waldeland, Dany Rueda Serrano, Martin Tygel, and Einar Iversen.

Studia Geophysica et Geodaetica. Accepted for publication, November 2019

Related Publications

The following papers are related to the thesis but not included in their full text:

Paper I

A New Generalized Screen Propagator for Wave Equation Depth Migration.

Hao Zhao, Leiv-J. Gelius, and Martin Tygel.

Extended abstract 77th EAGE Conference and Exhibition , Madrid, 2015

Paper II

Time-migration Tomography based on Reflection Slopes in Pre-stack Time-migrated Seismic Data.

Hao Zhao, Anders U. Waldeland, Dany Rueda Serrano, Martin Tygel and Einar Iversen.

Extended abstract 80th EAGE Conference and Exhibition , Copenhagen, 2018

Contents

List of Figures

List of Tables

Chapter 1

Introduction

In reflection seismology, reflected seismic waves are used to image, and estimate the elastic properties of, the subsurface. This method is widely used in the petroleum industry for hydrocarbon exploration and reservoir monitoring. The principle of reflection seismology is based on the reflection of acoustic waves generated from a seismic source, and the measurement of the propagation of those waves through the medium of the earth. In reflection experiments, the emitted seismic waves propagate down into the earth, and are reflected and refracted at each litho stratigraphic boundary. Those reflected waves are recorded by sensors near the surface within a defined time period, and are subsequently processed in order to image the subsurface structures, predict the types of rocks encountered and determine the presence of hydrocarbons (oil and gas).

Seismic migration – the major technique used for imaging Earth's interior – extrapolates and maps seismic events recorded at the surface to their true subsurface locations, thereby creating an accurate image of the subsurface. Migration algorithms are classified by time and depth based on the domain of the application. Both of these can be performed either after (poststack migration) or before (prestack migration) stacking. The time-migration method generates the migrated image in the time domain, which is known to be a fast and robust process that has enabled its wide use in the seismic industry for several decades. In comparison, depth migration produces the image in the depth domain, which can be directly used in hydrocarbon characterisation. The significant difference between time and depth migration is that time migration assumes mild, lateral velocity variations, while depth migration accommodates large velocity variations, both in vertical and lateral directions, thus deriving more accurate images under variable circumstances .

Depth-migration algorithms can be further classified into ray-based and wavefield-extrapolation-based methods. The ray-based depth migration methods, which solve the wave equation under the assumption of high-frequency approximation, have an advantage in being computationally efficient, but their weakness being in their limited accuracy in imaging complex structures. The wavefield-extrapolation-based depth migration methods directly solve the wave equation, and are able to handle more complex cases of seismic imaging. Based on differences in the way the dispersion relationship of the wave equation is solved, wavefield-extrapolation-based depth migration is divided into one-way and two-way wave equation migration (OWEM, TWEM). TWEM is represented by reverse-time migration (RTM), which utilises full wave fields in the imaging process, making it theoretically capable of handling the most complex cases of depth imaging. However, due to its high demand for computer memory and the computational costs, RTM use is still limited in large-scale industrial situations. OWEM, with appropriately-developed algorithms, is able to achieve migrations comparable to those from RTM in moderate to complex geological scenarios, but works more efficiently in large-scale situations. Moreover, due to its superior performance when compared to Kirchhoff-type depth-migration methods, OWEM still plays an import role in the industry for seismic depth imaging in complex subsurface areas.

The accuracy of depth imaging relies on the quality and details of the velocity model. Iterative depth-velocity model building, based on Kirchhoff-based depth-migration and ray-theory reflection tomography, is the most widely used approach in constructing detailed depth-velocity models. Two limitations of this approach are the heavy costs associated with the iterations, and it also usually requires an appropriate initial-velocity model generated by time-domain processing. Moreover, the process of velocity model building becomes more challenging if the subsurface contains complex geological structures, such as salt domes. Time-consuming manual interpretation of the geological bodies and the iterations are always needed in such circumstances. Reflection-based tomography methods rely on the quality of the seismic data, and deliver velocity models with limited resolution. In the case of data with a low signal-to-noise ratio (SNR), or associated with strong attenuation, these methods fail to provide satisfactory tomographic results. Full-waveform inversion (FWI) attempts to invert the high-resolution velocity model, using TWEM-based modelling and an inversion scheme for velocity optimisation. FWI calculates the difference between the modelled synthetic data and the seismic record, generating the gradient of the cost function for iterative velocity optimisation. Although FWI has been regarded as one of the best tools for velocity estimation and imaging in complex geological settings, its application requires preserved low frequencies, as well as considerably larger offsets, to record the direct/diving/refracted waves in seismic acquisition, which limits its application in conventional seismic reflection situations.

1.1 Motivations

With the progress of exploration and production, the petroleum industry has moved into exploring fields that have ever more complex geological structures. Examples include salt deposits in the Nordkapp Basin in the Norwegian Barents Sea, carbonate reservoirs in the Middle East and pre-salt discoveries in the Santos Basin in Brazil. Conventional seismic processing and imaging methods face challenges with resolution, SNR or accuracy of the image in such geological scenarios. Thus, there is a strong need to further develop the techniques employed in seismic processing and imaging to better handle these challenges.

The motivation behind this project was to develop improved techniques for high-resolution seismic imaging, in combination with the iterative, 3D depth-velocity model-building approach, in order to address velocity modelling and depth imaging in complex geological scenarios. Based on this motivation, we have developed three new methods for enhancing seismic images in complex environments. First, in order to improve the SNR in images of complex subsurface geological environments, we have proposed a fast parameter estimation approach for a common reflection surface (CRS) technique. Second, to improve the accuracy of seismic depth-domain imaging in vertical transversely-isotropic (VTI) media with large lateral contrasts and complex structures, we have developed a 3D prestack Fourier mixed-domain (FMD) depth-migration technique. Finally, to develop an accurate time-migration velocity model for time-domain migration, and an accurate initial model for depth imaging, we have developed a numerical algorithm for time-migration velocity estimation using nonlinear mapping processes based on kinematic time migration and demigration.

1.2 Scope of the thesis

This study constitutes part of the joint project *Improved seismic imaging based on resolution enhancement and pattern recognition*, which is a collaboration between the Department of Geosciences and the Department of Informatics at the University of Oslo. An outline of the entire project's workflow is shown in Fig.1.1.

As a first step, we employed the CRS method (e.g. Mann et al., 1999; Jäger et al., 2001) to estimate the kinematic wavefield attributes; that is, the CRS stack parameters. The CRS method is known to be an effective approach for improving the SNR and the continuity of the reflections in the stack, but is computationally expensive in terms of parameter estimation. For this project, we proposed a fast and robust approach for CRS parameter estimation that can effectively speed up the process. The conventional poststack CRS approach only derives a zero offset (ZO) stack. Zhang et al. (2001) generalised the CRS approach to produce a finite offset stack, thus extending the CRS approach to prestack application. In this project, a fast parameter searching approach was also provided in order to estimate the prestack CRS attributes (Waldeland et al., 2019). Based on the derived prestack CRS parameters, the SNR of the prestack data can be significantly enhanced, and used for subsequent seismic processing and imaging.

Next, in order to derive an accurate depth-velocity model for depth-domain seismic imaging, we started with an estimation of the time-migration velocity using kinematic wavefield parameters. Unlike formalising the tomography to obtain the depth-velocity model directly (Duveneck, 2004), we simplified the process using a more stable approach, including the estimation of time-migration velocity using first-order kinematic attributes, and mapped the derived time-migration velocity to the depth domain by image-ray tomography (Cameron et al., 2007; Dell et al., 2014; Gelius et al., 2015). The mapped depth velocity was then used as the initial velocity model for the following iterative process of depth-velocity model-building.

Finally, the conventional iterative depth-velocity modelling approach consists of prestack Kirchhoff depth migration (Claerbout, 1985; Biondi et al., 1996) and reflection tomography (Trier, 1990; Stork, 1992; Boehm et al., 1996). The

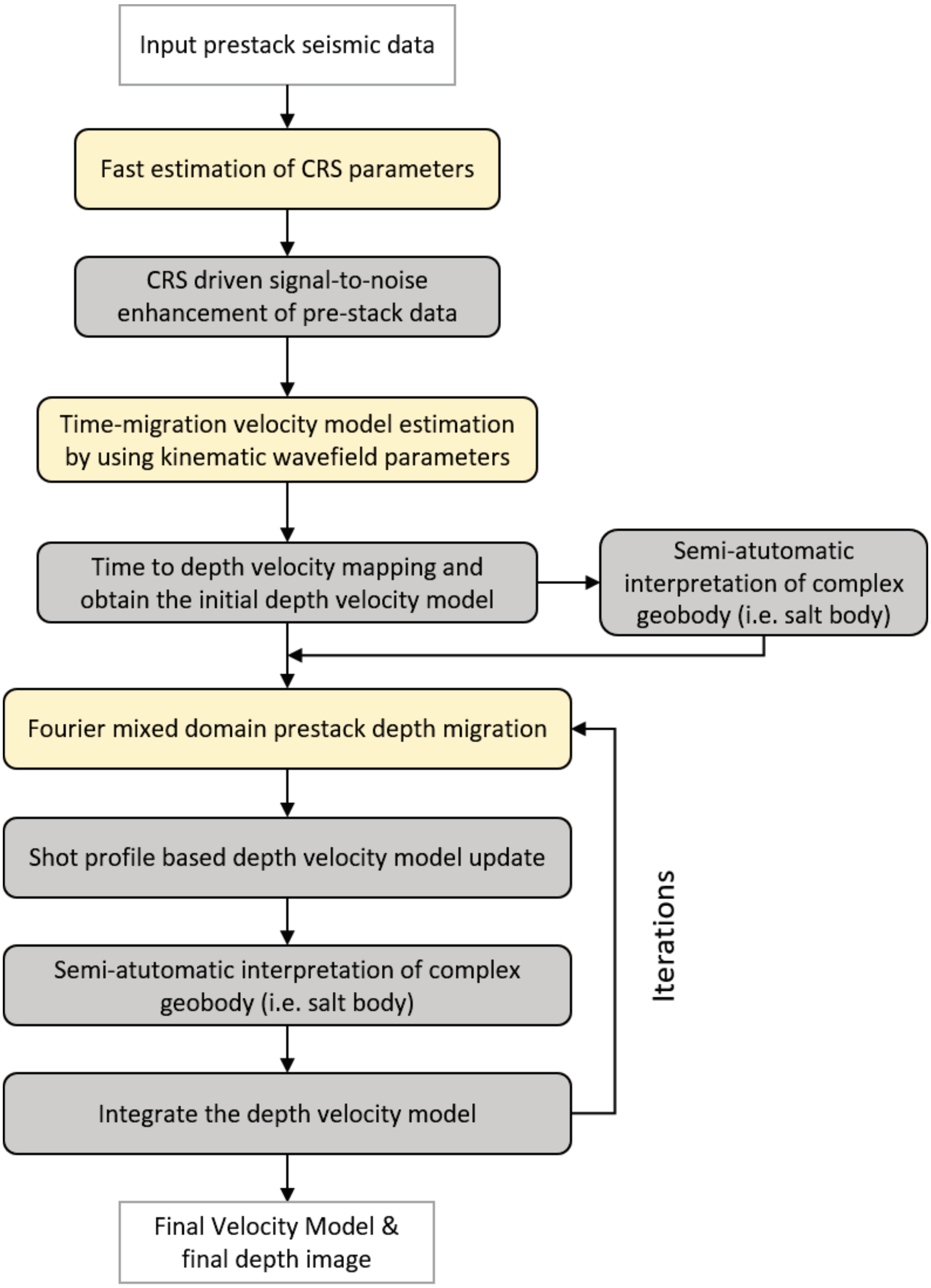

Figure 1.1: Iterative depth-velocity model-building and depth-imaging workflow. Those steps marked with yellow represent the content of this thesis.

prestack Kirchhoff method is widely used in the industry due to the attractiveness of its efficiency of computation. However, as a ray-based migration approach, it has limited accuracy in imaging complex structures with strong velocity variations and steep dips. We thus proposed an OWEM-based FMD depth-migration approach to handle such scenarios. The proposed FMD prestack depth-migration (PSDM) method, which provides greater accuracy than the Kirchhoff method in imaging complex geological areas, and is more computationally efficienct than RTM, was more suitable to be used for the iterative velocity estimation in complex geology. The FMD migration made use of shot gathers, and derived migrated shot profiles in the depth and summed depth images.

In order to fine-tune the depth-velocity model, a shot-profile-based depth-velocity update can be applied to derive the updated velocity model (Al-Yahya, 1989; Shen et al., 2008). In cases where the studied area also contains strong velocity anomalies related to salt or volcanic rocks, manual intervention is always needed to monitor the conventional velocity model-building process. Also, iterations of the manual interpretation of anomalous geological bodies are needed in the velocity modelling. On this join project, We therefore proposed a deep-learning-based (convolutional neural network), semi-automatic interpretation approach to assist in this process (Waldeland et al., 2018). As proved through testing, this automated method derived high-quality salt interpretation, and effectively reduced the cost of manual picking as part of the velocity modelling iterations. In the last step of velocity updating, the derived anomalies, delineated using interpreted contours and a predefined velocity, can be concatenated into the original velocity model. The FMD depth migration and velocity updating can then be applied iteratively in order to derive the optimal depth-velocity model and depth image. In this study, I focused on three topics from the workflow mentioned above (steps marked in yellow):

1. The CRS method is effective in improving the SNR and the continuity of the reflections on the stack. However, the conventional semblance-based CRS parameter search is computationally expensive. In order to speed up the parameter estimation process, we proposed a method based on gradient and quadratic structure tensors (GSTs, QSTs) to extract the CRS parameters (slope and curvature). This topic is described in Paper I.

2. In the iterative process of depth-velocity modelling, 3D prestack Kirchhoff depth migration is the most widely used algorithm; however, its loss of accuracy in imaging complex media with large lateral contrasts is well known. OWEM techniques are therefore more suitable, due to their better performance in complex media and their computational attractiveness compared to RTM. Although there are many different methods that can accomplish one-way wave propagation in VTI media, most of them struggle either with stability, anisotropic noise or computational cost. In Paper II, we presented a new method based on a mixed space and wavenumber propagator that overcomes these issues effectively.

3. The initial velocity used for PSDM always originates from a time-to-depth converted time-migration velocity. In conventional time-domain seismic processing, the time-migration velocity is derived from stacking velocity picking and Dix conversion. As an alternative, we proposed a time-migration velocity estimation method that directly uses the kinematic wavefield parameters, deriving the optimal time-migration velocity through an iterative linear inversion approach. This topic is described in Paper III.

1.3 Thesis outline

This thesis is organised as follows. In Chapter 2, we describe the basic concepts of the CRS method and introduce the GST and QST techniques, which were used in kinematic wavefield parameter extraction in Papers I and III. In Chapter 3, we firstly discuss the major (ray- and wavefield-based) categories of depth-migration imaging algorithms, going on to discuss wavefield extrapolation methods and migration imaging conditions in some detail, then explaining the advantages and disadvantages of major OWEM methods in the Fourier domain and pointing out the importance of improving those methods by using the proposed FMD migration (Paper II). In Chapter 4, we focus on the background underpinning Paper III, providing an overview of the approaches used in migration-velocity estimation. We then introduce the specific definition of the kinematic wavefield attribute, and the kinematic migration and demigration approach for nonlinear kinematic attribute mapping and time-migration velocity estimation. Finally, we summarise the three papers included in this thesis, present the main contributions made, and give suggestions for possible future work.

Chapter 2

Structure tensor methods for a common reflection-surface stack

The Common-Reflection-Surface (CRS) method is an effective approach in enhancing the SNR of a stack. The bottle-neck of CRS is the time-consuming semblance search to obtain CRS parameters. In order to speed up this parameter estimation process, we introduced a fast method in paper I for extracting the CRS parameters using local kinematic parameters: the slope and the curvature. To further demonstrate the application of local kinematic parameters, in paper III, we developed a time-migration velocity estimation method by employing the first-order local kinematic parameters (slopes). In this chapter, we first present an overview of the common-midpoint (CMP) method and the CRS method, and introduce the conventional CRS parameter estimation based on semblance search. Then, we give an introduction to the structure tensor method and demonstrate how this method is used to extract the local slope and curvature sought in the CRS parameter estimation.

2.1 Common reflection surface stack

The CRS stack (Mann et al., 1999; Jäger et al., 2001) was developed to enhance the SNR of seismic data. Compared to the conventional normal moveout (NMO) stack, the CRS stack provides a strong increase in redundancy and SNR, leading to clearer sections and more continuous events. The well-known problem with CRS is its expensive computation of the semblance-based parameter searches. In order to solve this problem, based on the gradient structure tensor (GST) method, we have introduced an efficient and robust method for the CRS parameter search. In this section, we provide an overview of the CMP method, then we extend this concept to the CRS method and introduce the conventional-semblance-search-based CRS parameter estimation.

2.1.1 Common-mid-point method

The CMP stacking method was introduced by Mayne (1962). It is an efficient and widely used method for improving the SNR in seismic imaging. As shown in Fig.2.1, the CMP is the central point between the source and receiver pairs at the surface. The set of traces recorded from different source/receiver pairs that have the same CMP is called a CMP gather. Under the assumption of a horizontally-layered model for the earth and a small offset spread, the travel time of the rays associated with the different source/receiver pairs can be approximated by a hyperbolic two-way travel-time equation (Eq.2.1),where t_0 is the two-way travel time at ZO, and h and v_{NMO} denote the half offset and NMO velocity, respectively.

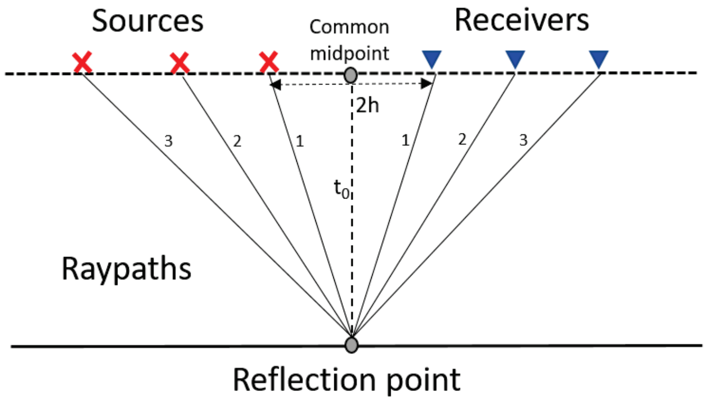

Figure 2.1: Schematics of CMP geometry

$$t^2 = t_0^2 + \frac{4h^2}{v_{NMO}^2} \tag{2.1}$$

Following acquisition, the recorded dataset is sorted into CMP gathers based on the coordinates of the sources and receivers. Traces in each of the CMP gathers are NMO corrected to remove the moveout effect on the travel times. The NMO-corrected traces are then summed to form a stacked trace. The summation of the NMO-corrected CMP traces leads to the enhancement of the SNR through the addition of coherent reflections and the stacking out of incoherent noise. Fig.2.2 shows a schematic of the recorded and sorted traces in a CMP gather, the NMO-corrected CMP traces, and the final stacked trace.

In most cases, CMP stacking is a robust process that will enhance the SNR of the stacked section. However, CMP stacking has limitations in its application. Because it assumes a straightforward stratigraphic earth model and a short spread in the acquisition, where complex geological structures or structures associated with strong lateral velocity variations exist, CMP stacking is less accurate and thus degrades the quality of the stack. The CRS stack can be regarded as an extension of the CMP stack. To obtain a stacked trace from a given midpoint, unlike stacking traces only in a CMP gather, CRS sums the traces along a common reflection surface that covers the traces from nearby midpoints. This leads to a significantly higher SNR in the final stack.

2.1.2 2D common reflection surface method

The CRS method (Mann et al., 1999; Jäger et al., 2001) was originally developed as an alternative to conventional stacking approaches, such as the NMO/DMO stack, as a way of enhancing the SNR. The CRS operator can be derived by paraxial ray theory (Schleicher et al., 1993) or by the geometrical approach of

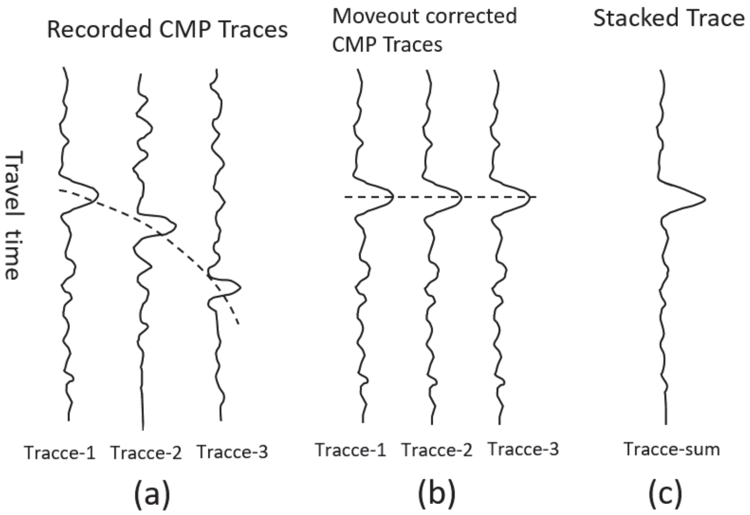

Figure 2.2: Illustration of the CMP stack. (a) CMP-sorted traces, (b) NMO-corrected CMP traces, and (c) the stacked trace.

Höcht et al. (1999). It resembles the polystack (Bazelaire, 1988) and multifocusing (Berkovitch et al.,1998) operators. The CRS method was initially developed for ZO CRS, and was then further generalised to handle the common offset (CO) case by Zhang et al. (2001). In this thesis, we focus on the ZO CRS and its related parameter estimation. Fig.2.3 shows a schematic comparison of the CMP and ZO CRS operators in the midpoint and half-offset domain .

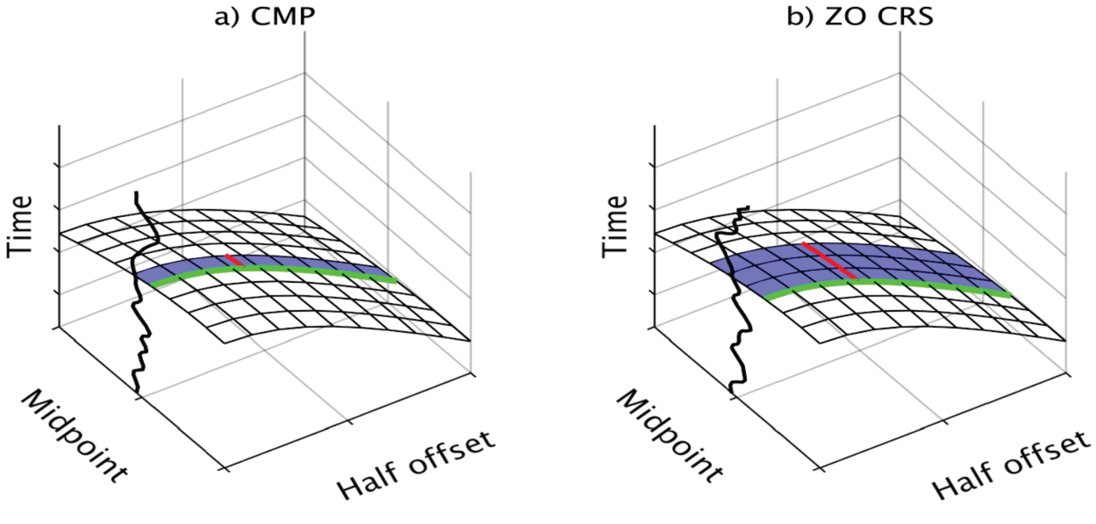

Figure 2.3: Comparison of the CMP and ZO CRS operators. (a) CMP operator in the midpoint and half-offset domain . (b) ZO CRS operator in the midpoint and half-offset domain . The aperture is centred around the midpoint, and is defined by the green line where the half-offset is used and the red line where the midpoint is used.

In the general case, the CO CRS in 2D can be formulated as a second-order

Taylor expansion of the travel-time surface around a central point with the coordinates x_0,h_0 (Faccipieri et al., 2016):

$$t^2_{CRS}(x,h) = (t_0 + A\Delta x + D\Delta h)^2 + B\Delta x^2 + C\Delta h^2 + \varepsilon\Delta x\Delta h, \tag{2.2}$$

where x and h denote the coordinates of the midpoint and half-offset of a selected point in the reflection surface. $\Delta x = x - x_0$ and $\Delta h = h - h_0$. A, B, C, D and E are the CRS model parameters defined in Eq.2.3, which represent the first- and second-order derivatives with respect to the reflection surface at the reference point.

$$A = \frac{\partial t}{\partial x}, \quad B = t_0\frac{\partial^2 t}{\partial x^2}, \quad C = t_0\frac{\partial^2 t}{\partial h^2}, \quad D = \frac{\partial t}{\partial h}, \quad \varepsilon = 2t_0\frac{\partial^2 t}{\partial x\partial h}|_{x=x_0,h=h_0}. \tag{2.3}$$

According to paraxial ray theory, and because the approximation of the CRS operator is truncated to the second order in the Taylor expansion, Eq.2.3 is only accurate in the vicinity of the reference midpoint (x_0,h_0). With respect to the ZO CRS case ($h_0 = 0$), the general 2D CRS operator simplifies to:

$$t^2_{CRS}(x,h) = (t_0 + A\Delta x)^2 + B\Delta x^2 + Ch^2, \tag{2.4}$$

where A, B and C are the CRS model parameters describing the ZO case. In the case of the 3D ZO CRS, these parameters are generalised to vectors and matrices, as given in Eqs. 2.5-2.7:

$$\mathbf{A} = \left[\begin{array}{c} \frac{\partial t}{\partial x} \\ \frac{\partial t}{\partial y} \end{array}\right]\Bigg|_{\mathbf{x}=\mathbf{x}_0,\,\mathbf{h}=0}, \tag{2.5}$$

$$\mathbf{B} = t_0\left[\begin{array}{cc} \frac{\partial^2 t}{\partial x^2} & \frac{\partial^2 t}{\partial x\partial y} \\ \frac{\partial^2 t}{\partial x\partial y} & \frac{\partial^2 t}{\partial y^2} \end{array}\right]\Bigg|_{\mathbf{x}=\mathbf{x}_0,\,\mathbf{h}=0}, \tag{2.6}$$

$$\mathbf{C} = t_0\left[\begin{array}{cc} \frac{\partial^2 t}{\partial h_x^2} & \frac{\partial^2 t}{\partial h_x\partial h_y} \\ \frac{\partial^2 t}{\partial h_x\partial h_y} & \frac{\partial^2 t}{\partial h_y^2} \end{array}\right]\Bigg|_{\mathbf{x}=\mathbf{x}_0,\,\mathbf{h}=0}. \tag{2.7}$$

We can see from Eq. 2.4 that three model parameters must be determined for the 2D (ZO) CRS, and eight for the 3D (ZO) CRS because **B** and **C** are symmetric matrices. Once we have derived the CRS parameters, the stack can be applied by summing all traces within a selected aperture. Bear in mind that a larger stacking aperture will increase the SNR, but may also lead to too much smoothing of details in the stack. Thus, the CRS operator in the offset and midpoint has to be selected carefully to retain both the high resolution and high SNR in the stack image (Faccipieri et al.,2016).

2.1.3 Common reflection surface parameter estimation

As indicated above, CRS parameter estimation is a challenging and expensive computational process. With respect to the number of parameters in the CRS calculation (Tab. 2.1), in the case of ZO CRS, there are three parameters in 2D and eight in 3D. The number of parameters increases to five for 2D and 13 for 3D in the case of CO CRS. Thus, the balance between accurate parameter estimation and feasible computational cost is always the issue with CRS.

	2D	**3D**
ZO CRS	3 parameters	8 parameters
CO CRS	5 parameters	13 parameters

Table 2.1: Number of parameters in CRS

A semblance-based parameter search (Neidell et al., 1971) is the most commonly used approach in CRS. As defined in Eq.2.8, semblance measures the ratio between the coherent energy and the total energy in a defined time window. As shown in Fig.2.4, the window used in the semblance calculation is given as a time gate along the CRS operator. Based on the criteria of the semblance, we can evaluate all possible CRS parameter combinations at any given point in the stack, and so derive the optimal CRS parameters.

$$S(t_{CRS}, x_0, h_0, t_0) = \frac{\sum\limits_{t=t_{CRS}-T_w}^{t_{CRS}+T_w} \left(\sum\limits_{x,\, h \in \mathcal{X}_0} \mathbf{I}(x,h,t) \right)^2}{N \sum\limits_{t=t_{CRS}-T_w}^{t_{CRS}+T_w} \sum\limits_{x,\, h \in \mathcal{X}_0} \mathbf{I}(x,h,t)^2}, \tag{2.8}$$

where $\mathbf{I}(x, h, t)$ is the 2D prestack data in the midpoint and offset domain , and N is the total number of traces. t_{CRS} is the CRS travel-time surface, defined at the reference point (x_0, h_0, t_0). The aperture of the surface is given by $\mathcal{X}_0$, and the time-window used in the semblance calculation is defined along the CRS travel-time surface within the time gate: $[t_{CRS} - T_w, t_{CRS} + T_w]$, where T_w is half of the window size.

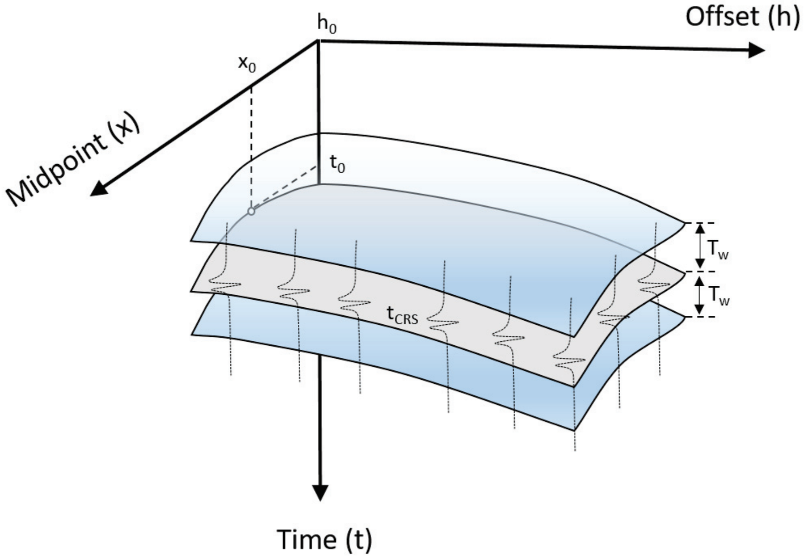

Figure 2.4: CRS semblance calculation window. The grey surface (t_{CRS}) represents the CRS travel-time surface calculated at the reference point (x_0, h_0, t_0), and the two light blue surfaces resemble the time gate used for semblance calculation.

The semblance-based global search is computationally expensive. It has to search all predefined parameter combinations to obtain the optimal parameters. The computational cost increases significantly from a ZO CRS to CO CRS, and from a 2D (ZO/CO) to 3D (ZO/CO) CRS. To overcome this limitation, alternative approaches have been proposed. The pragmatic searches proposed by Mann et al. (1999) and Jager et al. (2001) suggested finding the three parameters sequentially. In 2D, this begins with searching for the correlation parameter in the CMP domain, and subsequently by constructing the CMP stack and search for the remaining parameters – emergency angle and curvature. In the last step, based on the initial searched parameters, a global parameter optimisation is applied to further refine the parameters. A further pragmatic search approach was proposed by Garabito et al. (2001). Their hybrid method started with a simultaneous search for the emergence angle and velocity on prestack data, followed by a one-parametric semblance search to obtain the curvature, and a global optimisation employed to refine the parameters. In addition to these pragmatic CRS parameter approaches, other search strategies have been proposed. Most of them are based on optimisation algorithms that reduce the number of searches in the semblance approach. The most popular approach in this category is the CRS parameter search based on simulated annealing (Müller, 2003; Garabito et al., 2001; Minato et al., 2012).

One of the main challenges in CRS parameter estimation is to handle the case of conflicting dips, since conventional parameter estimation approaches lead to only one set of CRS parameters. This may lead to a problem of conflict in the dips. To solve this problem, Mann (2001) and Müller (2009) proposed deriving multiple CRS parameter sets for conflicting-dip regions that are identified by a threshold of multiple-semblance maxima on the emergence angle. The final stack is then constructed by merging the multiple sections generated by these individual parameter datasets.

2.2 Structure tensor methods

Structure tensor methods use the gradient information from an image to determine the orientation information of local structures in that image. This technique has been widely used in image processing and computer vision for pattern recognition and feature detection. In the following, we give an introduction to the structure tensor concept, and a demonstration of its application to local slope and curvature extraction from seismic data.

2.2.1 Gradient structure tensor

The structure tensor describes the local structures in an image by calculating the predominant directions of the gradient in a specified neighbourhood of a point. There are several implementations and applications of the structure tensor in the literature. Bigun et al. (1987) introduced the GST method to detect the orientation of a local neighbourhood, in both the frequency and space domains. Kass et al. (1988) used the structure tensor derived from first-order derivatives to calculate the local orientation of 2D images. Knutsson (1989) successfully used the structure tensor to estimate the orientation of 3D surfaces. The GST (Bigun et al., 1987), being an efficient and simplified implementation of the structure tensor, was used in the present study for the estimation of slopes and curvatures from the seismic data.

According to Bakker (2002), for a 3D seismic cube, represented by a vector $\mathbf{x}$ ($\mathbf{x} = [x, y, t]^T$), the generalised form of GST can be defined as:

$$\mathrm{T} \equiv \overline{\left(\frac{\mathbf{g}\mathbf{g}^T}{||\mathbf{g}||^n} \right)}, \tag{2.9}$$

where $\mathbf{g}$ is the gradient vector field $\mathbf{g} = [g_x(\mathbf{x}), g_y(\mathbf{x}), g_t(\mathbf{x})]^T$, $\mathbf{g}^T$ is the transposed vector, $||\ \mathbf{g}\ ||^n$ is the normalisation factor, and $\overline{()}$ represents the local smooth operation of the tensor.

The gradient vector field $\mathbf{g}$ can be derived from the finite difference scheme or the convolution of a gradient filter. The latter scheme is easy to implement and is less sensitive to noise, as shown in Eq.2.10, which derives the gradient fields (g_x, g_y, g_t) by convolving the input seismic image $I(\mathbf{x})$ with the derivative of a Gaussian function $G(\mathbf{x}, \sigma_g)$.

$$g_i = I(\mathbf{x}) * \frac{\partial}{\partial \mathbf{x}_i} G(\mathbf{x}, \sigma_g), \quad i = (x, y, t). \tag{2.10}$$

where $\frac{\partial}{\partial \mathbf{x}_i}$ is the differentiation operator applied to the Gaussian function, and the parameter σ_g is the variance that represents the scale of the defined Gaussian function.

Once the gradient vector fields are derived, the GST is constructed as Eq.2.11, which corresponds to the co-variance matrix of the gradient vector fields.

$$\overline{\mathbf{T}} = \begin{bmatrix} \overline{g_x^2} & \overline{g_y g_x} & \overline{g_t g_x} \\ \overline{g_x g_y} & \overline{g_y^2} & \overline{g_t g_y} \\ \overline{g_x g_t} & \overline{g_y g_t} & \overline{g_t^2} \end{bmatrix}, \tag{2.11}$$

where the elements g_x, g_y and g_z are the gradient vector fields obtained from Eq.2.10. The symbol $^-$ represents the additional smoothing operation on the gradients. The purpose of the additional smoothing is to further remove the noise in order to stabilise the GST in the subsequent matrix decomposition. The smoothing operation can be implemented through a normal spatial smoothing filter on the derived gradient volumes.

2.2.2 Local slope estimation by gradient structure tensor

Because the orientation information of local structures is associated with the eigenvalues and eigenvectors of the above-constructed GST $\overline{\mathbf{T}}$, the eigen decomposition of the tensor ($\overline{\mathbf{T}}$) is applied to derive the eigenvalues $(\lambda_1, \lambda_2, \lambda_3)$ and eigenvectors $(\mathbf{v_1}, \mathbf{v_2}, \mathbf{v_3})$, which are illustrated in Fig.2.5, where those three vectors point in the direction of the eigenvectors, and the length of each vector on each axis resembles the corresponding magnitude of the eigenvalues.

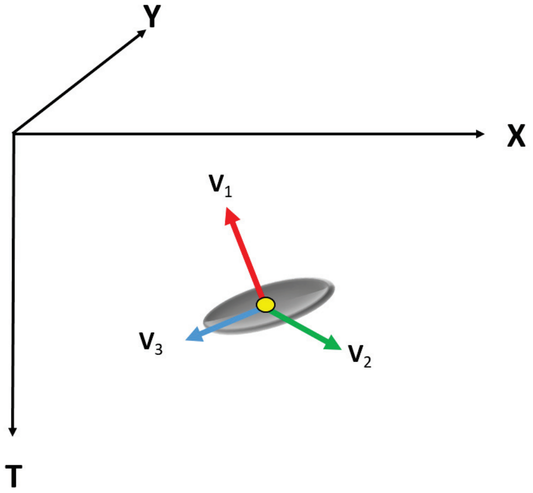

Figure 2.5: Schematic representation of the 3D structure tensor. Vectors $(\mathbf{v_1}, \mathbf{v_2}, \mathbf{v_3})$ are derived from the GST of a local point on a planar surface. The length of each vector represents the magnitude of the eigenvalues $(\lambda_1, \lambda_2, \lambda_3)$.

By analysing the decomposed eigenvalues and eigenvectors, we can obtain orientation information about the local structure in the image. The eigenvector associated with the largest eigenvalue corresponds to the dominant orientation of the gradient vector field. In the case of the derived eigenvalues ($\lambda_1 \geq \lambda_2 \geq \lambda_3$), the corresponding eigenvector $\mathbf{v_1}$ is then the dominant direction of the gradient vector field.

With respect to a seismic planar reflector, the GST-derived eigenvector $\mathbf{v_1}$ represents the normal vector to the reflector plane. Thus, by considering the components of $\mathbf{v}_1 = [v_{1x}, v_{1y}, v_{1t}]$, the corresponding slopes along the dominant direction can then be derived using Eqs. 2.12 and 2.13:

$$q_x = \frac{\widehat{\partial t}}{\partial x} = \frac{v_{1x}}{v_{1t}}, \tag{2.12}$$

$$q_y = \frac{\widehat{\partial t}}{\partial y} = \frac{v_{1y}}{v_{1t}}. \tag{2.13}$$

When the GST method is applied to 3D seismic data, we can obtain the slope and azimuth attributes of the local reflector surfaces, which are directly related to the CRS parameters defined by their kinematic wavefront attributes.

2.2.3 Local curvature estimation using the quadratic gradient structure tensor

The GST method can be extended from the estimation of first-order derivatives (slope) to second-order derivatives (curvature). This extended method – the QST – was proposed by Weijer et al. (2001) and Bakker (2002).

This method assumes that an arbitrary surface $S(\mathbf{x}) = 0$ can be described by a second-order polynomial approximation:

$$S(\mathbf{x}) \approx \mathbf{x}^T \mathbf{A} \mathbf{x} + \mathbf{b} \mathbf{x} + c = 0, \tag{2.14}$$

where $\mathbf{A}$ is a symmetric 3×3 matrix, with at least two non-zero eigenvalues, and $\mathbf{b}$ is a unit normal vector to this surface.

Assuming that this quadratic surface is described by two principal curvatures, the approximated second-order polynomial (Eq.2.14) can be expressed as Eq.2.15 in the reflector-oriented coordinate system:

$$S(\mathbf{x}) \approx \frac{1}{2}\kappa_1 \mathbf{v} + \frac{1}{2}\kappa_2 \mathbf{w} + \mathbf{u}, \tag{2.15}$$

where κ_1 and κ_2 are the two principal curvatures of the surface, and $(\mathbf{u}, \mathbf{v}, \mathbf{w})$ are the vectors describing the local reflector-oriented coordinate system (Fig.2.6).

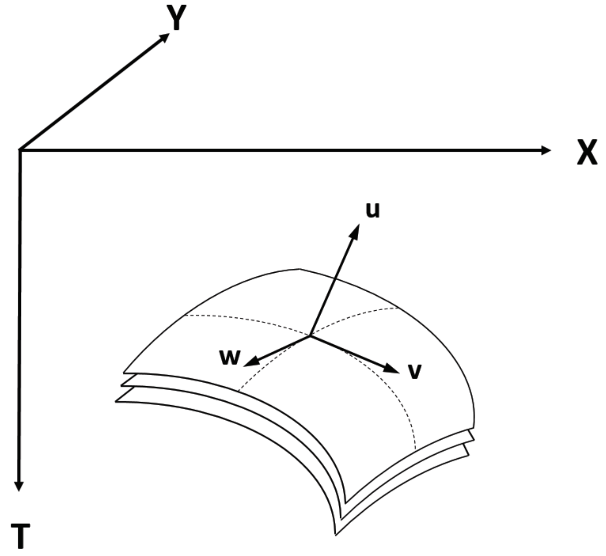

Figure 2.6: Schematic view of the local reflector-oriented coordinate system. The vector **u** is normal to the reflector, while vectors **v** and **w** are orthogonal to **u**, and correspond to the two principal curvatures (κ_1, κ_2).

As shown in Bakker (2002), this quadratic surface is described by two curvatures (κ_1, κ_2) and a local frame, which is oriented along the normal vector and the two vectors that correspond to the principal curvatures. By employing a coordinate transform scheme (Bakker, 2002), the quadratic surface can be deformed to a plane, and those curvatures can be estimated in the deformed surface system based on the traditional GST method. The two principle curvatures obtained from the reflector-oriented coordinate system can be expressed as:

$$\kappa_1 = \frac{\overline{\mathbf{v} g_u g_v}}{\overline{\mathbf{v}^2 g_u^2}}, \tag{2.16}$$

$$\kappa_2 = \frac{\overline{\mathbf{w} g_u g_w}}{\overline{\mathbf{w}^2 g_u^2}}, \tag{2.17}$$

where **v** and **w** are vectors derived from the traditional GST method, while g_u, g_v and g_w are the gradients along the axes in the reflector-oriented coordinate system.

Since the gradients (g_u, g_v, g_w) used in Eqs. 2.16 and 2.17 are computed in the local reflector-oriented coordinate system, this means that the gradient calculation is spatially variant with respect to different locations in the stack, which leads to a heavy computational cost. To avoid such a problem, Bakker (2002) introduced an approach based on a linear combination of the convolutions, which can be invariantly applied to the full stack, thus increasing the computational efficiency.

Finally, in order to obtain the derivatives with respect to x and y, the $\mathbf{v}$ and $\mathbf{w}$ must be set to be oriented along the x and y axes, in order to obtain the curvatures along axes x and y. Furthermore, to get the final curvatures in the 3D Cartesian coordinate system (x, y, t), the following coordinate rotations must be applied:

$$\kappa_x = \frac{\widehat{\partial t^2}}{\partial^2 x} = \kappa_1 \left(1 + \left(\frac{\partial t}{\partial x}\right)^2\right)^{\frac{3}{2}}, \tag{2.18}$$

$$\kappa_y = \frac{\widehat{\partial t^2}}{\partial^2 y} = \kappa_2 \left(1 + \left(\frac{\partial t}{\partial y}\right)^2\right)^{\frac{3}{2}}. \tag{2.19}$$

Chapter 3

Depth imaging with wavefield extrapolation migration

In Paper II, we proposed an OWEM depth-migration technique, Fourier Mixed-Domain (FMD) prestack depth migration. This can be regarded as a stable and explicit wavefield extrapolation-based migration algorithm. The FMD is a phase-screen type of migration, implemented both in the space and wavenumber domains, and valid for a 3D VTI medium with large lateral contrasts in vertical velocity and anisotropic parameters. In this chapter, we give an overview of the most important depth-migration methods and the necessary background for deriving the FMD migration algorithm.

3.1 Overview of seismic migration imaging methods

Seismic migration is a process that builds an image from recorded data by repositioning the recorded data to its true geological position in the subsurface. Fig.3.1 illustrates the concept of migration in the case of a dipping reflector. As shown in the figure, assuming a ZO seismic experiment was conducted in a constant-velocity medium (Fig.3.1(a)), the recorded traces are plotted vertically in time, causing a distorted image in the time domain (Fig.3.1(b)). In order to obtain the correct spatial position of the dipping reflector, migration needs to be applied to reposition the misplaced recorded data to its true geological position (Fig.3.1(c)).

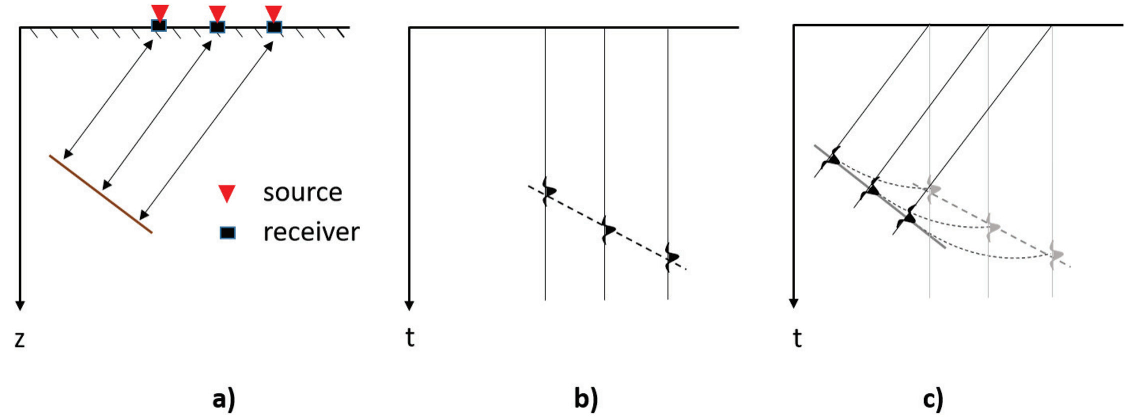

Figure 3.1: Illustration of the migration concept in relation to a dipping reflector. (a) Schematics of a ZO seismic acquisition for a dipping reflector. (b) The recorded seismic section. (c) The migrated (true) section.

Migration algorithms can be classified by time and depth, both of which can be performed either after stacking (poststack migration) or before stacking (prestack migration). Prestack migration applies to prestack data (shot, CMP or CO gather), while poststack migration operates on stacked data. In the following, we give a brief description of the major migration methods and discuss the strengths and weaknesses of these methods in different scenarios.

- **Poststack migration versus prestack migration**

Poststack migration is a cost-effective process. It assumes that the stacking process simulates a ZO section, and the migration performs in the ZO domain. However, with the growth of structural complexity, poststack migration becomes inaccurate because the stack is not able to approximate the ZO section; prestack migration must be applied in such scenarios.

- **Time migration versus depth migration**

Time migration builds a migrated image in two-way travel time, while the depth migration method directly outputs vertical-depth images. Apart from the cost efficiency of time migration over depth migration, the major difference between them is how they cope with lateral velocity variations. Time migration assumes that lateral velocities are invariant/homogeneous along a cable length and are generally gentle. Conversely, depth migration accommodates lateral velocity changes and is capable of correctly imaging complex structures associated with strong velocity variations. However, in order to get an accurate image from depth migration, accurate depth-velocity parameters (vertical velocity, anisotropic parameters) are required, which are always challenging to obtain.

- **Ray-based versus wavefield-extrapolation-based migration**

With respect to the implementation of migration algorithms, migration can be categorised into ray-based and wavefield-extrapolation-based methods. These are also known as integral migration algorithms and differential migration algorithms, respectively. Unlike the wavefield-extrapolation-based methods that solve the wave equation directly, ray-based migration methods are based on high-frequency approximations. Thus, seismic waves approximate rays and ray-paths, with the assumption that the scale of the structure is greater than the seismic wavelength. The Kirchhoff integral migration is the classic ray-based migration method, and it has been widely used in industry for both time and depth migrations. However, ray-based migration methods rely on a gently varying smooth velocity field for calculating travel times, which makes these less accurate than the wavefield-extrapolation-based methods in cases where the subsurface is complex and has strong velocity variations. An extension of the Kirchhoff migration method is the ray-based Gaussian beam migration (GBM). Compared to traditional Kirchhoof methods that migrate one trace at a time, the GBM processes a group of traces (a supergather) and maps the supergather collectively into the migration domain. The advantage of the GBM is that it can handle multi-path arrivals, as opposed to the single-path Kirchhoff method, and it can achieve comparable results to wavefield-extrapolation-based migration methods, but with less computational cost in imaging structures with moderate complexity.

- **One-way versus two-way wave equation migration**

Wavefield-extrapolation-based migration (also known as wave-equation migration (WEM)) models the full wavefield in a propagation so that it can image all the energy from the surface to the subsurface point in order to generate an accurate image in areas where the subsurface is complex. wave-equation migration can be classified into one-way wave-equation migration (OWEM) and two-way (full-wave) wave-equation migration (TWEM). Reverse time migration (RTM) is the best known algorithm based on TWEM, which utilises both down-going and up-coming wavefields. As an advanced WEM method, RTM is able to handle most of the challenges associated with seismic imaging, including large velocity variations, steep dips, multiple paths and caustics. However, RTM requires full wavefield modelling in each migration step, which leads to a heavy computational cost and large memory requirement. In comparison, OWEM is more cost-effective and requires less memory for computation. Moreover, OWEM is superior to ray-based migration methods, and is able to achieve comparable results to RTM in imaging complex structures, as well as strong velocity variations. Compared with RTM, the disadvantages of OWEM are that it has less accuracy in imaging very steep dips, and it does not treat turning waves and prismatic waves intrinsically. We give a detailed discussion of OWEM methods in the next section.

The above is summarised in Fig.3.2. This demonstrates the appropriate migration method needed, with respect to the complexity of the subsurface structures and of the lateral velocity. As can be seen, with an increase in the complexity of geological structures and lateral velocity, more advanced seismic migration methods, such as Kirchhoff PSDM, beam migration, one-way wavefield-extrapolation-based migration or RTM, must be applied. In this chapter, we focus our discussion on PSDM.

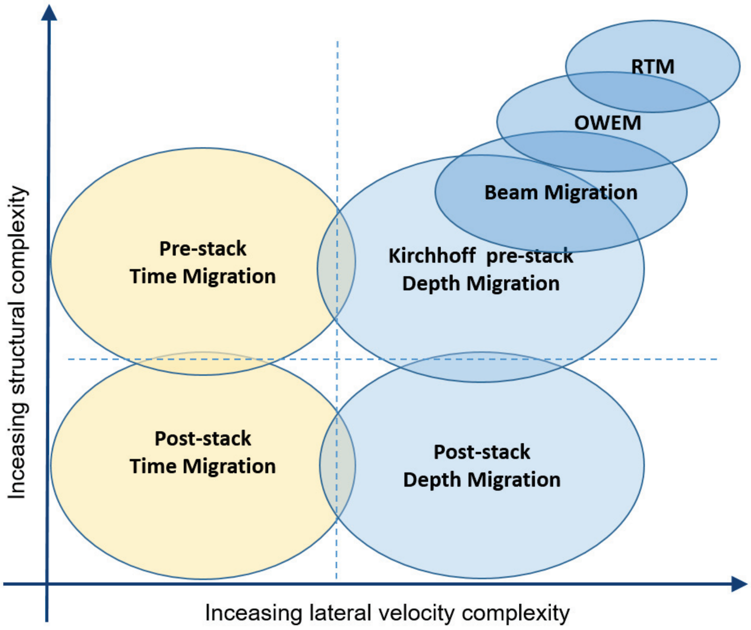

Figure 3.2: Comparison of migration methods.

3.2 Depth-migration methods

Depth migration handles complex subsurface structures with both vertical and lateral velocity variations, and generates an image directly in the depth domain. The quality of depth migration relies on an accurate depth-velocity model and an appropriate algorithm. Depth-migration methods can be categorised into ray-based and wavefield-extrapolation-based methods as already mentioned. We introduce these methods in more detail in the following sections.

3.2.1 Ray-based depth-migration methods

Ray-based migration methods, such as Kirchhoff and Gaussian beam migration, are based on solutions of the wave equation, assuming a high-frequency approximation. This assumption is acceptable if the seismic wavelength is much smaller than the scale of the structure(s) (Etgen et al., 2009; Jones, 2010). The classic method is Kirchhoff migration, as introduced by Schneider (1978) and developed further by Bleistein (1987), Bancroft et al. (1994) and Etgen et al., (1997). The basic formulation of Kirchhoff migration is given by Eq.3.1 (common-shot migration):

$$I(X;X_s) = \int dX_r \int W \frac{\partial P_u(X_r,X_s,t)}{\partial t} \delta[t-(t_s+t_r)]dt, \qquad (3.1)$$

where X is the image point location, X_s and X_r are, respectively, the locations of the source and receiver, t_s and t_r are travel times from the source and receiver locations to the image point, W is a weight function, P_u is the recorded wavefield, and δ is the Dirac function, representing the time shift in the integration.

This equation shows that the image point can be constructed by the integration of the combined rays from the source and receiver locations via the image point (as indicated in Fig.3.3). In practice, the Kirchhoff migration process is separated into two steps – the travel time table calculation, using dynamic ray tracing, and collection of the associated data samples for the summation. Due to the efficiency in its implementation and computation, Kirchhoff PSDM has been widely used in industry for depth imaging. However, as most of the commonly used Kirchhoff migration algorithms assume a single ray path between the source and receiver (although a multi-path Kirchhoff migration has recently been developed), these methods have limited accuracy in imaging complex structures. To solve this challenge, another type of ray-based migration – Gaussian beam migration (GBM) (Hill, 1990, 2001) – has been developed. GBM, being a directional Kirchhoff migration approach, is performed by applying the imaging to decomposed local-slant stacked traces and summing the contributions to form the migration image. Because this approach adds the contribution of different rays to the imaging, it naturally overcomes the single-path limitation of Kirchhoff migration, and thus derives improved image results for complex subsurface structures. However, as ray-based migration approaches, both GBM and Kirchhoff migration solve the wave equation under high-frequency approximation, which relies on a smooth velocity field for the ray path calculations.

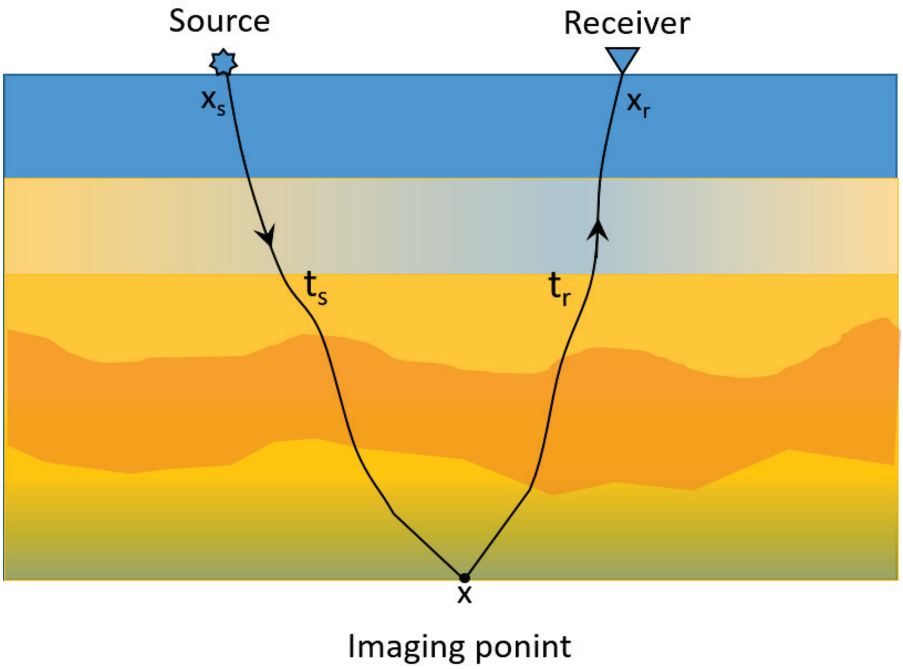

Figure 3.3: Kirchhoff prestack depth migration.

3.2.2 Wavefield-extrapolation-based depth migration

Wavefield-extrapolation-based depth migration is the most effective way to handle complex structures and strong velocity variations. Unlike the ray-based depth migration method, which uses ray tracing to construct the ray paths, wavefield-extrapolation-based depth migration uses the wave equation to model complete wavefronts. It can be classified into OWEM and TWEM, both of which use solutions of the (acoustic) scalar wave equation for the wavefield extrapolation. In general, all wavefield-extrapolation-based depth migration methods are based on two key steps: (1) extrapolation of the source wavefield and the receiver (record) wavefield; and (2) construction of the image by applying the imaging condition. Wavefield extrapolation can be implemented either in the time or depth domains. RTM (a TWEM method) employs both the down-going and up-coming wavefields. On the other hand, OWEM methods, such as shot-profile and survey-sinking migration, only utilise the one-way wavefield in the depth domain extrapolation. As mentioned above, RTM is able to solve most seismic-image challenges, but is characterised by expensive computational costs and significant memory demands. Thus, OWEM, as a cost-efficient WEM method, is still attractive in industrial application. We focus on discussing OWEM in the following sections.

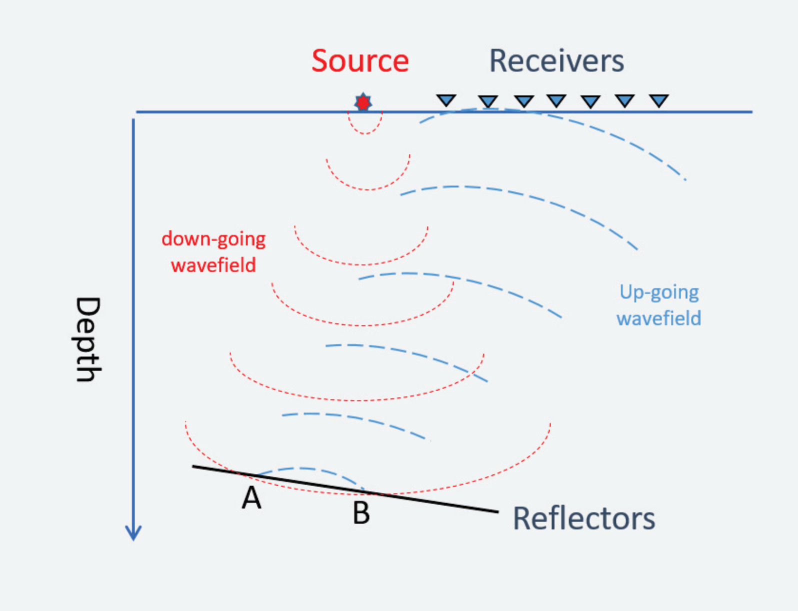

Figure 3.4: Wavefield extrapolation migration. The reflector image (A–B) is constructed by correlating the down-going (red curves) and up-coming (blue curves) wavefields.

Fig.3.4 illustrates the concept of wavefield extrapolation migration proposed by Claerbout (1971), who generalised it into two steps – computation of the down-going and up-going wavefield and application of an imaging condition to obtain an image of the reflectors. As illustrated in the figure, the down-going wavefield is derived from the forward propagation of the source field, and the up-coming wavefield is derived from the backward propagation of the recorded receiver field. The reflectors are then imaged when the down-going wavefield and up-going wavefield coincide in time (imaging condition).

3.3 Wavefield extrapolation and imaging condition

In wavefield-extrapolation-based migration, the wavefield extrapolation can be achieved by either directly solving the two-way wave equation through employing finite difference schemes, or by implementing the wavefield downward continuation, based on the one-way wave equation. We focus our discussion on the latter approach in this section.

Based on the 3D acoustic wave equation (Eqs. 3.2), we can split the two-way wave equation into two one-way wave equations (Eqs. 3.3 and 3.4) by applying a 3D Fourier transform with respect to the variables (x, y and t). The derived equations represent the solution of the down-going and up-going wavefields in the frequency-wavenumber domain.

$$\frac{\partial p^2}{\partial x^2}+\frac{\partial p^2}{\partial y^2}+\frac{\partial p^2}{\partial z^2}=\frac{1}{v^2}\frac{\partial p^2}{\partial t^2}, \tag{3.2}$$

where x and y are the spatial coordinates, z is the depth, v is the velocity of the medium and p is the pressure wavefield.

$$\frac{\partial \widetilde{d}}{\partial z}=-i\sqrt{\frac{\omega^2}{v^2}-(K_x^2+K_y^2)}\;\widetilde{d}, \tag{3.3}$$

$$\frac{\partial \widetilde{u}}{\partial z}=+i\sqrt{\frac{\omega^2}{v^2}-(K_x^2+K_y^2)}\;\widetilde{u}, \tag{3.4}$$

where K_x and K_y are horizontal wavenumbers, z is the depth, v is the velocity of the medium, ω is the angular frequency. $\widetilde{d}$ and $\widetilde{u}$ are respectively the 3D pressure down-going and up-going wavefield following the 3D Fourier transform, with respect to x, y and t.

From the integration of both sides of Eqs. 3.3 and 3.4, between limits z and z+dz, we derive the wavefield extrapolation equations for both the down-going (Eq.3.5) and up-going (Eq.3.6) wavefields in the frequency-wavenumber domain:

$$\widetilde{d}(z+\Delta z)=\widetilde{d}(z)\exp^{-i\sqrt{\frac{\omega^2}{v^2}-(k_x^2+k_y^2)}\Delta z}, \tag{3.5}$$

$$\widetilde{u}(z+\Delta z)=\widetilde{u}(z)\exp^{i\sqrt{\frac{\omega^2}{v^2}-(k_x^2+k_y^2)}\Delta z}, \tag{3.6}$$

where $\widetilde{d}$ and $\widetilde{u}$ denote the down-going and up-going 3D pressure wavefields in the frequency-wavenumber domain.

Eqs. 3.5 and 3.6 illustrate that wavefield extrapolation is a recursive process, where the wavefield can be extrapolated from one depth to another. In PSDM, the down-going wavefield is derived by the downward extrapolation of a predefined source function at the surface, and the up-going wavefield is the downward extrapolation from the receiver positions. The imaging condition is usually based on different versions of the concept: reflectivity = up-going wavefield/down-going wavefield. The original imaging condition was proposed by Claerbout (1971):

$$R(x, y, z_i) = \int \frac{u(x, y, z_i, \omega)}{d(x, y, z_i, \omega)} d\omega, \tag{3.7}$$

where $u(x, y, z_i, \omega)$ and $d(x, y, z_i, \omega)$ are the extrapolated up-going and down-going wavefields at depth level z_i, and R is the computed reflectivity.

In order to avoid instabilities associated with the division in Eq.3.7, the alternative formulation is used:

$$R(x, y, z_i) = \int \frac{u(x, y, z_i, \omega) d^*(x, y, z_i, \omega)}{d(x, y, z_i, \omega) d^*(x, y, z_i, \omega)} d\omega \approx \int u(x, y, z_i, \omega) d^*(x, y, z_i, \omega) d\omega, \tag{3.8}$$

where $d^*(x, y, z_i, \omega)$ is the complex conjugate of wavefield $d(x, y, z_i, \omega)$. The denominator $d(x, y, z_i, \omega).d^*(x, y, z_i, \omega)$ is treated as a negligible weight factor in the equation.

Eq.3.8 is known as the cross-correlation imaging condition. In practice, different extensions of the original imaging condition have been proposed (Sava et al., 2005; Guitton et al., 2007). In Paper II, we adapted a modified imaging condition (Eq.3.9), which demonstrated good qualities in numerical examples:

$$R(x, y, z_i) = \frac{\int u(x, y, z_i, \omega) d^*(x, y, z_i, \omega) d\omega}{\left\langle \int d(x, y, z_i, \omega) d^*(x, y, z_i, \omega) d\omega \right\rangle}, \tag{3.9}$$

where the notation $\langle\rangle$ denotes a smoothing operation with a triangular filter. Before applying the smoothing, a threshold can be applied to the illumination function ($\int d(x, y, z_i, \omega) d^*(x, y, z_i, \omega) d\omega$) to remove extremely small values. The imaging condition in Eq.3.9 is a deconvolution type of imaging condition.

3.4 One-way wave equation migration algorithms

Downward extrapolation/continuation, based on one-way wave equation methods, has been studied for decades. Many OWEM algorithms exist, including finite-difference migration, phase-shift migration, frequency-wavenumber domain migration and Fourier finite-difference (FFD) migration. Among them, the frequency-wavenumber and FFD techniques have attracted much attention due to their simplicity of implementation and computational efficiency. We introduce the most classic frequency wavenumber migration algorithms and FFD migration algorithms in the following. By following the same concept, the extension to the 3D code is straightforward.

3.4.1 Phase-shift migration method

Wave-equation migration by phase shift was proposed by Gazdag (1978). It is based on the downward extrapolation equation:

$$P_{z+\Delta z}(\omega, k) = P_z(\omega, k) \cdot e^{ik_z \Delta z}, \tag{3.10}$$

$$k_z = \sqrt{\frac{\omega^2}{v(z)^2} - (k_x)^2}, \tag{3.11}$$

where P_z and $P_{z+\Delta z}$ denote the pressure wavefield in the frequency and wavenumber domains at respective depth levels z and $z + \Delta z$, ω and k are the angular frequency and horizontal wavenumber respectively, $v(z)$ is the depth-dependent velocity, and k_z is the vertical wavenumber in a 2D migration; for 3D migration, $k_z = \sqrt{\frac{\omega^2}{v(z)^2} - (k_x)^2 - (k_y)^2}$.

Based on the phase-shift operator (Eqs. 3.10 and 3.11), the algorithm for the (2D) poststack phase-shift depth migration can be summarised into the workflow shown in Fig.3.5.

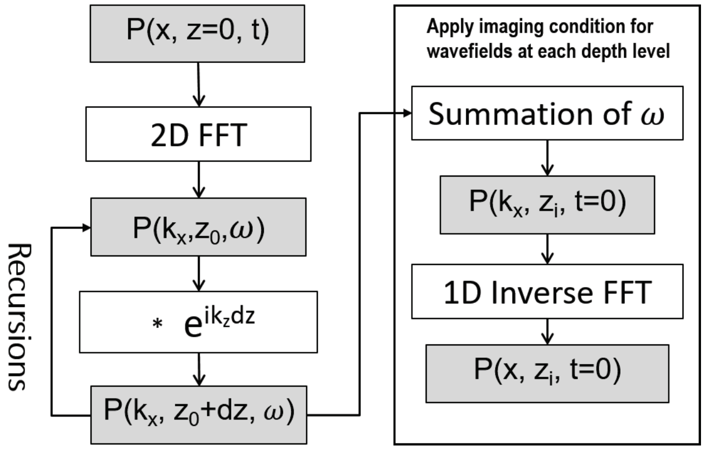

Figure 3.5: Workflow of the (2D) poststack phase-shift depth migration.

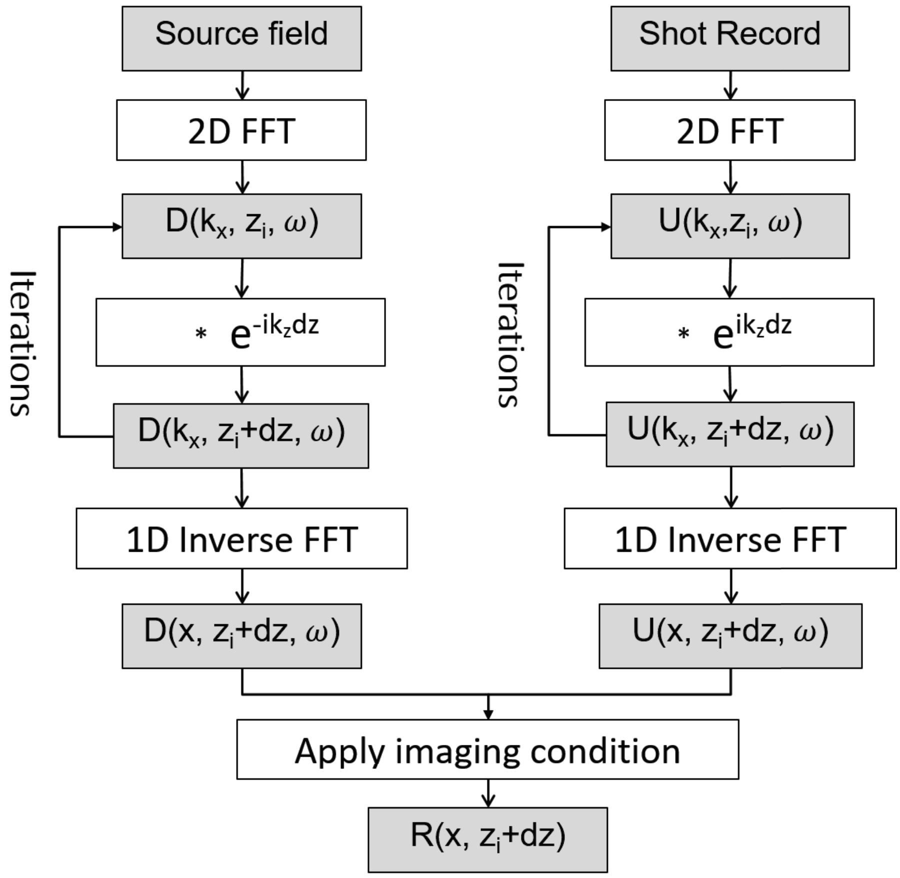

Figure 3.6: Workflow of the (2D) prestack phase-shift depth migration.

The poststack phase-shift migration algorithm can be easily extended to the prestack. As shown in Fig.3.6, the (2D) prestack phase-shift depth migration is based on the wavefield extrapolation of both the source field and shot records. ‘D’ and ‘U’ represent the forward-extrapolated down-going wavefield from the source and the backward-extrapolated up-going wavefield from the shot record (receivers), respectively. Compared to the backward operator applied to the up-going wavefield, a sign change in the operator has to be applied to forward-propagate the source field. Once the down-going and up-going wavefields have been extrapolated separately for each depth level, the prestack imaging condition is applied to derive the image of each level. By repeating this process, a prestack migrated section is finally obtained.

As can be seen, the phase-shift migration algorithm has the advantages of simple implementation and high computational efficiency. However, this method has not been widely used in practice due to its inability to handle laterally-variant velocity media. For this reason, other OWEM methods, implemented in a mixed frequency-wavenumber and frequency-space domain, were introduced.

3.4.2 Mixed frequency-wavenumber and frequency-space migration method

In order to improve the limitation of phase-shift migration, mixed frequency-wavenumber and frequency-space migration methods have been proposed. The phase-shift plus interpolation (PSPI) migration (Gazdag et al., 1984) and the split-step Fourier (SSF) migration (Stoffa et al., 1990) are representative methods of this category.

The main concept of these methods hangs on the decomposition of the laterally-varying velocity model into constant background and velocity perturbations (Fig.3.7) and application of the decomposed wavefield-extrapolation operators in the frequency-wavenumber and frequency-space domains.

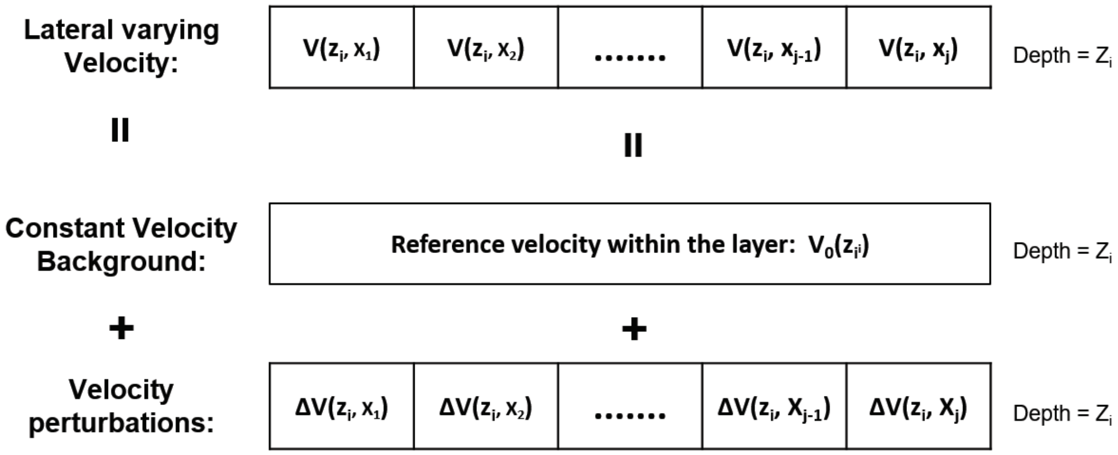

Figure 3.7: Schematics of velocity model decomposition

All of these mixed frequency-wavenumber and frequency-space migration methods concentrate on approximating the single-square-root (SSR) equation (3D case shown in Eq.3.12); the accuracy of the approximation is key to these OWEM methods.

$$k_z = \mathrm{SSR}(\omega, \mathbf{k}) = \sqrt{\frac{\omega^2}{v^2_{(\mathrm{z,x,y})}} - |\mathbf{k}|^2}, \tag{3.12}$$

where, ω and $\mathbf{k}$ denote the angular frequency and horizontal wavenumber vector, $v_{(\mathrm{z,x,y})}$ is the velocity model, with lateral and vertical variations, and k_z is the vertical wavenumber.

Various solutions have been proposed over the years to approximate the SSR operator. The generalised solution can be written symbolically as:

$$k_z = \mathrm{SSR}(\omega, \mathbf{k}) \approx \left(\sqrt{\frac{\omega^2}{v^2_{\mathrm{ref}}} - |\mathbf{k}|^2}\right) + \left(\frac{\omega}{v(z,x,y)} - \frac{\omega}{v_{\mathrm{ref}}}\right) + \epsilon, \tag{3.13}$$

where v_{ref} is the reference velocity and ϵ denotes high-order scattering terms.

Based on Eq.3.13, the vertical wavenumber k_z can then be decomposed into three terms – as indicated in Eq.3.14 – that correspond to the split vertical wavenumber, with respect to the reference velocity, velocity perturbations and high-order terms.

$$k_z = \text{SSR}(\omega, \mathbf{k}) \approx k_z^{ref} + k_z^{split-step} + k_z^{high\_order}$$

$$\left\{ \begin{array}{ccc} k_z^{ref} & = & \sqrt{\frac{\omega^2}{v_{\text{ref}}^2} - |\mathbf{k}|^2} \\ k_z^{split-step} & = & \frac{\omega}{v(z,x,y)} - \frac{\omega}{v_{\text{ref}}} \\ k_z^{high\_order} & = & \epsilon \end{array} \right. \tag{3.14}$$

, where k_z^{ref} is the vertical wavenumber, based on the reference velocity, the thin-lens term is the vertical wavenumber, based on velocity perturbations, and the high order is the vertical wavenumber, based on the remaining high-order terms.

With the generalised solution of SSR, we can rewrite the wavefield extrapolation equation as:

$$\begin{aligned} P_{z+\Delta z}(\omega, \mathbf{k}) &= P_z(\omega, \mathbf{k}) \cdot e^{ik_z \Delta z} \\ &\approx P_z(\omega, \mathbf{k}) \cdot e^{ik_z^{ref} \Delta z} \cdot e^{ik_z^{split-step} \Delta z} \cdot e^{ik_z^{high\_order} \Delta z}, \end{aligned} \tag{3.15}$$

where P_z and $P_{z+\Delta z}$ respectively denote the pressure wavefield in the frequency and wavenumber domain at depth levels z and $z + \Delta z$, and Δz is the depth interval in the migration.

It should be noted that, in the implementation, the three decomposed wavefield-extrapolation operators in the symbolic Eq.3.15 must be applied separately in the frequency-wavenumber and frequency-space domains. We give details of the relevant methods in the following. The discussion is limited to the 2D case, but further extension to 3D is trivial.

3.4.2.1 Phase-shift plus interpolation method

The PSPI migration method was developed to take into account lateral velocity variations by interpolating extrapolated wavefields using a phase shift employing two or more reference velocities.

The PSPI algorithm only utilises the first two operators in Eq.3.15, and can be arranged and expressed as Eqs. 3.16 and 3.17. The detailed 2D workflow shows in Fig.3.8.

$$P_z^*(\omega, x) = P_z(\omega, x) \cdot e^{i\frac{\omega}{v}\Delta z}, \quad v = v(x, z), \tag{3.16}$$

and

$$P_{z+\Delta z}(\omega, x) = \mathcal{F}_{k_x}^{-1}\left\{\mathcal{F}_x\left\{P_z^*(\omega, x)\right\} \cdot e^{i\left(k_z - \frac{\omega}{v'}\right)\Delta z}\right\}, k_z = \sqrt{\frac{\omega^2}{v'^2} - {k_x}^2}, \quad (3.17)$$

where $P_z(\omega, x)$ is the input wavefield in the time-space domain, $\mathcal{F}_x$ and $\mathcal{F}_{k_x}^{-1}$ denote forward and inverse Fourier transform with respect to x and k_x respectively. Moreover, v and v' are the input velocity and reference velocity.

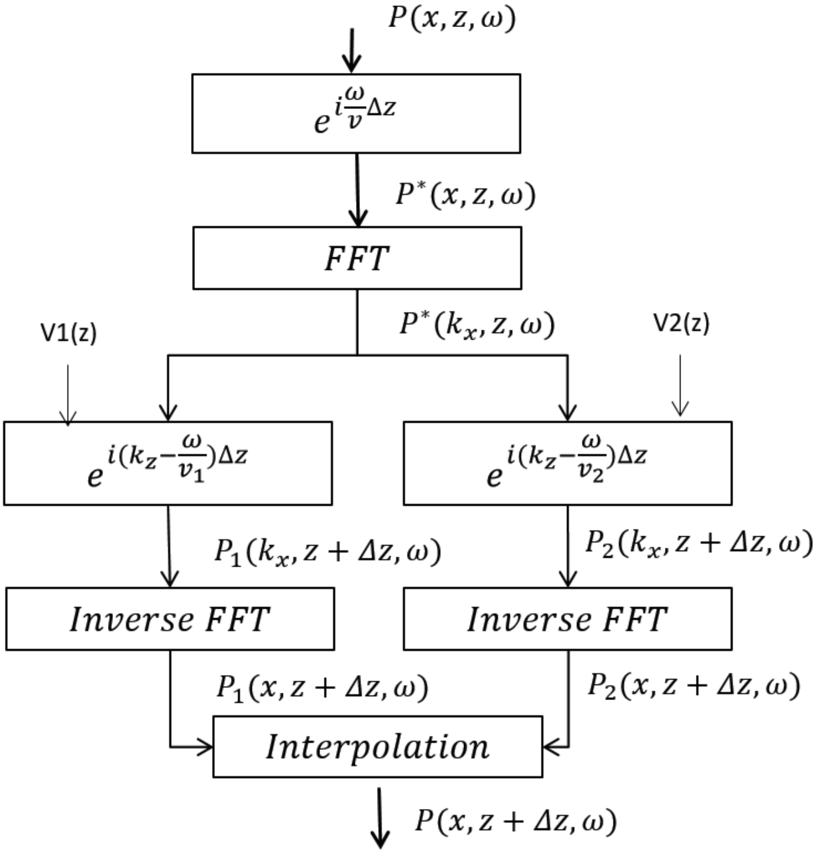

Figure 3.8: Workflow of poststack PSPI migration (Gazdag et al., 1984)

Following a similar scheme to that shown in Fig.3.6, we can also generate the prestack PSPI migration scheme (Fig.3.9). As can be seen from the workflow of prestack PSPI migration, the source and shot record wavefields have to be extrapolated separately, using multiple reference velocities in the frequency-wavenumber domain, and being interpolated in the frequency-space domain, leading to high computational costs.

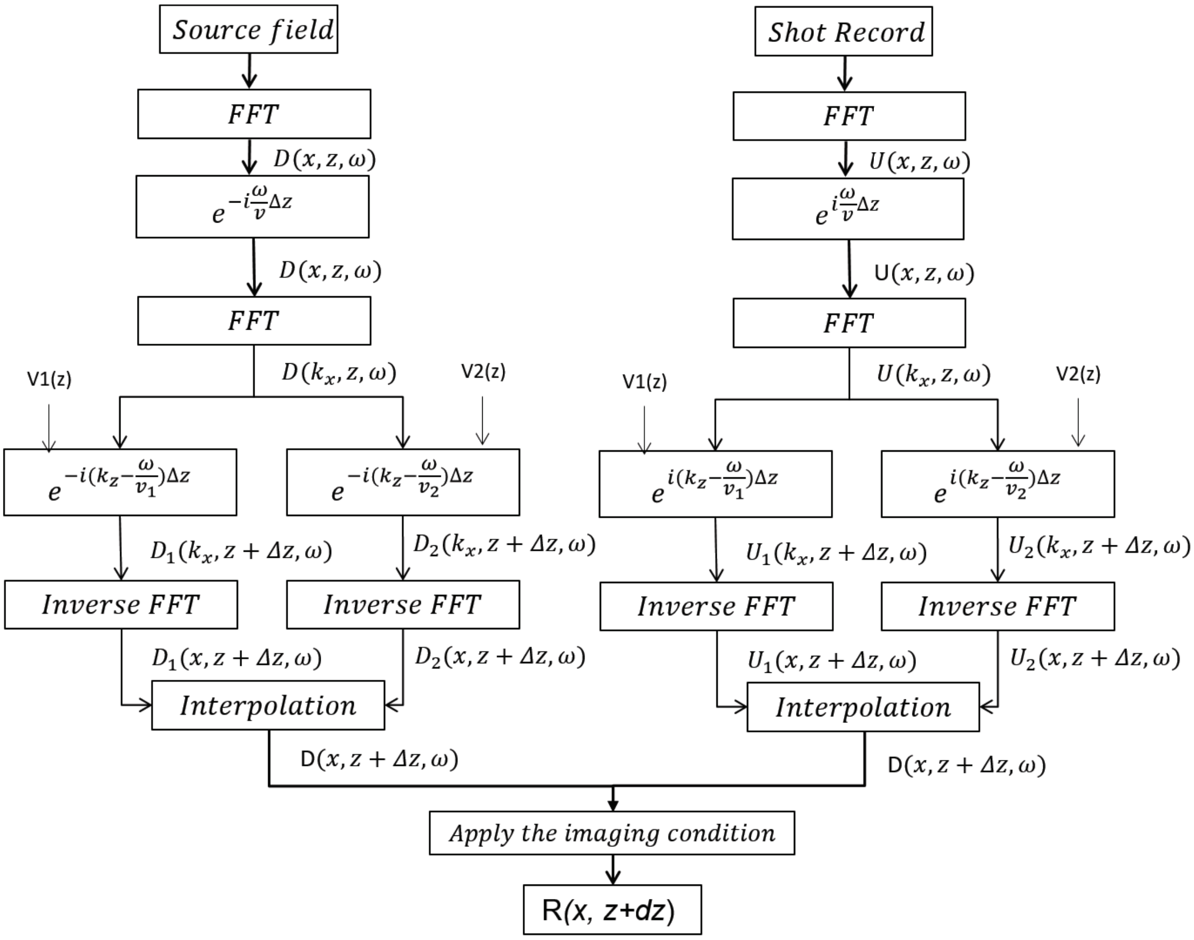

Figure 3.9: Workflow of prestack phase-shift plus interpolation migration.

PSPI migration is an extension of phase-shift migration, and is capable of handling media with lateral velocity variations. However, as the accuracy of the migration depends on the number of reference velocities used in the migration, and the interpolation has to be applied at each depth level, the PSPI migration performs less efficiently than other migration approaches.

3.4.2.2 Split-step Fourier method

SSF migration was introduced by Stoffa et al. (1990). This approach separates the velocity field into a constant background (reference) velocity field and a varying velocity perturbation field (thin-lens term), and approximates the SSR equation as:

$$k_z = \mathrm{SSR}(\omega, \mathbf{k}) \approx k_z^{ref} + k_z^{split-step}. \tag{3.18}$$

The corresponding wavefield extrapolation is then treated as a separate constant phase-shift operation in the frequency-wavenumber domain, followed by an additional phase correction in the frequency-space domain.

$$P_{z+\Delta z}(\omega, k) = \mathcal{F}_{t,x}\left\{P_z(t,x)\right\} \cdot e^{i\sqrt{\frac{\omega^2}{v_{ref}^2} - (k_x)^2}\Delta z}, \tag{3.19}$$

$$P_{z+\Delta z}(\omega, x) = \mathcal{F}_k^{-1}\left\{P_{z+\Delta z}(\omega, k)\right\} \cdot e^{i\omega(\frac{1}{V} - \frac{1}{V_{ref})}\Delta z}. \tag{3.20}$$

As shown in Fig.3.10 (poststack SSF workflow), this method splits the wavefield extrapolation into two steps: (1) operation of the phase-shift extrapolation, using a defined constant reference velocity (Eq.3.19); and (2) application of the additional thin-lens term correction to handle the velocity perturbation (Eq.3.20). The corresponding prestack SSF workflow is also shown in Fig.3.11.

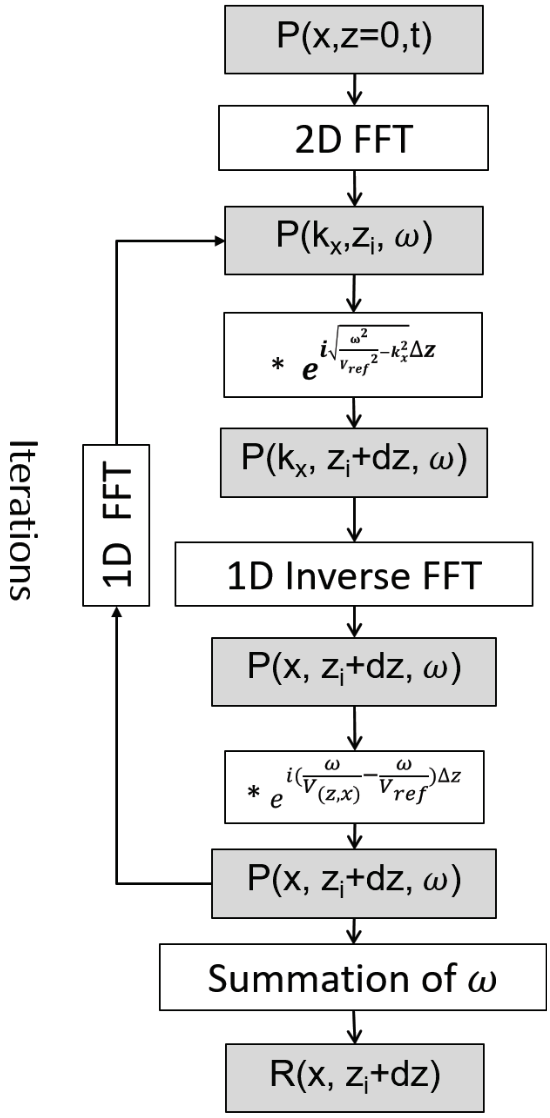

Figure 3.10: Workflow of SSF migration (2D).

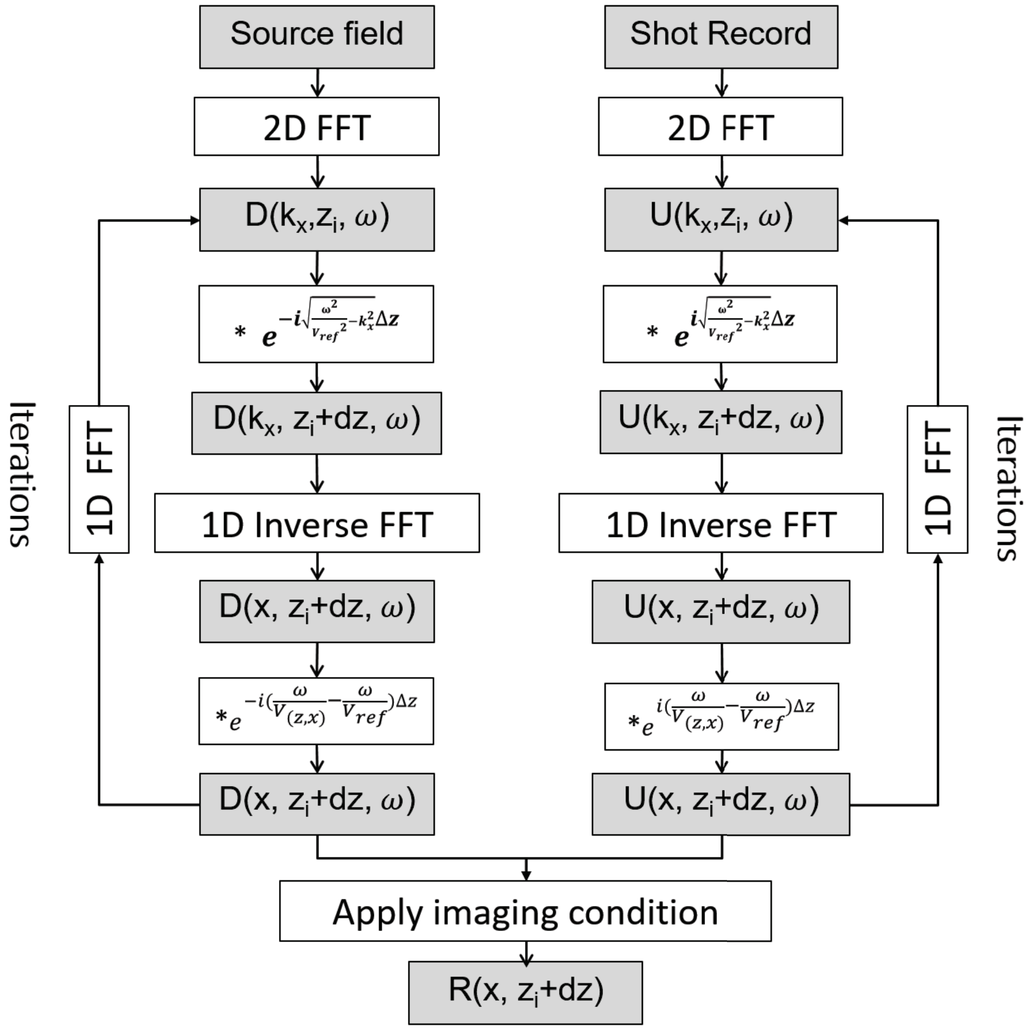

Figure 3.11: Workflow of prestack SSF migration (2D).

Compared to the PSPI method, SSF migration has a higher computational efficiency, since it does not require interpolation due to the use of only one reference velocity during the downward extrapolation. It is also unconditionally stable because the downward continuation only involves phase correction terms in the frequency-wavenumber and frequency-space domains. However, as the SSF operator assumes moderate lateral variations in velocity, it performs relatively poorly in cases where the subsurface has large velocity contrasts and structures with steep dips.

3.4.3 Fourier finite-difference migration method

SSF migration is unconditionally stable, and is capable of handling steep dips; however, it is inaccurate in cases where large lateral velocity contrasts exist. Another type of one-way wave migration – finite-difference migration (Claerbout, 1971, 1985) – is able to handle large velocity variations in both lateral and vertical directions, but has shortcomings in dealing with steeply-dipping events (Claerbout, 1985). Ristow et al. (1994) proposed the FFD migration, which combines the advantages of a SSF migration and a finite-difference migration to improve the migration performance in cases of large velocity contrasts and steep dips.

FFD is a high-order, hybrid algorithm implemented in mixed frequency-space and frequency-wavenumber domains. It is formulated by a direct expansion of the difference between the SSR equation, evaluated at the real medium velocity and the reference velocity. The (3D) SSR equation is approximated as:

$$k_z = \mathrm{SSR}(\omega, \mathbf{k}) \approx k_z^{ref} + k_z^{split-step} + k_z^{high\_order}$$

$$\begin{cases} k_z^{ref} & = & \sqrt{\frac{\omega^2}{v_{\mathrm{ref}}^2} - |\mathbf{k}|^2} \\ k_z^{split-step} & = & \frac{\omega}{v(z,x,y)} - \frac{\omega}{v_{\mathrm{ref}}} \\ k_z^{high\_order} & = & \left(\frac{\omega}{v(z,x,y)} - \frac{\omega}{v_{\mathrm{ref}}}\right)\left(\frac{2v_{\mathrm{ref}}vX^2}{4-\left(v_{\mathrm{ref}}^2+v^2+v_{\mathrm{ref}}v\right)X^2}\right) \end{cases} \tag{3.21}$$

where, k_z^{ref} is the vertical wavenumber based on the reference velocity, $k_z^{split-step}$ is the vertical wavenumber based on velocity perturbations, and $k_z^{high\_order}$ is the vertical wavenumber based on the remaining high-order terms (wherein $X = |\mathbf{k}| v_{ref}/\omega$).

The downward extrapolation can then be approximated as (B. L. Biondi, 2006):

$$P_{z+\Delta z}(\omega, \mathbf{k}) \approx P_z(\omega, \mathbf{k}) \cdot e^{ik_z^{ref}\Delta z} \cdot e^{ik_z^{split-step}\Delta z} \cdot e^{ik_z^{high\_order}\Delta z}, \tag{3.22}$$

where P_z and $P_{z+\Delta z}$ denote the pressure wavefield in the frequency and wavenumber domain at the respective depth levels z and $z + \Delta z$, and Δz is the depth interval in the migration.

As shown in Eqs. 3.21 and 3.22, FFD migration includes the constant phase-shift term applied in the frequency-wavenumber domain, the split-step (thin-lens) correction term in the frequency-wavenumber domain and the additional cascading high-order correction term implemented by an implicit finite-difference scheme in the frequency-wavenumber domain.

Compared to other OWEM methods, this hybrid FFD migration operator effectively improves the accuracy of the depth image in cases of complex structures with steep dips and large lateral velocity variations. Thus, it has been widely used in industry for OWEM. However, the FFD migration method has shortcomings in 3D. Although the FFD approach can be extended to a 3D wave-migration scheme, employing finite-difference operator splitting (e.g. Li, 1991; Ristow et al., 1997). This splitting process is not straightforward and generates numerical anisotropy. Furthermore, the extension of the FFD technique to the VTI case is also challenging due to difficulties in selecting appropriate references for the anisotropy parameters.

3.5 3D prestack Fourier mixed-domain (FMD) depth-migration method

As discussed above, although many OWEM methods exist for seismic depth migration, most of them struggle either with stability, accuracy, anisotropic noise or computational cost. Thus, in Paper II, we proposed a new OWEM method based on a mixed space- and wavenumber-propagator that effectively overcomes these issues and is feasible in VTI media.

FMD PSDM can be regarded as a high-order extension of the SSF migration method. Unlike the mixed domain depth migration methods (SSF and PSPI), FMD is capable of imaging complex geology with large lateral contrasts, in both isotropic and anisotropic cases. Furthermore, compared to the FFD migration method, FMD naturally avoids numerical anisotropy in its implementation, and achieves sufficient accuracy for 3D VTI media with large lateral contrasts in terms of the velocity and anisotropy parameters.

3.5.1 3D Fourier mixed-domain one-way propagator for a vertical transversely isotropic medium

For VTI media, the mixed-domain representation of the vertical wavenumber is formulated as (3D case):

$$k_{zj}(\boldsymbol{x},\boldsymbol{k},\omega) = \sqrt{\frac{k_j^2(\boldsymbol{x}) - (1+2\varepsilon_j(\boldsymbol{x}))\,k_T^2}{1-2\left[\varepsilon_j(\boldsymbol{x})-\delta_j(\boldsymbol{x})\right]k_T^2/k_j^2(\boldsymbol{x})}}, \tag{3.23}$$

with:

$$k_j = \frac{\omega}{c_j(\boldsymbol{x})}, \quad \boldsymbol{k}\cdot\boldsymbol{k} = \sqrt{k_x^2+k_y^2} = k_T^2, \tag{3.24}$$

where $c_j(\mathbf{x})$ is the laterally-varying vertical medium velocity in the j-th layer, and $\varepsilon_j(\mathbf{x})$ and $\delta_j(\mathbf{x})$ are the Thomson parameters.

In FMD migration, the VTI vertical wavenumber can be approximated by Eq.3.25, where the vertical wavenumber is decomposed into a background plane-wave term associated with a layered model, a thin-lens term to correct the velocity perturbations and an additional high-order correction term of order N, taking into account the strong lateral velocity variations and higher dip angles.

$$\begin{aligned} k_{zj}(\boldsymbol{x},\boldsymbol{k},\omega) &\cong k_{z0j}(\boldsymbol{k},\omega) + \left[k_j(\boldsymbol{x}) - k_{0j}\right](1+\xi) \\ &+k_{0j}\left[\frac{\left\{a_{0j}-\sqrt{1+\gamma_j(\boldsymbol{x})A_j(\boldsymbol{x})}\right\}^2_{\mathrm{T}}/k_{0j}^2}{\left\{1-b_{0j}k_T^2/k_{0j}^2\right\}} - \sum_{n=1}^{N}\frac{\sqrt{1+\gamma_j(\boldsymbol{x})}A_j(\boldsymbol{x})\{B_j(\boldsymbol{x})-b_{0j}\}^n\left(k_T^2/k_{0j}^2\right)^{n+1}}{\left\{1-b_{0j}k_T^2/k_{0j}^2\right\}^{n+1}}\right] , \end{aligned} \tag{3.25}$$

where:

$$A_j(\boldsymbol{x}) = \frac{a_j(\boldsymbol{x})}{1+\gamma_j(\boldsymbol{x})} \quad , \quad B_j(\boldsymbol{x}) = \frac{b_j(\boldsymbol{x})}{1+\gamma_j(\boldsymbol{x})}, \tag{3.26}$$

and

$$k_j(\boldsymbol{x}) = \sqrt{1+\gamma_j(\boldsymbol{x})}\cdot k_{0j}, \quad \gamma_j(\boldsymbol{x}) = \frac{c_{0j}^2}{c_j^2(\boldsymbol{x})} - 1, \quad k_{0j} = \frac{\omega}{c_{0j}}, \tag{3.27}$$

with coefficients defined as:

$$\begin{gathered} \xi = -0.00099915, a_j(\mathrm{x}) = 0.46258453\left(1+2\delta_j(\mathrm{x})\right), \\ b_j(\mathrm{x}) = 2\left(\varepsilon_j(\mathrm{x}) - \delta_j(\mathrm{x})\right) + 0.40961897\left(1+2\delta_j(\mathrm{x})\right), \end{gathered} \tag{3.28}$$

and

$$a_{0j} = 0.462584531\left(1+2\delta_{0j}\right), b_{0j} = 2\left(\varepsilon_{0j} - \delta_{0j}\right) + 0.40961897\left(1+2\delta_{0j}\right). \tag{3.29}$$

Based on Eq.3.25, the generalised mixed-domain VTI PSDM scheme can be formulated (after reorganisation and neglecting the high-order cross terms):

$$P\left(z_j+\Delta z\right) = P\left(z_j\right)\cdot e^{\left[ik_{z0j}\Delta z\right]}\cdot e^{\left[i\left(k_j(\boldsymbol{x})-k_{0j}\right)(1+\xi)\Delta z\right]}\cdot\left\{1+\Gamma_j(u,\boldsymbol{x})\right\}, \tag{3.30}$$

where: $u = k_T^2/k_{0j}^2$ and

$$\begin{aligned} \Gamma_j(u,\boldsymbol{x}) = &\left\{ik_{0j}\left\{a_{0j} - \sqrt{1+\gamma_j(\boldsymbol{x})}A_j(\boldsymbol{x})\right\}\Delta z\right\}\frac{u}{\left[1-b_{0j}u\right]} \\ &-\sum_{n=1}^{N} ik_{0j}\sqrt{1+\gamma_j(\boldsymbol{x})}A_j(\boldsymbol{x})\left[B_j(\boldsymbol{x})-b_{0j}\right]^n\Delta z\frac{u^{n+1}}{\left[1-b_{0j}u\right]^{n+1}}. \end{aligned} \tag{3.31}$$

To make the proposed FMD scheme unconditionally stable, a dip filter in the frequency-wavenumber domain is applied. Moreover, a dual-reference scheme for highly-complex geological models (with the inclusion of large velocity anomalies, such as salt bodies) is proposed. The corresponding updated scheme can be found in Eqs. (18) and (20) in Paper II.

3.5.2 Examples of Fourier mixed-domain migration

We can now demonstrate the potential of the FMD migration, using a controlled-data example based on prestack data from the Sigsbee2A model, made public by the Subsalt Multiples Attenuation and Reduction Technology Joint Venture (SMAART JV) between 2001 and 2002. As shown in Fig.3.12, this model describes the subsalt geological setting of the Sigsbee Escarpment in the deep-water Gulf of Mexico. Both the upper and lower parts of the Sigsbee2A model represent complex features. The shallow geology has a challenging combination of strong lateral variation and steep dip structures, defined by two synclines. Below the salt, faulted blocks with fine-layered structures are present, superimposed on a line of point scatterers.

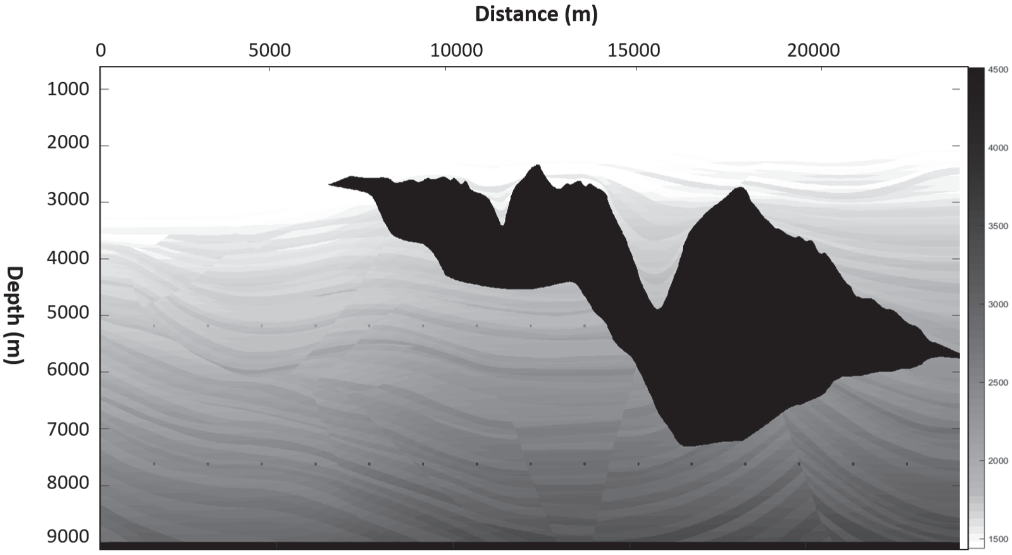

Figure 3.12: Sigsbee 2A stratigraphic model.

To test the poststack version of the FMD migration, a ZO dataset, based on the exploding reflector model, were generated using a finite-difference programme from the CREWES software package. The controlled data (shown in Fig.3.13) were characterised by a spatial sample interval of 7.62 m (25 ft), a temporal sample interval of 8 ms and a total recorded length of 12 s. A Ricker wavelet, with a centre frequency of 20Hz, was used in the modelling.

In poststack FMD migration, a frequency range of between 5 and 20Hz and a depth interval of 7.62 m (25 ft) were employed. The corresponding depth-migration results are shown in Fig.3.14. On direct comparison with the stratigraphic model, the migrated image demonstrates good quality for both the salt and most of the sedimentary structures. However, the image shows some dipping noise and degraded structures under the salt body, which would be expected in the poststack depth migration. This can be improved by using the prestack FMD migration, as shown in the following.

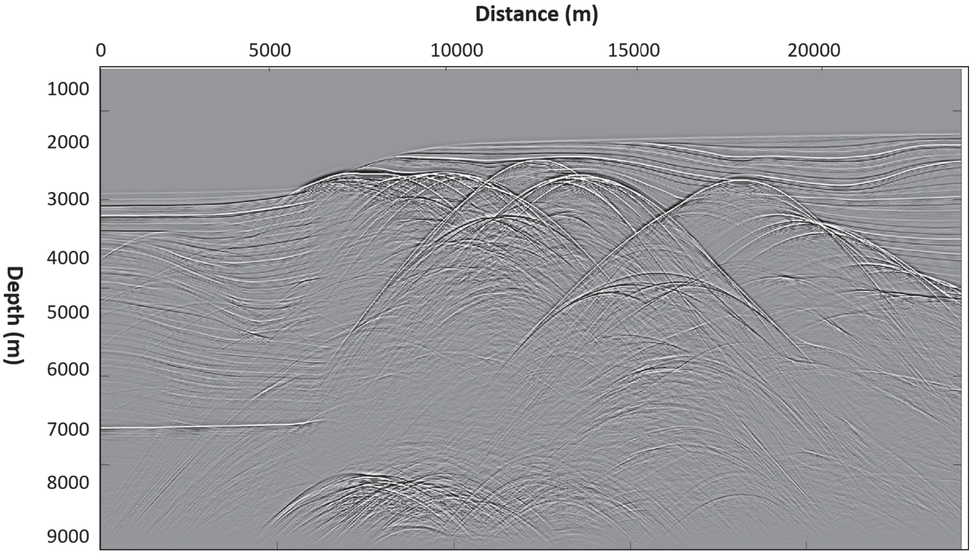

Figure 3.13: Sigsbee 2A ZO synthetic stack.

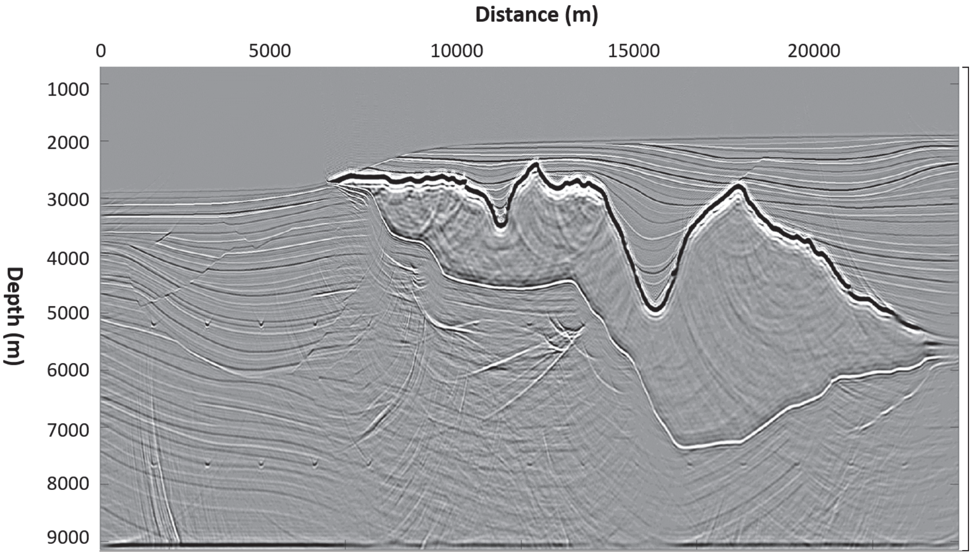

Figure 3.14: Poststack FMD migration image.

For the prestack FMD migration test, the prestack data consisted of 500 source gathers, each containing a total of 348 receivers. During the migration, we employed a bandwidth of 0–40 Hz, a dual-velocity reference and a second-order scattering scheme (Eq. (18) in Paper II).

We first give an example of a single-shot migration, employing a cross-correlation imaging condition (IC) (Fig.3.15a). By introducing the denominator from Eq. (23) in Paper II, we obtain the deconvolution IC actually employed, where the denominator can be interpreted as an illumination compensation. The corresponding result is given in Fig.3.15b, where it can be seen that the subsalt events have now been amplified. In addition, an appropriate mute has been applied. The final image is constructed by summing all the partial images output from each shot-point migration. The spatial sample interval of the final image is

37.5 ft along the horizontal direction and 25 ft along the vertical direction. As can be observed from Fig.3.16, most of the subsalt features were well recovered. The deep, flat reflector was also well reconstructed, and the scatterers along the two horizontal lines are mostly well focused.

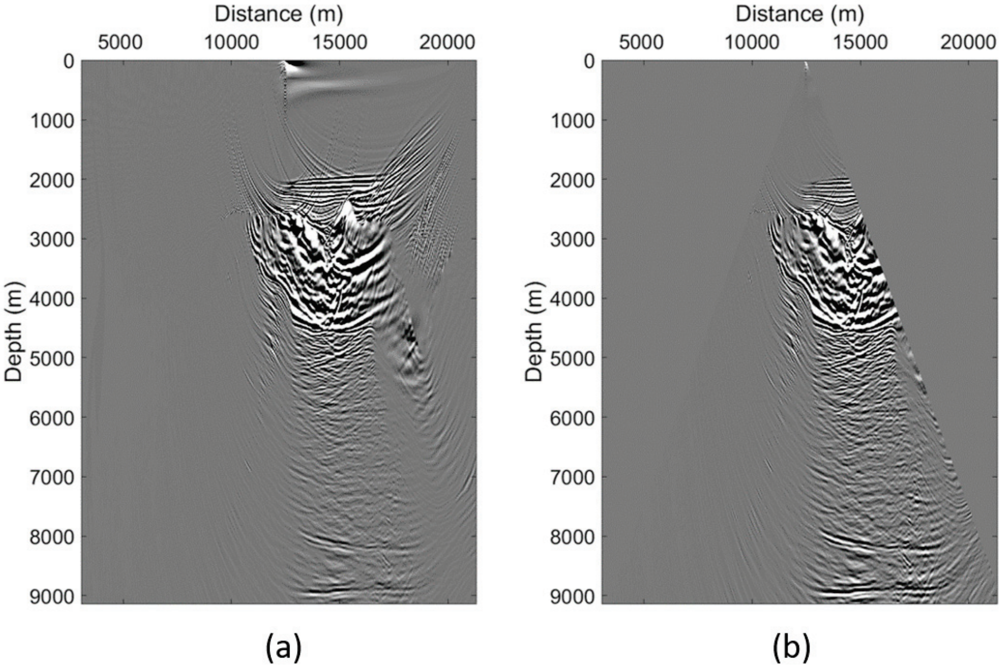

Figure 3.15: Single-shot migration profile. (a) First-order dual-velocity FMD with cross-correlation imaging condition, (b) first-order dual-velocity FMD with deconvolution imaging condition and mute applied.

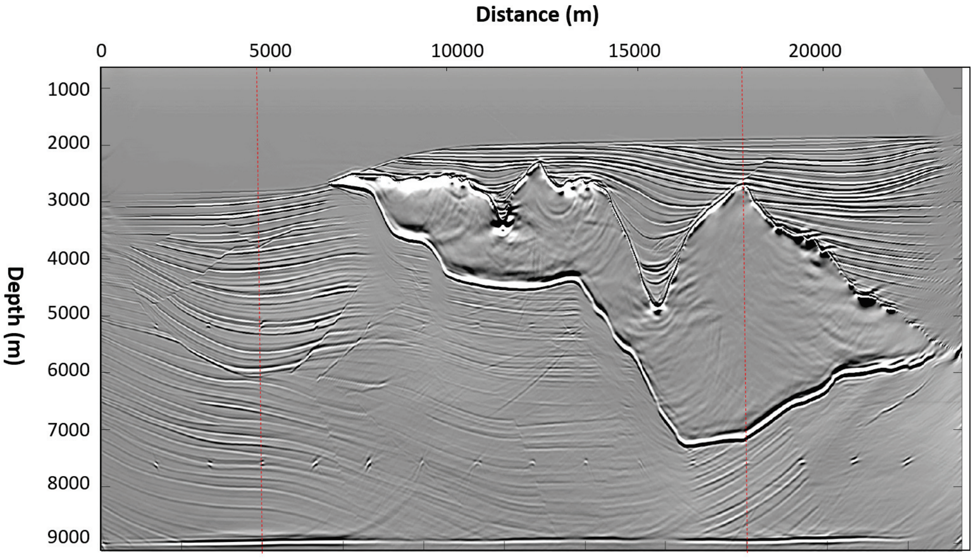

Figure 3.16: Prestack FMD migration image.

In Paper II, we further demonstrated the performance of the prestack FMD method in both 2D and 3D VTI anisotropic migration cases, which included controlled data and 3D field data from the Barents Sea. All the results demonstrated the good performance of the proposed FMD migration algorithm.

3.5.3 Schematics of iterative Fourier mixed-domain depth-migration and velocity-building

Besides being a powerful PSDM method in itself, a possible future application of the FMD technique might be in velocity model building, as part of an iterative migration loop. In cases of complex velocity fields associated with embedded salt bodies, or other strongly-contrasting inhomogeneities, the conventional approach that employs a Kirchhoff PSDM may give poor results in areas below such structures. In iterative Kirchhoff PSDM, typical input data will comprise constant-offset (or, alternatively, constant-angle) sections. Shifts in depth, picked in a series of common-image gathers (CIGs), are then used as inputs into a reflection-tomography programme to obtain an updated velocity model, followed by a new iterative migration step.

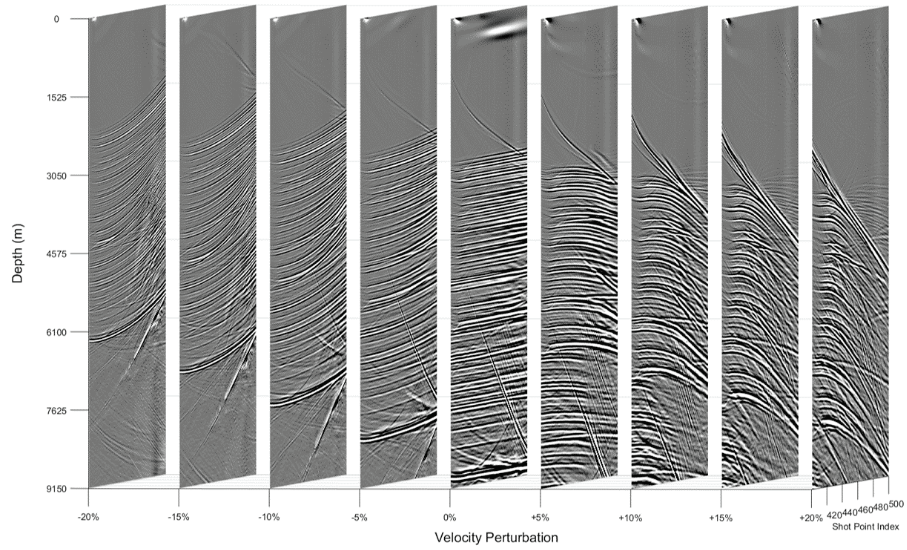

Figure 3.17: CIG from shot profile migration using perturbed velocity field. Location outside the salt indicated by the red vertical line to the left in Fig.3.17.

In the case of the FMD method, which is a shot-point-based PSDM technique, the concept of CIG is still valid, but the offsets are replaced by shot-point indices (or shot-point offsets). Figs. 3.17 and 3.18 illustrate examples of two CIGs from the Sigsbee2A model. In both figures, results are shown for a true velocity model and perturbed models in the range +20% to -20%. The locations of the two CIGs are indicated by the left (corresponding to Fig.3.17 and outside salt) and right (Fig.3.18 and inside salt) red vertical lines in Fig.3.16. In both examples, it can be seen that these CIGs demonstrate the same sensitivity to velocity errors as the more conventional CIGs formed from depth-migrated constant-offset sections.

Note that the number of traces in each CIG is about 100 for this dataset, which is actually higher than the fold of 87.

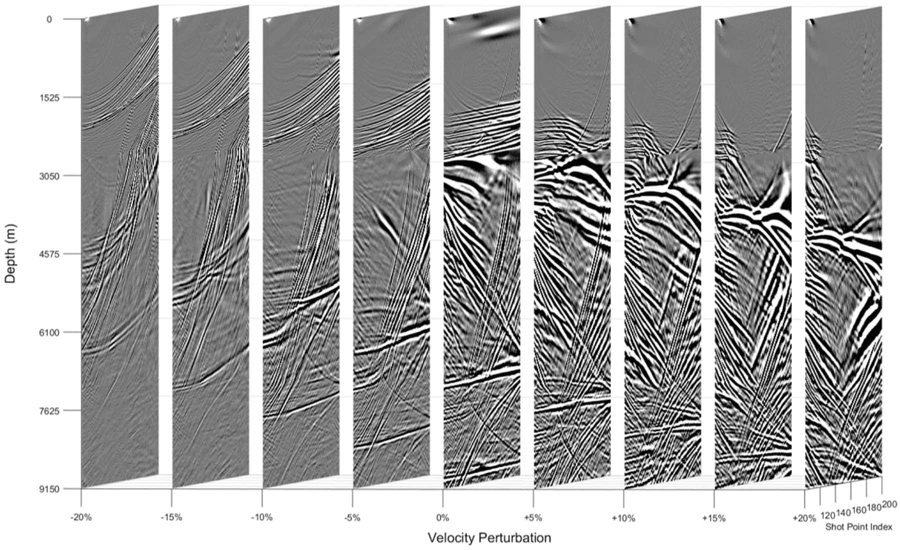

Figure 3.18: CIG from shot-profile migration using perturbed velocity field. Location inside the salt, indicated by the red vertical line to the right in Fig.3.17.

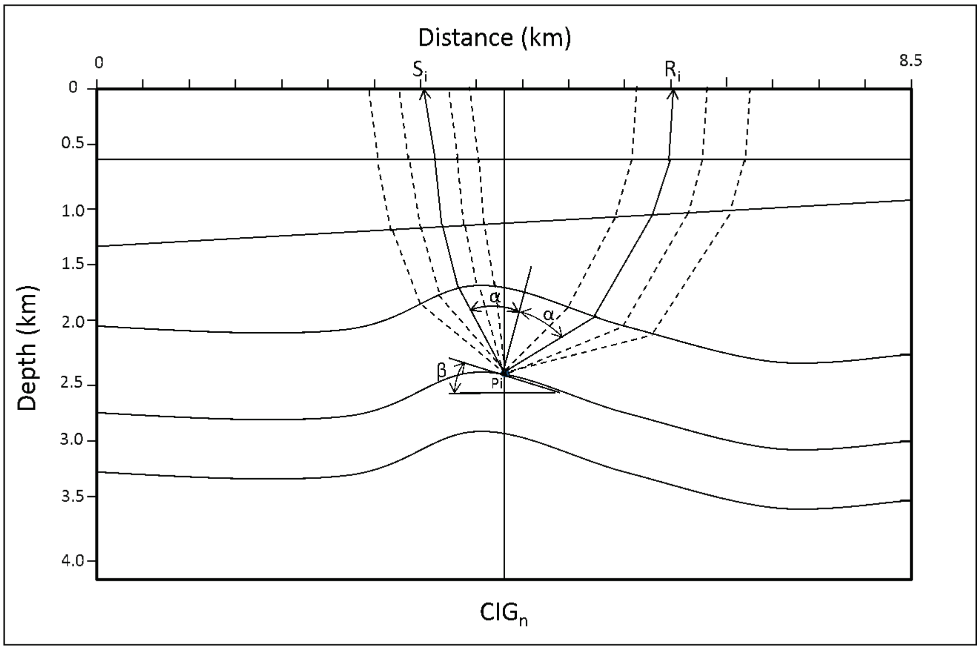

Figure 3.19: Initialisation step employed prior to reflection tomography. Rays are traced from a specific image point (P_i) on an interpreted horizon in the migrated CIG, and the ray (S_iP_i) closest to the selected source location is picked or interpolated. The corresponding receiver location (R_i) is now defined by the specular or stationary ray (R_iP_i), fulfilling Snell's law; that is, using information about the angle of incidence (α) and the local dip (β) of the reflection interface.

Thus, by analogy with the conventional Kirchhoff type of velocity analysis and model building, depth shifts can be (automatically) picked for each imaged trace in a given CIG. Before these picked data can be input into a reflection tomography programme, a preprocessing step needs to be carried out; for each shot-point index associated with an imaged trace in the CIG, the corresponding receiver location needs to be determined. This procedure is shown schematically in Fig.3.19. We assume an initial smooth velocity model and a set of interpreted key horizons.

In this short discussion, the 2D case is used as an illustration. Extension to 3D requires that a sophisticated regularisation technique can be applied to the data to compensate for the irregular source and receiver distribution.

Chapter 4

Migration velocity estimation based on kinematic wavefield attributes

In Paper III, we revisited the kinematic time migration and demigration, and developed a detailed numerical scheme for time-migration velocity estimation, using nonlinear mapping. This proposed time-migration velocity method is based on the input of kinematic attributes (travel times and local slopes), which are extracted from the prestack seismic dataset in the migration or recording domain. Using the derived kinematic attributes, an algorithm based on Fréchet derivatives, employing a nonlinear kinematic time-migration/demigration solver, was developed for the time-migration velocity estimation. This generalised scheme is valid for both 2D and 3D homogeneous and heterogeneous time-migration velocity estimation, and is feasible for use in both narrow- and wide-azimuth geometries. As an alternative to conventional time-migration velocity estimation, it can be used for initial velocity model building in depth-migration velocity modelling, and is likely to be extendable to direct depth-migration velocity estimation. In this chapter, we first give an overview of migration velocity estimation methods, then provide the key elements of the time-migration velocity estimation based on nonlinear kinematic migration/demigration solvers.

4.1 Overview of migration-velocity estimation methods

In seismic imaging, two main problems need to be addressed: (1) the estimation of the subsurface velocity model; and (2) the choice of an appropriate migration algorithm. As discussed in the previous chapter, seismic migration is a process of placing recorded data into the correct subsurface position, and it is classified into time and depth migration based on the domains being migrated. Prestack time migration (PSTM) (e.g. Claerbout, 1976, 1985; Bancroft et al., 1994; Fowler, 1997) uses prestack seismic data and a locally homogeneous time-migration velocity model to construct a migrated image in the time domain. The more sophisticated PSDM algorithm (e.g. Gazdag, 1978; Bleistein, 1987; Hill, 1990; Stoffa et al., 1990; Ristow et al., 1994) honours a complex depth-migration velocity model and generates a more accurate subsurface image. For both PSTM and PSDM, accurate migration-velocity models are relied on to obtain the correct migration image. We introduce the classic time/depth migration-velocity estimation in the following. The content of this section is based on Yilmaz (2001), B. L. Biondi (2006) and Jones (2010).

4.1.1 Time migration-velocity estimation

PSTM is a robust and efficient process that is routinely applied in seismic imaging. It achieves a reasonable accuracy in imaging simple to moderate structures with a homogeneous velocity background. An accurate time-migration velocity determines the image quality of PSTM, and affects the depth-migration result, as most depth-migration velocity estimations use this as the initial velocity model. In the following, we give an overview of the classic time-migration velocity estimation methods.

4.1.1.1 Migration-velocity analysis

To derive an accurate migration-velocity model, Al-Yahya (1989) proposed a migration-velocity analysis (MVA) based on the analysis of residual moveouts (RMOs) of migrated common-image-gathers (CIGs). Although the proposed scheme is based on the migration of shot gathers, and is used for depth-MVA, this MVA concept has been adapted for time MVA (e.g. Deregowski, 1990; Liu et al., 1995; Schleicher, Tygel, et al., 2007). Among all such analyses, the time MVA by iterative PSTM and residual MVA is the most used approach in the industry. As shown in Fig.4.1, this method uses multiple iterations of PSTM and NMO MVA on CIGs to estimate the time-migration velocity (Biondi, 2006). In this process, the flatness of events on the CIGs is used as a criterion for optimal time-migration velocity estimation.

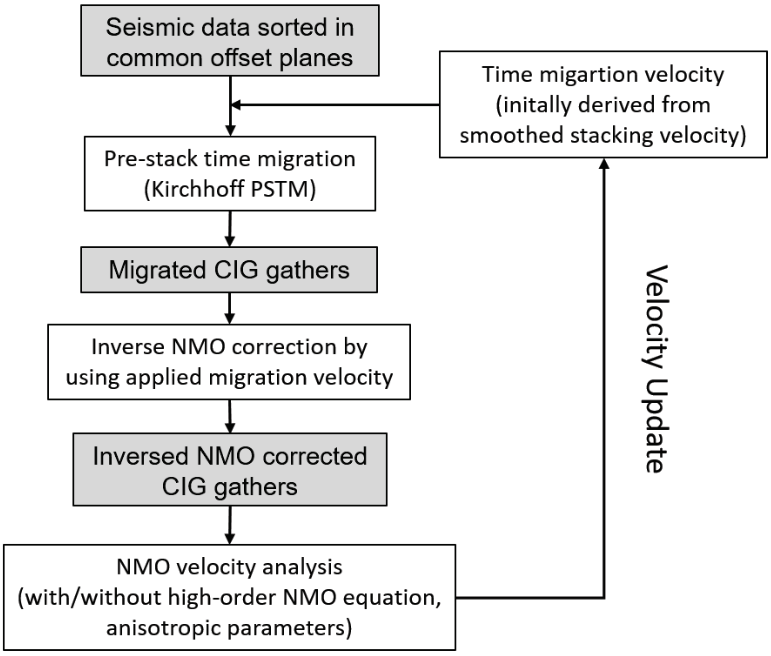

Figure 4.1: Conventional workflow of time MVA

Due to the simplicity of the method, this time-migration velocity-estimation method has been used routinely in the industry. However, the limitation of this method is that it assumes a horizontally-layered model without lateral velocity variations. Similar to the conventional NMO velocity analysis on CMP gathers, in the case of dipping reflectors or lateral velocity variations, this method is inaccurate in estimating the optimal time-migration velocity. Moreover, this approach requires manual NMO-velocity picking in every iteration, and the cost increases greatly as the density of the MVAs increase.

4.1.1.2 Migration velocity estimation by velocity continuation

Another type of time-migration velocity estimation – velocity continuation – was proposed by Fomel (1994), Hubral et al. (1996) and Schleicher et al. (1997). This migration velocity estimation method is based on the analysis of migrated images using a series of migration velocities. Applying velocity continuation to migration analysis includes the following steps (Fomel, 2003):

1. The prestack CO migration to generate the initial data for continuation.
2. Velocity continuation with stacking and semblance analysis across different offsets to transform the offset data dimension into the velocity dimension.
3. Picking the optimal velocity and slicing through the migrated data volume to generate an optimally-focused image.

This method is essentially a process of migration-velocity scanning, which determines the time-migration velocity based on searching of the optimal migration image. As mentioned above, the first step of this approach is to transform the prestack data into multiple migrated images, using a series of constant velocities, and time-migration velocity picking based on these migrated images.

4.1.1.3 Migration velocity estimation by using local event slopes

Ottolini (1983) proposed an PSTM method based on local event slopes. Fomel et al. (2007) further generalised this approach for time-domain imaging and the estimation of the NMO, interval and migration velocities.

Based on the 2D formulation of Fomel et al. (2007), using the oriented PSTM approach, the recorded data can be mapped from the prestack data domain (t, h, y) to the time-migrated image domain (τ, x) (Eqs4.1 and 4.2). Furthermore, a time-migration velocity model can be derived from mapping the prestack local event slopes (Eq.4.3):

$$\tau^2 = \frac{tp_h\left[(t-hp_h)^2 - h^2p_y^2\right]^2}{(t-hp_h)^2\left[tp_h + h\left(p_y^2 - p_h^2\right)\right]}, \tag{4.1}$$

$$x = y - \frac{htp_y}{tp_h + h\left(p_y^2 - p_h^2\right)}, \tag{4.2}$$

$$\frac{4}{v^2} = \frac{t\left[tp_h + h\left(p_y^2 - p_h^2\right)\right]}{h\left(t - hp_h\right)}, \tag{4.3}$$

where t, h and y are the prestack data coordinates, (τ, x) are the time-migrated image coordinates, $p_h and p_y$ are the prestack local event slopes in the offset and space direction, h is a half-offset and v is the time-migration velocity.

Based on this formulation, time-migration velocities turn into data attributes associated with local event slopes, which can be directly extracted from the input data. As discussed in the previous chapter, the local slopes in Eqs4.1–4.3 can be extracted from the prestack data based on the local slant stack (Ottolini, 1983), the Hilbert transform (Cooke et al., 2009), plane-wave destruction (Claerbout, 1992) and the GST (Bigun et al., 1987) methods.

4.1.2 Depth-migration velocity estimation

In the subsurface imaging of complex structures and laterally-varying velocities, depth migration provides a more accurate subsurface image than time migration. Unlike time migration, which assumes a laterally-invariant velocity model, depth migration honours the lateral velocity variation in the migration algorithm, and thus is capable of accurately imaging complex structures with strong velocity variations. In this sense, an accurate depth-velocity model is critical for depth-domain migration. Conventionally, the depth-migration velocity estimation can be divided into two categories – non-tomographic and tomography-based (Jones, 2003). We give an overview of each category in the following.

4.1.2.1 Non-tomographic type depth-velocity estimation

- **Dix conversion**

Dix conversion (Dix, 1955) was one of the most common non-tomographic velocity-estimation methods used before the development of tomographic methods. As shown in the schematic (Fig.4.2), the interval velocity in a series of flat layers can be derived from the associated rms velocities and travel times:

$$v_{int_n} = \sqrt{\frac{V_n^2 t_n - V_{n-1}^2 t_{n-1}}{t_n - t_{n-1}}}, \tag{4.4}$$

where v_{int_n} is the interval velocity in the layer bounded by interfaces n-1 and n, t_{n-1} and t_n are the corresponding ZO two-way travel times, and V_{n-1} and V_n are the corresponding rms velocities, which are approximated by the stacking velocity obtained from the NMO analysis of the CMP gathers.

Assuming the subsurface is composed of flat layers with homogeneous velocities, the Dix formula transforms rms velocities into interval velocities. The advantage of the Dix transform is its simple implementation. However, its fundamental problem is that the Dix conversion does not take into account

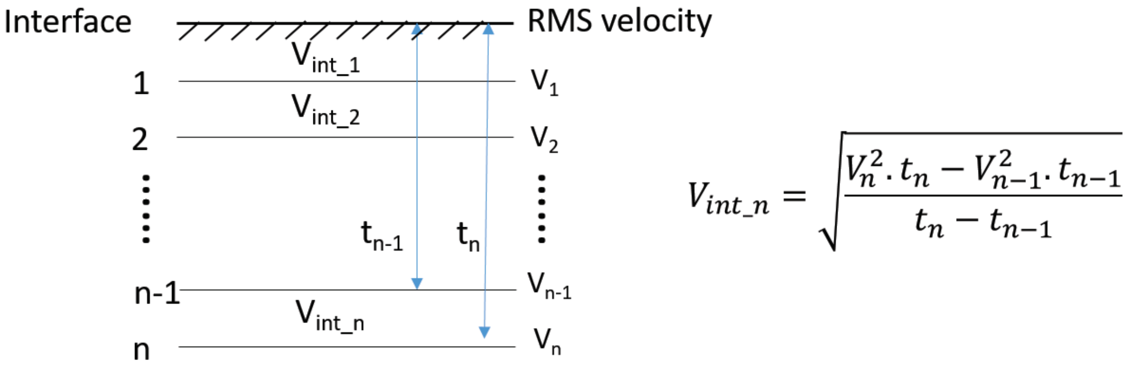

Figure 4.2: Schematics of Dix conversion

lateral velocity variations in the layers. As stacking-velocity estimation assumes a flat-layered and homogeneous velocity model in a cable length, where the structure is associated with lateral velocity variations, the stacking-velocity estimation becomes unfeasible, leading to inaccurate interval velocities.

In order to solve this problem, other non-tomographic velocity-estimation methods have been proposed, such as normal and image ray map migration (Hubral, 1975), stacking velocity inversion (Thorson et al., 1985), coherency inversion (Landa et al.,1987), the Deregowski loop (Deregowski, 1990), MVA based on RMO analysis (Audebert et al., 1997;I. F. Jones et al., 1998), and more advanced Dix inversion approaches (Cameron et al., 2007; Iversen et al., 2008). We briefly introduce two classic methods in the following.

- **Velocity-estimation techniques based on map migration**

Map migration is a mapping technique that has frequently been used in velocity-estimation approaches. It repositions picked time horizons at their ‘true’ depth locations, given an estimate of the interval velocities between the picked horizons. This technique can be grouped into normal and image ray map migration, and interval-velocity map migration. As far as the author is aware , for the map migration of events in the recording domain, the first reference is Kleyn (1977), whilst Hubral (1977) introduced the image ray. Concerning map migration from the time-migration domain, a useful reference is Hubral and Krey (1980). We give a short introduction to these methods in the following.

i Normal ray map migration: Using picked time horizons and the associated interval velocities, normal ray migration maps non-migrated time horizons to migrated horizons at depth by applying Snell ray-bending at each interface and calculating the positions at depth. This process gives an estimation of the depth horizons, but does not update the velocity between the horizons.

ii Image ray map migration: This maps the migrated horizons in time to the migrated horizons at depth by employing the known interval velocity and the lateral derivatives of the velocity field. Similarly to normal ray migration, this process does not update the velocity between the horizons. However, this process is more reliable than the normal ray migration because the horizon picking is applied to the migrated data.

iii Interval velocity map migration: This is a tool for velocity sensitivity analysis. In order to evaluate an effect of velocity perturbations on depth horizons, interval velocity mapping is applied, consisting of two key steps – a de-map-migration using the original migration velocity, and then a re-map-migration using the perturbed migration velocity.

- **Coherency velocity inversion**

Coherent inversion (shown in Fig.4.3) is an interval-velocity scanning technique. It uses ray tracing through predefined velocity models to compute moveout trajectories and calculate the coherency (semblance) along the trajectories in CMP gathers. The estimated velocity is the one with the highest semblances.

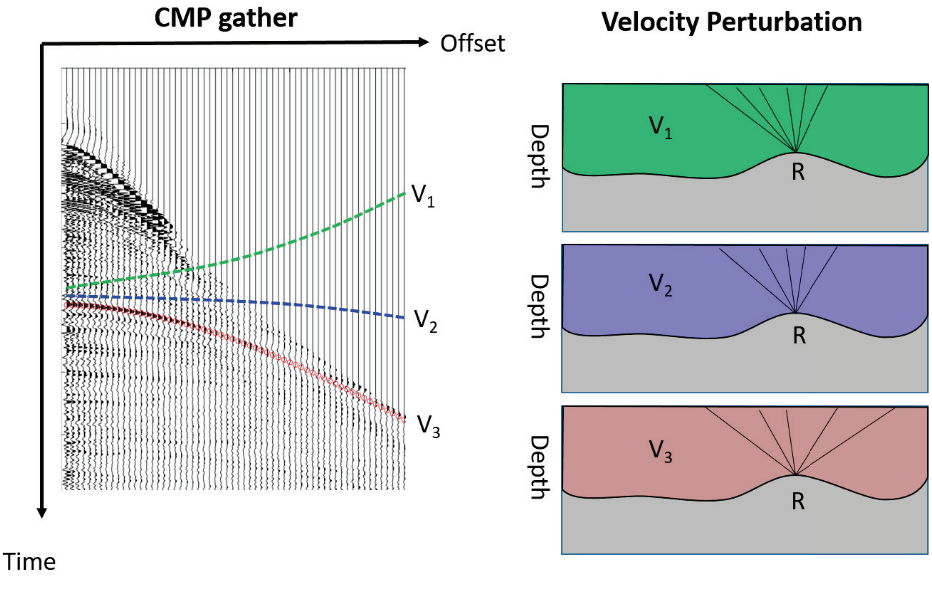

Figure 4.3: Coherent inversion.

As shown in Fig.4.3, with the perturbation of overburden velocities above the reflection point, the calculated trajectories vary. The trajectory calculated at the optimal velocity will best fit the seismic event and generate the highest semblance. The advantage of this method is that it employs ray tracing in the trajectory's modelling, thus being able to handle non-hyperbolic events in the data. However, the main disadvantage of this method is that it is not very accurate for complex structures, and is susceptible to noise in the seismic data. Therefore, this method is more commonly used to construct an initial depth-velocity model.

- **Deregowski loop**

This approach assumes that the seismic data has been migrated using an appropriate depth-migration velocity model to generate flat events on migrated gathers. In its operation, the migrated-depth gathers are scaled to time, and an inverse NMO correction is applied using the rms velocity converted from the depth-migration velocity. A new rms velocity picking is applied subsequently. Ideally, if the depth-migration velocity is accurate, the newly-derived rms velocity will be identical to the converted rms velocity. If not, the new rms velocity will be converted to an interval velocity using Dix, and used to update the existing migration velocity. The advantage of this method is that it is simple to apply. The disadvantage is that the process is a 1D operation that does not consider lateral variation caused by a velocity update and, also, the picked RMS velocity is used to update the existing depth-migration velocity by Dix transform, which will inevitably lead to errors in the velocity updates.

4.1.2.2 Tomography-based depth velocity estimation

The non-tomographic velocity-estimation methods mentioned above can be regarded as local velocity updating schemes. They are generally capable of handling moderately-complex structures, but are not suitable for geological scenarios with complex overburden structures. As global velocity update schemes, variant-tomography-based velocity-estimation approaches have been proposed and applied in the industry for several decades. Most of the tomographic methods were formulated to solve an inverse problem (Backus et al., 1968; Backus et al., 1970; Tarantola, 1987). With a predefined objective function, the tomographic inversion process measures the difference between the recorded data and the forward-modelled data derived from the existing velocity field, minimising the difference to obtain the next velocity update.

As shown in Tab.4.1, the tomographic velocity estimation can be categorised into ray- and waveform-based tomographies. Based on the domains used in the operation, they can be further classified into data domain/recording domain and image domain/migration domain tomographies. Ray-based tomography consists of reflection (e.g. Bishop et al., 1985), transmission (Brownell, 1984) and refraction (e.g. Osypov, 1999) tomographies. The waveform-based tomography represented by full waveform inversion (e.g. Pratt et al., 1996; Sirgue et al., 2004) integrates both the velocity estimation and depth migration into an inversion process to generate the optimal depth image and the migration velocity model. In this thesis, the focus is on a discussion of ray-based tomography in the data and image domains. We outline some of the main ray-based tomographic methods in the following.

	Data domain	**Image domain**
Ray-based tomography	Reflection travletime tomography Transmission tomography Refraction tomography	PSTM tomography PSDM tomography
Waveform-based tomography	Waveform tomography Full waveform inversion (FWI) Diffraction tomorgaphy	WEM velocity analysis Wavepath tomography

Table 4.1: Tomographic types and domains.

- **Reflection tomography**

Most of the ray-based tomographic velocity-estimation methods work by constructing an initial depth velocity model, followed by ray tracing to predict the travel times in the prestack datasets. The travel time differences are then minimised by iterative linear inversion to derive the velocity updates (e.g. Aki et al., 1977; Bishop et al., 1985; Williamson, 1986; Farra et al., 1988). The early reflection-tomography approaches use prestack datasets for tomographic velocity estimation, but suffer from the challenge of reflection-horizon picking in the data domain (i.e. the stacked data in the recording domain). To solve this problem, reflection-tomography methods based on depth-migrated data have been developed (e.g. Stork, 1992; Whitcombe et al., 1994; Ehinger et al., 1995). Stork, 1992 introduced the tomographic method based on a linear inversion of RMO on depth-migrated gathers. Due to the robustness of this method, it has been widely used in industrial applications of reflection tomography.

As shown in Fig.4.4, reflection tomography in the migrated domain includes the following steps: (1) the sorting of prestack data into the CO domain; (2) construction of an initial depth velocity model; (3) application of PSDM to CO sorted data using the velocity model derived from Step 2; (4) sorting the PSDM-migrated data into CIGs; (5) picking the RMO on the CIGs; (6) applying linearised tomography using the RMO to derive the velocity update; (7) updating the initial velocity model; and (8) repeating Steps 3–7 until the CIGs are flattened.

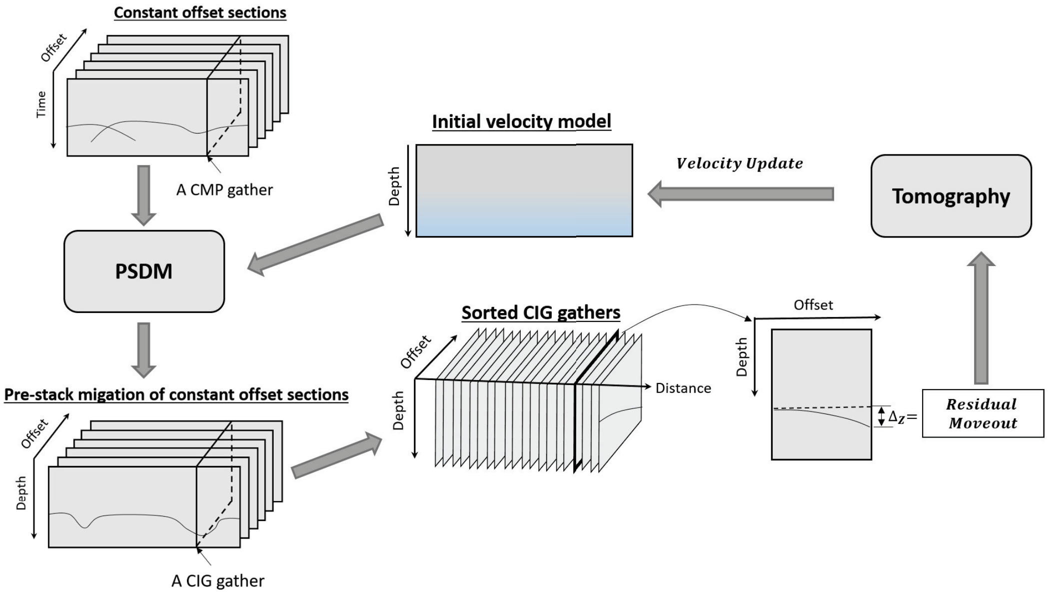

Figure 4.4: Schematics of reflection tomography in the migrated domain.

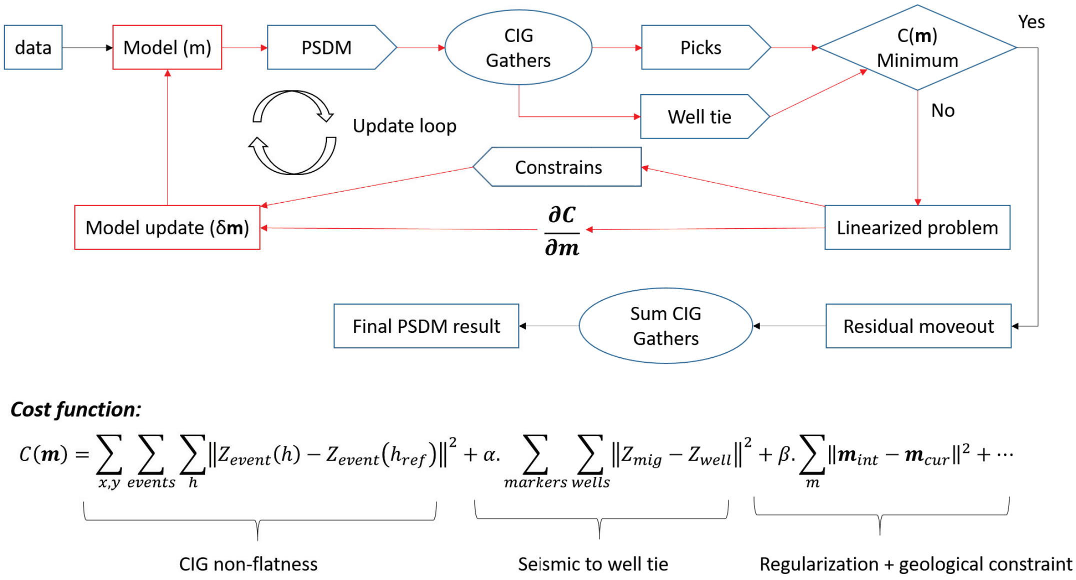

Figure 4.5: Schematic workflow of linearized tomography. After the first model is set up. PSDM is run with this model. CIG gathers are analysed in terms of event flatness. The model is updated in such a way as to reduce the coset function C(m). The process is iterated until C(m) reaches a minimum value. A PSDM is needed in each iteration.

The goal of the depth-velocity estimation is to find the depth-velocity model that best flattens the CIGs. This is achieved through a tomographic inversion process. Tomography can be regarded as an optimisation problem. With a defined cost function, the tomography must find the best velocity-model parameters to minimise the cost function. With respect to the reflection tomography, a linearised tomography workflow is formulated, as shown in Fig.4.5. As shown, the cost function of the reflection tomography is mathematically quantified by the RMO on the CIGs and additional constraints (seismic-to-well ties, regularisation and geological constraints, etc.). With the defined cost function, the tomography is formulated to give a linearised problem, and is solved by an optimisation method.

To solve a linearised tomography, the equivalent optimisation problem is to minimise the RMOs (ΔZ) of the events on the CIGs. Assuming a prestack dataset has been migrated using an initial depth-migration velocity $\mathbf{m}_{\text{cur}}$, we can characterise the RMO of the event on the CIGs by comparing the migrated depth at offset 2h with the depth at the reference (ZO) offset:

$$\Delta Z_{\text{event}}\left(x, y, h, \mathbf{m}_{\text{cur}}\right) = Z_{\text{event}}\left(x, y, h, \mathbf{m}_{\text{cur}}\right) - Z_{\text{event\_ref}}, \left(x, y, h=0, \mathbf{m}_{\text{cur}}\right), \tag{4.5}$$

where Z_{event} is the migrated depth for a given event, $Z_{\text{event\_ref}}$ is the migrated depth at the reference offset, ΔZ is the depth difference representing the RMO of the picked event, x and y are the coordinates of a CIG location, h is the half-offset and $\mathbf{m}_{\text{cur}}$ is the current velocity model.

After quantifying the RMO, we hope to obtain a more accurate velocity model ($m_{\text{final}} = m_i + dm_i$) to flatten the events on the gathers and to remove the RMO. Based on the linearised inversion theory, if the current RMO is small, we can linearise the problem by finding the small velocity perturbation dm_i to correct the RMO. Thus, by using the first-order Taylor expansion, Eq.4.5 can be written as:

$$\Delta Z_{\text{event}}\ \left(x, y, h, m_{\text{final}}\ \right) = \Delta Z_{\text{event}}\ \left(x, y, h, m_{\text{cur}}\ \right) + \sum_{m_i} \frac{\partial \Delta z}{\partial m_i} \cdot dm_i \equiv 0, \tag{4.6}$$

The quantity $\frac{\partial \Delta z}{\partial m_i}$ is the gradient representing perturbations of the RMO Δz, with respect to the small changes in a single velocity-model parameter m_i. Eq.4.6 can be further rewritten as a matrix notation:

$$\left[\partial \Delta Z_j / \partial m_i\right]_{i=1,N;j=1,M} \cdot \begin{bmatrix} \vdots \\ dm_i \\ \vdots \end{bmatrix}_{i=1,N} = - \begin{bmatrix} \vdots \\ \Delta Z_j \\ \vdots \end{bmatrix}_{j=1,M}, \tag{4.7}$$

where $[\partial \Delta Z_j / \partial m_i]$ is a Jacobian matrix represented by M x N gradients, $\left[\ \ldots dm_i \ldots \ \right]^T$ is the N x 1 vector, representing the velocity perturbation to be solved, and $\left[\ \ldots \Delta Z_j \ldots \ \right]^T$ is the M x 1 vector, denoting the RMOs.

Based on the known RMOs, and the necessary gradients (calculated by ray tracing), the velocity perturbations are then estimated by solving the linear equations (Eq.4.7). In practice, as the formulated linearised equations may have billions of parameters, and need to be repeated for many iterations, some numerical algorithm-like conjugate gradients can be employed to solve the system. Once the velocity perturbations have been derived from Eq.4.7, the migration velocity is updated for the next iteration of the reflection tomography. After several iterations, we can finally obtain the optimal depth-migration velocity model.

- **Stereotomography**

Stereotomography (another type of reflection-based tomography) was developed by Billette et al., 1998, and is based on the concept of slope tomography, introduced by Rieber, 1936, Riabinkin, 1957 and Sword, 1986. This technique makes use of the picked travel times and slopes from the shot and receiver gathers, and constructs a ray-based tomographic system to derive the velocity-model update.

The idea behind this method is to use locally-coherent events in the prestack non-migration domain, which are characterised by travel times and slopes, to derive information about the velocity model. As shown in Fig.4.6, each locally-coherent event of the tomographic dataset **d** is described by:

$$\mathbf{d} = \left(\mathbf{s}, \mathbf{r}, T_{\text{sr}}, \mathbf{P}_s, \mathbf{P}_r \right), \tag{4.8}$$

where s and r are the source and receiver positions, respectively, T_{sr} is the two-way travel time, and $\mathbf{P}_s$ and $\mathbf{P}_r$ are slopes of the event in the common-receiver and common-shot gathers.

Any locally-coherent event is associated with a pair of model parameters (ray-segment parameters):

$$\left(\mathbf{x}, \phi_{\mathbf{s}}, \phi_{\mathbf{r}}, T_s, T_{\mathbf{r}} \right), \tag{4.9}$$

where $\mathbf{x}$ is the position of the reflector, ϕ_s and ϕ_r are the ray-shooting angles from $\mathbf{x}$ toward $\mathbf{s}$ and $\mathbf{r}$, and T_s and T_r are two one-way travel times from $\mathbf{x}$ toward $\mathbf{s}$ and from $\mathbf{x}$ toward $\mathbf{r}$.

Meanwhile, the stereotomographic model is defined as a combination of the velocity model, described by a set of velocity parameters (V_m) and a set of pairs of ray segments associated with each picked event:

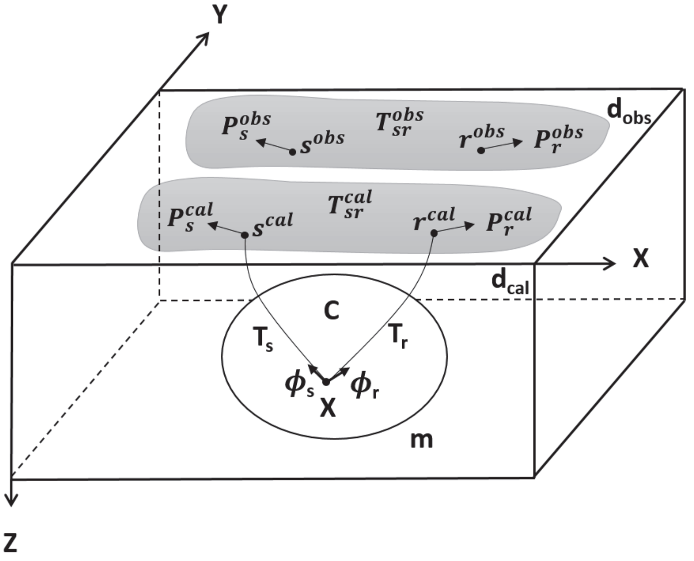

Figure 4.6: Stereotomography data and model. The dataset consists of a set of shot and receiver positions ($\mathbf{s}$ and $\mathbf{r}$), travel times (T_{sr}) and slopes at both the receiver and shot locations ($\mathbf{P}_r$ and $\mathbf{P}_s$), picked on locally-coherent events. The model is composed of a discrete description of the velocity field C_m, and a set of diffracting points ($\mathbf{x}$), two scattering angles (ϕ_s, ϕ_r), and two one-way travel times (T_s, T_r) associated with each picked event (Billette et al., 1998, figure redrawn)

.

$$\mathbf{m} = \left[(V_m)_{m=1}^{M} , [(\mathbf{x}, \beta_s, \beta_{\mathbf{r}}, T_s, T_{\mathbf{r}})_n]_{n=1}^{N} \right] , \tag{4.10}$$

where $\mathbf{x}$ is the position of the reflector/diffractor point, $\beta_{\mathbf{s}}$ and $\beta_{\mathbf{r}}$ are the ray-shooting angles from $\mathbf{x}$ toward $\mathbf{x}$, and T_s and T_r are two one-way travel times from $\mathbf{x}$ toward $\mathbf{s}$ and from $\mathbf{x}$ toward $\mathbf{r}$.

At the modelling stage, assuming the model parameters and associated ray-segment parameters are known, a set of stereotomographic data attributes (Eq.4.11) can be calculated by ray tracing from scatter point X to the surface, using the initial ray-shooting angles ϕ_s and ϕ_r, and with the travel time lengths corresponding to T_s and T_r.

$$\mathbf{d}_{\text{calc}} = (\mathbf{s}, \mathbf{r}, T_{\text{sr}}, \mathbf{P}_s, \mathbf{P}_r)_{\text{calc}} , \tag{4.11}$$

Once the initially-picked locally-coherent event attributes $\mathbf{d}$ and the velocity-model-calculated attributes $\mathbf{d}_{\text{calc}}$ have been prepared, a tomographic scheme can be formulated to minimise the calculated and observed data. The corresponding cost function is defined as:

$$C(\mathbf{m}) = \frac{1}{2} (\mathbf{d}_{\text{calc}}(\mathbf{m}) - \mathbf{d}_{\text{obs}})^T C_D^{-1} (\mathbf{d}_{\text{calc}}(\mathbf{m}) - \mathbf{d}_{\text{obs}}) , \tag{4.12}$$

where C_D denotes a prior covariance matrix for the data parameters (Tarantola, 1987).

To solve this optimisation problem, an iterative nonlinear local optimisation scheme, such as a quasi-Newton method, can be used to calculate the velocity update, and the Fréchet derivatives of the data $\mathbf{d}$, with respect to model $\mathbf{m}$, can be derived by paraxial ray tracing (Billette et al., 1998).

As an effective tomographic method, stereotomography has been one of the most popular methods used for depth-velocity estimation. However, because this approach requires accurate slope picking on the shot and receiver gathers in the recording domain, the quality and cost of the picking becomes a major limitation. To solve this problem, Chauris et al. (2002a,b) proposed a flatness criterion for locally-coherent events in the migrated domain for the linear tomographic inversion. It proposed locally-coherent event-picking on the CIGs in the migrated domain, a demigration process to map the attributes to the recording domain, and a tomographic inversion for the velocity estimation. This approach improves the stability of the stereotomographic method because of the more feasible picking in the migrated domain. However, the limitation of this method is that it still needs tedious manual interaction and careful quality control for the locally-coherent event picking.

- **Tomography based on CRS wavefront kinematic attributes**

As understood from previous chapters, CRS stacking provides enhanced ZO stack and local kinematic wavefront attributes. These kinematic attributes can also be used in tomographic inversion to derive velocity information. The concept of tomography based on (CRS) kinematic wavefront attributes was proposed by Duveneck and Hubral (2002) and Duveneck (2004).

Assuming the CRS stack has been applied to a dataset, and the kinematic wavefront attributes (i.e. the emergence angle ϕ, the radius of curvature R_{NIP} of the NIP wave emerging at the surface position ξ, and the two-way-travel time t0) have been generated, the tomographic problem can then be set as: given input data $(T, M, \phi, \xi)_i$, $i = 1, ..., n_{data}$, find velocity model parameters m_{jk}, $j = 1, ..., n_x, k = 1, ..., n_z$, and normal ray starting parameters at depth $(x, z, \theta)_i$, $i = 1, ..., n_{data}$ that correctly model the input data (shown in Fig.4.7). Here, $M = 1/v_0 R_{\mathrm{NIP}}$ and $T = t_0/2$ are used in the calculations (V_0 is the near-surface velocity); M is the second derivative of the travel time, with respect to the ray-centre coordinate; x and z are the coordinates of the reflection point; and θ is the starting angle of the normal ray (i.e. the reflector dip). Once the data and model have been parameterised, the tomographic problem can be set up to minimise the misfit between the measured values $(T, M, \phi, \xi)_i$ and those obtained by dynamic ray tracing in the model. This nonlinear tomography problem is then linearised and solved by iterative least squares inversion.

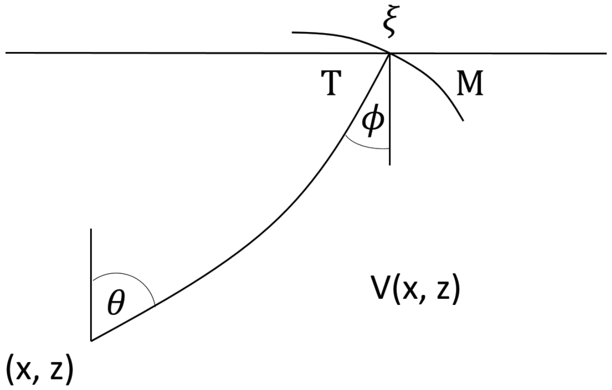

Figure 4.7: Definition of data and model components. The data consist of the quadruples (T, M, ϕ, ξ), while the model consists of the corresponding triples (x, z, θ) and the velocity field $v(x, z) = \sum_{j=1}^{n_x} \sum_{k=1}^{n_z} m_{jk}\beta_j(x)\beta_k(z)$.

Another tomographic method utilising (CRS) kinematic wavefront attributes was proposed by Lavaud et al. (2004) – poststack stereotomography. Contrary to the approach introduced by Duveneck and Hubral (2002) and Duveneck (2004), this method converts CRS wavefront kinematic attributes into stereotomographic parameters, and uses the stereotomography to solve the velocity estimation. The workflow of this method is summarised as:

i Calculation of CRS and wavefront parameters for each CMP position and time sample.

ii Picking locally-coherent events on the CRS stacked section.

iii Prestack travel time and slope calculations using the picked events and the associated wavefront parameters. For each picked event at $(\mathbf{X_{cmp}}, t_0)$, we compute for a given offset $\mathbf{h}$:

  a) the source position $\mathbf{s} = \mathbf{X_{cmp}} - \mathbf{h}/2$ and the receiver position $\mathbf{r} = \mathbf{X_{cmp}} + \mathbf{h}/2$.
  b) the associated prestack traveltime $t(\mathbf{s}, \mathbf{r}) = t_{CRS}\,(X_{cmp}, \mathbf{h})$ using the CRS operator.
  c) the local slopes in the offset direction $\mathbf{p_h} = \frac{\partial t_{CRS}}{\partial h}$ and in the CMP direction $\mathbf{p_m} = \frac{\partial t_{CRS}}{\partial x_{cmp}}$. The local slopes at the source andreceiver are then given by $\mathbf{p_s} = \frac{(\mathbf{p_m} - \mathbf{p_h})}{2}, \mathbf{p_r} = \frac{(\mathbf{p_m} + \mathbf{p_h})}{2}$.

Based on these steps, a set of prestack data parameters $(\mathbf{s}, \mathbf{r}, \mathbf{p_s}, \mathbf{p_r} and t_{sr})$ for stereotomographic inversion is prepared. A stereotomographic scheme can then be applied to estimate the depth-migration velocity model.

- **Non-linear tomography**

Most of these depth-velocity estimation methods require a full PSDM at each iteration of the tomography. Thus, this linear tomography process is expensive, and may converge slowly in complex areas. In order to reduce the cost of the tomography, another tomographic approach – nonlinear tomography – was introduced by Adler et al. (2008). This method proposed employing nonlinear 3D tomographic inversion to replace the conventional linear tomographic processes. As shown in Fig.4.8, the nonlinear tomography only applies full PSDM once in the tomographic process. Unlike linear tomographic methods that pick the events in the recording or migrated domain, nonlinear tomography first demigrates a horizon picked on the RMO-corrected stack in the migrated domain to its ZO equivalent horizon in the recording domain, and then uses ray tracing to emulate PSDM by finite-offset map migration, and models synthetic CIGs in the migrated domain. Ultimately, the modelled synthetic gathers are compared with the PSDM gathers (RMO applied) to derive misfits for velocity tomographic optimisation.

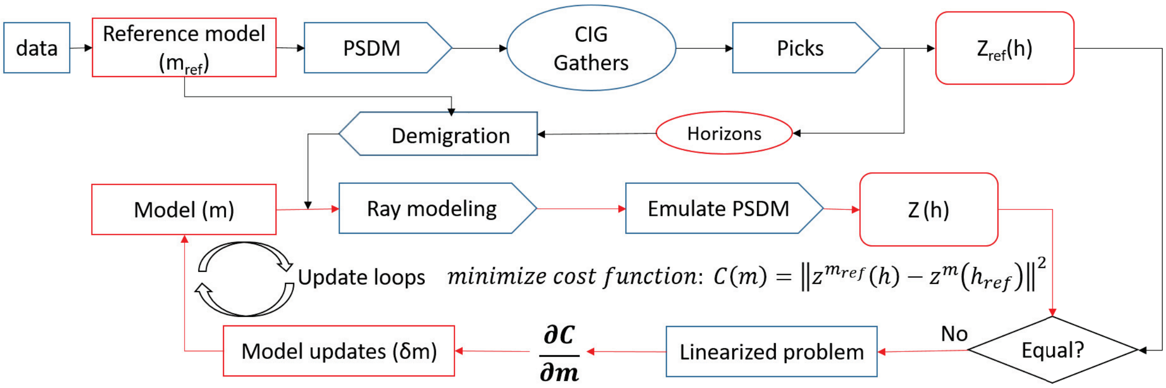

Figure 4.8: Schematic workflow of nonlinear tomography.

Apart from the method proposed by Adler et al. (2008), Guillaume et al. (2008) addressed the flexibility of using the kinematic invariants (travel times and slopes in the unmigrated recording domain) for nonlinear depth tomography. Lambaré et al. (2009) also demonstrated the concept of nonlinear tomography for time-migration velocity estimation. These proposed nonlinear tomographic approaches greatly reduce the turnaround time and costs associated with depth-migration velocity estimation by replacing the conventional PSDM and velocity RMO analysis with the kinematic migration/demigration-based internal velocity updating scheme. Due to the their efficiency and effectiveness, The nonlinear tomographic technique has attracted much more attention and development for industrial application and from academic research in recent years (Guillaume et al.,2013; Messud et al., 2015).

4.2 Time-migration velocity estimation based on nonlinear kinematic migration/demigration solvers

As discussed in previous sections, nonlinear tomography is an effective and efficient technique for seismic migration velocity estimation. Compared to linear tomography, nonlinear tomography does not require complete PSDM and RMO picking in each iteration, which greatly reduces project costs. Moreover, nonlinear tomography quantifies the RMO by its kinematic attributes, and uses those kinematic attributes (travel times and slopes) in the tomographic velocity estimation, which also increases the flexibility and stability of the tomography.

In Paper III, we revisited the nonlinear tomographic technique, introducing a time-migration velocity-estimation technique based on the concept of nonlinear kinematic migration and demigration. In this paper, based on available explicit and analytic expressions that relate kinematic attributes (namely, travel times and local slopes) of locally-coherent events in the recording (demigration) and migrated domains, we revisited tomographic methodologies for velocity-model building with a specific focus on the time domain. We particularly focused on the ones that made use of local slopes, as well as travel times, as key attributes for imaging. We adopted a strategy of estimating local inclinations in the time-migrated domain (where there is less noise and better focus), and use demigration to estimate those inclinations in the recording domain.

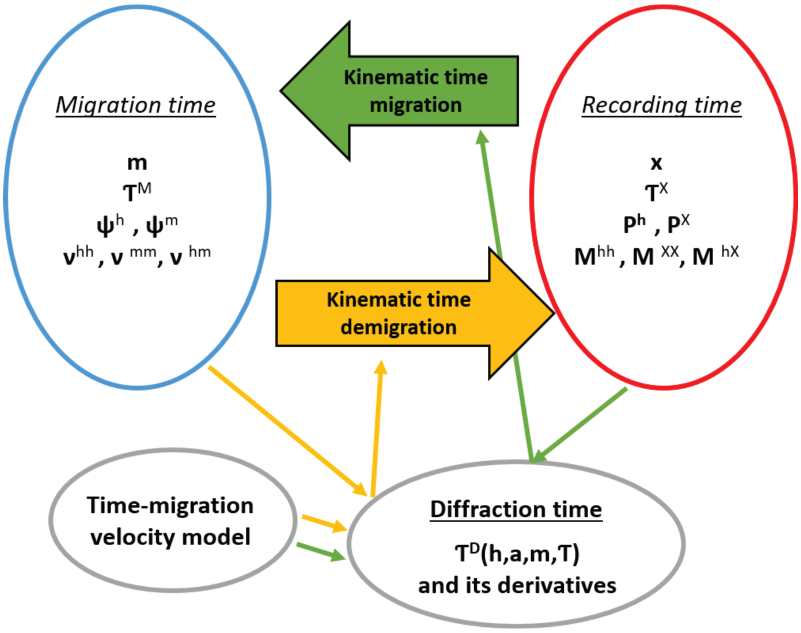

Figure 4.9: Kinematic time migration (green) and demigration (orange) processes for constant offset, with indicated input and output reflection-time parameters. The process estimates the aperture vector and a number of diffraction-time partial derivatives, using the given input parameters and the known time-migration velocity model. Small green/orange arrows signify the data flow. Redrawn from Iversen et al. (2012).

As shown in the kinematic migration and demigration scheme from Iversen et al. (2012) (Fig.4.9), assuming the time-migration velocity model and a diffraction function with its derivatives are known, the kinematic attributes in the recording and migration domains can be mapped correspondingly with the kinematic migration/demigration. In Paper III , we revisited this kinematic time-migration and -demigration scheme (Iversen et al., 2012) and develop a detailed numerical scheme for time-migration velocity estimation, employing the kinematic attributes. In the following, we provide an introduction to the basic elements of the proposed method.

4.2.1 Overview of kinematic attributes

Kinematic attributes (kinematic parameters) refer to the local kinematic parameters of a seismic event point, which are represented by the local slopes and curvatures of the individual event point. It is known that such quantities provide the travel time approximation of the seismic event in the vicinity of that reference event point (e.g, Ursin, 1982; Landa et al., 1999; Hubral, 1999; Jäger et al., 2001; Fomel et al., 2012), and that they are associated with the first- and second-order derivatives of the measured travel time (Bortfeld, 1989; Schleicher et al., 1993).

Kinematic attributes have been used for a number of applications in seismic processing, imaging and inversion. These include: (1) poststack/prestack data enhancement (e.g. Baykulov et al., 2009; Faccipieri et al., 2016); (2) diffraction separation and imaging (e.g., Berkovitch et al., 2009; Klokov et al., 2012); (3) time migration/demigration (e.g. Dell et al., 2011; Iversen et al., 2012); (4) data interpolation and regularisation (e.g. Hoecht et al., 2009; Coimbra et al. (2016)); and (5) attribute-oriented seismic processing (e.g. Zhang et al., 2002; Cooke et al., 2009).

Iversen et al (2012) systematically generalised and extended kinematic time migration and demigration using kinematic attributes. We follow the convention for defining the kinematic attributes, as explained below. We first define the coordinate system used for the kinematic attributes and the associated kinematic mapping, then we present the analytic diffraction function, which can be used to derive the derivatives, and ultimately provide the generalised kinematic attributes.

- *Coordinate systems for recorded and migrated seismic data*

We use a 2D Cartesian coordinate system (ξ_1, ξ_2) to describe the acquisition geometry of 3D seismic experiments. As shown in Fig.4.10, in the horizontal measurement plane, we consider a source point, $\mathbf{s} = (s_1, s_2)$, and a receiver point, $\mathbf{r} = (r_1, r_2)$. The midpoint and half-offset coordinates are given as:

$$\mathbf{x} = \frac{1}{2}(\mathbf{r}+\mathbf{s}), \qquad \mathbf{h} = \frac{1}{2}(\mathbf{r}-\mathbf{s}). \tag{4.13}$$

We also define the output point of the time migration using the notation $\mathbf{m}$. Then we can derive the aperture vector $\mathbf{a}$ as:

$$\mathbf{a} = \mathbf{x} - \mathbf{m}. \tag{4.14}$$

and define $\mathbf{h^S}$ and $\mathbf{h^R}$ as the source-offset vector and the receiver-offset vector, respectively.

$$\begin{aligned} \mathbf{h^S} &= \mathbf{s}-\mathbf{m} = \mathbf{a}-\mathbf{h}, \\ \mathbf{h^R} &= \mathbf{r}-\mathbf{m} = \mathbf{a}+\mathbf{h}. \end{aligned} \tag{4.15}$$

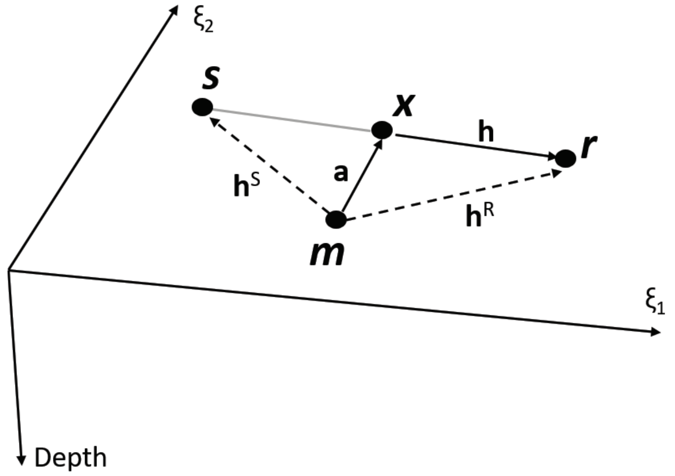

Figure 4.10: Coordinate system used for describing 3D seismic experiments. The source ($\mathbf{s}$), receiver ($\mathbf{r}$), CMP ($\mathbf{x}$) and common-image point ($\mathbf{m}$) are defined in the horizontal measurement plane. The vectors of the aperture ($\mathbf{a}$), half-offset $\mathbf{h}$, source-offset $\left(\mathbf{h}^S\right)$ and receiver-offset $\left(\mathbf{h}^R\right)$ are outlined.

- *Diffraction Time Function for Time Migration and Demigration*

The analytic diffraction-time function is used to generate the kinematic attribute-related derivatives. The example given here uses one widely-used diffraction-time function – the double-square-root (DSR) equation – which is based on the exact travel-time function for both P- and S-wave-propagation homogeneous isotropic media. The formulation is:

$$T^D = T^S + T^R, \tag{4.16}$$

$$T^S = \sqrt{\frac{\tau^2}{4} + (\mathbf{a}-\mathbf{h})^T S^M(\mathbf{m},\tau)(\mathbf{a}-\mathbf{h})}), \tag{4.17}$$

$$T^R = \sqrt{\frac{\tau^2}{4} + (\mathbf{a}+\mathbf{h})^T S^M(\mathbf{m},\tau)(\mathbf{a}+\mathbf{h})}), \tag{4.18}$$

where $T^S, T^R and T^D$ represent the travel time from source to diffraction point, travel time from diffraction point to receiver, and total travel time, respectively. $S^M(m,\tau)$ is defined as the time-migration velocity model.

- *Diffraction-time function partial derivatives*

Based on the predefined diffraction-time function, such as the presented DSR travel time function, we can derive the analytic expression of the partial derivatives used in the kinematic migration and demigration. Those derivatives are the partial derivative of the diffraction time T^D, with respect to the half-offset, h, aperture, a, image gather location, m, and migration time, τ, which are given as:

i *First order partial derivatives*

$$u = \frac{\partial T^D}{\partial \tau}, \quad \mathbf{q}^h = \frac{\partial T^D}{\partial \mathbf{h}}, \quad \mathbf{q}^a = \frac{\partial T^D}{\partial \mathbf{a}}, \quad \mathbf{q}^m = \frac{\partial T^D}{\partial \mathbf{m}}. \tag{4.19}$$

ii *Second order partial derivatives*

$$\begin{aligned}
\mathbf{u}^h &= \frac{\partial^2 T^D}{\partial \mathbf{h}\partial \tau}, & \mathbf{u}^a &= \frac{\partial^2 T^D}{\partial \mathbf{a}\partial \tau}, & \mathbf{u}^m &= \frac{\partial^2 T^D}{\partial \mathbf{m}\partial \tau} \\
\mathbf{U}^{hh} &= \frac{\partial^2 T^D}{\partial \mathbf{h}\partial \mathbf{h}^T}, & \mathbf{U}^{aa} &= \frac{\partial^2 T^D}{\partial \mathbf{a}\partial \mathbf{a}^T}, & \mathbf{U}^{mm} &= \frac{\partial^2 T^D}{\partial \mathbf{m}\partial \mathbf{m}^T} \\
\mathbf{U}^{ha} &= \frac{\partial^2 T^D}{\partial \mathbf{h}\partial \mathbf{a}^T}, & \mathbf{U}^{hm} &= \frac{\partial^2 T^D}{\partial \mathbf{h}\partial \mathbf{m}^T}, & \mathbf{U}^{am} &= \frac{\partial^2 T^D}{\partial \mathbf{a}\partial \mathbf{m}^T} \\
\mathbf{U}^{ah} &= \mathbf{U}^{ha^T}, & \mathbf{U}^{mh} &= \mathbf{U}^{hm^T}, & \mathbf{U}^{ma} &= \mathbf{U}^{am^T}
\end{aligned} \tag{4.20}$$

where,$\mathbf{q}^h, \mathbf{q}^a, \mathbf{q}^m, \mathbf{u}^h, \mathbf{u}^a, \mathbf{u}^m$ are 2x1 diffraction-time partial derivative vectors, and $\mathbf{U}^{hh}, \mathbf{U}^{aa}, \mathbf{U}^{mm}, \mathbf{U}^{ha}, \mathbf{U}^{hm}, \mathbf{U}^{am}, \mathbf{U}^{ah}, \mathbf{U}^{mh}, \mathbf{U}^{ma}$ are 2x2 diffraction-time partial derivative matrices.

- *Reflection-time function partial derivatives*

For the reflection-time function, we generalise two single-valued reflection-time functions corresponding to symmetrically-reflected waves:

$$t = T(\mathbf{h}, \mathbf{x}), \quad \tau = \tau(\mathbf{h}, \mathbf{m}), \tag{4.21}$$

where T and τ are the reflection time function in the recording and time-migration domains, respectively.

By obeying the same convention, we can also define the reflection-time parameters in the recording and time-migration domains:

i *First- and second-order partial derivatives in the recording domain*

$$\mathbf{p} = \frac{\partial T}{\partial \mathbf{x}} = \begin{pmatrix} \mathbf{p}^h \\ \mathbf{p}^x \end{pmatrix}, \quad \mathbf{M} = \frac{\partial^2 T}{\partial \mathbf{x} \partial \mathbf{x}^T} = \begin{pmatrix} \mathbf{M}^{hh} & \mathbf{M}^{hx} \\ \mathbf{M}^{hx^T} & \mathbf{M}^{xx} \end{pmatrix}, \tag{4.22}$$

where we define the kinematic parameters for a reflection event at a given trace location in the recording domain thus: reflection time, $T^X = T(\mathbf{h}, \mathbf{x})$,, slope (first-order derivative) vectors $\mathbf{p}^h = \partial T / \partial \mathbf{h}, \mathbf{p}^x = \partial T / \partial \mathbf{x}$, and second-order derivative matrices $\mathbf{M}^{hh} = \partial^2 T / \partial \mathbf{h} \partial \mathbf{h}^T, \mathbf{M}^{hx} = \partial^2 T / \partial \mathbf{h} \partial \mathbf{x}^T$, $\mathbf{M}^{\mathbf{xx}} = \partial^2 T / \partial \mathbf{x} \partial \mathbf{x}^T$.

ii *First- and second-order partial derivatives in the migration domain*

$$\psi = \frac{\partial \mathcal{T}}{\partial \mathbf{m}} = \begin{pmatrix} \boldsymbol{\psi}^h \\ \boldsymbol{\psi}^m \end{pmatrix}, \quad \mathcal{M} = \frac{\partial^2 \mathcal{T}}{\partial \mathbf{m} \partial \mathbf{m}^T} = \begin{pmatrix} \mathcal{M}^{hh} & \mathcal{M}^{hm} \\ \mathcal{M}^{hm^T} & \mathcal{M}^{mm} \end{pmatrix}, \tag{4.23}$$

where we also define the kinematic parameters for a reflection event at a given trace location in the migration domain: migrated reflection time, $\mathcal{T}^M = \mathcal{T}(\mathbf{h}, \mathbf{m})$,, slope vectors $\boldsymbol{\psi}^h = \partial \mathcal{T} / \partial \mathbf{h}, \boldsymbol{\psi}^m = \partial \mathcal{T} / \partial \mathbf{m}$, and second-order derivative matrices $\mathcal{M}^{hh} = \partial^2 \mathcal{T} / \partial \mathbf{h} \partial \mathbf{h}^T, \mathcal{M}^{hm} = \partial^2 \mathcal{T} / \partial \mathbf{h} \partial \mathbf{m}^T, \mathcal{M}^{mm} = \partial^2 \mathcal{T} / \partial \mathbf{m} \partial \mathbf{m}^T$.

In our method, considering the implementation efficiency and calculation robustness, we chose the GST method for the first-order kinematic parameter (slope) extraction and the QST for the second-order kinematic parameter (curvature) extraction. The numerical GST and QST schemes are described in Chapter I. This operation is applied either to stacked data in the migration domain or to the NMO stack in the recording domain.

4.2.2 Kinematic migration and kinematic demigration

Kinematic migration and its counterpart kinematic demigration have been used to map kinematic local wavefront attributes (travel times, slopes and curvatures) from/to the recording time domain to/from the migrated time or depth domain (e.g. Hubral et al., 1980; Gjøystdal et al., 1981; Ursin, 1982; Iversen et al., 1996; Iversen, 2004). With respect to the kinematic demigration, Whitcombe et al. (1994) introduced a ZO kinematic time demigration scheme using the constant migration velocity assumption. Söllner et al. (2004) further investigated ZO kinematic migration and demigration under the framework of ray theory.

A systematic generalisation and extension of kinematic time migration and demigration was developed by Iversen et al., (2012). The proposed technique extends the kinematic time migration and demigration from ZO to finite-offset, includes both the first-order (slope) and second-order (curvature) travel time derivatives during the mapping, and generalises for any type of diffraction-time functions. We illustrate the concept of kinematic migration and demigration using the 2D prestack schematics in Fig.4.11, which use the diffraction-time function and time-migration velocity to nonlinearly map the kinematic parameters (travel time and slope) between the recording and migration domains. In Paper III, we presented a detailed and generalised numerical scheme for kinematic time demigration and migration.

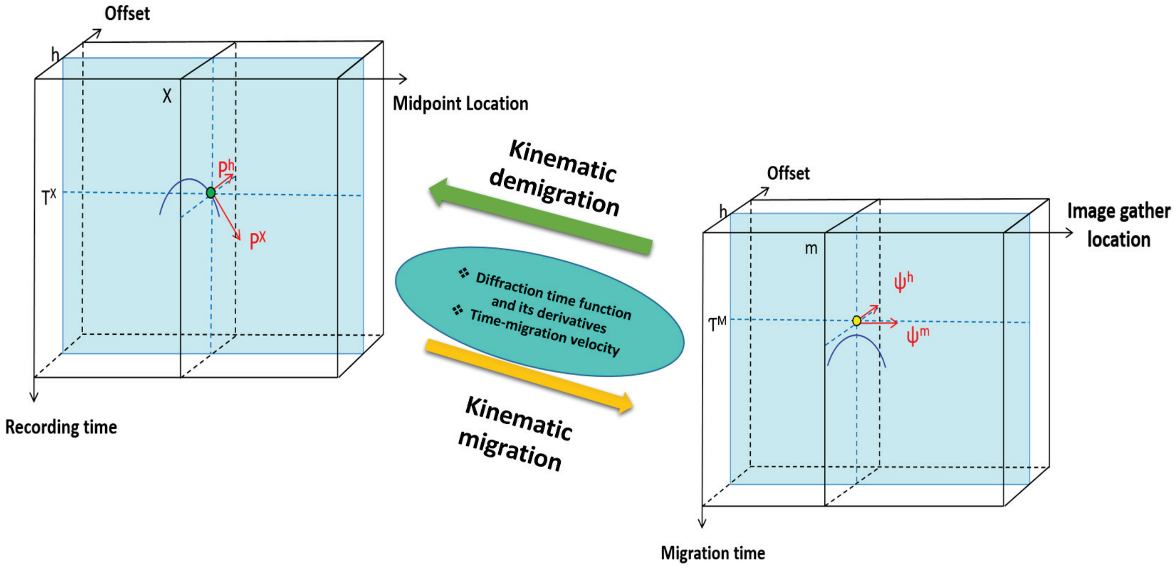

Figure 4.11: Schematic overview of kinematic time migration and demigration for a 2D prestack seismic dataset. Based on the known diffraction-time function, with its associated derivatives, and a time-migration velocity model, the local kinematic parameters $(\mathbf{x}, T^x, \mathbf{p}^x, \mathbf{p}^h)$ in the recording domain can be forward/backward-mapped to/from the counterpart $(\mathbf{m}, \mathcal{T}^M, \boldsymbol{\psi}^m, \boldsymbol{\psi}^h)$ in the migration domain by kinematic time migration/demigration.

4.2.3 Time-migration velocity model

In this proposed algorithm, we use the grid-based velocity model to describe the time-migration velocity. The time-migration velocity model is defined on a 3D rectangular grid in the variables $\xi_1 = m_1$, $\xi_2 = m_2$ and $\xi_3 = \tau$, where we add ξ_3 to describe the velocity model in the time domain. Model parameters related to cells or vertices within the grid will be unknowns in the velocity-estimation process. The velocity model is described in terms of a multi-component vector function, (M_λ), $\lambda = 1, \ldots, N^\lambda$, where each component function $M_\lambda(\xi_1, \xi_2, \xi_3)$ corresponds to one of the coefficients of the diffraction-time function.

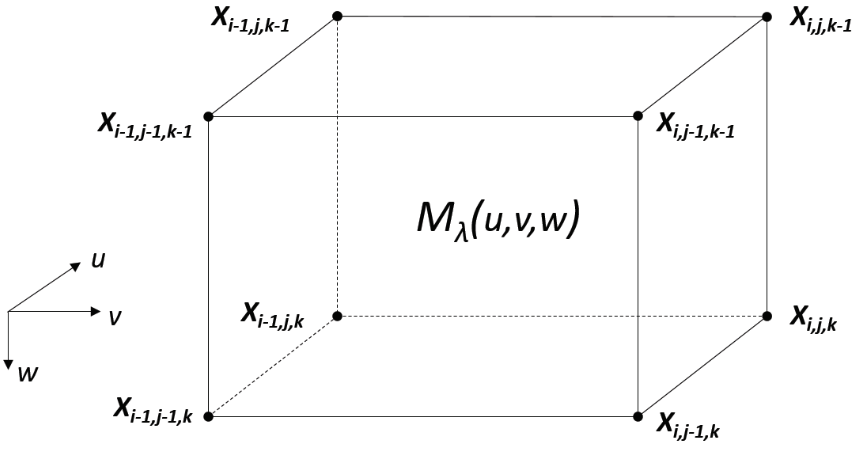

Figure 4.12: Grid cell and local dimensionless coordinate (u, v, w) used for describing the 3D time-migration velocity model.

As shown in Fig.4.12, the time-migration model is defined on a 3D rectangular grid. The model parameters relate to the cells and the corresponding vertices within the grid. A rectangular grid cell (i, j, k) is defined in terms of eight vertices. We assume that the value of the function M_λ is known in all relevant grid vertices $X_{i,j,k}$, and these values are denoted as ${M_\lambda}^{i,j,k}$.

In the tomography, we apply a local function $\mathcal{M}_\lambda(u, v, w)$ that pertains to only one selected cell. The variables u, v, w are dimensionless, and take values in the interval $[0, 1]$ (in this case, $M_\lambda\,(\xi_1, \xi_2, \xi_3) = \mathcal{M}_\lambda(u, v, w)$). The function $\mathcal{M}_\lambda$ is then expressed as values in the grid vertices that are neighbours to the cell. To allow the differentiability of this function up to the second order, we use a local cubic spline function to describe the velocity model (bicubic and tricubic spline functions are used for 2D and 3D grids, respectively).

4.2.4 Inversion scheme of time-migration velocity estimation

Based on the formulated kinematic time-migration/-demigration scheme, we set up an inversion scheme to estimate the time-migration velocity. In the following, we first give an overview of a common way of linearising a generally nonlinear inversion problem, then we introduce the approach of iterative linearised inversion to estimate the optimal time-migration velocity model.

Assuming we have observed (true) data and predicted data in the migration domain, the misfit between these can be expressed as a function $\mathcal{D}_m(\boldsymbol{\nu})$, where $\boldsymbol{\nu}$ is the model parameter vector with M components:

$$\mathcal{D}_m(\boldsymbol{\nu}) = d_m^{\text{true}} - d_m^{\text{pred}}(\boldsymbol{\nu}), \quad m = 1, \ldots, M. \tag{4.24}$$

This equation can be linearised with respect to a reference model $\boldsymbol{\nu}^0$, where the quantity $\partial d_m^{\text{pred}} / \partial \nu_n$ is the Fréchet derivative of $\mathcal{D}_m$, with respect to $\boldsymbol{\nu}$.

$$\mathcal{D}_m(\boldsymbol{\nu}) = \mathcal{D}_m\left(\boldsymbol{\nu}^0\right) + \frac{\partial \mathcal{D}_m}{\partial \nu_n}\left(\boldsymbol{\nu}^0\right)\left(\nu_n - \nu_n^0\right). \tag{4.25}$$

Given $\mathcal{D}_m(\boldsymbol{\nu}) = 0$ with optimal model parameters, the equation is rearranged as:

$$\frac{\partial \mathcal{D}_m}{\partial \nu_n}\left(\boldsymbol{\nu}^0\right)\left(\nu_n - \nu_n^0\right) = -\mathcal{D}_m\left(\boldsymbol{\nu}^0\right). \tag{4.26}$$

In our time-migration velocity estimation, the observed data represent ideal slopes in the offset coordinates of the CIGs, which are zero and correspond to an optimal time-migration velocity model. The predicted data represent the corresponding slopes of the CIGs migrated using the current time-migration velocity model. The Fréchet derivative of $\mathcal{D}_m$, with respect to $\boldsymbol{\nu}$, is now $\frac{\partial \psi_I^h}{\partial \nu_n}$, which is a partial derivative of the reflection slope in the offset coordinates ψ_I^h, with respect to the parameters ν_n of the time-migration velocity model.

$$\frac{\partial \psi_I^h}{\partial \nu_n}\left(\boldsymbol{\nu}^0\right)\left(\nu_n - \nu_n^0\right) = -\psi_I^h\left(\boldsymbol{\nu}^0\right). \quad I = 1, 2. \tag{4.27}$$

To derive the Fréchet derivative of the above linear system, $\frac{\partial \psi_I^h}{\partial \nu_n}$, we applied the sensitivity analysis of kinematic time migration, with respect to the time-migration velocity model, and derived the analytic expression of the first-order changes of the reflection location, with respect to the time-migration velocity model (i.e. the derivatives $\mathrm{d}\hat{m}_I/\mathrm{d}\nu$ and $\mathrm{d}\hat{\tau}/\mathrm{d}\nu$), as well as the the first-order changes of the reflection slopes (i.e. the derivatives$\mathrm{d}\psi_I^h/\mathrm{d}\nu$).

Based on the above inversion scheme as set up above, and the derived Fréchet derivatives, we are able to estimate the time-migration velocity by using the kinematic parameters and the nonlinear mapping of the kinematic migration/demigration.

4.2.5 Workflow of time-migration velocity estimation based on kinematic migration/demigration

Based on the formulated inversion scheme, we can summarise the workflow of the time-migration velocity estimation based on the nonlinear kinematic migration/demigration solvers as:

i Sort prestack data into common offset planes.

ii Construct an initial time-migration velocity model by smoothing the stacking velocities.

iii Apply PSTM with the initial time-migration velocity model to derive the migrated CIGs.

iv Derive the kinematic attributes in the migration domain $\left(\mathbf{m}, \tau, \boldsymbol{\psi}^{\mathbf{h}}, \boldsymbol{\psi}^{\mathbf{m}}\right)$ by applying the GST methods and picking the locally-coherent events.

v Apply the kinematic demigration to generate the invariant kinematic attributes in the recording domain $\left(\mathbf{x}, T, \mathbf{p}^{h}, \mathbf{p}^{x}\right)$.

vi Apply the internal iterations for time-migration velocity estimation, employing the invariant kinematic attributes in the recording domain. This process includes kinematic migration and a constrained linear inversion scheme.

vii Apply full PSTM, once the optimal time-migration velocity is obtained.

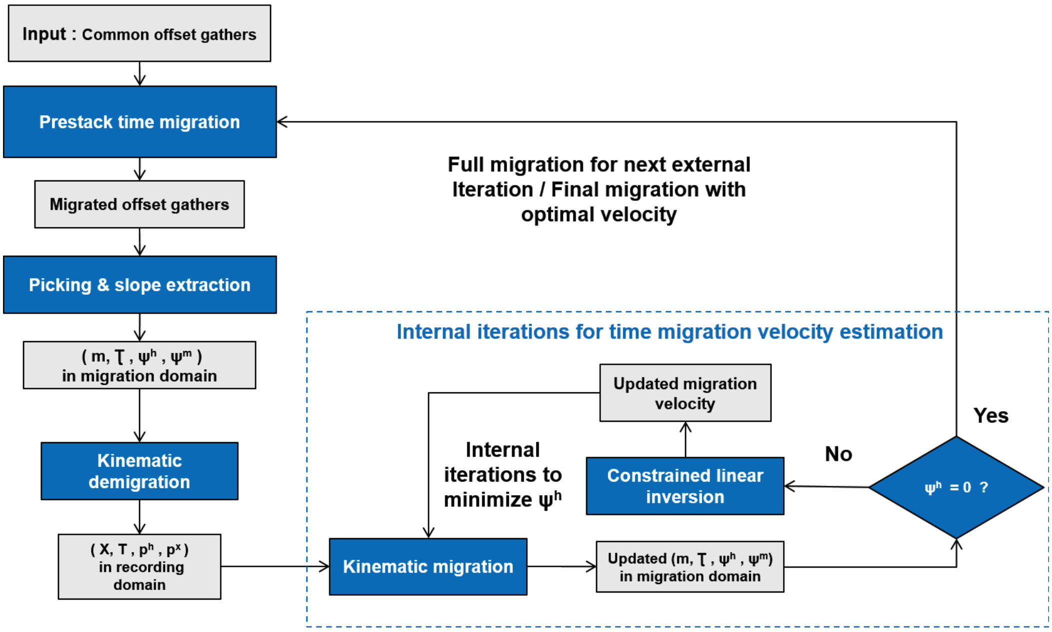

Figure 4.13: Time-migration velocity estimation workflow

Chapter 5

Summary of publications and discussion of future work

In this chapter, the contributions of the papers are summarised, and potential future work is proposed.

5.1 Paper I

Fast and robust Common Reflection Surface (CRS) parameter estimation
Anders U. Waldeland, Hao Zhao, Jorge H. Faccipieri, Anne H. Schistad Solberg, and Leiv-J. Gelius
Geophysics, 83, O1-013, January, 2018.

The CRS method is an effective way to enhance the SNR of seismic data. Compared to the conventional NMO stack, the CRS stack provides a strong increase in redundancy and SNR. Conventionally, CRS parameters are obtained by semblance-based parameter searches, which require expensive computation. In order to solve this problem, we proposed a fast and robust (ZO) CRS parameter-estimation technique in this paper. The proposed method can be generalised as the following steps: (1) assume that a velocity guide is provided and derive parameter C based on the velocity field; (2) construct a CMP stack based on the known velocity; and (3) apply GST and QST methods to derive parameters A and B. In numerical examples, we compared the proposed method with an existing slope-based CRS parameter-estimation method. Our proposed method demonstrated comparable accuracy and considerably improved efficiency over the conventional semblance search- and slope-based CRS parameter-estimation methods.

Although the proposed method is robust and efficient for CRS parameter estimation, there are some limitations to its application. First, the proposed approach assumes that an appropriate initial velocity field is provided for the stack and parameter estimation. If a poor initial velocity field is used in the stacking process, the stacked section will not have consistent reflections, or it will be contaminated by noise, which will deteriorate the CRS parameter estimation. In such a case, we would suggest applying the proposed method with a limited aperture size to estimate the initial CRS parameters, and then employ the semblance-based search to further refine the parameters. Moreover, the proposed approach has limitations in its application to complex structures or structures with conflicting dips. This is because the GST and QST methods assume that there is only one dominant direction for a local structure. To address this challenge in a future work, we would propose implementing an extended (higher-order) structure tensor method for multi-directional estimation (Barmpoutis et al., 2007; Herberthson et al., 2007; Andersson et al., 2013). Alternatively, the kinematic parameters can also be estimated in the time-migration domain, as we proposed in Paper III, and mapped back to the recording domain via a nonlinear kinematic demigration scheme. As discussed above, the CRS parameters can be utilised to estimate the time- and depth-migration velocities (Duveneck et al., 2002; Duveneck, 2004; Lavaud et al., 2004; Gelius et al., 2015). In a future study, we would integrate the GST- and QST-based CRS parameter estimation into those velocity estimation methods to further improve the efficiency of the migration-velocity estimation based on CRS parameters.

5.2 Paper II

3D Prestack Fourier Mixed-Domain (FMD) depth migration for VTI media with large lateral contrasts
Hao Zhao, Leiv-J. Gelius, Martin Tygel, Espen Harris Nilsen, and Andreas Kjelsrud Evensen
Journal of Applied Geophysics, 168C, 118-127, September, 2019.

The superiority of RTM in imaging complex media is well known. However, as a costly and computer-intensive technique, RTM is typically used in processing data from complex models. OWEM, as an effective wave-equation depth-migration approach, is still widely used among the contracting companies for 2D and 3D fast-track depth migration. Although many OWEM methods exist for isotropic depth migration, most of them struggle either with accuracy, stability or computational costs. The problem becomes more complicated when extending OWEM from 2D isotropic media to 3D anisotropic media. Thus, in this paper we presented a new method based on a mixed space- and wavenumber-propagator that overcomes these issues very effectively, as demonstrated by provided examples. The proposed method is a new OWEM algorithm for 2D and 3D prestack data that is also valid for VTI media, which can be regarded as a higher-order version of the split-step Fourier (SSF) method, and is denoted as a FMD migration. We tested the FMD technique in numerical experiments, using both the control data generated by the synthetic models (the 3D SEG/EAGE salt model and the 2D anisotropic Hess model) and the 3D field dataset, including anisotropy from the Barents Sea. All the tests demonstrated the superior image resolution provided by FMD migration.

The current version of the FMD method can handle 3D VTI media. Further extension to the more general (Tilted Transverse Isotropy) TTI case is the subject of ongoing research. In addition to the set of perturbed media parameters inherent in the present formulation, the tilt of the symmetry axis also needs to be included in a computer-efficient manner. Several similar studies have indicated the potential for an extension of the phase-screen methods, from 3D VTI to 3D TTI media (Shan et al., 2005; Bale et al., 2007; Shin et al., 2014). Future potential use of the FMD technique, besides it being an efficient PSDM method, might include iterative PSDM velocity building as an alternative to the industry-preferred Kirchhoff method.

5.3 Paper III

Time-migration velocity estimation with Fréchet derivatives based on nonlinear kinematic migration/demigration solvers
Hao Zhao, Anders Ueland Waldeland, Dany Rueda Serrano, Martin Tygel, and Einar Iversen
Studia Geophysica et Geodaetica, submitted, August 2019

PSTM is a robust and efficient process that is routinely applied in seismic imaging. It achieves reasonably accuracy in imaging simple to moderate structures with a homogeneous velocity background. An accurate time-migration velocity determines the image quality of the PSTM and affects the depth-migration result, as most depth-migration velocity estimations are highly dependent on a sufficiently accurate initial depth-velocity model, derived from the time-migration velocity, to guarantee convergence in iterative tomographic schemes. Conventionally, the most commonly-used approach of time-migration velocity estimation is migration-velocity-analysis (MVA). This is based on the iterative PSTM and residual moveout (RMO) analysis of migrated CIGs. Because this approach assumes a horizontally-layered model and invariant lateral velocities in the MVA, it is inaccurate in handling dipping structures and lateral velocity variations. Recently, seismic wavefield kinematic parameters (i.e. travel time, local slopes and local curvatures) have been more widely used in seismic processing, imaging and inversion. Migration-velocity estimation methods employing kinematic attributes have also been proposed, and have demonstrated their robustness and efficiency in depth-migration velocity estimation (e.g. Rieber, 1936; Riabinkin, 1957; Billette et al., 1998; Chauris et al., 2002a,b; Adler et al., 2008).

In this paper, we revisited nonlinear tomography, and introduced a time-migration velocity-estimation technique based on the concept of nonlinear kinematic migration and demigration. This approach utilises the kinematic attributes (travel time and local slopes) of locally-coherent events in the recording (demigration) and migrated domains, and estimates the time-migration velocity model via nonlinear kinematic migration and demigration. In order to derive accurate kinematic parameters, we adopted the gradient structure tensor (GST) method of estimating local slopes in the time-migrated domain, where we have less noise and better focus, and used demigration to estimate those slopes in the recording domain. We also formulated an iterative linear inversion scheme, and derived the Fréchet derivatives for the time-migration velocity estimation. In the numerical test, we demonstrated proof-of-concept examples, employing both 2D control and

3D field datasets. Based on the proposed approach, the time-migration velocity estimation could be further extended to construct the initial depth-migration velocity model in a future study. The nonlinear time- to depth-migration velocity mapping proposed by Cameron et al. (2007) and Iversen et al. (2008) could be employed for the velocity conversion.

Bibliography

Adler, F., Baina, R., Soudani, M. A., Cardon, P., and Richard, J.-B. (2008). "Nonlinear 3D tomographic least-squares inversion of residual moveout in Kirchhoff prestack-depth-migration common-image gathers". In: *Geophysics* vol. 73, no. 5, VE13–VE23.

Aki, K., Christoffersson, A., and Husebye, E. S. (1977). "Determination of the three-dimensional seismic structure of the lithosphere". In: *Journal of Geophysical Research* vol. 82, no. 2, pp. 277–296.

Andersson, F. and Duchkov, A. A. (2013). "Extended structure tensors for multiple directionality estimation". In: *Geophysical Prospecting* vol. 61, no. 6, pp. 1135–1149.

Audebert, F., Diet, J. P., Guillaume, P., Jones, I. F., and Zhang, X. (1997). "CRP-scans: 3D PreSDM velocity analysis via zero-offset tomographic inversion". In: *SEG Technical Program Expanded Abstracts 1997*. Society of Exploration Geophysicists.

Backus, G. and Gilbert, F. (1970). "Uniqueness in the Inversion of Inaccurate Gross Earth Data". In: *Philosophical Transactions of the Royal Society A: Mathematical, Physical and Engineering Sciences* vol. 266, no. 1173, pp. 123–192.

Backus, G. and Gilbert, F. (1968). "The Resolving Power of Gross Earth Data". In: *Geophysical Journal International* vol. 16, no. 2, pp. 169–205.

Bakker, P. (2002). "Image structure analysis for seismic interpretation". PhD thesis. Technische Universiteit Delft.

Bale, R. A., Gray, S. H., and Grech, M. G. K. (2007). "TTI Wave Eequation Migration Using Phase-Shift Plus Interpolation". In: *69th EAGE Conference and Exhibition incorporating SPE EUROPEC 2007*. EAGE.

Bancroft, J. C. and Geiger, H. D. (1994). "Equivalent offset CRP gathers". In: *SEG Technical Program Expanded Abstracts 1994*. Society of Exploration Geophysicists.

Barmpoutis, A., Vemuri, B. C., and Forder, J. R. (2007). "Registration of high angular resolution diffusion MRI images using 4th order tensors". In: *International Conference on Medical Image Computing and Computer-Assisted Intervention MICCAI* vol. 10, no. Pt 1, pp. 908–15.

Baykulov, M. and Gajewski, D. (2009). "Prestack seismic data enhancement with partial common-reflection-surface (CRS) stack". In: *Geophysics* vol. 74, no. 3, pp. V49–V58.

Bazelaire, E. de (1988). "Normal moveout revisited: Inhomogeneous media and curved interfaces". In: *Geophysics* vol. 53, no. 2, pp. 143–157.

Berkovitch, A., Belfer, I., Hassin, Y., and Landa, E. (2009). "Diffraction imaging by multifocusing". In: *Geophysics* vol. 74, no. 6, WCA75–WCA81.

Berkovitch, A., Keydar, S., Landa, E., and Trachtman, P. (1998). “Multifocusing in Practice”. In: *SEG Technical Program Expanded Abstracts 1998.* Society of Exploration Geophysicists.

Bigun, J. and Granlund, G. H. (1987). “Optimal Orientation Detection of Linear Symmetry”. In: *Proceedings of the IEEE First International Conference on Computer Vision* vol. 54, pp. 433–438.

Billette, F. and Lambaré, G. (1998). “Velocity macro-model estimation from seismic reflection data by stereotomography”. In: *Geophysical Journal International* vol. 135, no. 2, pp. 671–690.

Biondi, B. L. (2006). *3D seismic imaging.* Society of Exploration Geophysicists.

Biondi, B. and Palacharla, G. (1996). “3-D prestack migration of common-azimuth data”. In: *Geophysics* vol. 61, no. 6, pp. 1822–1832.

Bishop, T. N. et al. (1985). “Tomographic determination of velocity and depth in laterally varying media”. In: *Geophysics* vol. 50, no. 6, pp. 903–923.

Bleistein, N. (1987). “On the imaging of reflectors in the earth”. In: *Geophysics* vol. 52, no. 7, pp. 931–942.

Boehm, G., Carcione, J., and Vesnaver, A. (1996). “Reflection tomography versus stacking velocity analysis”. In: *Journal of Applied Geophysics* vol. 35, no. 1, pp. 1–13.

Bortfeld, R. (1989). “Geometrical ray theory: Rays and traveltimes in seismic systems (second-order approximations of the traveltimes)”. In: *Geophysics* vol. 54, no. 3, pp. 342–349.

Brownell, G. (1984). “Emission and transmission tomography: An overview”. In: *Nuclear Instruments and Methods in Physics Research* vol. 221, no. 1, pp. 87–92.

Cameron, M. K., Fomel, S. B., and Sethian, J. A. (2007). “Seismic velocity estimation from time migration”. In: *Inverse Problems* vol. 23, pp. 1329–1369.

Chauris, H., Noble, M. S., Lambaré, G., and Podvin, P. (2002a). “Migration velocity analysis from locally coherent events in 2-D laterally heterogeneous media, Part I: Theoretical aspects”. In: *Geophysics* vol. 67, no. 4, pp. 1202–1212.

— (2002b). “Migration velocity analysis from locally coherent events in 2-D laterally heterogeneous media, Part II: Applications on synthetic and real data”. In: *Geophysics* vol. 67, no. 4, pp. 1213–1224.

Claerbout, J. F. (1971). “Toward a unified theory of reflection mapping”. In: *Geophysics* vol. 36, no. 3, pp. 467–481.

— (1976). *fundamentals of geophysical data processing.* McGraw-Hill.

— (1985). *Imaging the earth interior.* Boston: Blackwell Scientific Publications.

— (1992). “Earth soundings analysis: processing versus inversion”. In: *Boston: Blackwell Scientific Publications.*

Coimbra, T. A., Novais, A., and Schleicher, J. (2016). “Offset-continuation stacking: Theory and proof of concept”. In: *Geophysics* vol. 81, no. 5, pp. V387–V401.

Cooke, D., Bóna, A., and Hansen, B. (2009). “Simultaneous time imaging, velocity estimation, and multiple suppression using local event slopes”. In: *Geophysics* vol. 74, no. 6, WCA65–WCA73.

Dell, S., Gajewski, D., and Tygel, M. (2014). “Image-ray Tomography”. In: *Geophysical Prospecting* vol. 62, no. 3, pp. 413–426.

Dell, S. and Gajewski, D. (2011). “Common-reflection-surface-based workflow for diffraction imaging”. In: *Geophysics* vol. 76, no. 5, S187–S195.

Deregowski, S. (1990). “Common-offset migrations and velocity analysis”. In: *First Break* vol. 8, no. 1232.

Dix, C. H. (1955). “Seismic velocities from surface measurements”. In: *Geophysics* vol. 20, no. 1, pp. 68–86.

Duveneck, E. (2004). “3D tomographic velocity model estimation with kinematic wavefield attributes”. In: *Geophysical Prospecting* vol. 52, no. 6, pp. 535–545.

Duveneck, E. and Hubral, P. (2002). “Tomographic velocity model inversion using kinematic wavefield attributes”. In: *SEG Technical Program Expanded Abstracts 2002*. Society of Exploration Geophysicists.

Ehinger, A. and Lailly, P. (1995). “Velocity model determination by the SMART method, part 1: Theory”. In: *SEG Technical Program Expanded Abstracts 1995*. Society of Exploration Geophysicists.

Etgen, J., Rietveld, W., and Alford, R. (1997). “3D V(z) Prestack Migration - an Alternative to Conventional Processing”. In:

Etgen, J., Gray, S. H., and Zhang, Y. (2009). “An overview of depth imaging in exploration geophysics”. In: *Geophysics* vol. 74, no. 6, WCA5–WCA17.

Faccipieri, J. H., Coimbra, T. A., Gelius, L. J., and Tygel, M. (2016). “Stacking apertures and estimation strategies for reflection and diffraction enhancement”. In: *Geophysics* vol. 81, no. 4, pp. V271–V282.

Faccipieri, J. H., Coimbra, T. A., Gelius, L.-j., and Tygel, M. (2016). “Stacking apertures and estimation strategies for reflection and diffraction enhancement”. In: *Geophysics* vol. 81, no. 4, pp. V271–V282.

Farra, V. and Madariaga, R. (1988). “Non-Linear Reflection Tomography”. In: *Geophysical Journal International* vol. 95, no. 1, pp. 135–147.

Fomel, S. (1994). “Kinematically equivalent differential operator for offset continuation of seismic sections: Russian”. In:

— (2003). “Asymptotic pseudounitary stacking operators”. In: *Geophysics* vol. 68, no. 3, pp. 1032–1042.

Fomel, S. and Kazinnik, R. (2012). “Non-hyperbolic common reflection surface”. In: *Geophysical Prospecting* vol. 61, no. 1, pp. 21–27.

Fomel, S., Landa, E., and Taner, M. T. (2007). “Poststack velocity analysis by separation and imaging of seismic diffractions”. In: *Geophysics* vol. 72, no. 6, U89–U94.

Fowler, P. J. (1997). “A comparative overview of prestack time migration methods”. In: *SEG Technical Program Expanded Abstracts 1997*. Society of Exploration Geophysicists.

Garabito, G., Cruz, J. C., Hubral, P., and Costa, J. (2001). “Common Reflection Surface Stack: A new parameter search strategy by global optimization”. In: *SEG, Expanded Abstracts*. SEG, pp. 2009–2012.

Gazdag, J. (1978). “Wave equation migration with the phase-shift method”. In: *Geophysics* vol. 43, no. 7, pp. 1342–1351.

Gazdag, J. and Sguazzero, P. (1984). “Migration of seismic data by phase shift plus interpolation”. In: *Geophysics* vol. 49, no. 2, pp. 124–131.

Gelius, L.-J. and Tygel, M. (2015). “Migration-velocity building in time and depth from 3D (2D) Common-Reflection-Surface (CRS) stacking - theoretical framework”. In: *Studia Geophysica et Geodaetica* vol. 59, no. 2, pp. 253–282.

Gjøystdal, H. and Ursin, B. (1981). “Inversion of reflection times in three dimensions”. In: *Geophysics* vol. 46, no. 7, pp. 972–983.

Guillaume, P., Lambare, G., et al. (2008). “Kinematic invariants: an efficient and flexible approach for velocity model building”. In: *SEG Technical Program Expanded Abstracts 2008*. Society of Exploration Geophysicists.

Guillaume, P., Reinier, M., Lambaré, G., Cavalié, A., Adamsen, M. I., and Bruun, B. M. (2013). “Dip constrained non-linear slope tomography: an application to shallow channels characterization”. In: *13th International Congress of the Brazilian Geophysical Society and EXPOGEF,Rio de Janeiro, Brazil, 26–29 August 2013*. Society of Exploration Geophysicists and Brazilian Geophysical Society.

Guitton, A., Valenciano, A., Bevc, D., and Claerbout, J. (2007). “Smoothing imaging condition for shot-profile migration”. In: *GEOPHYSICS* vol. 72, no. 3, S149–S154.

Herberthson, M., Brun, A., and Knutsson, H. (2007). “Representing pairs of orientations in the plane”. In: *Scandinavian Conference on Image Analysis*, pp. 661–670.

Hill, N. R. (1990). “Gaussian beam migration”. In: *Geophysics* vol. 55, no. 11, pp. 1416–1428.

— (2001). “Prestack Gaussian-beam depth migration”. In: *Geophysics* vol. 66, no. 4, pp. 1240–1250.

Höcht, G., Bazelaire, E. D., Majer, P., and Hubral, P. (1999). “Seismics and optics: hyperbolae and curvatures”. In: *Geophysical Prospecting* vol. 42, no. 3, pp. 261–281.

Hoecht, G., Ricarte, P., Bergler, S., and Landa, E. (2009). “Operator-oriented CRS interpolation”. In: *Geophysical Prospecting* vol. 57, no. 6, pp. 957–979.

Hubral, P. (1975). “locating a diffractor below plane layers of constant interval velocity and varying dip”. In: *Geophysical Prospecting* vol. 23, no. 2, pp. 313–322.

— (1977). “Time migration - some ray theoretical aspects”. In: *Geophysical Prospecting* vol. 25, no. 4, pp. 738–745.

— (1999). “Special issue: Macro model independent seismic imaging”. In: *Journal of Applied Geophysics* vol. 42, no. 3-4.

Hubral, P. and Krey, T. (1980). *Interval Velocities from Seismic Reflection Time Measurements*. Tulsa, USA: Society of Exploration Geophysicists (SEG).

Hubral, P., Schleicher, J., and Tygel, M. (1996). “A unified approach to 3-D seismic reflection imaging,Part II: Theory”. In: *Geophysics* vol. 61, no. 3, pp. 759–775.

Iversen, E. and Tygel, M. (2008). “Image-ray tracing for joint 3D seismic velocity estimation and time-to-depth conversion”. In: *Geophysics* vol. 73, no. 3, S99–S114.

Iversen, E. (2004). “The isochron ray in seismic modeling and imaging”. In: *Geophysics* vol. 69, no. 4, pp. 1053–1070.

Iversen, E. and Gjoystdal, H. (1996). “Event-oriented velocity estimation based on prestack data in time or depth domain1”. In: *Geophysical Prospecting* vol. 44, no. 4, pp. 643–686.

Iversen, E., Tygel, M., Ursin, B., and Hoop, M. V. de (2012). “Kinematic time migration and demigration of reflections in pre-stack seismic data”. In: *Geophysical Journal International* vol. 189, no. 3, pp. 1635–1666.

Jäger, R., Mann, J., Höcht, G., and Hubral, P. (2001). “Common-reflection-surface stack: Image and attributes”. In: *Geophysics* vol. 66, no. 1, pp. 97–109.

Jones (2003). “A review of 3D preSDM velocity model building techniques”. In: *First Break* vol. 21, no. 3, pp. 45–58.

— (2010). *An introduction to: velocity model building.* European Association of Geoscientists and Engineers.

Jones, I. F., Ibbotson, K., Grimshaw, M., and Plasterie, P. (1998). “3-D prestack depth migration and velocity model building”. In: *The Leading Edge* vol. 17, no. 7, pp. 897–906.

Kass, M., Witkin, A., and Terzopoulos, D. (1988). *Snakes: Active contour models.*

Kleyn, A. H. (1977). “On the migration of reflection time contour maps”. In: *Geophysical Prospecting* vol. 25, no. 1, pp. 125–140.

Klokov, A. and Fomel, S. (2012). “Separation and imaging of seismic diffractions using migrated dip-angle gathers”. In: *Geophysics* vol. 77, no. 6, S131–S143.

Knutsson, H. (1989). “Representing local structure using tensors”. In: *Proceedings of 6th Scandinavian Conference on Image Analysis, Oulu, Finland.* Linköping University Electronic Press, pp. 244–251.

Lambaré, G., Deladerrière, N., Traonmilin, Y., Touré, J. P., Moigne, J. L., and Herrmann, P. (2009). “Non-linear Tomography for Time Imaging”. In: *71st EAGE Conference and Exhibition incorporating SPE EUROPEC 2009.* EAGE.

Landa, E., Shtivelman, V., and Gelchinsky, B. (1987). “A method for detection of diffracted waves on common-offset sections”. In: *Geophysical Prospecting* vol. 35, no. 4, pp. 359–373.

Landa, E., Gurevich, B., Keydar, S., and Trachtman, P. (1999). “Application of multifocusing method for subsurface imaging”. In: *Journal of Applied Geophysics* vol. 42, no. 3-4, pp. 283–300.

Lavaud, B., Baina, R., and Landa, E. (2004). “Automatic robust velocity estimation by poststack Stereotomography”. In: *SEG Technical Program Expanded Abstracts 2004.* Society of Exploration Geophysicists.

Li, Z. (1991). “Compensating finite-difference errors in 3-D migration and modeling”. In: *Geophysics* vol. 56, no. 10, pp. 1650–1660.

Liu, Z. and Bleistein, N. (1995). “Migration velocity analysis: Theory and an iterative algorithm”. In: *Geophysics* vol. 60, no. 1, pp. 142–153.

Mann, J. (2001). “Common-Reflection-Surface Stack and Conflicting Dips”. In: *63rd EAGE Conference & Exhibition*.

Mann, J., Jäger, R., Müller, T., Höcht, G., and Hubral, P. (1999). “Common-reflection-surface stack: a real data example”. In: *Journal of Applied Geophysics* vol. 42, no. 3-4, pp. 301–318.

Mayne, W. H. (1962). “Common-reflection-point horizontal data stacking techniques”. In: *Geophysics* vol. 27, no. 6, pp. 927–938.

Messud, J., Lambaré, G., Guillaume, P., and Rohel, C. (2015). “Non-linear Slope Tomography for Orthorhombic Pre-stack Time Imaging”. In: *77th EAGE Conference and Exhibition 2015*. EAGE.

Minato, S., Tsuji, T., Matsuoka, T., Nishizaka, N., and Ikeda, M. (2012). “Global optimisation by simulated annealing for common reflection surface stacking and its application to low-fold marine data in southwest Japan”. In: *Exploration Geophysics* vol. 43, no. 2, pp. 59–69.

Müller (2003). “The 3D Common – Reflection – Surface Stack Theory and Application”. PhD Thesis. Universität Karlsruhe, pp. 1–110.

— (2009). “Treatment of conflicting dips in the 3D common-reflection-surface stack”. In: *Geophysical Prospecting* vol. 57, no. 6, pp. 981–995.

Neidell, N. S. and Taner, M. T. (1971). “Semblance and other coherency measures for multichannel data”. In: *Geophysics* vol. 36, no. 3, pp. 482–497.

Osypov, K. (1999). “Refraction tomography without ray tracing”. In: *SEG Technical Program Expanded Abstracts 1999*. Society of Exploration Geophysicists.

Ottolini, R. (1983). “Velocity independent seismic imaging”. In: *SEP-37: Stanford Exploration Project*.

Pratt, R. G., Song, Z.-M., Williamson, P., and Warner, M. (1996). “Two-dimensional velocity models from wide-angle seismic data by wavefield inversion”. In: *Geophysical Journal International* vol. 124, no. 2, pp. 323–340.

Riabinkin (1957). “Fundamentals of resolving power of Controlled Directional Reception (CDR) of seismic waves”. In: vol. 14, pp. 36–60.

Rieber, F. (1936). “Visual presentation of elastic wave patterns under various structural conditions”. In: *Geophysics* vol. 1, no. 2, pp. 196–218.

Ristow, D. and Rühl, T. (1994). “Fourier finite-difference migration”. In: *Geophysics* vol. 59, no. 12, pp. 1882–1893.

— (1997). “3-D implicit finite-difference migration by multiway splitting”. In: *Geophysics* vol. 62, no. 2, pp. 554–567.

Sava, P. C., Biondi, B., and Etgen, J. (2005). “Wave-equation migration velocity analysis by focusing diffractions and reflections”. In: *Geophysics* vol. 70, no. 3, U19–U27.

Schleicher, J., Hubral, P., Tygel, M., and Jaya, M. S. (1997). “Minimum apertures and Fresnel zones in migration and demigration”. In: *Geophysics* vol. 62, no. 1, pp. 183–194.

Schleicher, J., Tygel, M., and Hubral, P. (1993). “Parabolic and hyperbolic paraxial two-point traveltimes in 3d media”. In: *Geophysical Prospecting*, no. June 1992, pp. 495–513.

Schleicher, J., Tygel, M., and Hubral, P. (2007). *Seismic True-Amplitude Imaging.* Society of Exploration Geophysicists (SEG).

Schneider, W. A. (1978). "Integral formulation for migration in two and three dimensions". In: *Geophysics* vol. 43, no. 1, pp. 49–76.

Shan, G. and Biondi, B. (2005). "3D wavefield extrapolation in laterally-varying tilted TI media". In: *SEG Technical Program Expanded Abstracts 2005.* Society of Exploration Geophysicists.

Shen, P. and Symes, W. W. (2008). "Automatic velocity analysis via shot profile migration". In: *GEOPHYSICS* vol. 73, no. 5, VE49–VE59.

Shin, S.-I., Seol, S. J., and Byun, J. (2014). "Imaging Tilted Transversely Isotropy Media with a Generalized-Screen Propagator". In: *CPS-SEG Beijing 2014 International Geophysical Conference.* Society of Exploration Geophysicists and Chinese Petroleum Society.

Sirgue, L. and Pratt, R. G. (2004). "Efficient waveform inversion and imaging: A strategy for selecting temporal frequencies". In: *Geophysics* vol. 69, no. 1, pp. 231–248.

Söllner, W., Andersen, E., and Lima, J. (2004). "Fast time-to-depth mapping by first-order ray transformation in a 3-D visualization system". In: *SEG Technical Program Expanded Abstracts 2004.* Society of Exploration Geophysicists.

Stoffa, P. L., Fokkema, J. T., Luna Freire, R. M. de, and Kessinger, W. P. (1990). "Split-step Fourier migration". In: *Geophysics* vol. 55, no. 4, pp. 410–421.

Stork, C. (1992). "Reflection tomography in the postmigrated domain". In: *Geophysics* vol. 57, no. 5, pp. 680–692.

Sword, C. H. (1986). "Tomographic determination of interval velocities from picked reflection seismic data". In: *SEG Technical Program Expanded Abstracts 1986.* Society of Exploration Geophysicists.

Tarantola, A. (1987). "Inverse problem theory: Elsevier". In:

Thorson, J. R. and Claerbout, J. F. (1985). "Velocity-stack and slant-stack stochastic inversion". In: *Geophysics* vol. 50, no. 12, pp. 2727–2741.

Trier, J. V. (1990). "Reflection tomography after depth migration: Field data results". In: *SEG Technical Program Expanded Abstracts 1990.* Society of Exploration Geophysicists.

Ursin, P. (1982). "Quadratic wavefront and traveltime approximations in inhomogeneous layered media with curved interfaces". In: *Geophysics* vol. 47, no. 7, pp. 1012–1021.

Waldeland, A. U., Coimbra, T. A., Faccipieri, J. H., Solberg, A. H. S., and Gelius, L. J. (2019). "Fast estimation of prestack common reflection surface parameters". In: *Geophysical Prospecting* vol. 67, no. 5, pp. 1163–1183.

Waldeland, A. U., Jensen, A. C., Gelius, L.-J., and Solberg, A. H. S. (2018). "Convolutional neural networks for automated seismic interpretation". In: *The Leading Edge* vol. 37, no. 7, pp. 529–537.

Weijer, J. van de, Vliet, L. J. van, Verbeek, P. W., and Ginkel, M. van (2001). "Curvature Estimation in Oriented Patterns Using Curvilinear Models Applied to Gradient Vector Fields". In: *IEEE Transactions on Pattern Analysis and Machine Intelligence* vol. 23, no. 9, pp. 1035–1042.

Whitcombe, D. N., Murray, E. H., Aubin, L. A. S., and Carroll, R. J. (1994). "The application of 3-D depth migration to the development of an Alaskan offshore oil field". In: *Geophysics* vol. 59, no. 10, pp. 1551–1560.

Williamson, P. R. (1986). "Tomographic inversion in reflection seismology". In: *Workshop on Inverse Problems*. Canberra AUS: Centre for Mathematical Analysis, The Australian National University, pp. 115–131.

Al-Yahya, K. (1989). "Velocity analysis by iterative profile migration". In: *Geophysics* vol. 54, no. 6, pp. 718–729.

Yilmaz, Ö. (2001). *Seismic Data Analysis*. Society of Exploration Geophysicists.

Zhang, Y., Bergler, S., and Hubral, P. (2001). "Common-reflection-surface (CRS) stack for common offset". In: *Geophysical Prospecting* vol. 49, no. 6, pp. 709–718.

Zhang, Y., Bergler, S., Tygel, M., and Hubral, P. (2002). "Model-independent travel-time attributes for 2-D, finite-offset multicoverage reflections". In: *Pure and Applied Geophysics* vol. 159, pp. 1601–1616.

Papers

Paper II

3D Prestack Fourier Mixed-Domain (FMD) depth migration for VTI media with large lateral contrasts

Hao Zhao, Leiv-J. Gelius, Martin Tygel, Espen Harris Nilsen, Andreas Kjelsrud Evensen

Published in *Journal of Applied Geophysics*, September 2019, volume 168, issue C, pp.118-127. DOI: 10.1016/j.jappgeo.2019.06.009.

Journal of Applied Geophysics 168 (2019) 118–127

Contents lists available at ScienceDirect

Journal of Applied Geophysics

journal homepage: www.elsevier.com/locate/jappgeo

3D Prestack Fourier Mixed-Domain (FMD) depth migration for VTI media with large lateral contrasts

H. Zhao [a],*, L.-J. Gelius [a], M. Tygel [b], E. Harris Nilsen [c], A. Kjelsrud Evensen [c]

[a] University of Oslo, Department of Geosciences, Sem Sælands vei 1, 0371 Oslo, Norway
[b] University of Campinas, Center for Petroleum Studies, Rua Cora Coralina, 350 Campinas, SP, Brazil
[c] Lundin Norway AS, Oslo, Norway

ARTICLE INFO

Article history:
Received 14 January 2019
Received in revised form 30 May 2019
Accepted 10 June 2019
Available online 18 June 2019

Keywords:
Seismic migration
PSDM
Anisotropic
Fourier mixed domain

ABSTRACT

Although many 3D One-Way Wave-equation Migration (OWEM) methods exist for VTI media, most of them struggle either with the stability, the anisotropic noise or the computational cost. In this paper we present a new method based on a mixed space- and wavenumber-propagator that overcome these issues very effectively as demonstrated by the examples. The pioneering methods of phase-shift (PS) and Stolt migration in the frequency-wavenumber domain designed for laterally homogeneous media have been followed by several extensions for laterally inhomogeneous media. Referred many times to as phase-screen or generalized phase-screen methods, such extensions include as main examples of the Split-step Fourier (SSF) and the phase-shift plus interpolation (PSPI). To further refine such phase-screen techniques, we introduce a higher-order extension to SSF valid for a 3D VTI medium with large lateral contrasts in vertical velocity and anisotropy parameters. The method is denoted Fourier Mixed-Domain (FMD) prestack depth migration and can be regarded as a stable explicit algorithm. The FMD technique was tested using the 3D SEG/EAGE salt model and the 2D anisotropic Hess model with good results. Finally, FMD was applied with success to a 3D field data set from the Barents Sea including anisotropy.

1. Introduction

In seismic processing and imaging, the terminology seismic migration refers to methods designed to correct the distortions in position and shape of reflections and diffraction events, in such a way that the transformed (migrated) data are amenable to geological interpretation. Because of its prominent role in extracting meaningful information from seismic data, migration has always been a topic of active research, leading to a large variety of methodologies and applications. A general overview of migration methods, in particular their advantages and disadvantages in theory and practice, can be found in Gray et al. (2001) (see also references therein). Gray and collaborators provide a rough classification of the migration techniques into four main categories: Kirchhoff migration (performed, e.g., by stacking along diffraction curves), finite-difference migration (employing one-way wavefield continuation in space-time or space-frequency domain), reverse-time migration (using finite-differences to solve the full wave equation) and frequency-wavenumber migration (using one-way wavefield continuation in the frequency-wavenumber domain).

As an extension to the latter category, we can define the class of phase-screen propagators that represent a hybrid frequency-wavenumber formulation where also parts of the operations are carried out in the space-domain (a typical example being the thin-lens term). Well-known isotropic algorithms include the Split-Step Fourier (SSF) method (Stoffa et al., 1990) and the Phase Shift Plus Interpolation technique (PSPI) (Gazdag and Sguazzero, 1984). However, SSF degrades severely in accuracy for large velocity contrasts in combination with non-vertically travelling waves. The PSPI can handle lateral velocity variations by using multiple reference velocities within each depth level. However, the accuracy of the method relies on the number of multiple reference functions employed, which again in combination with necessary interpolations unavoidably increases the computational cost. More importantly, an extension of the PSPI method to the anisotropic case represents a major challenge with respect to the construction of an optimized range of reference functions for the anisotropic parameter set. The authors are not aware of any such successful implementation reported. Based on these observations, a new 3D phase-screen propagator scheme is derived in this paper which can handle large contrasts in the anisotropy parameters and the vertical velocity (both laterally and in depth in a VTI medium). The method is denoted Fourier Mixed-Domain (FMD) prestack depth migration (PSDM), due to its combined use of both wavenumber- and space-domain calculations. FMD can be

---

* Corresponding author.
E-mail address: zhaohao7109@gmail.com (H. Zhao).

https://doi.org/10.1016/j.jappgeo.2019.06.009
0926-9851/

regarded as a stable explicit formulation implemented as a phase-screen operator. For completeness, it should be noted that the higher-order correction terms could alternatively be implemented using an implicit finite-difference scheme. This approach is known in the literature as the Fourier Finite-Difference (FFD) method (Ristow and Rühl, 1994). However, by avoiding a finite-difference implementation in 3D as in the FMD proposed here, numerical anisotropy will not be an issue to cope with (Collino and Joly, 1995). Note also that the extension of the FFD technique to the VTI case is more challenging than that of the implicit FD technique due to difficulties in selecting appropriate references of anisotropy parameters (Hua et al., 2006 Shan, 2009). As pointed out by Zhang and Yao (2012), the choice of the reference anisotropy parameters as the minimum of each layer, will imply construction of a large table of coefficients, whereas the zero-value reference choice will lead to a simplified table but significant loss of accuracy.

The potential superiority of Reverse-Time Migration (RTM) to One-Way Wave-equation Migration (OWEM) in case of complex media is well known. However, RTM is still a costly and computer-intensive technique which typically will be employed in the late stage of processing data from complex models. OWEM is therefore still used as a pragmatic and effective wave-equation depth migration approach and is widely used among the contracting companies for 2D and 3D fast-track depth migration. Thus, the proposed 3D FMD-PSDM technique introduced here should represent a good alternative to current OWEM techniques due to its accuracy and computational efficiency. Moreover, in the velocity model building of complex media, 3D prestack Kirchhoff depth migration is still the 'working horse', due to its computational attractiveness. FMD will outperform Kirchhoff migration in image quality in case of complex geology, and may also be used as an alternative in the iterative velocity-model building due to its computational attractiveness.

This paper is organized as follows. In the first section, we derive the FMD one-way VTI propagator and then introduce the full PSDM scheme. In the section to follow, we discuss the stable implementation of the algorithm in case of strong contrasts in velocity and anisotropy parameters. The FMD method is then tested on controlled data employing the 3D SEG/EAGE salt model and the 2D anisotropic Hess model. In addition, FMD is applied with success to a 3D field data set from the Barents Sea, including anisotropy where the high-velocity target zone representing Permian carbonate rocks is well imaged.

2. 3D Fourier Mixed-Domain (FMD) one-way propagator for a VTI-medium

With some abuse of notation, we introduce the Fourier transform pairs for a general 3D seismic pressure field $p(\mathbf{x},z,t)$ with $\mathbf{x} = (x,y)$ representing a position vector in the horizontal plane

$$\begin{aligned} p(\mathbf{x},z,\omega) &= \mathfrak{I}_t\{p(\mathbf{x},z,t)\} = \int_{-\infty}^{\infty} dt\ \exp(-i\omega t)p(\mathbf{x},z,t), \\ p(\mathbf{x},z,t) &= \mathfrak{I}_\omega^{-1}\{p(\mathbf{x},z,\omega)\} = \left(\frac{1}{2\pi}\right)\int_{-\infty}^{\infty} d\omega\ \exp(i\omega t)p(\mathbf{x},z,\omega), \end{aligned} \tag{1}$$

and

$$\begin{aligned} p(\mathbf{k},z,\omega) &= \mathfrak{I}_\mathbf{x}\{p(\mathbf{x},z,\omega)\} = \int_{-\infty}^{\infty}\int_{-\infty}^{\infty} d\mathbf{x}\ \exp[-i\mathbf{k}\cdot\mathbf{x}]p(\mathbf{x},z,\omega), \\ p(\mathbf{x},z,\omega) &= \mathfrak{I}_\mathbf{k}^{-1}\{p(\mathbf{k},z,\omega)\} = \left(\frac{1}{2\pi}\right)^2\int_{-\infty}^{\infty}\int_{-\infty}^{\infty} d\mathbf{k}\ \exp[i\mathbf{k}\cdot\mathbf{x}]p(\mathbf{k},z,\omega), \end{aligned} \tag{2}$$

with $\mathbf{k} = (k_x,k_y)$ representing the wavenumber vector. Our aim is to back-propagate $p(\mathbf{x},z,\omega)$ from level z_j to $z_{j+1} = z_j + \Delta z$ by downward extrapolation in the frequency and dual space-wavenumber domains. In symbols, we assume that $p(\mathbf{x},z_j,\omega)$ is known and wish to find an approximation of $p(\mathbf{x},z_{j+1},\omega)$.

The starting point is the following ansatz for a mixed-domain representation of the vertical wavenumber (dispersion relation)

$$k_{zj}(\boldsymbol{x},\boldsymbol{k},\omega) = \sqrt{\frac{k_j^2(\boldsymbol{x}) - (1+2\varepsilon_j(\boldsymbol{x}))k_T^2}{1-2[\varepsilon_j(\boldsymbol{x})-\delta_j(\boldsymbol{x})]k_T^2/k_j^2(\boldsymbol{x})}} \tag{3}$$

with

$$k_j = \frac{\omega}{c_j(\boldsymbol{x})}, \quad \boldsymbol{k}\cdot\boldsymbol{k} = \sqrt{k_x^2+k_y^2} = k_T^2 \tag{4}$$

Note that in Eq. (3), the positive sign in front of the square root corresponds to the backpropagation (migration) case. Correspondingly, forward propagation is obtained by introducing a negative square root. In Eq. (4), ω is a fixed angular frequency, $\varepsilon_j(\mathbf{x})$ and $\delta_j(\mathbf{x})$ are the Thompson parameters, and $c_j(\mathbf{x})$ is the laterally varying vertical medium velocity within the j-th layer. We assume that evanescent waves are removed in Eq. (3), namely that $k_j^2(\boldsymbol{x}) - [1+2\varepsilon_j(\boldsymbol{x})]k_T^2 \geq 0$.

In case of no anisotropy, Eq. (3) takes the form of the mixed-domain representation as proposed by Margrave (1998) and Margrave and Ferguson (1999) for the isotropic case within the framework of nonstationary filter theory. In case of a constant medium, Eq. (3) resembles the dispersion relation introduced by Alkhalifah (1998) for a VTI medium.

Let $\mathbf{x}'$ and $\mathbf{x}$ represent position vectors in the horizontal plane at input level z_j and output level $z_j + \Delta z$, respectively. Based on Eq. (3), the following one-way wavefield extrapolation scheme can be constructed:

$$p(\mathbf{x},z_j+\Delta z,\omega) = \mathfrak{I}_\mathbf{k}^{-1}\left[\mathfrak{I}_{\mathbf{x}'}\{p(\mathbf{x}',z_j,\omega)\}\cdot\ \exp\left[ik_{z_j}(\mathbf{x},\mathbf{k},\omega)\Delta z\right]\right] \tag{5}$$

Eq. (5) can be regarded as a generalization of the continuous-velocity PSPI algorithm of Margrave and Ferguson (1999) to the anisotropic case. The name continuous-velocity PSPI is given with reference to the original PSPI-method of Gazdag and Sguazzero (1984).

To achieve efficient implementation of the algorithm in Eq. (5), we seek to factorize the dispersion relation in Eq. (3) in separate wavenumber and spatial terms. We begin by introducing the globally optimized cascaded form of the VTI dispersion relation to second order (Zhang and Yao, 2012)):

$$k_{zj}(\boldsymbol{x},\boldsymbol{k},\omega) \cong k_j(\boldsymbol{x})\left[1+\xi-\frac{a_j(\boldsymbol{x})k_T^2/k_j^2(\boldsymbol{x})}{1-b_j(\boldsymbol{x})k_T^2/k_j^2(\boldsymbol{x})}\right] \tag{6}$$

with coefficients defined as

$$\begin{aligned} &\xi = -0.00099915,\ \ a_j(x) = 0.46258453(1+2\delta_j(x)),\ \ b_j(x) \\ &\quad = 2(\varepsilon_j(x)-\delta_j(x)) + 0.40961897(1+2\delta_j(x)) \end{aligned} \tag{7}$$

We are seeking a solution to Eq. (5) which allows a split into a background plane-wave term associated with a layered model and additional correction terms taking into account lateral velocity variations and higher dip angles. This approach is by analogy with the well-known Split-Step Fourier (SSF) method of Stoffa et al. (1990). Thus, we introduce a constant background or reference medium characterized by the parameters$\{c_{0j},\varepsilon_{0j},\delta_{0j}\}$ and with a corresponding dispersion relation:

$$k_{z0j}(\boldsymbol{k},\omega) = \sqrt{\frac{k_{0j}^2-(1+2\varepsilon_{0j})k_T^2}{1-2[\varepsilon_{0j}-\delta_{0j}]k_T^2/k_{0j}^2}} \cong k_{0j}\left[1+\xi-\frac{a_{0j}k_T^2/k_{0j}^2}{1-b_{0j}k_T^2/k_{0j}^2}\right],\ k_{0j} = \frac{\omega}{c_{0j}} \tag{8}$$

where

$$a_{0j} = 0.462584531(1+2\delta_{0j}), b_{0j} = 2(\varepsilon_{0j} - \delta_{0j}) + 0.40961897(1+2\delta_{0j}) \tag{9}$$

We also introduce the following useful relation:

$$k_j(\boldsymbol{x}) = \sqrt{1+\gamma_j(\boldsymbol{x})}\cdot k_{0j}, \quad \gamma_j(\boldsymbol{x}) = \frac{c_{0j}^2}{c_j^2(\boldsymbol{x})} - 1 \tag{10}$$

with γ_j being the scattering potential or velocity contrast. By the use of Eq. (10) and a Taylor expansion (finite number of terms N assumed), we can approximate Eq. (3) as follows:

$$\begin{aligned}
&k_{zj}(\boldsymbol{x},\boldsymbol{k},\omega) \cong k_j(\boldsymbol{x})\left[1+\xi-\frac{a_j(\boldsymbol{x})k_T^2/k_j^2(\boldsymbol{x})}{1-b_j(\boldsymbol{x})k_T^2/k_j^2(\boldsymbol{x})}\right] = k_{0j}\sqrt{1+\gamma_j(\boldsymbol{x})}\cdot\\
&\left[1+\xi-\frac{A_j(\boldsymbol{x})k_T^2/k_{0j}^2}{1-B_j(\boldsymbol{x})k_T^2/k_{0j}^2}\right] = k_{0j}\sqrt{1+\gamma_j(\boldsymbol{x})}\cdot\\
&\left[1+\xi-\frac{A_j(\boldsymbol{x})k_T^2/k_{0j}^2}{\left\{1-b_{0j}k_T^2/k_{0j}^2\right\}\left\{1-\frac{(B_j(\boldsymbol{x})-b_{0j})k_T^2/k_{0j}^2}{\left[1-b_{0j}k_T^2/k_{0j}^2\right]}\right\}}\right] \cong k_{0j}\sqrt{1+\gamma_j(\boldsymbol{x})}\cdot\\
&\left[1+\xi-\sum_{n=0}^{N}\frac{A_j(\boldsymbol{x})\left(B_j(\boldsymbol{x})-b_{0j}\right)^n\left(k_T^2/k_{0j}^2\right)^{n+1}}{\left\{1-b_{0j}k_T^2/k_{0j}^2\right\}^{n+1}}\right]
\end{aligned} \tag{11}$$

where

$$A_j(\boldsymbol{x}) = \frac{a_j(\boldsymbol{x})}{1+\gamma_j(\boldsymbol{x})} \quad , \quad B_j(\boldsymbol{x}) = \frac{b_j(\boldsymbol{x})}{1+\gamma_j(\boldsymbol{x})} \tag{12}$$

Next, we introduce the equation

$$k_{zj}(\boldsymbol{x},\boldsymbol{k},\omega) \cong k_{z0j}(\boldsymbol{k},\omega) + \left[k_{zj}(\boldsymbol{x},\boldsymbol{k},\omega) - k_{z0j}(\boldsymbol{k},\omega)\right]_{approx} \tag{13}$$

where the quantities inside the bracket are calculated employing Eq. (8) and Eq. (11) giving as a final result:

$$\begin{aligned}
&k_{zj}(\boldsymbol{x},\boldsymbol{k},\omega) \cong k_{z0j}(\boldsymbol{k},\omega) + \left[k_j(\boldsymbol{x}) - k_{0j}\right](1+\xi)\\
&+k_{0j}\left[\frac{\left\{a_{0j}-\sqrt{1+\gamma_j(\boldsymbol{x})}A_j(\boldsymbol{x})\right\}k_T^2/k_{0j}^2}{\left\{1-b_{0j}k_T^2/k_{0j}^2\right\}} - \sum_{n=1}^{N}\frac{\sqrt{1+\gamma_j(\boldsymbol{x})}A_j(\boldsymbol{x})\left\{B_j(\boldsymbol{x})-b_{0j}\right\}^n\left(k_T^2/k_{0j}^2\right)^{n+1}}{\left\{1-b_{0j}k_T^2/k_{0j}^2\right\}^{n+1}}\right]
\end{aligned} \tag{14}$$

The three terms on the right-hand side of Eq. (14) can now be easily identified as the background term, the modified thin-lens term and a higher-order correction term of order N.

To test the robustness of the approximation given by Eq. (14), we calculated the relative dispersion error as a function of phase or propagation angle (no lateral variation in parameters). We considered two cases: (i) weak-contrast case with $\frac{c_0}{c} = \frac{\varepsilon_0}{\varepsilon} = \frac{\delta_0}{\delta} = 4/5$ and a (ii) strong-contrast case with $\frac{c_0}{c} = \frac{\varepsilon_0}{\varepsilon} = \frac{\delta_0}{\delta} = 1/2$. In both simulations, we let $\varepsilon = 0.3$, $\delta = 0.1$, but the velocity c changed from 2500 m/s to 4000 m/s between the two runs. It can be easily seen from Fig. 1 that the strong contrast case performs almost as well as the weak-contrast case and that the 1% phase-error limit is around 55–60 degrees. Due to the use of an *optimized* version of the anisotropic dispersion relation to second order, it may happen that for a given combination of anisotropy parameters, the weak-contrast case will locally perform slightly more poorly than the strong-contrast case (e.g. in the current example for the largest angles).

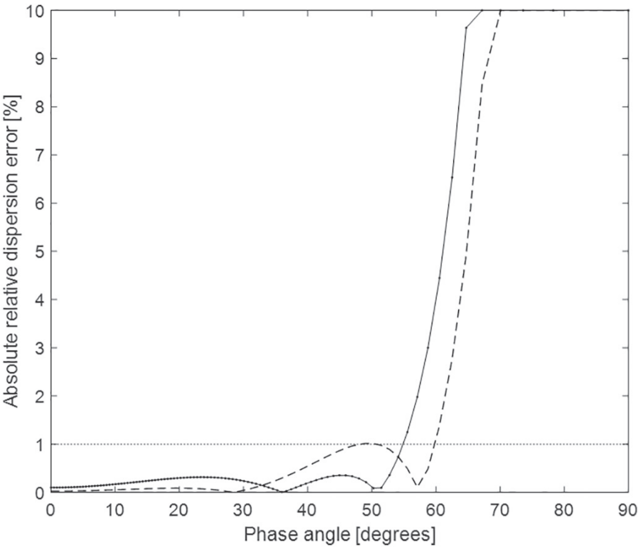

Fig. 1. Relative dispersion error versus phase angle: weak-contrast case (solid line) and strong-contrast case (broken line). The 1% dispersion-error line has also been superimposed.

Improved accuracy can be obtained if the analytical expressions for the parameters A_j and B_j are replaced by parameter fitting at higher angles formulated as an optimization problem. Such an approach is used by Shan (2009) to obtain optimized implicit finite-difference schemes for VTI media. However, because our ultimate goal is to carry out 3D prestack PSDM in complex geological models, such an optimization approach will be a highly time-consuming task, building several predefined tables of coefficients. However, such tables are typically built once for a given dataset and applied to all the shots in the survey. In this paper, we also avoid a finite-difference implementation of the perturbation term in Eq. (14) but introduce a stable explicit propagator in the Fourier mixed-domain. Accordingly, we denote our method as Fourier Mixed-Domain (FMD) PSDM. By avoiding a finite-difference implementation in 3D, numerical anisotropy will not be an issue to cope with (Collino and Joly, 1995) as in Ristow and Rühl (1994). These latter authors derived an alternative expression for the dispersion relation in Eq. 14 with one perturbation term and implemented this term as a cascading Fourier finite-difference (FFD) operator (implicit and stable scheme).

Based on Eq. (14), a one-way VTI propagator can now be constructed:

$$\begin{aligned}
&exp\left[ik_{zj}(\boldsymbol{x},\boldsymbol{k},\omega)\Delta z\right] = exp\left[ik_{z0j}(\boldsymbol{k},\omega)\Delta z\right]\cdot \exp\left[i\left(k_j(\boldsymbol{x})-k_{0j}\right)(1+\xi)\Delta z\right]\cdot\\
&exp\left[\frac{k_T^2/k_{0j}^2}{\left\{1-b_{0j}k_T^2/k_{0j}^2\right\}}\left\{ik_{0j}\left(a_{0j}-\sqrt{1+\gamma_j(\boldsymbol{x})}A_j(\boldsymbol{x})\right)\Delta z\right\}\right]\cdot\\
&exp\left[-\sum_{n=1}^{N}\frac{\left(k_T^2/k_{0j}^2\right)^{n+1}}{\left\{1-b_{0j}k_T^2/k_{0j}^2\right\}^{n+1}}\left\{ik_{0j}\sqrt{1+\gamma_j(\boldsymbol{x})}A_j(\boldsymbol{x})\left(B_j(\boldsymbol{x})-b_{0j}\right)^n\Delta z\right\}\right]
\end{aligned} \tag{15}$$

The two last exponential factors on the right-hand side of Eq. (15) are approximated using a first-order Taylor expansion, an approach which leads to the following symbolic version of a mixed-domain VTI PSDM scheme (after reorganization and neglecting high-order cross-terms):

$$\begin{aligned} P(z_j+\Delta z) = {} & exp\left[ik_{z0j}\Delta z\right]\ exp\left[i\left(k_j(\boldsymbol{x})-k_{0j}\right)(1+\xi)\Delta z\right] \\ & \times\left\{1+\Gamma_j(u,\boldsymbol{x})\right\}P(z_j),\Gamma_j(u,\boldsymbol{x}) \\ = {} & \left\{ik_{0j}\left\{a_{0j}-\sqrt{1+\gamma_j(\boldsymbol{x})}A_j(\boldsymbol{x})\right\}\Delta z\right\}\frac{u}{\left[1-b_{0j}u\right]}-\textstyle\sum_{n=1}^{N}ik_{0j}\sqrt{1+\gamma_j(\boldsymbol{x})}A_j(\boldsymbol{x})\left[B_j(\boldsymbol{x})-b_{0j}\right]^n\Delta z\frac{u^{n+1}}{\left[1-b_{0j}u\right]^{n+1}} \quad , \qquad u=k_T^2/k_{0j}^2 \end{aligned} \tag{16}$$

To make the explicit formulation in Eq. (16) unconditionally stable, we introduce a dip-filter $\Psi_j(u)$ defined by the condition.

$$\Psi_j(u)=\frac{1}{max\left(\left|1+\Gamma_j(u,\boldsymbol{x})\right|\right)} \quad , \quad 0\leq u\leq 1 \tag{17}$$

To ensure that this dip-filter harms the data as little as possible, reference values of the vertical velocity and the anisotropy parameters are computed using the mean values. In the explicit migration of Hale (1991), a stability constraint similar to Eq. 17 is employed but in the space domain. It should be noted that the conventional FD method is not stable when the medium velocity has sharp discontinuities (Biondi, 2002). Zhang et al. (2003) also use similar ideas to stabilize an isotropic phase-screen migration scheme.

The final version of the FMD scheme now takes the form:

$$\begin{aligned} & p(\boldsymbol{x},z_j+\Delta z,\omega)= \\ & exp\left[i\left(k_j(\boldsymbol{x})-k_{0j}\right)(1+\xi)\Delta z\right]\Im_{\boldsymbol{k}}^{-1}\left\{\ exp\left[ik_{z0j}\Delta z\right]\Psi_j\left(k_T^2/k_{0j}^2\right)\Im_{\boldsymbol{x}'}\left[p(\boldsymbol{x}',z_j,\omega)\right]\right\}+ \\ & \left\{ik_{0j}\left\{a_{0j}-\sqrt{1+\gamma_j(\boldsymbol{x})}A_j(\boldsymbol{x})\right\}\Delta z\right\}\ exp\left[i\left(k_j(\boldsymbol{x})-k_{0j}\right)(1+\xi)\Delta z\right]\cdot \\ & \Im_{\boldsymbol{k}}^{-1}\left\{\ exp\left[ik_{z0j}\Delta z\right]\Psi_j\left(k_T^2/k_{0j}^2\right)\frac{k_T^2/k_{0j}^2}{\left[1-b_{0j}k_T^2/k_{0j}^2\right]}\Im_{\boldsymbol{x}'}\left[p(\boldsymbol{x}',z_j,\omega)\right]\right\}- \\ & \textstyle\sum_{n=1}^{N}ik_{0j}\sqrt{1+\gamma_j(\boldsymbol{x})}A_j(\boldsymbol{x})\left[B_j(\boldsymbol{x})-b_{0j}\right]^n\Delta z\left[\ exp\left[i\left(k_j(\boldsymbol{x})-k_{0j}\right)(1+\xi)\Delta z\right]\cdot\right. \\ & \left.\Im_{\boldsymbol{k}}^{-1}\left\{\ exp\left[ik_{z0j}\Delta z\right]\Psi_j\left(k_T^2/k_{0j}^2\right)\frac{\left(k_T^2/k_{0j}^2\right)^{n+1}}{\left[1-b_{0j}k_T^2/k_{0j}^2\right]^{n+1}}\Im_{\boldsymbol{x}'}\left[p(\boldsymbol{x}',z_j,\omega.\right]\right\}\right] \end{aligned} \tag{18}$$

In case of an isotropic medium, the parameters in Eq. (18) take the simplified forms

$$a_{0j}=0.46258453, \quad b_{0j}=0.40961897, \quad A_j=\frac{a_{0j}}{\left(1+\gamma_j(\boldsymbol{x})\right)}, \quad B_j=\frac{b_{0j}}{\left(1+\gamma_j(\boldsymbol{x})\right)} \tag{19}$$

2.1. Dual-referencemodel

Our overall goal is to develop a reconstruction (migration) scheme that is able to image complex geological models (e.g., with the inclusion of salt diapers), and at the same time being computationally attractive. Due to its formulation, the FMD technique fulfils the last criterion, but inaccuracies in phases are to be expected in case of very strong vertical-velocity contrasts (i.e., velocity jumps of a factor of three and more) and/or similar large contrasts in the anisotropic parameters. In order to handle such more extreme cases, we propose dual-reference FMD for which the basic idea is as follows:

- if a region exists within a given depth-migration strip where the velocity and/or the anisotropy contrasts are larger than a user-defined factor (e.g. 2.5), backpropagation employing FMD is carried out twice for that extrapolation depth: first with the mean values as the references and second with a parameter set chosen as the mean of the values of the anomalous region(s);
- for such a migration strip, the two results are finally merged at the output level in the space domain.

The above conditions can be mathematically described as

$$p(\mathbf{x},z_j+\Delta z,\omega)=\sum_{i=1}^{2}\mathrm{M}_i(\mathbf{x})p_i(\mathbf{x},z_j+\Delta z,\omega), \tag{20}$$

where p_i $(i=1{,}2)$ represents the extrapolated field using as a reference velocity field the mean-velocity of the non-anomalous regions (say, $i=1$) and the anomalous regions ($i=2$) respectively. Moreover, as in the equation, $\mathrm{M_i}$ denote corresponding mask functions as follows: If $i=1$ specifies the mean velocity, then M_1, as in the equation, takes the value 1 at all location points corresponding to the non-anomalous regions and 0 otherwise. Correspondingly, the second mask-function M_2 represents the complementary case, $\mathrm{M}_2=1\text{-}\mathrm{M}_1$.

2.2. Comparison with literature of screen-propagators

The attractive features of simplicity and computational efficiency of frequency-wavenumber techniques have motivated a series of works aiming to generalize the approach to be valid in a more realistic geological setting. The most popular frequency-wavenumber migration schemes are Phase Shift (Gazdag, 1978) and Stolt f-k migration (Stolt, 1978). Although very quick and inexpensive, both techniques have the drawback of being limited to velocity media that varies only with depth. In order to handle lateral velocity variations, Gazdag and Sguazzero (1984) introduced PSPI. It can handle lateral velocity variations by using multiple reference velocities within each depth level. However, the accuracy of the method relies on the number of multiple reference functions employed, an approach which again in combination with necessary interpolation unavoidably increases the computational cost. An extension of the PSPI method to the anisotropic case represents a major challenge regarding how to construct an optimized range of reference functions of the anisotropic parameter set. The authors are not aware of any such successful implementation being reported.

If we consider the limit of vertically travelling waves (e.g., $k_T\rightarrow 0$) and an isotropic case, Eq. (16) will take the form of the Split-Step Fourier (SSF) method introduced by Stoffa et al. (1990). SSF can handle lateral variations and only requires a single reference velocity for each depth level. The SSF operator is unconditionally stable but degrades in accuracy for large velocity contrasts in combination with non-vertically travelling waves. Popovici (1996) extended SSF to the prestack case formulated in the offset-midpoint domain employing the DSR equation. Jin and Wu (1999) extended this latter work to also include higher-order terms. Still, the combination of strong velocities and steep angles is not treated in an accurate manner. Within an isotropic formulation, other higher-order alternatives to the SSF technique have been proposed to cope with larger propagation angles. Huang et al. (1999) introduced the Extended Local Born Fourier (ELBF) propagator to include waves propagating at non-vertical angles and Chen and Ma (2006) proposed a higher-order version of ELBF. However, despite being able to handle larger angles more accurately, this class of screen-propagators still suffers from the underlying Born assumption in case of larger velocity contrasts and the propagators become unstable in use in the frequency-wavenumber domain. Le Rousseau and de Hoop (2001a) introduced an isotropic higher-order scheme which they denoted Generalized Screen (GS) propagators. The GS scheme is more robust to velocity variations than ELBF type of schemes, but all of these techniques suffer from a singularity at the evanescent boundary. Le Rousseau and de Hoop proposed a phase normalization to stabilize the algorithm, but the accuracy of this normalization degrades with the complexity of the model (only exact for a homogeneous model). In an accompanying work, Le Rousseau and de Hoop (2001b) extended the GS scheme to a VTI type of medium. However, only weak approximations of the anisotropy parameters were introduced, and the demonstration part was limited to one modeling example (thus, no imaging results provided).

Note that all techniques discussed above are restricted to a range of propagation angles when it comes to accuracy. Thus, they do not perform better than FMD in terms of this issue in case of an isotropic medium.

2.3. 3D common-shot implementation of FMD

Applied to each common-shot gather, the FMD migration follows the classical procedure (see Claerbout, 1971) of computing, as a first step, the frequency-domain reflectivity function $r(\mathbf{x},z_j,\omega)$ at all levels $z = z_j$, and next applying the imaging condition of inverse Fourier transforming that reflectivity to the time domain and evaluating it at time zero.

We now explain the algorithm to extrapolate the reflectivity $r(\mathbf{x},z_j,\omega)$ at level $z = z_j$ (supposedly already known) to the (unknown) reflectivity $r(\mathbf{x},z_j+\Delta z,\omega)$ at the new level $z = z_j + \Delta z$. Following Claerbout (1985), an estimate of the reflectivity function $r(\mathbf{x},z_j+\Delta z,\omega)$ can be written in the form

$$r(\mathbf{x},z_j+\Delta z,\omega)=\frac{U(\mathbf{x},z_j+\Delta z,\omega)}{D(\mathbf{x},z_j+\Delta z,\omega)}=\frac{U(\mathbf{x},z_j+\Delta z,\omega)D^*(\mathbf{x},z_j+\Delta z,\omega)}{D(\mathbf{x},z_j+\Delta z,\omega)D^*(\mathbf{x},z_j+\Delta z,\omega)}. \tag{21}$$

Here, $U(\mathbf{x},z_j+\Delta z,\omega)$ and $D(\mathbf{x},z_j+\Delta z,\omega)$ are upward and downward pressure wavefields defined as follows. On one hand, $U(\mathbf{x},z_j+\Delta z,\omega)$ represents the backward extrapolation of the recorded common-source surface data to level $z = z_j + \Delta z$. On the other hand, $D(\mathbf{x},z_j+\Delta z,\omega)$ represents the forward extrapolation of the common-source point wavefield from the surface to level $z = z_j + \Delta z$. We assume that $U(\mathbf{x},z_j,\omega)$ and $D(\mathbf{x},z_j,\omega)$ at level $z = z_j$ are already available. Then, the FMD extrapolations to $U(\mathbf{x},z_j+\Delta z,\omega)$ and $D(\mathbf{x},z_j+\Delta z,\omega)$ can symbolically be expressed as

$$U(\mathbf{x},z+\Delta z,\omega)=\ell_{FMD}U(\mathbf{x},z,\omega)\ \text{ and }\ D(\mathbf{x},z+\Delta z,\omega) =\ell^*_{FMD}D(\mathbf{x},z,\omega), \tag{22}$$

where ℓ_{FMD} represents the backward FMD propagator and ℓ^*_{FMD} the corresponding FMD forward propagator. Thus, we assume that our FMD propagator can be well approximated by a pure-phase or plane-wave propagator. In such a case, the forward propagator is readily obtained from its backward propagator counterpart by means of a simple complex conjugation.

Finally, taking the inverse Fourier Transform over frequency and applying it to $t = 0$ and an additionally summation over number of shot points, provides the sought-for pre-stack FMD depth migration

$$R(\mathbf{x},z_j+\Delta z)\cong\sum_k\frac{\sum_i U_k(\mathbf{x},z_j+\Delta z,\omega_i)D^*_k(\mathbf{x},z_j+\Delta z,\omega_i)}{\left\langle\sum_i D_k(\mathbf{x},z_j+\Delta z,\omega_i)D^*_k(\mathbf{x},z_j+\Delta z,\omega_i)\right\rangle}, \tag{23}$$

the summations running over all available discrete frequencies (i) and shot points (k). Note that Eq. (23) represents a slightly different deconvolution imaging condition (IC) than the classical version of Claerbout (1985). The summation over frequencies is here carried out separately for the nominator and denominator in Eq. (23). We found that this approach gave an improved image in case of the data investigated in this paper. The notation < > in Eq. (23) indicates smoothing with a triangular filter. Before the smoothing was applied, the spatial average value I_{av} of the illumination function $I(\mathbf{x},z_j+\Delta z)=\sum_i D_k(\mathbf{x},z_j+\Delta z,\omega_i)D^*_k(\mathbf{x},z_j+\Delta z,\omega_i)$ was calculated and the following threshold introduced: if $I(\mathbf{x},z_j+\Delta z) < 0.2I_{av}$ then replace it with that value.

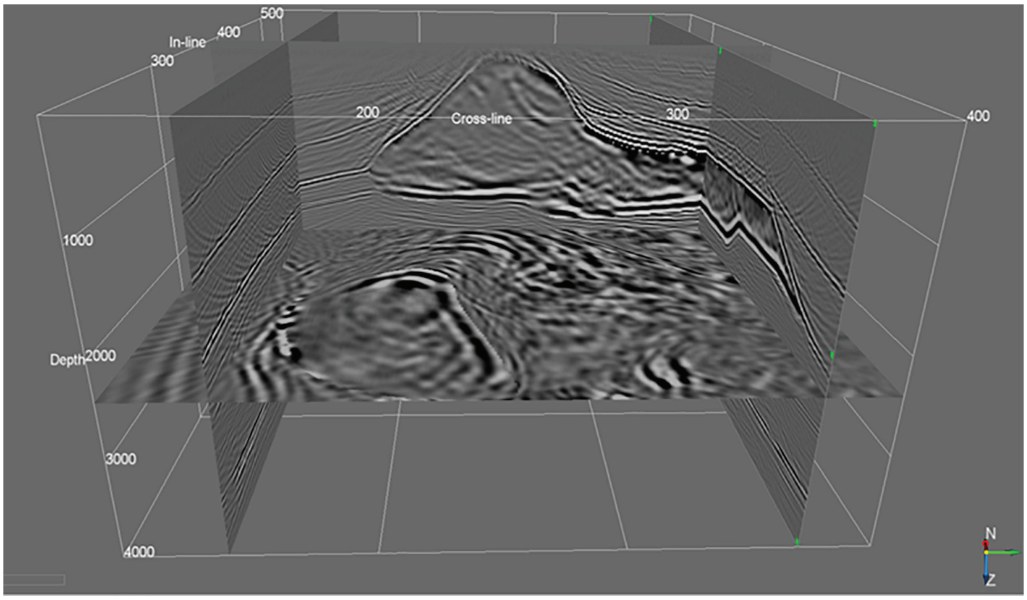

Fig. 2. Slices through final image cube.

From experience based on the datasets considered in this study, the scale-factor of 0.2 in this threshold equation seemed to be a good choice. However, in general this scale-factor can be user selected and depend on the data being employed.

3. Controlled data examples

In this section, we demonstrate the ability of the proposed FMD technique to provide accurate imaging results in case of complex controlled models. The first example involves the 3D isotropic SEG/EAGE model, whereas the second study is based on the 2D VTI Hess model.

3.1. 3D isotropic SEG/EAGE model

Data were taken from the SEG/EAGE Salt Model Phase C WA (Wide Azimuth) survey (Aminzadeh et al., 1996). For this data set, each shot has eight streamers with a maximum of 68 groups per streamer. The group interval is 40 m, the cable separation is 80 m and the shot interval is 80 m. The sample interval is 8 ms, the recording length is 5 s and the centre frequency of the source pulse is 20 Hz. The survey consists of 26 sail lines separated by 320 m and with 96 shots per line. In order to properly apply the FK-part of our imaging technique, the original 2D receiver layout corresponding to each shot point was interpolated to a finer and regular grid of 20 m × 20 m. This interpolation was carried out in the frequency domain employing a 2D spline algorithm. It is likely that the use of the more sophisticated 5D-type of interpolation algorithms would have given even better results. However, the authors did not have access to such techniques. A depth increment of 20 m was used in the FMD migration scheme. In this example, we employed the dual-velocity concept and a second-order scattering scheme (corresponding to $n = 2$ in Eq. (18)).

Fig. 2 shows a 3D visualization of the final imaging results based on representative slices through the image cube. The overall quality seems

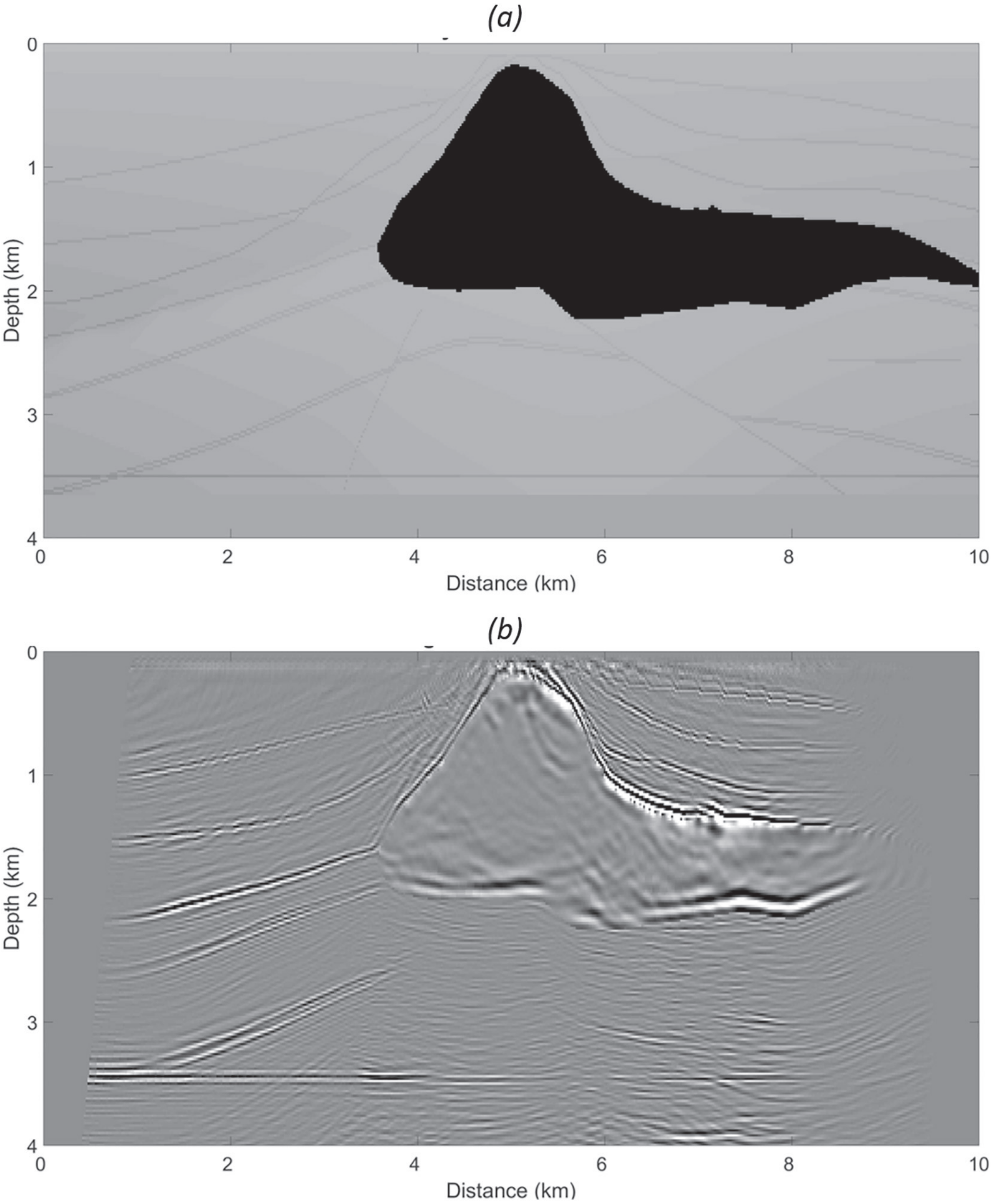

Fig. 3. (a) Stratigraphic interval velocity model and (b) corresponding FMD image.

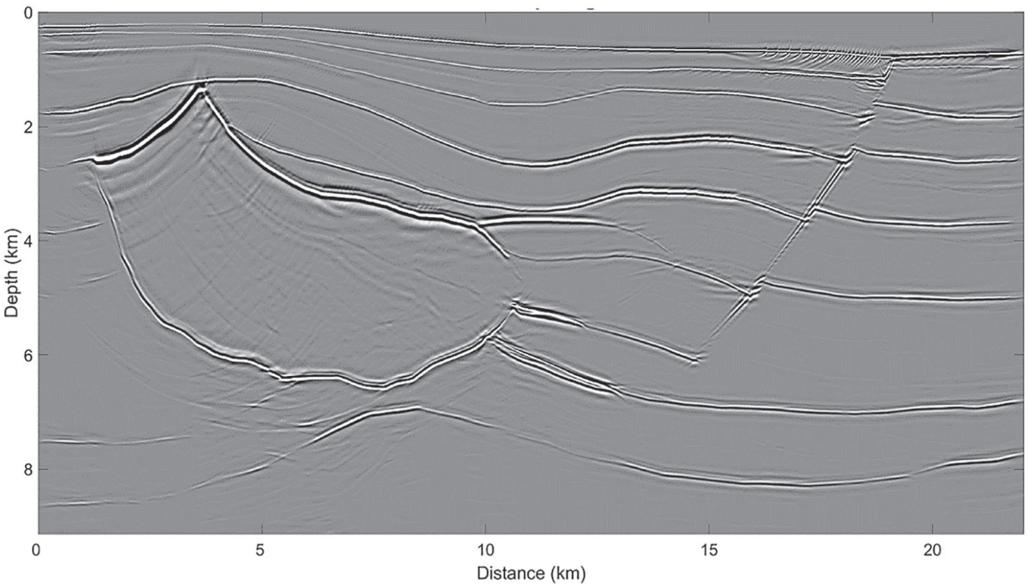

Fig. 4. Image of the Hess model obtained using 2D VTI-FMD.

to be quite satisfactory, given the complexity of the model and the imperfectness in the data generation and acquisition geometry.

To further address the quality of the FMD technique, we selected the inline profile located at X = 7700 m. Fig. 3a represents the corresponding velocity model and with the associated imaged line shown in Fig. 3b. The obtained reconstruction shown in Fig. 3b can now be compared with recently published results in the literature:

- Jang and Kim (2016) gave examples of the implementation under the use of Parallel 3D PSPI migration. The cited work is one of the latest articles of a 3D screen-propagator technique employed to the 3D SEG/EAGE salt model. In this way, it is appropriate to include their results in this paper. Their Fig. 6 represents the same inline profile as the one in our Fig. 3b. Direct comparison shows that the 3D FMD result is superior with respect to resolution and accuracy. The image obtained by Jang and Kim (2016) demonstrates the difficulties when going from 2D to 3D using Fourier techniques; in particular, the issue of spatial aliasing is a main challenge.
- Li et al. (2015) introduces 3D weak-dispersion RTM using a so-called Stereo-Modeling Operator. They apply the RTM method to the SEG/EAGE Salt Model, and their Fig. 5 gives the image of the same profile as in our Fig. 3b. However, note that Li et al. (2015) employed data from Phase A, an approach which implies that each shot has six streamers and not eight as in Phase C. More importantly, the coverage of the right part of the model is larger in Phase A. Thus, the most-right part of our image is missing simply because of this lack of coverage. When the relevant parts of the image are compared, our method is superior with more reflectors present.

3.2. 2D Hess VTI model

This model was originally built by J. Leveille and F. Qin of Amerada Hess Corp, and is considered to be representative of several exploration areas in the Gulf of Mexico. The overall structural complexity is moderate, but it includes a salt body surrounded by sedimentary layers and a relatively steep fault plane. The magnitudes of the coefficients ε and δ are in some of the intervals considered to fall between moderate to strongly anisotropic. In this study, we employ the multiple-free version of the data generated by SEP at the Stanford University. The data set consists of a 2D line with 720 shots separated by 100 ft. and with offsets ranging from 0 ft. and 26,200 ft. (receiver spacing of 40 ft). The trace length is 8 s and the temporal sampling interval is 6 msec. A depth increment of 20 ft. was used in the imaging stage. Fig. 4 shows the final image obtained using the VTI-FMD technique. In this example, we used the dual-velocity approach and a first-order scattering approximation (i.e. use of $n = 1$ in Eq. (18)). The reconstruction is well resolved with respect to both the fault system, the steep salt flank and the anisotropic anomalous regions.

We can also compare the image in Fig. 4 with recent results reported in the literature:

- Shin and Byun (2013) implemented the VTI version of the GS scheme (Le Rousseau and de Hoop, 2001a, 2001b) and tested it using the Hess model. Direct comparison with their Fig. 7b shows that the FMD technique is superior in quality: better resolved shallow parts and top salt, better-defined faulting system and the ability to image the steep flank of the salt structure. Due to the fact that the VTI-GS scheme is generally regarded as the most optimal one among the phase-screen propagators, the result obtained by our FMD technique is therefore rather encouraging.
- Han et al. (2018) introduced a wavelength-dependent Fresnel-beam migration (FBM) technique valid for VTI media. They applied the wavelength-dependent FBM to the Hess model and obtained the result shown in their Fig. 9c. In addition, a comparison with standard FBM was included (cf. their Fig. 9b). Han et al. (2018) employed Gaussian smoothing of the model parameters in advance of the migration. Direct comparison with the FMD reconstruction in Fig. 4 shows

Table 1
Key acquisition parameters.

Number of sources	2
Depth of source arrays	6 m
Shot point interval	18.75 m
Number of streamers	12
Active streamer length	7050 m
Depth of streamers	18.0–29.0 m ± 2.0 m
Group interval	12.5 m
Number of groups	564 per streamer
Streamer separation	75 m
Nominal near offset	120.9 m
Sample rate	2 ms
Record length	7060 ms
Nominal fold	94

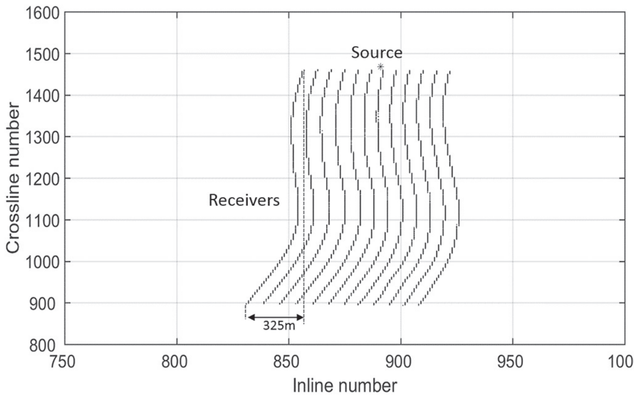

Fig. 5. Example of strong cable feathering for selected shot point.

that the two results are very similar in quality, but with FMD recovering more structures at the far-most left part of the model. However, a slight variation in amplitude of events to the right of the salt exists in the FMD result. This is due to a tighter mute applied to the migrated shots closer to the major fault to minimize spurious events.

4. 3D Marine field data example

A 3D marine dataset provided by Lundin Norway AS and acquired in the Barents Sea is used as a benchmark of the full 3D VTI-FMD method. The dataset was acquired with 12 streamers separated by 75 m and a dual-source configuration. Table 1 provides a summary of the key acquisition parameters.

Several challenges were associated with this field data set. Firstly, strong ocean currents forced the seismic survey to be acquired along the strike direction of the subsurface geology to increase the operational efficiency. However, this approach implied increased challenges for both the 3D seismic processing and imaging due to the increased amount of out-of-plane contributions. The strong ocean current also led to a significant amount of cable feathering. Fig. 5 gives an example of cable feathering for one selected shot point, where the feathering is seen to amount to approximately 300 m or more. Finally, the hard sea floor in the Barents Sea also caused strong noise interference in the marine data set.

The field data had been pre-processed by a contracting company prior to being employed in this study. This pre-processing involved navigation merging, debubble, attenuation of swell noise, and seismic interference noise as well as 3D SRME. The authors, to improve data quality and save computational time, further processed the data set. This additional processing involved the following steps:

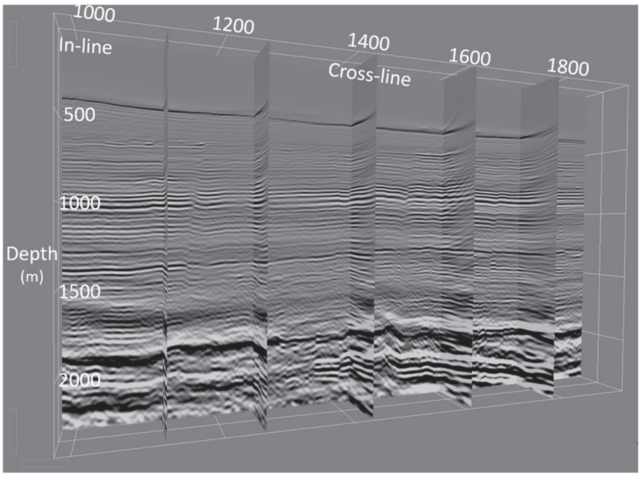

Fig. 7. 3D VTI-FMD depth migration: slices through the image cube. Note that the result is based on one sail-line only (cross-line sections stretched for ease of visualization).

- resampling from 2 to 4 ms,
- application of a tau-p mute to remove residual linear noise,
- bandpass-filtering to keep frequencies between 2 and 80 Hz only,
- data regularization employing a 2D spline interpolation in the frequency and space domain (12.5 m by 12.5 m inline and crossline sampling after regularization),
- mute in offset keeping only smaller offsets for larger travel times (due to a large increase in velocity from overburden to target zone), and
- keeping only a recording length of 2 s (sufficient to image the main target area).

In case of a real production processing, interpolation using 2D splines should be avoided due to possible smearing effects. Thus, more advanced 5D interpolation algorithms like Minimum Weighted Norm Interpolation (MWNI) (Liu and Sacchi, 2004) or Anti-Leakage Fourier Transform (ALFT) reconstruction (Xu et al., 2005) should be the preferred choice.

Before the actual 3D shot-point migration was executed, an appropriate zero-padding was introduced in space and time to minimize transform and migration noise. The contracting company had provided 3D depth cubes of the vertical velocity, as well as the anisotropy parameters ε and δ (cf. Fig. 6). It can be seen from Fig. 6 that a significant jump in the vertical velocity characterizes the area at larger depths and that

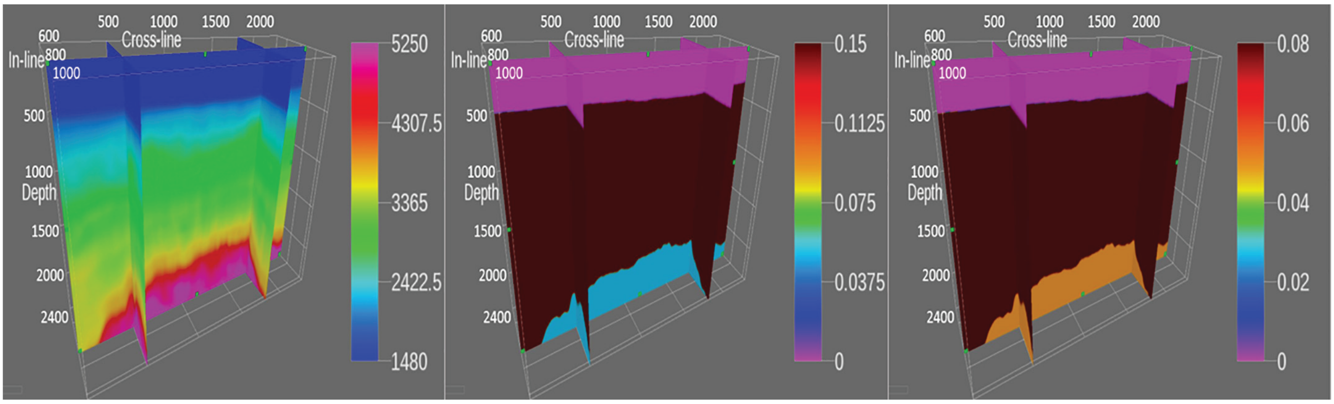

Fig. 6. Vertical-velocity cube, epsilon cube and delta cube (from left to right).

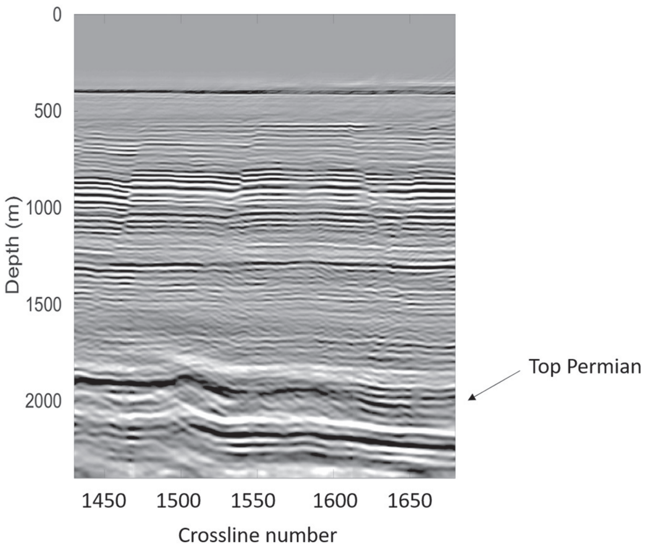

Fig. 8. Inline section taken from the image cube in Fig. 7.

the anisotropy parameters are reflecting the same jump and in general with a simple step-like variation.

A depth increment of 4 m was chosen for the migration. In this field data example, we applied a single-velocity approach and a first-order scattering approximation to lower the computational burden. Fig. 7 shows a 3D visualization of the final imaging results based on representative slices through the image cube. The fits between the inline and crossline sections seem to be overall good. Note that due to the heavy computational burden associated with 3D VTI type of PSDM using our prototype-software in Matlab, we limited the 3D demonstration of our algorithm to three sail lines in Fig. 7. To investigate further the quality of the migrated cube, one representative inline section is shown in Fig. 8. This reconstruction is formed by employing a depth-dependent aperture that only included one sail-line in the overburden and a smooth transition to the use of three sail lines within the carbonate target zone. The overall image quality is seen to be highly satisfactory. The overburden is well imaged with its highly-resolved fault systems. The high-velocity target zone starting at Top Permian reconstructs equally well both the top structures and the faulted reflector band below.

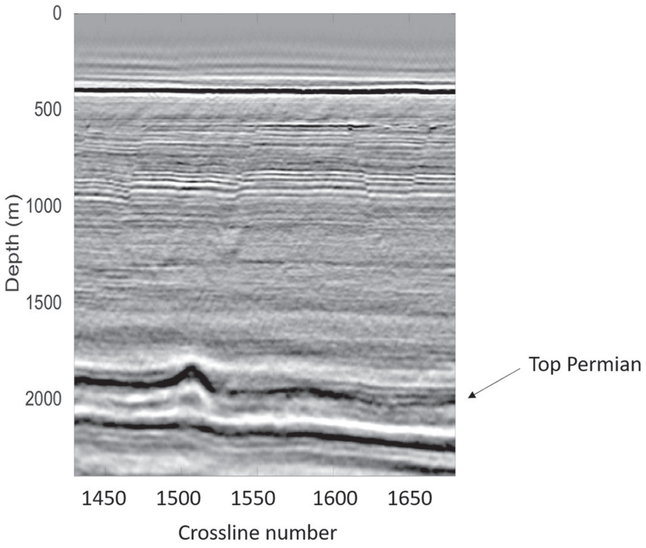

Fig. 9. Same inline section as in Fig. 8, but as provided by the contracting company using 3D VTI common-angle migration.

Because these Permian carbonate rocks represent a major jump in the velocities, only a smaller band of offsets were employed within this zone in order to avoid critically refracted events harming the overall image quality.

To further demonstrate the good performance of our proposed method, the corresponding image result obtained by the previously mentioned contracting company is shown in Fig. 9. The contracting company made use of a sophisticated common-angle migration approach implemented in the offset-midpoint domain. Direct comparison between Figs. 8 and 9 support our claim regarding the excellent image quality provided by the FMD technique. It represents a better-resolved and less noisy migration except for the left-most part of the image at a depth of approximately 2 km where some dipping noise appears, which is due to the use of a smaller lateral aperture than the contractor.

4.1. Computational issues

In this work, we have followed common practice and developed a research prototype of our method employing Matlab. To develop a commercial C++ code has been outside the scope of this paper. However, by the use of figures reported from the literature describing typical speed improvements when converting a Matlab code to an optimized C++ version, we can make estimates regarding how well the FMD technique will perform after such a conversion.

The Matlab code ran on a supercomputer consisting of 650+ Supermicro X9DRT computing nodes. All nodes are dual Intel E5–2670 (Sandy Bridge) running at 2.6 GHz, yielding 16 physical cores. Each node has 64 GB of DDR3 memory operating at 1600 MHz, giving 4 GB memory per physical core at approximately 58 GB/s aggregated bandwidth using all physical cores. Because this super computer is a shared resource for several universities, we only had access to a limited part of its computing capacity (typically not >40–60 nodes). The computational time for 100 3D shots, taken from the field data set, distributed on 20 nodes (16 cores each) was typically about 20 h, a result which implies that on average, five 3D shots per node consumed the same amount of time.

If a program written in a high-level language such as Matlab is converted to an optimized C^{++} code, we can expect a typical improvement in computational speed in the range of 10–100 based on the experiences reported by professional program developers. Andrews (2012) even reports an improvement in speed of several hundreds. If we employ the conservative factor of 20, it implies that we can compute five 3D shots per node using about 60 min (or approximately 12 min per 3D shot per node). From a major contracting company, we have been informed that for 3D depth migration based on 1-way formulation, the computational cost for an optimized code with the same source-receiver layout will be typically around eight minutes per 3D shot per node. However, to obtain such a computational speed, the company also *made use of a GPU environment*. Thus, based on this industry example as well as our conservative analysis of possible gain in computational speed within a CPU environment, it is highly likely that a significantly efficient and competitive implementation can be achieved for the FMD method on a C^{++}/GPU platform.

5. Conclusion

In this paper, a new migration technique for 2D and 3D prestack data also valid for vertical transverse isotropic media has been presented. It can be regarded as a higher-order version of the Split-Step Fourier (SSF) method and is denoted Fourier Mixed-Domain (FMD) migration. By applying an optimized dip filter, the FMD is shown to be stable for strong variations in anisotropy and velocity parameters despite being an explicit type of scheme.

In contrast to Fourier Finite Difference migration, the high-order correction terms are implemented as screen-propagator terms, avoiding the issues of anisotropic noise in 3D finite-difference implementations.

The FMD technique was tested using the 3D SEG/EAGE salt model and the 2D anisotropic Hess model with good results. Finally, FMD was applied with success to a 3D field data set from the Barents Sea including anisotropy where the high-velocity target zone representing Permian carbonate rocks was well imaged. Direct comparison with the result obtained by a contracting company using a sophisticated common-angle migration technique, further demonstrated the superior image resolution provided by FMD imaging.

The current version of the FMD method can handle 3D VTI media. Further extension to the more general TTI case is ongoing research. In addition to the set of perturbed medium parameters inherent in the present formulation, also the tilt of the symmetry axis needs to be included in a computer efficient manner.

Future potential use of the FMD technique, besides being an efficient prestack depth migration (PSDM) method, could also be in iterative PSDM velocity building as an alternative to the industry-preferred Kirchhoff method.

Acknowledgements

H. Z. and L.-J. G. acknowledge support from the Norwegian Research Council through a PETROMAKS 2 project (NFR/234019).

M. T. acknowledges support from the National Council for Scientific and Technological Development (CNPq-Brazil), the National Institute of Science and Technology of Petroleum Geophysics (INCT-GP-Brazil) and the Center for Computational Engineering and Sciences (Fapesp/Cepid # 2013/08293-7-Brazil). He also acknowledges support of the sponsors of the Wave Inversion Technology (WIT) Consortium and the Brazilian Oil Company (Petrobras).

Finally, the authors thank Lundin Norway AS for making the 3D field data set available for this study. The authors also thank SEG and Hess Corporation for providing the SEG and Hess synthetic data.

References

Alkhalifah, T., 1998. Acoustic approximations for processing in transversely isotropic media. Geophysics 63, 623–631.

Aminzadeh, F., Burkhard, N., Long, J., Kunz, T., Duclos, P., 1996. Three dimensional SEG/EAEG models—an update. Lead. Edge 15 (2), 131–134.

Andrews, T., 2012. Computation Time Comparison Between Matlab and C++ Using Launch Windows. American Institute of Aeronautics and Astronautics (6 pages).

Biondi, B., 2002. Stable-wide angle Fourier finite difference downward extrapolation of 3D wavefields. Geophysics 67 (3), 872–882.

Chen, S.C., Ma, Z.T., 2006. High order generalized screen propagator for wave equation prestack depth migration. Chin. J. Geophys. 49 (5), 1290–1297.

Claerbout, J.F., 1971. Toward a unified theory of reflector mapping. Geophysics 36 (3), 467–481.

Claerbout, J., 1985. Imaging the Earth's Interior. Blackwell Scientific Publications, Inc.

Collino, F., Joly, P., 1995. Splitting of operators, alternate directions and paraxial approximations for the three-dimensional wave equation. SIAM J. Sci. Comput. 16, 1019–1048.

Gazdag, J., 1978. Wave equation migration with the phase-shift method. Geophysics 43 (7), 1342–1351.

Gazdag, J., Sguazzero, P., 1984. Migration of seismic data by phase shift plus interpolation. Geophysics 49 (2), 124–131.

Gray, S.H., Etgen, J., Dellinger, J., Whitmore, D., 2001. Y2K Review Article: Seismic migration problems and solutions. Geophysics 66, 1622–1640.

Hale, D., 1991. 3-D depth migration via McClellan transforms. Geophysics 56, 1778–1785.

Han, B., Gu, H., Liu, S., Yan, Z., Tang, Y., Liu, C., 2018. Wavelength-dependent Fresnel beam propagator and migration in VTI media. J. Appl. Geophys. 155, 176–186.

Hua, B.L., Calandra, H., Williamson, P., 2006. 3D common azimuth Fourier finite-difference depth migration in transversely isotropic media. 76th Annual International Meeting, SEG, Expanded Abstracts, pp. 2387–2391.

Huang, L.-J., Fehler, M.C., Wu, R.-S., 1999. Extended local born Fourier migration method. Geophysics 64 (5), 1524–1534.

Jang, S., Kim, T., 2016. Prestack depth migration by a parallel 3D PSPI. Int. J. Geosci. 7, 904–914.

Jin, S., Wu, R.S., 1999. Common-offsetpseudo-screen depth migration. 69th Annual International Meeting, SEG, Expanded Abstracts, pp. 1516–1519.

Le Rousseau, J.H., de Hoop, M.V., 2001a. Modeling and imaging with the scalar generalized-screen algorithms in isotropic media. Geophysics 66, 1551–1568.

Le Rousseau, J.H., de Hoop, M.V., 2001b. Scalar generalized-screen algorithms in transversely isotropic media with a vertical symmetry axis. Geophysics 66, 1538–1550.

Li, J., Fehler, M., Yang, D., Huang, X., 2015. 3D weak-dispersion reverse time migration using a stereo-modeling operator. Geophysics 80, S19–S30.

Liu, B., Sacchi, M.D., 2004. Minimum weighted norm interpolation of seismic records. Geophysics 69, 1560–1568.

Margrave, G.F., 1998. Theory of nonstationary linear filtering in the Fourier domain with application to time-variant filtering. Geophysics 63 (1), 244–259.

Margrave, G.F., Ferguson, R.J., 1999. Wavefield extrapolation by nonstationary phase shift. Geophysics 64 (4), 1067–1078.

Popovici, A.M., 1996. Prestack migration by split-step DSR. Geophysics 61, 1412–1416.

Ristow, D., Rühl, T., 1994. Fourier Finite difference migration. Geophysics 59 (12), 1882–1893.

Shan, G., 2009. Optimized implicit finite-difference and Fourier finite-difference migration for VTI media. Geophysics 74, WCA189–WCA197.

Shin, S., Byun, J., 2013. Development of a prestack generalized-screen migration module for vertical transversely isotropic media. Jigu-Mulli-wa-Mulli-Tamsa 16, 71–78.

Stoffa, P.L., Fokkerna, J.T., Luna Freire, R.M., Kessinger, W.P., 1990. Split-step Fourier migration. Geophysics 55 (4), 410–421.

Stolt, R.H., 1978. Migration by Fourier transform. Geophysics 43 (1), 23–48.

Xu, S., Zhang, Y., Pham, D., Lambare, G., 2005. Antileakage Fourier transform for seismic data regularization. Geophysics 70, V87–V95.

Zhang, J.-H., Yao, Z.-X., 2012. Globally optimized finite-difference extrapolator for strongly VTI media. Geophysics 77, T125–T135.

Zhang, Y., Notfors, C., Xie, Y., 2003. Stable xk wavefield extrapolation in a v(x,y,z) medium. SEG 74th Annual Meeting (Expanded Abstracts).

Paper III

Time-migration velocity estimation using Fréchet derivatives based on nonlinear kinematic migration/demigration solvers

Hao Zhao, Anders Ueland Waldeland, Dany Rueda Serrano, Martin Tygel, Einar Iversen

Accepted with minor revision, *Studia Geophysica et Geodaetica*, November 2019,

Time-migration velocity estimation using Fréchet derivatives based on nonlinear kinematic migration/demigration solvers

Hao Zhao[1]

Anders Ueland Waldeland[2]

Dany Rueda Serrano[3]

Martin Tygel[3]

Einar Iversen[4]

[1] *University of Oslo, Department of Geosciences, P.O. Box 1047 Blindern, N-0316 Oslo, Norway,*
e-mail: zhaohao7109@gmail.com

[2] *University of Oslo, Department of Informatics, P.O. Box 1080 Blindern, N-0316 Oslo, Norway*

[3] *Center for Petroleum Studies, Rua Cora Coralina 350, Cidade Universitária, Campinas - SP,*
13083-896, Brazil

[4] *University of Bergen, Department of Earth Science, P.O. Box 7803, N-5020 Bergen, Norway*

9 September 2019

SUMMARY

Advanced seismic imaging and inversion are dependent on a velocity model that is sufficiently accurate to render reliable and meaningful results. For that reason, methods for extracting such velocity models from seismic data are always in high demand and are topics of active investigation. Velocity models can be obtained from both the time and depth domains. Relying on the former, time migration is an inexpensive, quick and robust process. In spite of its limitations, especially in the case of complex geologies, time migration can, in many instances (e.g. simple to moderate geological structures), produce image results compatible to the those required for the project at hand. An accurate time-velocity model can be of great use in the construction of an initial depth-velocity, from which a high-quality depth image can be produced. Based on available explicit and analytical expressions that relate the kinematic attributes (namely, traveltimes and local slopes) of local events in the recording (demigration) and migrated domains, we revisit tomographic methodologies for velocity-model building, with a specific focus on the time domain, and on those that makes use of local slopes, as well as traveltimes, as key attributes for imaging. We also adopt the strategy of estimating local inclinations in the time-migrated domain (where we have less noise and better focus) and use demigration to estimate those inclinations in the recording domain. On the theoretical side, the main contributions of this work are twofold: 1) we base the velocity model estimation on kinematic migration/demigration techniques that are nonlinear (and therefore more accurate than simplistic linear approaches) and 2) the corresponding Fréchet derivatives take into account that the velocity model is laterally heterogeneous. In addition to providing the comprehensive mathematical algorithms involved, three proof-of-concept numerical examples are demonstrated, which confirm the potential of our methodology.

INTRODUCTION

In seismic data, wave responses to subsurface structures (e.g. layer interfaces or geological bodies) manifest themselves in the form of signal alignments, referred to as seismic events. In the simplest case of a 2D section, such as shot or common-midpoint (CMP) gathers, data points along an event occupy a traveltime strip around a curve within that section. In the case of 2D acquisition, with the arbitrary location of sources and receivers, an event aligns on a strip around a surface in a 3D data volume. For 3D data acquisition, the alignment occurs in the neighbourhood of a hypersurface within a 5D data volume. Seismic events in the data set represent the time link for accessing information on depth geological structures. For complex geologies and noisy environments, however such events, are generally obscured or hidden within the data, requiring proper processing schemes for their identification and use.

As recognised in the literature, it is advantageous to describe an event alignment by means of slopes and curvatures that pertain to their individual points. Referred to as local kinematic parameters of an event point, such quantities are able to provide parametric traveltime approximations of the seismic event in the vicinity of that original event point (see, e.g., Ursin 1982; Hubral 1999; Landa et al. 1999; Perroud et al. 1999; Jäger et al. 2001; Bergler et al. 2002; Hertweck et al. 2007; Landa 2007; Tygel & Santos 2007; Berkovitch et al. 2008; Landa et al. 2010; Fomel & Kazinnik 2012; Gelius & Tygel 2015; Bloot et al. 2018). In this way, the search for seismic events is reduced to the search for event points and their corresponding local kinematic parameters. Each of the traveltimes is associated with specific events (e.g. primary reflections or diffractions) for which, conceptually, best approximations are expected. As also documented in the literature, the formulation outlined above allows for the use of coherence (e.g. semblance) analysis (see, e.g., Neidell & Taner 1971) for the detection of the desired information (see, e.g., Bonomi et al. 2009; Minato et al. 2012; Barros et al. 2015; Walda & Gajewski 2017; Garabito et al. 2017; Waldeland et al. 2019). Local kinematic parameters have shown to be rather instrumental in a number of applications of seismic processing, imaging and inversion. These include a) poststack/prestack data enhancement (Baykulov & Gajewski 2009; Faccipieri et al. 2016); b) diffraction separation and imaging (Rad et al. 2018; Bauer et al. 2009; Berkovitch et al. 2009; Faccipieri et al. 2013; Klokov & Fomel 2012); c) time migration/demigration (Spinner & Mann 2006; Bóna 2011; Dell & Gajewski 2011; Iversen et al. 2012; Coimbra et al. 2013; Dell et al. 2014; Coimbra et al. 2016a); d) data interpolation and regularisation (Hoecht et al. 2009; Coimbra et al. 2016b); e) attribute-oriented seismic processing (Fomel 2002; Zhang et al. 2002; Fomel 2007a,b; Cooke et al. 2009; Khoshnavaz et al. 2016a,b; Stovas & Fomel 2015; Khoshnavaz 2017; Vanelle et al. 2018).

In addition to the applications mentioned above, local kinematic parameters have made a substantial impact on ray-based reflection tomography through the introduction of new algorithms that are able to use slope parameters in addition to the traveltimes normally used in conventional schemes. In the classic literature, such an approach is referred to as *slope tomography.* (Rieber 1936; Riabinkin 1957; Sword 1986). A powerful extension of slope tomography was proposed by Billette & Lambaré (1998) under the name of *stereotomography.* Such an extension takes full advantage of the more recently available theoretical and practical (computational) advances in inverse-problem solving. To overcome the difficulties of traveltimes and slope picking of local coherent events in the recording time domain, Guillaume et al. (2001) and Chauris et al. (2002a,b) proposed that the picking should first be done in the prestack depth migration (PSDM), and then demigrated back to the recorded domain. Such an approach demonstrates the interest in using kinematic migration and its counterpart kinematic demigration for velocity-model building. In fact, kinematic migration and kinematic demigration also have a history in the seismic literature, having been used to map the local kinematic parameters (traveltimes, slopes and curvatures) from/to the recording time domain to/from the migrated time or depth domain (Shah 1973; Kleyn 1977; Hubral & Krey 1980; Gjøystdal & Ursin 1981; Ursin 1982; Iversen & Gjøystdal 1996; Iversen 2004; Douma & de Hoop 2006; Stolk et al. 2009).

Concerning kinematic demigration, Whitcombe et al. (1994) introduced a zero-offset kinematic time demigration scheme using the constant migration velocity assumption. Söllner et al. (2004); Söllner & Andersen (2005) further investigated zero-offset kinematic migration and demigration under the framework of ray theory. A more systematic generalisation and extension of kinematic time migration and demigration was developed by Iversen et al. (2012). Their proposed technique extends the kinematic time migration and demigration from a zero-offset to a finite-offset, including both first-order (slope) and second-order (curvature) travel time derivatives during the mapping, and taking into account the diffraction time functions of the second order in the common-image gather location, the source-receiver offset and the migration aperture. To use kinematic migration and demigration in velocity estimation, another type of tomography technique, nonlinear tomography, has been proposed by different authors. Adler et al. (2008) proposed a technique of nonlinear 3D tomographic inversion to replace the conventional linear process of PSDM using residual moveout analysis (RMO).

Guillaume et al. (2008) addressed the flexibility of using the kinematic invariants (traveltimes and slopes in the unmigrated recording domain) for nonlinear depth tomography. Lambaré et al. (2009) extended this nonlinear inversion concept to time imaging. These proposed nonlinear tomographic approaches greatly reduce the turnaround times and cost of the PSDM and velocity estimation by replacing the conventional PSDM-plus-velocity-RMO analysis with the kinematic demigration and migration internal velocity updating scheme. Due to its mentioned efficiency and effectiveness, the non-linear tomography technique attracted much more attention and development through industrial application and academic research in recent years (Guillaume et al. 2013; Messud et al. 2015).

In this paper, we revisit the kinematic time migration and demigration scheme (Iversen et al. 2012), developing a detailed numerical scheme for time-migration velocity estimation. As the authors are aware, a general description of time-migration velocity estimation using nonlinear mapping processes, based on kinematic time migration and demigration, has been missing from the geophysical theory. Considering the importance of the generalisation of time-migration velocity estimation using Fréchet derivatives based on nonlinear kinematic migration and demigration solvers, this paper provides the missing element for event-oriented seismic velocity estimation. In the following, we first describe the diffraction time function for time migration, the time-migration velocity model. Thereafter, we review the algorithms for kinematic time migration and demigration, and derive the Fréchet derivatives using sensitivity analysis of the kinematic time migration with respect to the time-migration velocity model. Finally, we formulate the linear system for time-migration velocity estimation. Based on the derived mathematical algorithms, we provide three proof-of-concept examples. First, we verify the derived formulation for kinematic time migration and the calculation of the Fréchet derivatives based on a constant time-migration velocity model. Next, we present an example of a time-migration velocity estimation based on a 2D synthetic dataset. In the last - a 3D real-data example, in which we did not have access to the individual, non-stacked, time-migrated common-offset panels - we use a workaround by identifying the times and slopes on a stacked image in the time-migration domain, and verifing the availability of the 3D time-migration velocity estimation based on the theoretical formulations. The three examples confirm the potential of our methodology.

1 DIFFRACTION TIME FUNCTION FOR TIME MIGRATION

We describe the diffraction time function for time migration and the coordinates and coefficients related to it. The description follows Iversen et al. (2012) but includes an extension from second to fourth order.

1.1 Coordinates

We use a 2D Cartesian coordinate system (ξ_1, ξ_2) for describing the acquisition geometry of 3D seismic experiments. As shown in Figure 1, in the horizontal measurement plane, consider a source point, $\mathbf{s} = (s_1, s_2)$, and a receiver point, $\mathbf{r} = (r_1, r_2)$. The midpoint and half-offset coordinates are given as

$$\mathbf{x} = \frac{1}{2}(\mathbf{r} + \mathbf{s}), \qquad \mathbf{h} = \frac{1}{2}(\mathbf{r} - \mathbf{s}). \tag{1}$$

For the output point of time migration, i.e., the image-gather location, we use the notation $\mathbf{m}$. The aperture vector $\mathbf{a}$ is defined as

$$\mathbf{a} = \mathbf{x} - \mathbf{m}. \tag{2}$$

We will also need the quantities $\mathbf{h}^S$ and $\mathbf{h}^R$,

$$\begin{aligned} \mathbf{h}^S &= \mathbf{s} - \mathbf{m} = \mathbf{a} - \mathbf{h}, \\ \mathbf{h}^R &= \mathbf{r} - \mathbf{m} = \mathbf{a} + \mathbf{h}. \end{aligned} \tag{3}$$

referred to, respectively, as the source-offset vector and the receiver-offset vector.

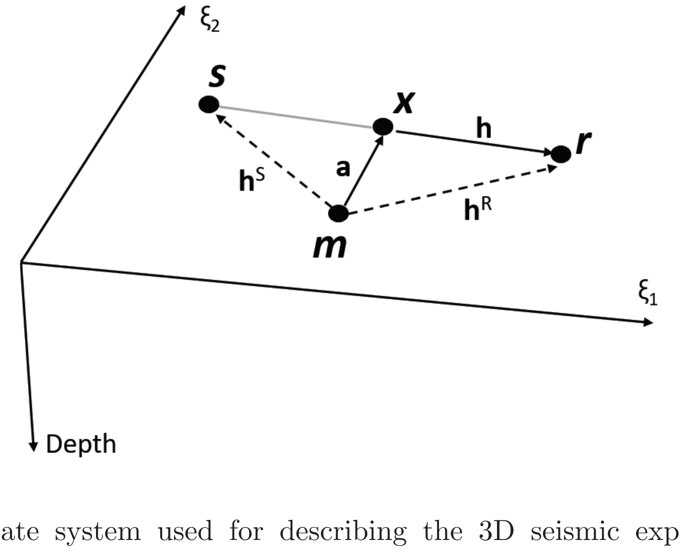

Figure 1: Coordinate system used for describing the 3D seismic experiments. Source($\mathbf{s}$), receiver($\mathbf{r}$), common-mid point($\mathbf{x}$) and common-image point($\mathbf{m}$) are defined in the horizontal measurement plane. The vectors of aperture($\mathbf{a}$), half-offset($\mathbf{h}$), source-offset($\mathbf{h}^S$) and receiver-offset ($\mathbf{h}^R$) are outlined.

1.2 Diffraction time

Assuming single scattering and traveltime fields without caustics, the diffraction time function for time migration, T^D, can be introduced as the traveltime from the source point to the scattering point, T^S, plus the traveltime from the scattering point to the receiver, T^R,

$$t = T^D(\mathbf{h}, \mathbf{a}, \mathbf{m}, \tau) \quad = \quad T^S(\mathbf{h}^S, \mathbf{m}, \tau) + T^R(\mathbf{h}^R, \mathbf{m}, \tau). \tag{4}$$

In equation (3) the source- and receiver-offset vectors are expressed in terms of **a** and **h**. We note that $t = T^D$ is the (two-way) diffraction time from source to receiver, while τ is the migration time, i.e., the time coordinate of the domain of the time-migrated data. The diffraction time function T^D is required stationary for $\mathbf{h} = \mathbf{a} = \mathbf{0}$.

Let the source and receiver traveltime fields correspond to the same wave type, e.g., a direct P wave. We establish a Taylor expansion for the squared one-way time ${T^S}^2$,

$$\begin{aligned} {T^S}^2 \quad &= \quad \left(\frac{\tau}{2}\right)^2 \; + \; \frac{1}{2} \frac{\partial^2 (T^S)^2}{\partial h_I^S \, \partial h_J^S} \, h_I^S \, h_J^S \\ &\quad + \; \frac{1}{6} \frac{\partial^3 (T^S)^2}{\partial h_I^S \, \partial h_J^S \, \partial h_K^S} \, h_I^S \, h_J^S \, h_K^S \; + \; \frac{1}{24} \frac{\partial^4 (T^S)^2}{\partial h_I^S \, \partial h_J^S \, \partial h_K^S \, \partial h_L^S} \, h_I^S \, h_J^S \, h_K^S \, h_L^S \; + \; \ldots, \end{aligned} \tag{5}$$

and an analogous expansion for ${T^R}^2$. The first order derivatives of ${T^S}^2$ and ${T^R}^2$ are zero, as the diffraction time function is stationary for $\mathbf{h} = \mathbf{a} = \mathbf{0}$. Since the source and receiver traveltime fields have the same wave type, the Taylor coefficents in the expansions of ${T^S}^2$ and ${T^R}^2$ must be equal. Hence, we can write

$$\begin{aligned} {T^S}^2 \quad &= \quad \left(\frac{\tau}{2}\right)^2 \; + \; S_{IJ}^{M(2)} \, h_I^S \, h_J^S \; + \; S_{IJK}^{M(3)} \, h_I^S \, h_J^S \, h_K^S \; + \; S_{IJKL}^{M(4)} \, h_I^S \, h_J^S \, h_K^S \, h_L^S \; + \; \ldots, \\ {T^R}^2 \quad &= \quad \left(\frac{\tau}{2}\right)^2 \; + \; S_{IJ}^{M(2)} \, h_I^R \, h_J^R \; + \; S_{IJK}^{M(3)} \, h_I^R \, h_J^R \, h_K^R \; + \; S_{IJKL}^{M(4)} \, h_I^R \, h_J^R \, h_K^R \, h_L^R \; + \; \ldots. \end{aligned} \tag{6}$$

If the lateral variations within the medium are small, and anisotropy effects are laterally symmetric, the odd terms in equation (6) can be neglected. Applying this assumption and truncating the series after the fourth order terms, our diffraction time function is given by equation (4) with arguments (3) and source/receiver time fields

$$\begin{aligned} T^S \quad &= \quad \left[\left(\frac{\tau}{2}\right)^2 \; + \; S_{IJ}^{M(2)} \, h_I^S \, h_J^S \; + \; S_{IJKL}^{M(4)} \, h_I^S \, h_J^S \, h_K^S \, h_L^S\right]^{1/2}, \\ T^R \quad &= \quad \left[\left(\frac{\tau}{2}\right)^2 \; + \; S_{IJ}^{M(2)} \, h_I^R \, h_J^R \; + \; S_{IJKL}^{M(4)} \, h_I^R \, h_J^R \, h_K^R \, h_L^R\right]^{1/2}. \end{aligned} \tag{7}$$

For the subtle details on the partial derivatives of the diffraction-time function, see Appendix A.

1.3 Diffraction time coefficients

The coefficients in equation (7) may be expressed, for example, as

$$S_{IJ}^{M(2)} = 2\tau \frac{\partial^2 T^S}{\partial a_I \partial a_J}, \tag{8}$$

$$\begin{aligned} S_{IJKL}^{M(4)} = \tfrac{1}{12} & \left[2\tau \frac{\partial^4 T^S}{\partial a_I \partial a_J \partial a_K \partial a_L} \right. \\ & \left. + \frac{\partial^2 T^S}{\partial a_I \partial a_J} \frac{\partial^2 T^S}{\partial a_K \partial a_L} + \frac{\partial^2 T^S}{\partial a_I \partial a_K} \frac{\partial^2 T^S}{\partial a_J \partial a_L} + \frac{\partial^2 T^S}{\partial a_I \partial a_L} \frac{\partial^2 T^S}{\partial a_J \partial a_K} \right], \end{aligned} \tag{9}$$

where all derivatives are taken for $\mathbf{a} = \mathbf{h} = \mathbf{0}$. Observe, however, that the coefficients $S_{IJ}^{M(2)}$ and $S_{IJKL}^{M(4)}$ are functions of $\mathbf{m}$ and τ. We can relate these coefficients to derivatives of the diffraction time function and its square, as follows,

$$\frac{\partial^2 T^D}{\partial a_I \partial a_J} = \frac{4}{\tau} S_{IJ}^{M(2)}, \tag{10}$$

$$\frac{\partial^4 T^D}{\partial a_I \partial a_J \partial a_K \partial a_L} = \frac{16}{\tau} \left[3 S_{IJKL}^{M(4)} - \frac{1}{\tau^2} \left(S_{IJ}^{M(2)} S_{KL}^{M(2)} + S_{IK}^{M(2)} S_{JL}^{M(2)} + S_{IL}^{M(2)} S_{JK}^{M(2)} \right) \right], \tag{11}$$

$$\frac{\partial^2 (T^D)^2}{\partial a_I \partial a_J} = 8\, S_{IJ}^{M(2)}, \tag{12}$$

$$\frac{\partial^4 (T^D)^2}{\partial a_I \partial a_J \partial a_K \partial a_L} = 96\, S_{IJKL}^{M(4)}. \tag{13}$$

1.4 A simplified setup of diffraction time coefficients

Equation (7) is formulated to allow for a full coverage of directions and magnitudes of the source- and receiver-offset vectors. For situations with limited coverage it is however useful to have a simplified setup for the diffraction time coefficients.

One approach often used is to assume that the diffraction time moveout is rotationally symmetric. We then write

$$S_{IJ}^{M(2)} = S^{M(2)} \delta_{IJ}, \qquad S_{IJKL}^{M(4)} = S^{M(4)} \delta_{IJ} \delta_{KL}, \tag{14}$$

where $S^{M(2)}$ and $S^{M(4)}$ are scalar functions of the coordinates $(\mathbf{m}, \tau)$. Using the relations (14) in equation (7) yields

$$\begin{aligned} T^S &= \left[\left(\frac{\tau}{2}\right)^2 + S^{M(2)} (h^S)^2 + S^{M(4)} (h^S)^4 \right]^{1/2}, \\ T^R &= \left[\left(\frac{\tau}{2}\right)^2 + S^{M(2)} (h^R)^2 + S^{M(4)} (h^R)^4 \right]^{1/2}. \end{aligned} \tag{15}$$

Here, the quantities h^S and h^R denote the magnitudes of the respective source- and receiver offset vectors, $\mathbf{h}^S$ and $\mathbf{h}^R$.

1.5 Time-migration velocity model

The time-migration velocity model is defined on a three-dimensional rectangular grid in the variables $\xi_1 = m_1$, $\xi_2 = m_2$, $\xi_3 = \tau$, where we add ξ_3 to describe the velocity model in time domain. Model parameters related to cells or vertices within the grid will be unknowns in a velocity estimation process.

Our velocity model is described in terms of a multi-component vector function, (M_λ), $\lambda = 1, \ldots, N^\lambda$, where each component function $M_\lambda(\xi_1, \xi_2, \xi_3)$ corresponds to one of the coefficients of the diffraction time function. For different contexts for these coefficients, see equations (6), (7), and (15). The vector function (M_λ) is introduced to yield a compact equivalent of the diffraction time coefficients under consideration. For example, for the simplified situation (15) we take

$$M_1 = S^{M(2)}, \qquad M_2 = S^{M(4)}. \tag{16}$$

To allow the differentiability up to the second order, we use a local cubic spline function (see Appendix C) to describe the velocity model. Bicubic and tricubic spline functions are used for 2D and 3D grids respectively. In Appendix E, we give a detailed description of the parameterization of the time-migration velocity model.

2 KINEMATIC TIME MIGRATION AND DEMIGRATION

Kinematic time migration maps the local kinematic parameters (traveltimes, slopes and curvatures) from the recording time domain of seismic data to the time-migration domain. The inverse process, kinematic time demigration, maps the local kinematic parameters in time-migration domain back to the recording time domain. As illustrated in Figure 2, by using the diffraction function with its associated partial derivatives, and a known time-migration velocity model, kinematic time migration and demigration are able to map the local kinematic parameters between the recording time domain and the migration time domain. In this paper, we focus on the utilization of the kinematic parameters up to the first order for time-migration velocity estimation. For mapping of second order kinematic parameters, see Iversen et al. (2012).

The local kinematic parameters can be extracted from both the recording domain and the migration domain. Since the time-migrated dataset in general contains less noise and is more easily interpreted, the kinematic parameters extraction is commonly often applied in the migration domain, and subsequently demigrated to the recording domain. The time-migrated dataset is normally generated by pre-stack time migration of the recorded seismic data with an initial time-migration velocity model. The migrated dataset is not necessarily to be optimal but is assumed to have a good resolution for the local kinematic parameters picking. Once the picking process applied in the migration domain, the local kinematic parameters are able to be mapped to the recording domain by kinematic demigration with the same initial velocity model. This process needs the computation of the first and second order partial derivatives of the known diffraction-time function (i.e. equations (4), (7), and (15)), which are then used in the kinematic demigration and migration for velocity estimation. We give the formulation of kinematic time demigration and migration in the following context.

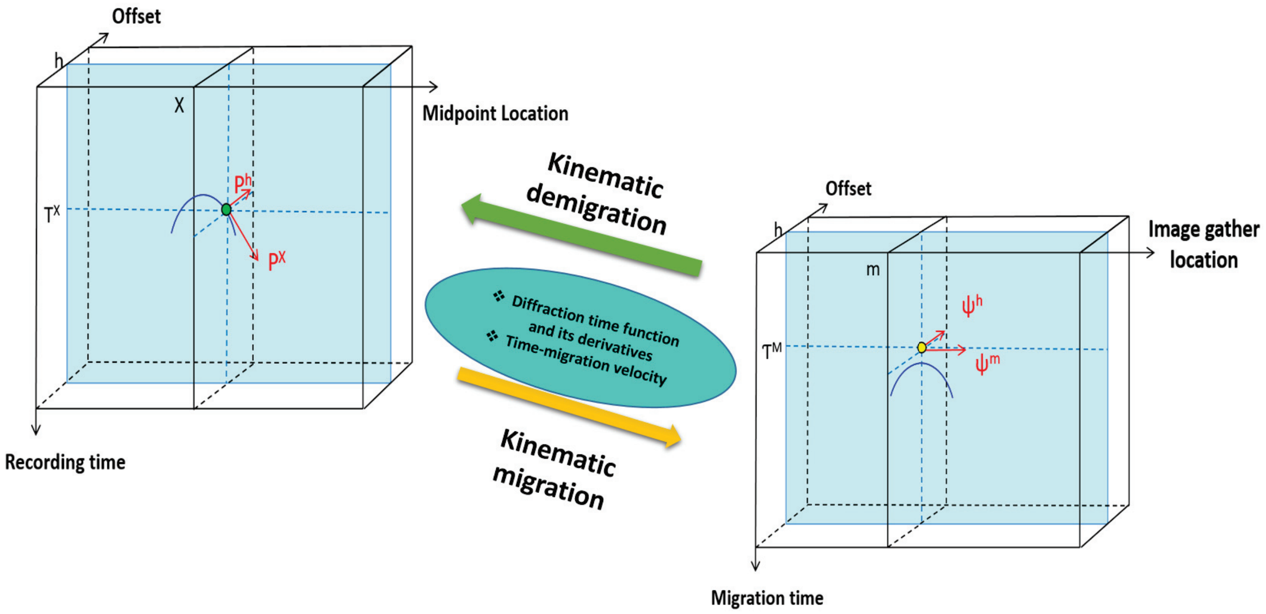

Figure 2: Schematic overview of kinematic time migration and demigration for 2D pre-stack seismic data set. Based on the known diffraction time function with its associated derivatives, and a time-migration velocity model, the local kinematic parameters (x, T^x, p^x, p^h) in recording domain can be forward/backward mapped to/from the counterpart $(m, \mathcal{T}^M, \psi^m, \psi^h)$ in migration domain by kinematic time migration/kinematic time demigration.

2.1 Algorithm for kinematic time demigration

Consider equation (43) in Iversen et al. (2012), referred to as the *consistency equation*,

$$\frac{\partial T^D}{\partial a_I} - \frac{\partial T^D}{\partial m_I} \;=\; \frac{\partial T^D}{\partial \tau}\frac{\partial \mathcal{T}}{\partial m_I}, \tag{17}$$

with $I = 1, 2$. We can use equation (17) to obtain the aperture vector corresponding to a kinematic time demigration,

$$\hat{a}_I \;=\; \hat{x}_I - m_I. \tag{18}$$

Under special conditions the vector $\hat{\mathbf{a}} = (\hat{a}_I)$ can be obtained analytically, see equation 78 in Iversen et al. (2012).

Based on equation (17) we introduce a vector function $(f_I(\mathbf{a}))$ so that

$$f_I(\mathbf{a}) \;=\; \frac{\partial T^D}{\partial a_I} - \frac{\partial T^D}{\partial m_I} - \frac{\partial T^D}{\partial \tau}\frac{\partial \mathcal{T}}{\partial m_I}, \tag{19}$$

where $\mathbf{a} = \hat{\mathbf{a}}$ is the sought unknown aperture vector. As a consequence, the system of equations to be solved has the general form

$$f_I(\mathbf{a}) \;=\; 0. \tag{20}$$

One possible approach to obtain a solution is to use the Newton-Raphson iteration method. Let us assume that the component values of the function f_I is known for some starting component values $\mathbf{a} = \mathbf{a}^{(0)}$. For these starting values we compute the first-order partial derivatives of f_I,

$$\frac{\partial f_I}{\partial a_J}(\mathbf{a}^{(0)}) \;=\; \frac{\partial^2 T^D}{\partial a_I \partial a_J} - \frac{\partial^2 T^D}{\partial m_I \partial a_J} - \frac{\partial^2 T^D}{\partial \tau \partial a_J}\frac{\partial \mathcal{T}}{\partial m_I}, \tag{21}$$

with all the partial derivatives on the right-hand side evaluated for $\mathbf{a} = \mathbf{a}^{(0)}$. To first order we can then write

$$0 - f_I(\mathbf{a}^{(0)}) \;=\; \frac{\partial f_I}{\partial a_J}(\mathbf{a}^{(0)})\left(a_J^{(1)} - a_J^{(0)}\right). \tag{22}$$

Defining

$$W_{IJ}(\mathbf{a}^{(0)}) = \frac{\partial f_I}{\partial a_J}(\mathbf{a}^{(0)}), \qquad \bar{W}_{MN}(\mathbf{a}^{(0)}) = \left\{\left\{\frac{\partial f_I}{\partial a_J}(\mathbf{a}^{(0)})\right\}^{-1}\right\}_{MN}, \tag{23}$$

equation (22) yields

$$a_J^{(1)} \;=\; a_J^{(0)} - \bar{W}_{JL}(\mathbf{a}^{(0)})\, f_L(\mathbf{a}^{(0)}), \tag{24}$$

Equation (24) provides a first-order update of the aperture vector. We can now compute the components $f_I(\mathbf{a}^{(1)})$ and check if these are sufficiently close to zero. Should that be the case, the Newton-Raphson process is completed and has returned the solution $\hat{\mathbf{a}} = \mathbf{a}^{(1)}$. Otherwise, the process goes on to the next iteration. The process is stopped when both components f_I

are sufficiently close to zero. It is also stopped if we do not attain convergence to a meaningful solution.

Equations (19) and (21) contain first- and second-order partial derivatives of the diffraction-time function, T^D. For the calculation of such derivatives, see Appendices C and D in Iversen et al. (2012).

Now that we know the kinematic demigration aperture vector, $\hat{\mathbf{a}} = (\hat{a}_I)$, it is easy to find the time T^X and the slopes $p_I^x = \partial T/\partial x_I$ and $p_I^h = \partial T/\partial h_I$ resulting from the kinematic demigration. To compute T^X and p_I^x we simply use the equalities

$$T^X = T^D(\mathbf{h}, \hat{\mathbf{a}}, \mathbf{m}, \mathcal{T}^M), \qquad p_I^x = \frac{\partial T^D}{\partial a_I}(\mathbf{h}, \hat{\mathbf{a}}, \mathbf{m}, \mathcal{T}^M). \tag{25}$$

The slope p_I^h is given by equation (45) in Iversen et al. (2012),

$$p_I^h = \frac{\partial T^D}{\partial h_I}(\mathbf{h}, \hat{\mathbf{a}}, \mathbf{m}, \mathcal{T}^M) + \psi_I^h \frac{\partial T^D}{\partial \tau}(\mathbf{h}, \hat{\mathbf{a}}, \mathbf{m}, \mathcal{T}^M). \tag{26}$$

2.1.1 Half-offset vector with only one degree of freedom

The coverage of azimuthal directions for the half-offset vector $\mathbf{h}$ may be two small to permit extraction of two slope components ψ_I^h to be input to kinematic time demigration. For this situation the (two-component) half-offset vector has effectively only one degree of freedom, so that we can parametrize the components of $\mathbf{h}$ by a single scalar, σ. The quantity σ will then be a distance variable for traces belonging to a common-image gather in the migration-time domain or a common-midpoint gather in the recording-time domain. The parametrization reads

$$h_I(\sigma) \quad = \quad h(\sigma)\, n_I(\sigma), \tag{27}$$

where h is the magnitude of $\mathbf{h}$ and $\mathbf{n} = (n_I)$ is a unit vector. The quantity σ is a distance variable for traces belonging to a common-image gather in the migration-time domain or a common-midpoint gather in the recording-time domain. The first derivative of h_I with respect to σ is

$$\frac{\mathrm{d}h_I}{\mathrm{d}\sigma} \quad = \quad \frac{\mathrm{d}h}{\mathrm{d}\sigma} n_I + h \frac{\mathrm{d}n_I}{\mathrm{d}\sigma}. \tag{28}$$

The slope mapping in equation (26) can now be restated

$$p^\sigma = \frac{\partial T^D}{\partial h_I} \frac{\mathrm{d}h_I}{\mathrm{d}\sigma} + \psi^\sigma \frac{\partial T^D}{\partial \tau}, \tag{29}$$

where we have introduced new, effective, slopes with respect to offset in the recording-time and migration-time domains,

$$p^\sigma = \frac{\partial T}{\partial \sigma}, \qquad \psi^\sigma = \frac{\partial \mathcal{T}}{\partial \sigma}. \tag{30}$$

2.2 Algorithm for kinematic time migration

In the case of kinematic time demigration we first solved a system of two equations in two unknowns, i.e., the components of the aperture vector, followed by a straightforward evaluation of the diffraction-time function to obtain the output time. In the kinematic time *migration* situation there will still be three unknowns of the same type, the aperture vector components plus an output time, but now we will in general need to solve simultaneously a system of three equations in the three unknowns. The equations under consideration are given as (68) and (69) in Iversen et al. (2012); we restate them here as

$$\frac{\partial T}{\partial x_I}(\mathbf{h},\mathbf{x}) = \frac{\partial T^D}{\partial a_I}(\mathbf{h},\hat{\mathbf{a}},\mathbf{x}-\hat{\mathbf{a}},\hat{\tau}), \tag{31}$$

$$T(\mathbf{h},\mathbf{x}) = T^D(\mathbf{h},\hat{\mathbf{a}},\mathbf{x}-\hat{\mathbf{a}},\hat{\tau}). \tag{32}$$

To describe the unknowns it is convenient to introduce a three-component vector (ζ_i) such that $\zeta_I = \hat{a}_I$ and $\zeta_3 = \hat{\tau}$.

We use equations (31)–(32) to formulate a three component vector function $(g_i(\boldsymbol{\zeta}))$, as follows

$$g_I(\boldsymbol{\zeta}) = \frac{\partial T^D}{\partial a_I} - \frac{\partial T}{\partial x_I}, \tag{33}$$

$$g_3(\boldsymbol{\zeta}) = T^D - T, \tag{34}$$

where function arguments on the right-hand side have been skipped. Equations (31)–(32) can then be restated

$$g_i(\boldsymbol{\zeta}) = 0. \tag{35}$$

To solve the system of equations (35) we may proceed in the same way as described for equation (20). That means, to use a Newton-Raphson approach using derivatives $\partial g_i/\partial \zeta_j$. These derivatives are given explicitly as

$$\frac{\partial g_I}{\partial \zeta_J} = \frac{\partial^2 T^D}{\partial a_I \partial a_J} - \frac{\partial^2 T^D}{\partial a_I \partial m_J}, \tag{36}$$

$$\frac{\partial g_I}{\partial \zeta_3} = \frac{\partial^2 T^D}{\partial a_I \partial \tau}, \tag{37}$$

$$\frac{\partial g_3}{\partial \zeta_J} = \frac{\partial T^D}{\partial a_J} - \frac{\partial T^D}{\partial m_J}, \tag{38}$$

$$\frac{\partial g_3}{\partial \zeta_3} = \frac{\partial T^D}{\partial \tau}. \tag{39}$$

To obtain them, we have used that the time T and the slopes $\partial T/\partial x_I$ in equations (33)–(34) are invariant in kinematic time migration.

Knowing the output point $(\mathbf{h}, \hat{\mathbf{m}}, \hat{\tau})$ resulting from a kinematic time migration, it means that any requested partial derivative of the diffraction-time function T^D in the variables h_I, a_I, m_I, and τ_I may be computed. The natural next task is to obtain the slopes ψ_I^m and ψ_I^h at the point $(\mathbf{h}, \hat{\mathbf{m}}, \hat{\tau})$. For that, we reuse here equation (70) in Iversen et al. (2012),

$$\psi_I^h = \left(\frac{\partial T^D}{\partial \tau}\right)^{-1} \left(p_I^h - \frac{\partial T^D}{\partial h_I}\right), \tag{40}$$

$$\psi_I^m = \left(\frac{\partial T^D}{\partial \tau}\right)^{-1} \left(p_I^x - \frac{\partial T^D}{\partial m_I}\right). \tag{41}$$

For a half-offset vector with only one degree of freedom, see equation (27), equation (40) can be restated

$$\psi^\sigma = \left(\frac{\partial T^D}{\partial \tau}\right)^{-1} \left(p^\sigma - \frac{\partial T^D}{\partial h_I}\frac{\mathrm{d}h_I}{\mathrm{d}\sigma}\right). \tag{42}$$

3 SENSITIVITY OF KINEMATIC TIME MIGRATION WITH RESPECT TO THE TIME-MIGRATION VELOCITY MODEL

Considering one selected parameter ν of the time-migration velocity model, we study how the kinematic time migration is affected by a perturbation in ν. We investigate the first-order changes of the reflection location with respect to the time-migration velocity model (i.e. the derivatives $\mathrm{d}\hat{m}_I/\mathrm{d}\nu$ and $\mathrm{d}\hat{\tau}/\mathrm{d}\nu$), as well as the the first-order changes of the reflection slopes with respect to the time-migration velocity model (i.e. the derivatives $\mathrm{d}\psi_I^h/\mathrm{d}\nu$).

In view of the model representation described in Appendix E, we take ν specifically as the node value

$$\nu = {M_\lambda}^{r,s,t}. \tag{43}$$

3.1 First-order changes of the reflection location with respect the time-migration velocity model

The location of a reflection in the migration-time domain can be expressed in terms of the parameter ν as $(\mathbf{h}, \hat{\mathbf{m}}(\mathbf{h}, \nu), \hat{\tau}(\mathbf{h}, \nu))$. As shown in Figure 3, we investigate how this location $(\hat{\mathbf{m}}, \hat{\tau})$ is affected, to first order, by a perturbation in ν.

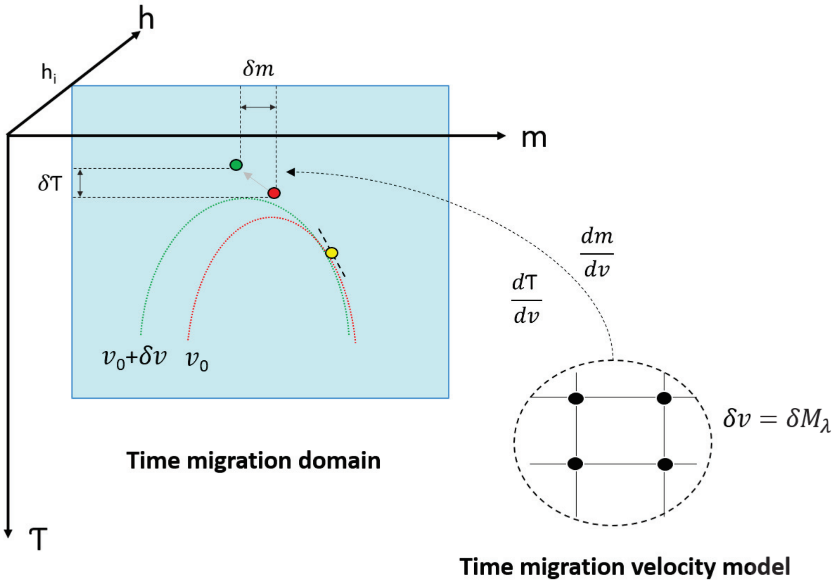

Figure 3: Schematic overview (2D) of the first-order changes of the reflection location with respect to the time-migration velocity model. The symbol h_i signify a specific common-offset section. The figure shows, perturbation of a time-migration velocity model parameter $(\delta\nu)$ leads to the position change $(\delta m, \delta\tau)$ of the kinematic migration result: the kinematic migrated output is shifted from red point to green point. These perturbations are described by the derivatives: $\mathrm{d}m/\mathrm{d}\nu$ and $\mathrm{d}\tau/\mathrm{d}\nu$. In the figure, the yellow point and the dash black line represent the input event point and its local slope. The red point and the red dash line represent the migrated point and its diffraction traveltime curve by using the initial time-migration velocity of ν_0. Correspondingly, the green point and the green dash line represent the migrated point and its diffraction traveltime curve by using the updated time-migration velocity $\nu_0 + \delta\nu$.

Equation (35) yields a mapping from a location in the recording-time domain to a location in the migration-time domain. The relation is valid regardless of which time-migration velocity model we use. As a consequence, we have

$$\frac{\mathrm{d}g_i}{\mathrm{d}\nu} = 0. \tag{44}$$

Also, we note that the time T and the slopes $\partial T/\partial x_I$ in equations (33)–(34) are insensitive to the value of ν. A differentiation of these equations with respect to ν therefore yields

$$\frac{\mathrm{d}}{\mathrm{d}\nu}\left(\frac{\partial T^D}{\partial a_I}\right) = 0, \tag{45}$$

$$\frac{\mathrm{d}T^D}{\mathrm{d}\nu} = 0. \tag{46}$$

Equations (45)–(46) contain information to estimate the derivatives $\mathrm{d}\hat{m}_I/\mathrm{d}\nu$ and $\mathrm{d}\hat{\tau}/\mathrm{d}\nu$. The total derivative operator in these equations can be stated as

$$\frac{\mathrm{d}}{\mathrm{d}\nu} = \frac{\partial}{\partial \nu} + \frac{\mathrm{d}\hat{a}_J}{\mathrm{d}\nu}\frac{\partial}{\partial a_J} + \frac{\mathrm{d}\hat{m}_J}{\mathrm{d}\nu}\frac{\partial}{\partial m_J} + \frac{\mathrm{d}\hat{\tau}}{\mathrm{d}\nu}\frac{\partial}{\partial \tau}.$$

Using that the location (x_I) is insensitive to the value of ν, the operator appears in the form

$$\frac{\mathrm{d}}{\mathrm{d}\nu} = \frac{\partial}{\partial \nu} + \frac{\mathrm{d}\hat{m}_J}{\mathrm{d}\nu}\left(\frac{\partial}{\partial m_J} - \frac{\partial}{\partial a_J}\right) + \frac{\mathrm{d}\hat{\tau}}{\mathrm{d}\nu}\frac{\partial}{\partial \tau}. \tag{47}$$

The specific partial derivatives of the diffraction time with respect to ν are given in Appendix B.

Applying equation (47) in (45)–(46) yields

$$\left[\frac{\mathrm{d}\hat{m}_J}{\mathrm{d}\nu}\left(\frac{\partial}{\partial m_J} - \frac{\partial}{\partial a_J}\right) + \frac{\mathrm{d}\hat{\tau}}{\mathrm{d}\nu}\frac{\partial}{\partial \tau}\right]\left(\frac{\partial T^D}{\partial a_I}\right) = -\frac{\partial^2 T^D}{\partial \nu \partial a_I},$$

$$\left[\frac{\mathrm{d}\hat{m}_J}{\mathrm{d}\nu}\left(\frac{\partial}{\partial m_J} - \frac{\partial}{\partial a_J}\right) + \frac{\mathrm{d}\hat{\tau}}{\mathrm{d}\nu}\frac{\partial}{\partial \tau}\right]\left(T^D\right) = -\frac{\partial T^D}{\partial \nu},$$

and hence,

$$\left(\frac{\partial^2 T^D}{\partial a_I \partial m_J} - \frac{\partial^2 T^D}{\partial a_I \partial a_J}\right)\frac{\mathrm{d}\hat{m}_J}{\mathrm{d}\nu} + \frac{\partial^2 T^D}{\partial a_I \partial \tau}\frac{\mathrm{d}\hat{\tau}}{\mathrm{d}\nu} = -\frac{\partial^2 T^D}{\partial \nu \partial a_I}, \tag{48}$$

$$\left(\frac{\partial T^D}{\partial m_J} - \frac{\partial T^D}{\partial a_J}\right)\frac{\mathrm{d}\hat{m}_J}{\mathrm{d}\nu} + \frac{\partial T^D}{\partial \tau}\frac{\mathrm{d}\hat{\tau}}{\mathrm{d}\nu} = -\frac{\partial T^D}{\partial \nu}. \tag{49}$$

Equations (48)–(49) can be restated as the matrix equation

$$\mathbf{A}\boldsymbol{\eta} = \mathbf{b}, \tag{50}$$

which includes the 3×1 matrix of unknowns

$$\boldsymbol{\eta} = \begin{bmatrix} \left\{\frac{\mathrm{d}\hat{m}_J}{\mathrm{d}\nu}\right\} \\ \frac{\mathrm{d}\hat{\tau}}{\mathrm{d}\nu} \end{bmatrix}, \tag{51}$$

and the 3×3 and 3×1 coefficient matrices

$$\mathbf{A} = \begin{bmatrix} \left\{\frac{\partial^2 T^D}{\partial a_I \partial m_J} - \frac{\partial^2 T^D}{\partial a_I \partial a_J}\right\} & \left\{\frac{\partial^2 T^D}{\partial a_I \partial \tau}\right\} \\ \left\{\frac{\partial T^D}{\partial m_J} - \frac{\partial T^D}{\partial a_J}\right\} & \frac{\partial T^D}{\partial \tau} \end{bmatrix}, \tag{52}$$

$$\mathbf{b} = -\begin{bmatrix} \left\{\frac{\partial^2 T^D}{\partial \nu \partial a_I}\right\} \\ \frac{\partial T^D}{\partial \nu} \end{bmatrix}. \tag{53}$$

Inversion of equation (50),

$$\boldsymbol{\eta} \;=\; \mathbf{A}^{-1}\mathbf{b}, \tag{54}$$

will then yield the sought derivatives $\mathrm{d}\hat{m}_I/\mathrm{d}\nu$ and $\mathrm{d}\hat{\tau}/\mathrm{d}\nu$.

3.2 First-order changes of reflection slopes with respect to the time-migration velocity model

Apart from the investigation of the reflection position changes of a kinematic time migration output, we also need study the variation of reflection slopes with respect to the perturbation of time-migration velocity. As presented in the Figure 4, the derivative $\mathrm{d}\psi_I^h/\mathrm{d}\nu$ describes the sensitivity of the variation of the reflection slopes with respect to the velocity perturbation. In the following, we derive an expressions for the first-order derivatives of reflection slopes in offset, resulting from a kinematic time migration, taken with respect to parameters of the time-migration velocity model.

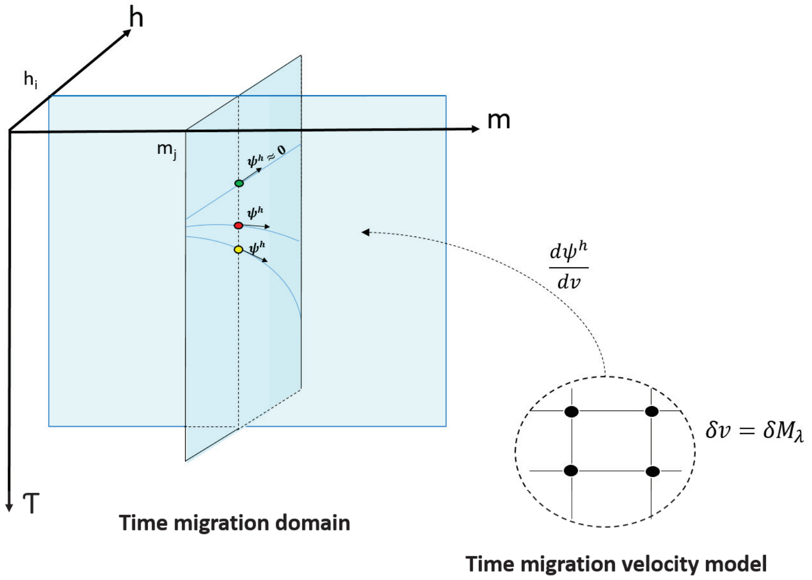

Figure 4: Schematic overview (2D) of the first-order changes of the reflection (offset) slopes with respect to the time-migration velocity model. The symbols h_i and m_j signify, respectively, a common-offset section and a common-image gather. The figure shows, with a fixed input point from the recording domain, the perturbation of time-migration velocity model leads to the changes of the reflection slopes in the kinematic migration domain. The yellow and red points represent the initial migrated point, the further migrated point after the velocity update respectively. The green point resembles the idea time-migration result ($\psi^h = 0$)derived from the optimal migration velocity.

3.2.1 Half-offset vector with two effective degrees of freedom

The most general mapping of reflection slopes ψ_I^h is given by equation (40), for which the half-offset vector has two degrees of freedom. We differentiate this equation with respect to the parameter ν, which yields,

$$\frac{\mathrm{d}}{\mathrm{d}\nu}\left(\frac{\partial T^D}{\partial h_I}+\frac{\partial T^D}{\partial \tau}\psi_I^h\right) = 0. \tag{55}$$

Using the differentiation operator in equation (47), we obtain after some elaboration

$$\begin{aligned}\frac{\mathrm{d}\psi_I^h}{\mathrm{d}\nu} = & -\left(\frac{\partial T^D}{\partial \tau}\right)^{-1}\left\{\frac{\partial^2 T^D}{\partial \nu \partial h_I}+\frac{\partial^2 T^D}{\partial \nu \partial \tau}\psi_I^h\right.\\ & +\frac{\mathrm{d}\hat{m}_J}{\mathrm{d}\nu}\left[\frac{\partial^2 T^D}{\partial m_J \partial h_I}-\frac{\partial^2 T^D}{\partial a_J \partial h_I}+\left(\frac{\partial^2 T^D}{\partial m_J \partial \tau}-\frac{\partial^2 T^D}{\partial a_J \partial \tau}\right)\psi_I^h\right]\\ & \left.+\frac{\mathrm{d}\hat{\tau}}{\mathrm{d}\nu}\left[\frac{\partial^2 T^D}{\partial \tau \partial h_I}+\frac{\partial^2 T^D}{\partial \tau^2}\psi_I^h\right]\right\}.\end{aligned} \tag{56}$$

3.2.2 Half-offset vector with one effective degree of freedom

When the half-offset vector has effectively only one degree of freedom, we take the mapping equation (42) as a starting point for obtaining a derivative of the slope along offset, ψ^σ, with respect the model parameter, ν. The result is

$$\begin{aligned}\frac{\mathrm{d}\psi^\sigma}{\mathrm{d}\nu} = & -\left(\frac{\partial T^D}{\partial \tau}\right)^{-1}\left\{\frac{\partial^2 T^D}{\partial \nu \partial h_I}\frac{\mathrm{d}h_I}{\mathrm{d}\sigma}+\frac{\partial^2 T^D}{\partial \nu \partial \tau}\psi^\sigma\right.\\ & +\frac{\mathrm{d}\hat{m}_J}{\mathrm{d}\nu}\left[\left(\frac{\partial^2 T^D}{\partial m_J \partial h_I}-\frac{\partial^2 T^D}{\partial a_J \partial h_I}\right)\frac{\mathrm{d}h_I}{\mathrm{d}\sigma}+\left(\frac{\partial^2 T^D}{\partial m_J \partial \tau}-\frac{\partial^2 T^D}{\partial a_J \partial \tau}\right)\psi^\sigma\right]\\ & \left.+\frac{\mathrm{d}\hat{\tau}}{\mathrm{d}\nu}\left[\frac{\partial^2 T^D}{\partial \tau \partial h_I}\frac{\mathrm{d}h_I}{\mathrm{d}\sigma}+\frac{\partial^2 T^D}{\partial \tau^2}\psi^\sigma\right]\right\}.\end{aligned} \tag{57}$$

In the calculation of equation (57), the partial derivatives related to the time-migration velocity model are needed. The detailed description of this calculation is described in Appendix F.

4 VELOCITY ESTIMATION FORMULATION

Once we formulated the kinematic time migration/demigration scheme and derived the Fréchet derivatives of kinematic time migration with respect to the time-migration velocity model, we are now able to set up an inversion scheme to estimate the time-migration velocity. In the following, we first review a common way to linearize a generally non-linear inversion problem, then we introduce the approach of iterative linearized inversion to estimate the optimal time-migration velocity model.

4.1 Linearization of the inversion problem

Consider a parameter vector $\boldsymbol{\nu}$ containing N parameters belonging to a general data model (not necessarily related to seismics) and a vector function $\boldsymbol{\mathcal{D}}(\boldsymbol{\nu})$ with M components

$$\mathcal{D}_m(\boldsymbol{\nu}) \;=\; d_m^{\text{true}} - d_m^{\text{pred}}(\boldsymbol{\nu}), \qquad m = 1, \ldots, M, \tag{58}$$

where d_m^{pred} is a quantity predicted on the basis of the model parameter vector $\boldsymbol{\nu}$, and d_m^{true} is the corresponding true (observed or idealized) quantity. Linearization of equation (58) with respect to a certain reference vector $\boldsymbol{\nu}^0$ yields

$$\mathcal{D}_m(\boldsymbol{\nu}) \;=\; \mathcal{D}_m(\boldsymbol{\nu}^0) + \frac{\partial \mathcal{D}_m}{\partial \nu_n}(\boldsymbol{\nu}^0)\;(\nu_n - \nu_n^0). \tag{59}$$

Furthermore, assume that $\mathcal{D}_m = 0$ for all values of the index m. The first-order update $\boldsymbol{\nu}$ of the model parameter vector $\boldsymbol{\nu}^0$ must then satisfy the equation

$$\frac{\partial \mathcal{D}_m}{\partial \nu_n}(\boldsymbol{\nu}^0)\;(\nu_n - \nu_n^0) \;=\; -\mathcal{D}_m(\boldsymbol{\nu}^0). \tag{60}$$

Using the definition of the vector function $\boldsymbol{\mathcal{D}}$ in equation (58) we can alternatively write

$$\frac{\partial d_m^{\text{pred}}}{\partial \nu_n}(\boldsymbol{\nu}^0)\;(\nu_n - \nu_n^0) \;=\; d_m^{\text{true}} - d_m^{\text{pred}}(\boldsymbol{\nu}^0). \tag{61}$$

Equation (61) describes a system of M linear equations with N unknown parameters to be determined. The quantity $\partial d_m^{\text{pred}}/\partial \nu_n$ is commonly referred to as a Fréchet derivative.

4.2 Iterative linearized inversion

We use an iterative linearized inversion approach where the objective is to minimize the misfit between idealized and predicted slopes in the offset coordinates of the common-image gathers. The idealized slopes are zero and correspond to an optimal time-migration velocity model. It is remarked that such a model may not exist in practice, because of the limitations of time migration.

In our situation, the linear equations are obtained by adaption of equation (61), so that each slope event under consideration will give rise to two equations or a single equation, depending on the effective degree of freedom for the variation of the half-offset vector. The resulting equations for these two situations are, respectively,

$$\frac{\partial \psi_I^h}{\partial \nu_n}(\boldsymbol{\nu}^0)\;(\nu_n - \nu_n^0) \;=\; -\psi_I^h(\boldsymbol{\nu}^0). \quad I = 1, 2\ , \tag{62}$$

and

$$\frac{\partial \psi^\sigma}{\partial \nu_n}(\boldsymbol{\nu}^0)\;(\nu_n - \nu_n^0) \;=\; -\psi^\sigma(\boldsymbol{\nu}^0). \tag{63}$$

The Fréchet derivatives of our tomographic approach are partial derivatives of the reflection slope in the offset direction, ψ_I^h or ψ^σ, with respect to the parameters, ν_n, of the time-migration velocity model. These derivatives can be obtained using, respectively, equation (56) or equation (57).

To avoid artificial jumps of the solution in areas with little data coverage, it is important to include regularization in the system of linear equations. We use Tikhonov regularization of zeroth, first, and second order (e.g., Aster et al., 2013). The first- and second-order regularization equations are included separately for each coordinate direction under consideration.

5 EXTRACTION OF LOCAL KINEMATIC PARAMETERS

With the above formulation, we are now able to estimate the time-migration velocity model based on the kinematic time migration and demigration by using the local kinematic parameters (traveltimes, slopes, and curvatures). In our method, considering the efficiency in implementation and the robustness in the calculation, we choose the gradient structure tensor (GST) method for the first-order kinematic parameters (slopes) extraction and quadratic gradient structure tensor (QST) for the second-order kinematic parameters (curvatures) extraction. This operation is applied either on stacked data in the migration domain or the seismic stack in recording domains. In the following, we review the gradient structure tensor method and GST method for slope extraction. we also give the description of curvature extraction in Appendix D.

5.1 The Gradient Structure Tensor

Structure tensors provide a description of the local structure in images using a tensor field. For a 3D image, this yields a 3×3 tensor matrix for each voxel. Knutsson (1989) showed that this tensor could be optimally obtained using six spatially oriented quadrature filters. The gradient structure tensor (GST) (Bigun 1987), is a simplified implementation of the structure tensor, where the tensor is estimated using three gradient filters.

For a 3D seismic cube, the GST is computed using gradient estimates along the three image dimensions ($\mathbf{x} = [x, y, t]^T$). The gradient tensor:

$$\overline{\mathbf{T}} \equiv \overline{\mathbf{g}\mathbf{g}^T}, \tag{64}$$

is the estimated covariance matrix of the gradient vector field:

$$\mathbf{g}(\mathbf{x}) = \begin{bmatrix} g_x(\mathbf{x}) \\ g_y(\mathbf{x}) \\ g_t(\mathbf{x}) \end{bmatrix}. \tag{65}$$

The gradients (g_x, g_y, g_t) along the three axes (x, y, t) are obtained by convolving the seismic data cube $(I(\mathbf{x}))$ with the derivative of the 3D Gaussian function $G(\mathbf{x}, \sigma)$:

$$g_i = I(\mathbf{x}) * \frac{\partial}{\partial \mathbf{x}_i} G(\mathbf{x}, \sigma_g). \tag{66}$$

where σ_g is the gradient scale. As the GST is sensitive to structures at different scales depending on σ_g, when applied to seismic data, we want the GST to be sensitive to reflections. This can be achieved by setting σ_g to match half the typical thickness of the reflections. (full width at half maximum of the Gaussian function). The GST is then computed as the smoothed outer product of the gradient vector:

$$\overline{\mathbf{T}} = \begin{bmatrix} \overline{g_x^2} & \overline{g_y g_x} & \overline{g_t g_x} \\ \overline{g_x g_y} & \overline{g_y^2} & \overline{g_t g_y} \\ \overline{g_x g_t} & \overline{g_y g_t} & \overline{g_t^2} \end{bmatrix}, \tag{67}$$

where $^-$ is the smoothing operator. The smoothed tensor elements are computed using the Gaussian window function:

$$\overline{\mathbf{T}}_{ij} = \mathbf{T}_{ij} * G(\mathbf{x}, \sigma_T), \tag{68}$$

where σ_T is the smoothing scale. The parameter σ_T controls the spatial smoothing. By having a large σ_T, the GST becomes more robust against noise. By having a smaller σ_T, more detailed information about the structure may be obtained.

5.2 Slope estimation

The local structure in the image can be analyzed by considering the eigenvalues $(\lambda_1 \geq \lambda_2 \geq \lambda_3)$ and corresponding eigenvectors $(\mathbf{v_1}, \mathbf{v_2}, \mathbf{v_3})$ of $\overline{\mathbf{T}}$. Since $\overline{\mathbf{T}}$ is the estimated covariance matrix of the gradient vector field, the eigenvectors span the axes of the covariance ellipsoid. This means that $\mathbf{v}_1$ will have the same direction as the locally dominant direction of the gradient vector field. It is also possible to derive attributes from the eigenstructure (Randen et al. 2000).

By considering the components of $\mathbf{v}_1 = [v_{1x}, v_{1y}, v_{1t}]$, the slopes (estimates of the derivatives) are given as:

$$q_x = \frac{\widehat{\partial t}}{\partial x} = \frac{v_{1x}}{v_{1t}}, \tag{69}$$

$$q_y = \frac{\widehat{\partial t}}{\partial y} = \frac{v_{1y}}{v_{1t}}. \tag{70}$$

The eigenvector analysis is carried out for all locations in space, which produces the slope-fields.

6 NUMERICAL EXAMPLES

In this section, we demonstrate the viability of the proposed time-migration velocity estimation technique using three numerical examples. In the first example, we evaluate the derived formulation of kinematic time migration and the calculation of the Fréchet derivatives based on a constant time-migration velocity model. In the next, we present an example based on a 2D synthetic dataset. In the last example, we provide an application of time-migration velocity estimation on real 3D marine data from the Barents Sea.

6.1 Test of the Fréchet derivative formula for time-migration velocity estimation

First, we tested the kinematic migration using single event (point) mapping from the recording domain to the migration domain. As shown in Figure 5, we used an input event point at CMP location $x = 2.5$ km, with travel time $T^D = 2.2676$ s and a half offset of $\mathbf{h} = 1$ km. The corresponding event slopes were $p^x = 0.6840$ s/km and $p^h = 0.0694$ s/km. In the example, a true time-migration velocity model with $S^M = 0.16\ s^2/km^2$ was known, and a time-migration velocity model with $S^M = 0.175\ s^2/km^2$ was used in the test. The diffraction traveltime curves based on the true and test are plotted, represented by the solid black and the broken black lines, respectively in Figure 5. During the test, we applied the kinematic migration to the selected input event in the recording domain based on the test and true models, and observed that the kinematic migration using the test migration velocity misplaced the reflection event in the migration domain and derived kinematic parameters, $m = 0.1889$ m, $\tau = 1.1011$ s, $\psi^m = 1.2692$ and $\psi^h =$ -0.0447 s/km, while the kinematic migration using the true migration velocity correctly mapped the event back to the known diffraction point location, and derived the correct kinematic parameters, $m = 0$ km, $\tau = 1.0$ s, $\psi^m = 1.4009$ and $\psi^h = 0\ s/km$ in the migration domain.

In the next example, we verified the accuracy of the Fréchet derivative approximations derived in Equations (56) or (57). In the test, we first numerically generated the function $\psi^h(v)$ using the input migration velocity quantities $v = S^M$ and the reflection slope quantities in the offset direction ψ^h, derived from the kinematic migration (Figure 6). Since the Fréchet derivatives of our constrained linear inversion are partial derivatives of the reflection slope in the offset direction, ψ_I^h or ψ^σ, with respect to the parameters ν_n of the time-migration velocity model, we could then calculate these derivatives by using Equations (56) or (57). In Figure 6,we plotted the linear approximation of $\psi^h(v)$ using an explicit formula for the derivative $\partial\psi^h/\partial\nu$ at velocity model coordinate $v = S^M = 0.175\ s^2/km^2$. The derived Fréchet derivative $\partial\psi^h/\partial\nu =$ -2.7389 km/s, using the explicit formula in Equation (56), is very close to the numerically-derived Fréchet derivative $\partial\psi^h/\partial\nu =$ -2.7390 km/s. However, if we ignore the movement of the point ($\mathbf{m}$,τ) in Equation (56), the derived linear approximation of $\psi^h(v)$ at the selected velocity model coordinate gives the wrong slope approximation.

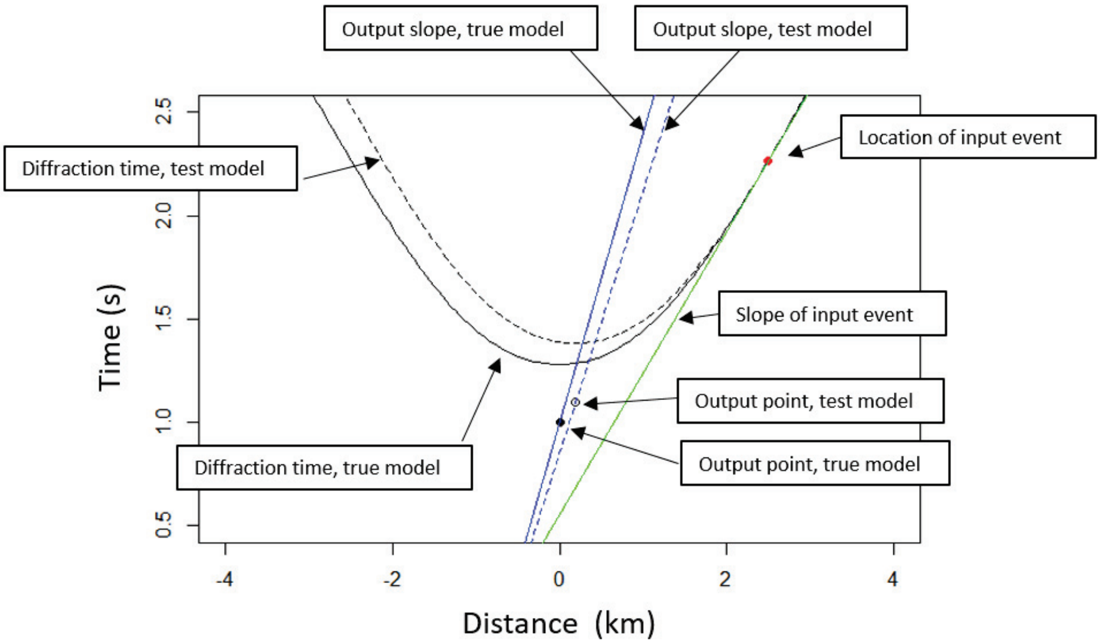

Figure 5: Kinematic time-migration test using different velocity models. The red dot represents an input event point in the recording domain. The black dot represents the output event point of the kinematic migration based on the true velocity model, while the black circle represents the migrated output based on the test velocity model. The diffraction time functions using the true and test velocity models are represented by the solid and dashed black lines, respectively.

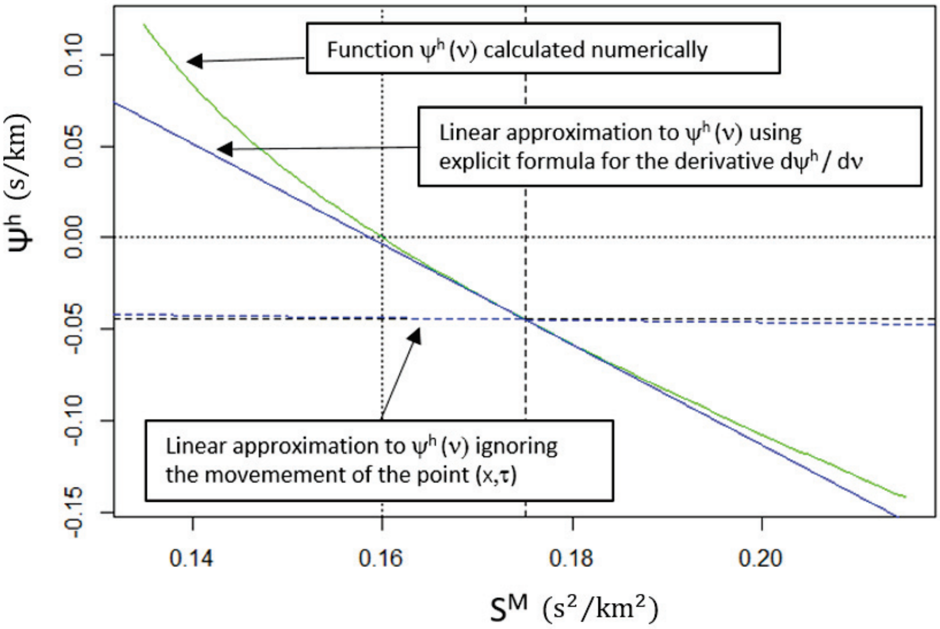

Figure 6: Verification of the Fréchet derivative approximations. The green line represents the numerically-calculated function $\psi^h(v)$. The solid blue line denotes the calculated Fréchet derivative based on Equation (56) at the velocity model coordinate $v = S^M = 0.175\ s^2/km^2$, while the dashed blue line is the Fréchet derivative calculated for the same velocity-model coordinate, but ignoring the movement of the point.

6.2 2D time-migration velocity estimation

In the 2D velocity estimation example, we used a 2D synthetic data set to demonstrate the proposed time-migration velocity estimation workflow (1), shown in Figure 7. This is based on fully using all common-offset gathers, reflection surface picking and slope extraction in the migration domain, and iterations of the internal time-migration velocity estimation.

In this example, a 2D depth-velocity model (Figure 8) was generated, consisting of five geological layers with predefined velocities (1500m/s, 2000m/s, 2500m/s, 3000m/s and 3500m/s), delineated by four interfaces. A surface with a syncline and anticline is defined on Interface 2, and a dipping surface is defined on Interface 3. The prestack shot-gather dataset was simulated by Kirchhoff modelling in NORSAR using a conventional 2D marine seismic geometry: shot interval 12.5 m, trace interval 25 m, minimal offset 100 m, maximum offset 3100 m, group number 121, and total number of shots 953.

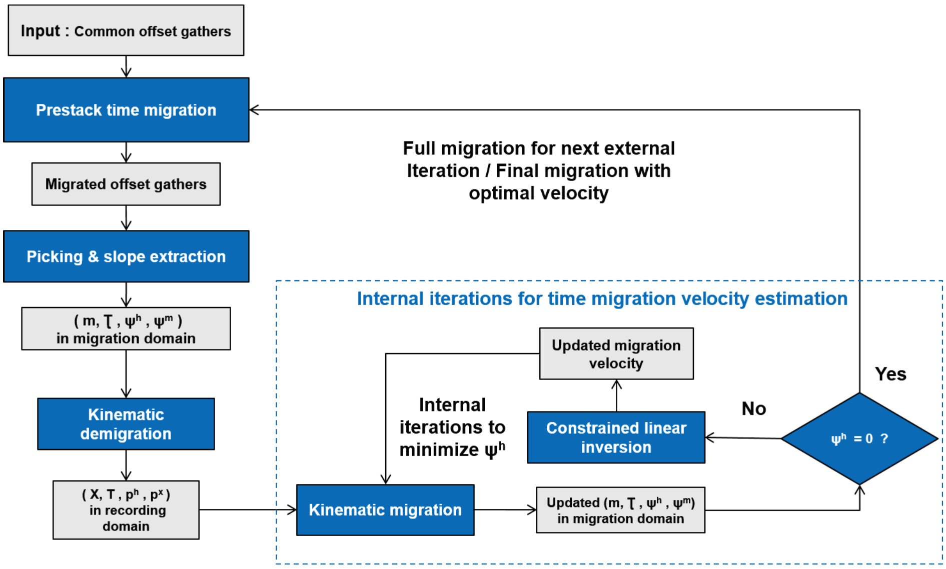

Figure 7: Time-migration velocity estimation workflow (1)

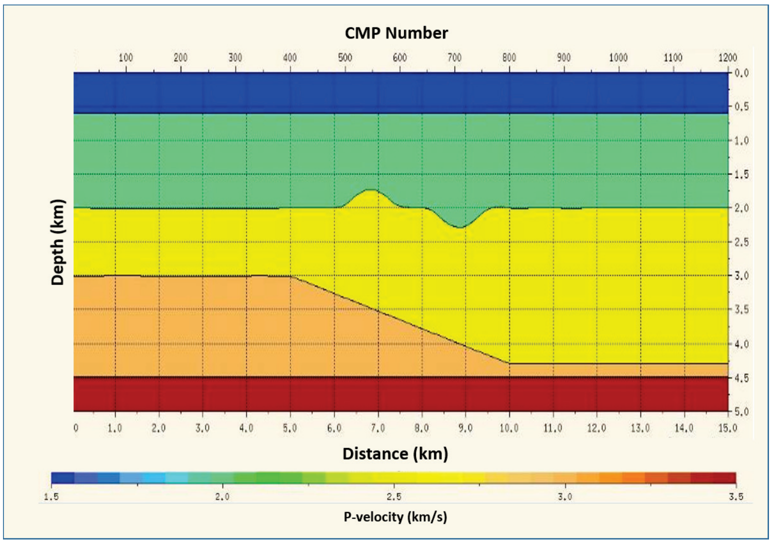

Figure 8: 2D synthetic depth velocity model

Based on the simulated prestack dataset, we applied 2D Kirchhoff prestack time migration using an initial migration velocity field. To test the feasibility of the velocity estimation algorithm, we deliberately used a constant water velocity 1500 m/s as an initial migration velocity model for the Kirchhoff prestack time migration. After the migration, the gradient structure tensor-based slopes extraction was applied to the migrated volume to derive slopes volumes, and a semi-automated seed-point-based horizon tracking was applied so as to derive the reflection traveltime surface in the common image point and offset domain. The corresponding slopes were extracted along the four interpreted surfaces in the migration domain.

Based on the derived kinematic parameters in the migration domain - the half-offset h, the common image point coordinate, m, the migration time τ, and the reflection slopes ψ^m and ψ^h the kinematic demigration was applied to map those kinematic parameters to the recording domain and derive the half-offset h, the common midpoint coordinate x, the reflection time T^D and the reflection slopes p^x and p^h. Based on the kinematic demigration, the reflection surfaces in the recording domain were recreated. Figure 9 shows the picked surfaces in the migration domain and the corresponding kinematic demigrated surfaces in the recording domain, selected from the finite-offset panels.

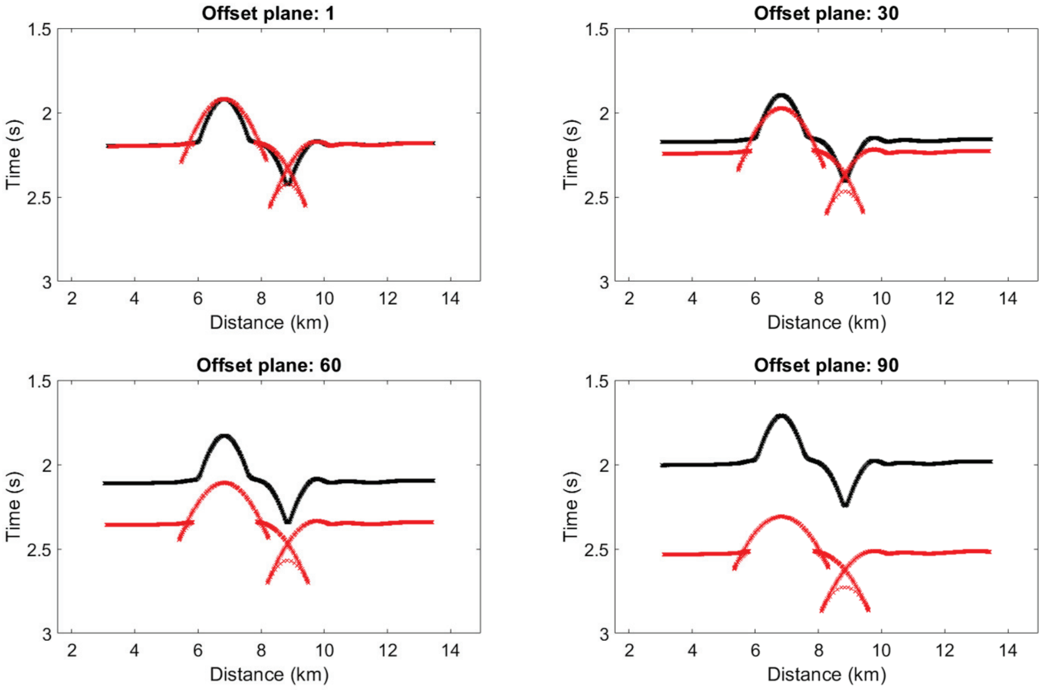

Figure 9: Input finite surface planes in the migration domain (black), and kinematic demigrated finite surface planes in the recording domain (red). The selected offset planes (1, 30, 60 and 90) from the second interface are displayed from top left to bottom right.

Using the input of kinematic parameters in the recording domain, the internal iterations for the time-migration velocity estimation were applied. Each iteration consisted of a kinematic migration with a defined velocity field, and the following constrained linear inversion for deriving the velocity update in order to minimise the reflection slope ψ^h in the migration domain. In this synthetic example, we started the kinematic migration, based on the water velocity (1500 m/s), and the estimated time-migration velocity, by running three internal iterations. Figure 10 shows the kinematic migrated reflection surfaces based on the input/estimated time-migration velocity fields. We projected all the finite-offset surfaces onto the zero-offset plane to verify the improvement of the estimated time-migration velocity field. As mentioned earlier, the best estimated time-migration velocity field is able to flatten all the common image gathers in the offset direction, which is equivalent to zero for the quantity of reflection slope ψ^h in the migration domain. From the reduced residual moveout from Figure 10 a-d, the rapid convergence of the algorithm can be seen.

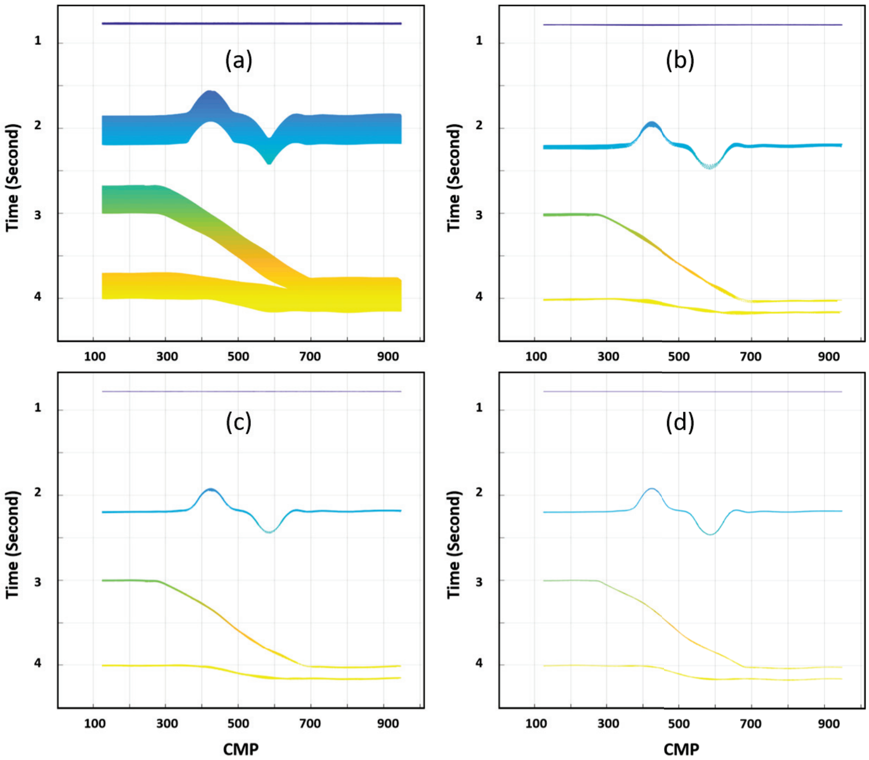

Figure 10: Kinematically-migrated reflection surfaces based on the estimated time-migration velocity field. a): Reflection surface derived from initial water velocity. b-d): Reflection surface derived from velocity estimation's iterations 1-3. All surfaces in the finite-offset were projected onto the zero offset plane for this comparison.

The constrained linear inversion estimated time-migration velocity field was compared with the original depth-model-converted time-migration velocity field for the whole section, as shown in Figure 11, and for the selected common-image-gather (CIG) locations in Figure 12. The estimated time-migration velocity shows good consistency with the model converted reference time-migration velocity within the spatial coordinates 0 to 10 km. From 10 km to the end of the model, the estimated velocity presents a slightly slower velocity trend than the reference velocity, which might be the result of the sparse sampling between the second and third horizons at the right end of the original model.

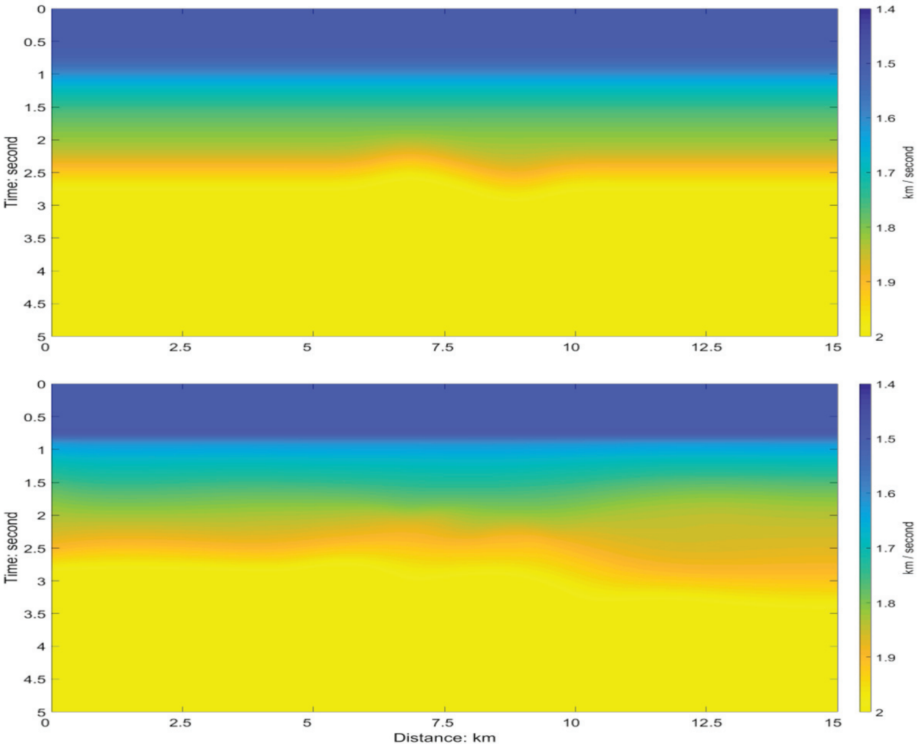

Figure 11: Comparison of time-migration velocity (top) and constrained linear inversion derived time-migrated velocity (bottom).

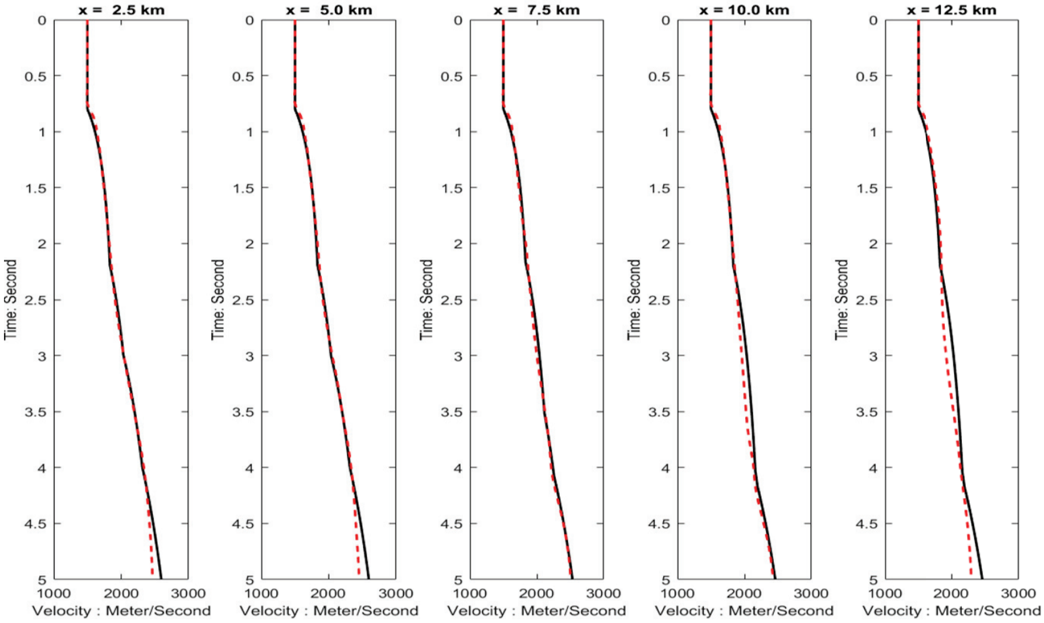

Figure 12: Comparison of derived time-migrated velocity (red) and Dix converted time-migration velocity (black) at selected CIG locations.

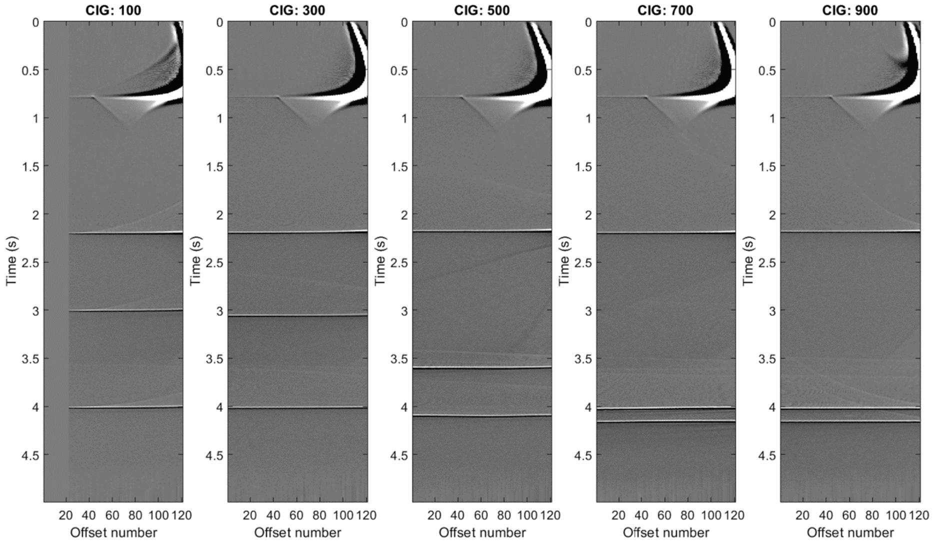

Figure 13: CIG gathers migrated using derived migration velocity.

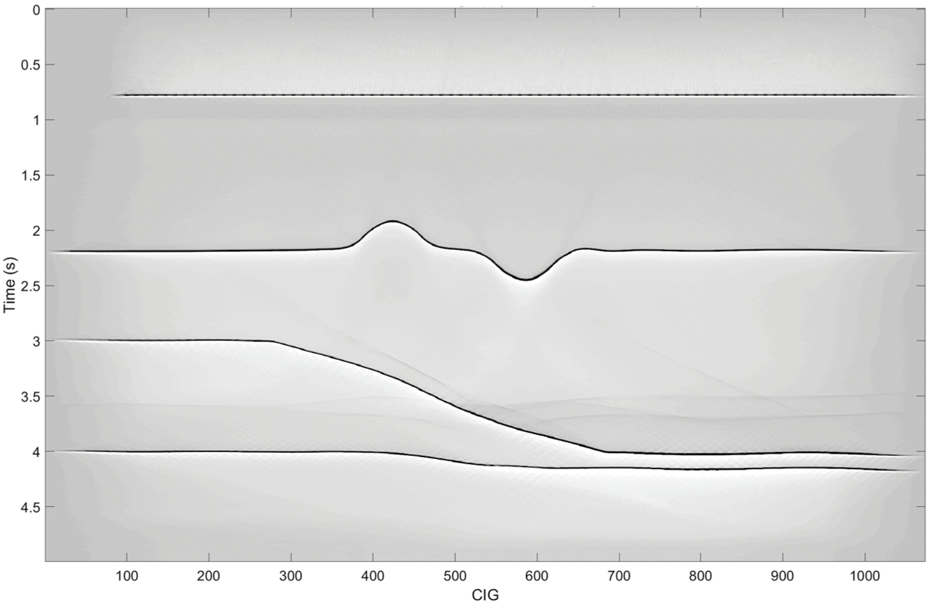

Figure 14: Migration stacked image from PSTM with derived time-migration velocity.

In order to verify the quality of the derived time-migration velocity field, we applied Kirchhoff prestack time migration to the synthetic common-offset gathers using the derived time-migration velocity field. Figure 13 shows the selected CIG gathers after the migration. It can be seen that most of the events on the CIG gathers are flat following the migration using the estimated time-migration velocity. The final migrated stack, shown in Figure 14, also proves the good quality of the estimated time-migration velocity field.

6.3 3D time-migration velocity estimation

In this final example, we employed a 3D marine dataset, acquired in the Barents Sea, to demonstrate the time-migration velocity estimation in 3D scenarios. The dataset contains the migrated stacked 3D volume, the interpreted geological horizons, the pre-migration CMP gathers, and the time-migration velocity field derived from the conventional migration velocity estimation. As the migrated common image gathers were not available for the study, we modified the prior workflow (1) of the time-migration velocity estimation demonstrated in the 2D example, and proposed an alternative version of the workflow (2) (Figure 15) for the 3D time-migration velocity estimation. Instead of the application of an initial prestack time migration to the input data, and the subsequent picking of each migrated offset volume, the algorithm uses the interpreted key reflectors from the time-migrated zero-offset volume as the input and replaces the reflection surface picking and slope extraction in the migration domain with the reflection surface modelling, fitting and slope extraction in the recording domain. In the following 3D numerical example, we used the provided migration velocity as the reference velocity model, and derived the demigrated zero-offset kinematic parameters. Using the subsequent application of reflection surface modeling, seismic to surface fitting and slope extraction, we estimated the 3D time-migration velocity based on the internal iteration of nonlinear constrained 3D velocity inversion. Ultimately, the derived migration velocity field was compared with the reference velocity model to demonstrate the effectiveness of the proposed 3D time-migration velocity estimation approach.

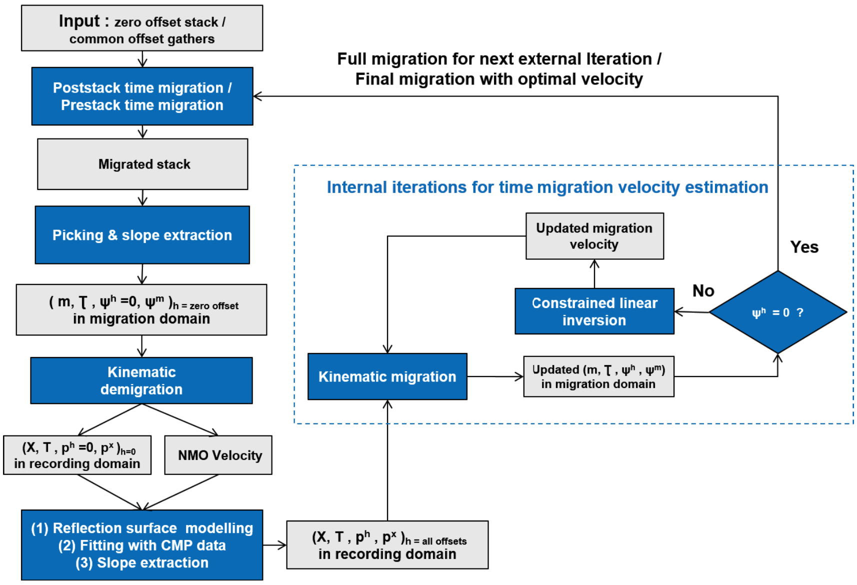

Figure 15: time-migration velocity estimation workflow (2)

The 3D marine dataset was acquired using 12 streamers separated by 75 m and a dual-source configuration with a shot point interval of 18.75 m. The data on each cable was recorded using 564 receivers per streamer at interval of 12.5 m. The sorted 3D CMP dataset, a prestack time-migrated stack volume, the 3D time-migration velocity field and the interpreted horizons from the operating company were used in this numerical example.

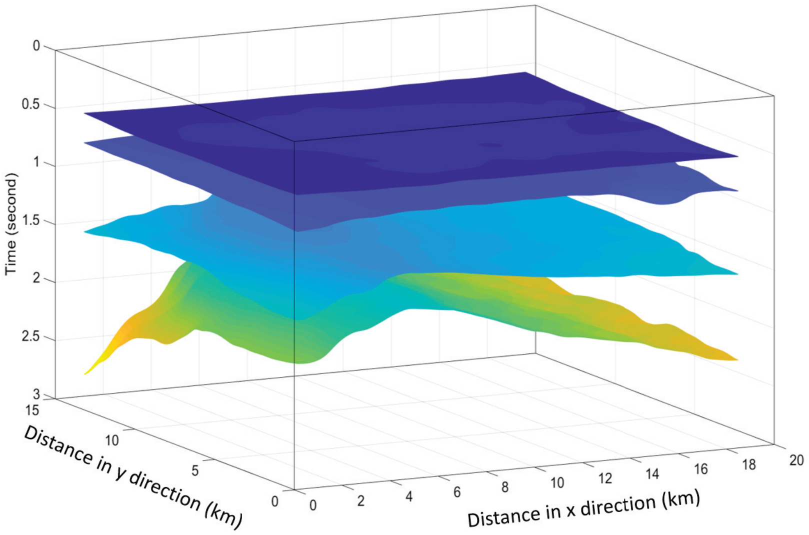

Figure 16: 3D surfaces picked from zero-offset migrated volume, which represent the geological interfaces of the seabed, top Triassic, intra-Triassic, and top Permian, from top to bottom respectively.

Based on legacy seismic processing, four horizons (Figure 16) were interpreted based on the migrated stack volume, which represents the geological interfaces of the seabed, top Triassic, intra-Triassic and top Permian respectively. The original surfaces covered a 300-km^2 area. In this example , we selected an area of interest of 25 km^2 (x = 1.625-6.625 km, y = 0.375-5.375 km) for the time-migration velocity estimation.

In the first step of the algorithm (Figure 15), we proposed applying an initial pre-stack or post-stack time migration using a raw time-migration velocity field, derived either from stacking velocity analysis or a manually-defined velocity trend, then applying the key reflections picking and slope extraction based on the migrated zero-offset dataset. In this example, based on the provided pre-stack time-migration (PSTM) volume and the interpreted key reflection horizons, we first derived the kinematic attribute slope ψ^m using the gradient structure tensor method and extracted the slopes along the interpreted surfaces to derive the zero-offset kinematic parameters ($\mathbf{m}$, τ, $\psi^h = 0$, ψ^m) in the migration domain. Kinematic demigration was applied subsequently to generate the zero-offset kinematic parameters in the recording domain ($\mathbf{x}$, T^D, $p^h = 0$, p^x) by employing the original prestack time-migration velocity. In Figure 17, the fourth zero-offset surface in the migration domain, the demigrated surface in the recording domain and the corresponding slopes of ψ^m are displayed as an example.

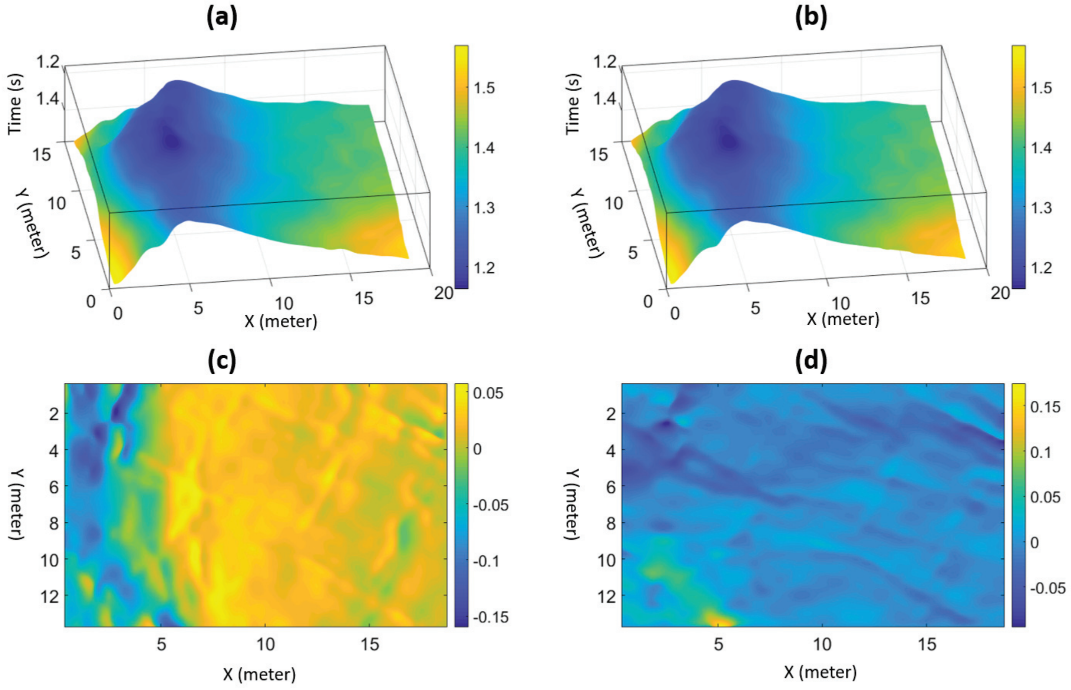

Figure 17: Input and output of zero-offset kinematic demigration, and the derived slopes ψ^m in the recording domain. (a) Interpreted fourth surface in the migration domain. (b) Kinematic demigrated fourth surface in the recording domain. (c) Slopes ψ^m of the demigrated surface along the x direction. (d) Slopes ψ^m of the demigrated surface along the y direction.

Next, in order to obtain the kinematic parameters of the finite-offsets in the recording domain, we introduced a fast-track approach to reflection-surface modelling and surface-to-seismic fitting in the recording domain. In this process, referring to the derivation of Iversen et al. (2012) (Eq. 84), we derived the normal moveout matrices S^{NMO} based on the migration velocity S^M and zero-offset slope p^x. In Figure 17, we display all four components of the normal moveout (NMO) matrices derived from the kinematic demigration of the fourth reflection surface. We then modelled the traveltime surfaces of the finite-offset reflections (Figure 18) using the CMP approximation. The NMO matrices S^{NMO}, zero-offset reflection surfaces T^0, and offset vectors $\mathbf{h}$ extracted from the CMP gathers were used in this calculation. The generated finite-offset reflection surfaces in the recording domain are shown in Figure 18.

Meanwhile, considering that the CMP traveltime equation is under the assumption that the reflection travel time, as the function of the offset, follows hyperbolic trajectories, which are not valid in the case of complex overburden structures that give rise to strong lateral variations, in this case, we assumed the gentle velocity variation within the migration aperture and only tackled the time-migration velocity estimation for the isotropic medium. Thus, at next step in traveltime surfaces/curves to seismic fitting is needed to match the derived reflection curves to the seismic events on the CMP gathers. A semblance-based parameter searching approach was applied in this fitting process. The fitting was applied to the selected CMP locations using the defined grid size of 500 x 500 m. Once the traveltime was calculated at the selected offset and CMP locations, the individual finite-offset surfaces were created using the bi-cubic spline interpolation based on the local traveltime control points. The original modelled reflection events and the fitted reflection events were overlaid on the corresponding CMP gather, and are shown in Figure 19.

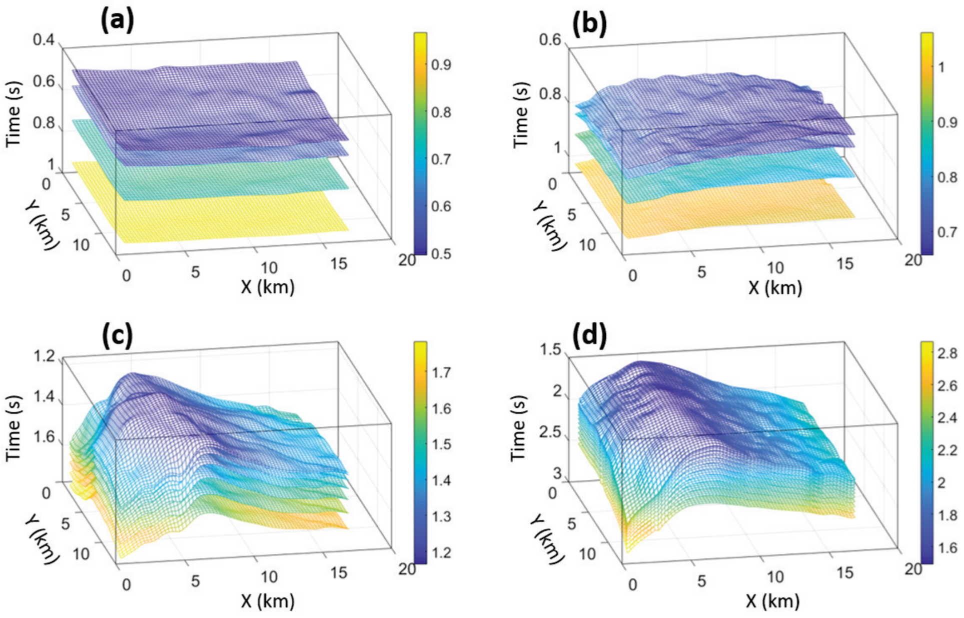

Figure 18: Modelled finite-offset reflection surfaces in the recording domain. (a) First finite-offset reflection surfaces using selected offset planes from the zero offset panel to the maximal offset panel of 15 with step 5. (b) Second finite-offset reflection surfaces using selected offset planes from the zero offset panel to the maximal offset panel of 15 with step 5. (c) Third finite-offset reflection surfaces using selected offset planes from the zero offset panel to the maximal offset panel of 30 with step 5. (d) Fourth finite-offset reflection surfaces with selected offset planes from the zero offset panel to the maximal offset panel of 60 with step 5.

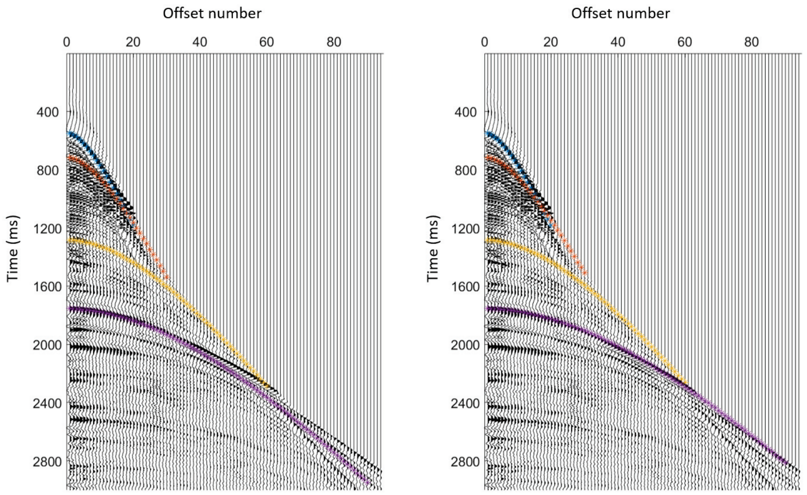

Figure 19: Modelled reflection events overlain on the CMP gather (left), and fitted reflection events overlain on the CMP gather (right)

To derive the finite-offset kinematic parameters in the recording domain, polynomial fitting and slope extraction along the selected directions were applied on each reflection surface. The second order polynomial and cubic smoothing spline were used to fit and derive the slopes p^x and p^h, respectively. Figure 20 shows the reflection surfaces and their corresponding extracted slopes on the selected offset.

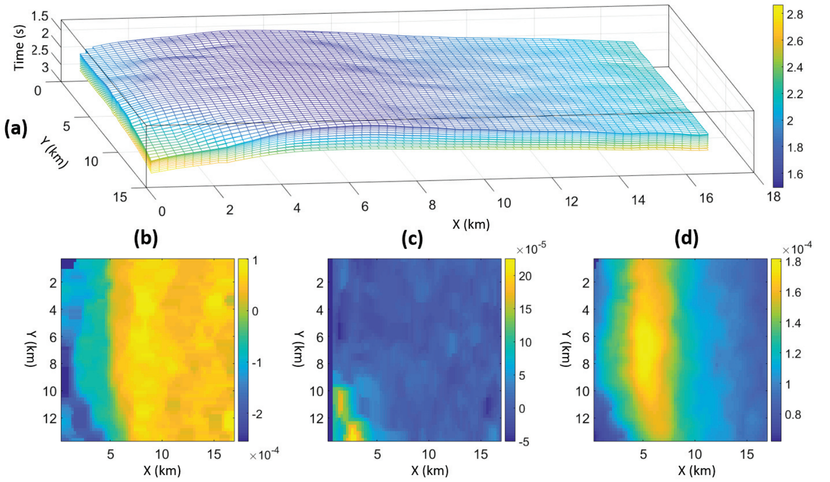

Figure 20: Finite-offset reflection surfaces of the fourth surface and the corresponding extracted slopes on the tenth offset panel. (a) Finite-offset reflection surfaces. (b) Extracted slope surface p^x along x direction. (c) Extracted slope surface p^x along y direction. (d) Extracted slope surface p^h.

In the next step, based on the derived finite-offset kinematic parameters ($\mathbf{h}$, $\mathbf{x}$, T^D, p^h, p^x) in the recording domain, we applied the 3D kinematic migration and constrained the linear inversion in order to estimate the time-migration velocity. As mentioned in the section on the velocity estimation formulation, the internal time-migration velocity estimation is formulated as an iteration of the kinematic time migration and the constrained linear inversion. The kinematic time migration is applied on a defined velocity model to map the kinematic parameters from the recording domain to the migration domain, while the constrained linear inversion provides the time-migration velocity perturbation that minimises the misfit between the idealised slope $p^h = 0$ and the current slope p^h in the common-image gathers. In the 3D time-migration velocity estimation example, we selected a testing area (5 km x 5 km x 2 s) for the velocity field estimation. Unlike using the constant-velocity model in the 2D time-migration velocity estimation example, we derived an initial 3D velocity model from a previous 2D time-migration velocity estimation using a specified sparse grid sampling (1 km x 1 km x 0.1 s), which was used to constrain and stabilise the 3D linear inversion. The derived initial velocity field is shown in Figure 21.

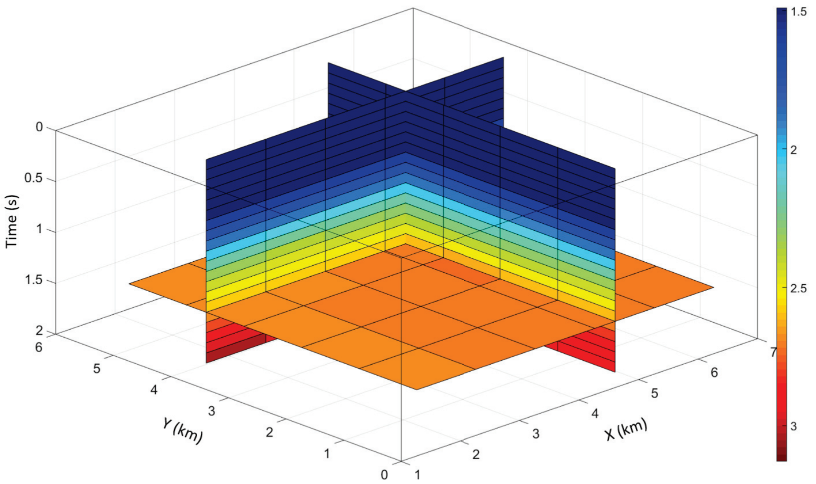

Figure 21: Initial 3D velocity field model (5km x 5km x 2s)

In the 3D time-migration velocity estimation, we applied three iterations of velocity inversion using the setting of variant grid sizes. The grid parameters of the migration velocity used for each iteration are listed in Table 1. The regularisation condition of the first order of Tikhonov using an adaptive damping scheme, was applied to all the iterations. The initial velocity model, and the derived migration velocities of each iteration, are shown in Figure 22 for selected inline location (x = 3.4 km).

Table 1. Grid parameter setting for 3D time-migration velocity estimation

	X sampling(m)	Y sampling(m)	Time sampling(m)
Iteration 1	1000	1000	100
Iteration 2	500	500	50
Iteration 3	250	250	25

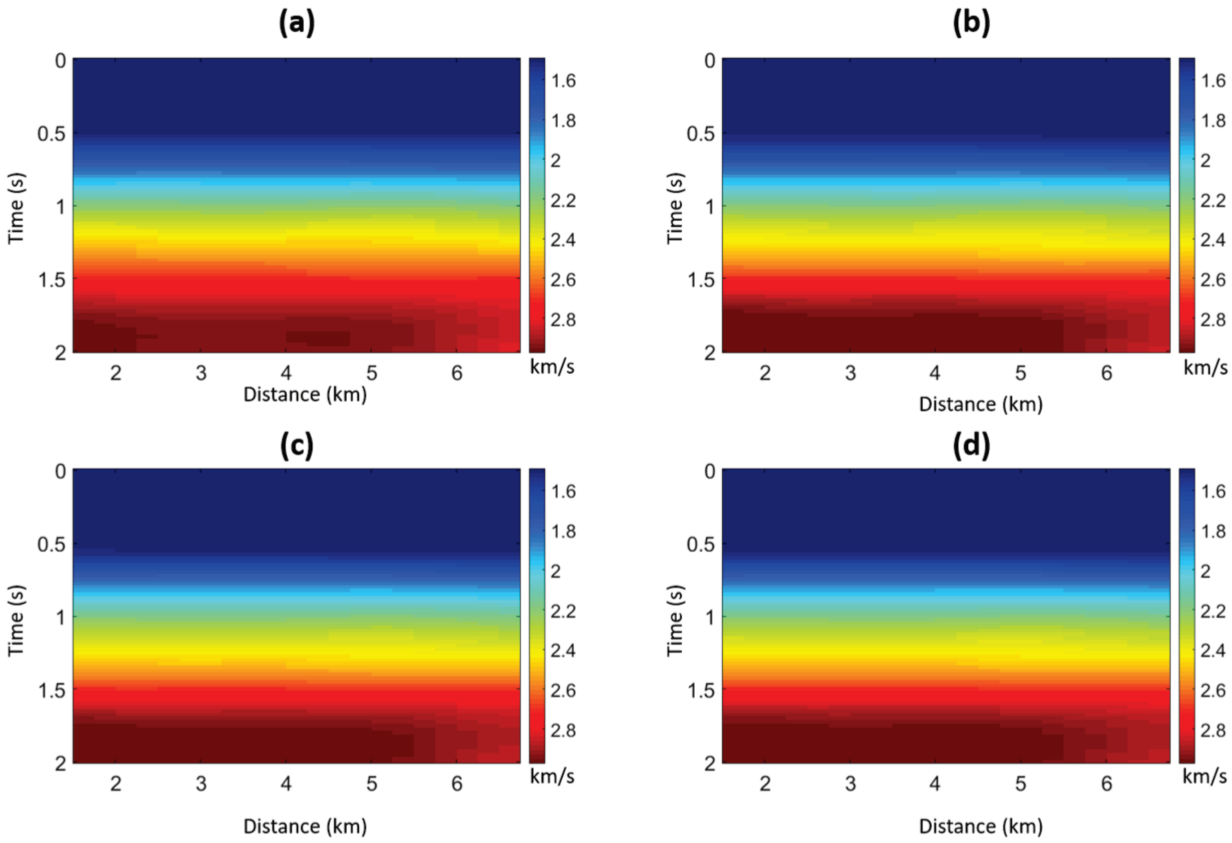

Figure 22: Time-migration velocity from the 3D velocity estimation (selected location at x = 3.4 km). (a) Initial time-migration velocity. (b) Time-migration velocity from the first iteration of the velocity estimation, (c) Time-migration velocity from the second iteration of the velocity estimation, (d) Time-migration velocity from the third iteration of the velocity estimation.

In the last step, for quality controlling the derived 3D time-migration velocity field, we used the reference time-migration velocity field, which was derived from conventional migration velocity analysis as a benchmark against which to compare the velocity field derived from our approach. The two velocity volumes are compared in Figure 23. The selected inline and xline velocity profiles are compared in Figures 24 and 25 , respectively. These two velocity fields were also compared at randomly-selected CIG locations, as shown in Figure 26. From these figures, it can be clearly seen that the inversion-generated velocity field has good consistency with the velocity derived by the conventional approach, especially within the time range 0-1.6 s. In the deeper part, from 1.6 s to 2 s, it can be observed that there is a mismatch between the inversion-derived velocity and the conventional-approach-derived velocity. The inversion-derived velocity gives a slower velocity than the conventional approach; however, upon investigation of the locations that were mismatched, we found that uplift of the bottom horizon and regularisation were the main reasons, and that, potentially, if more deep horizons were included, the version might better constrain the inversion, giving an even better velocity estimation at the bottom.

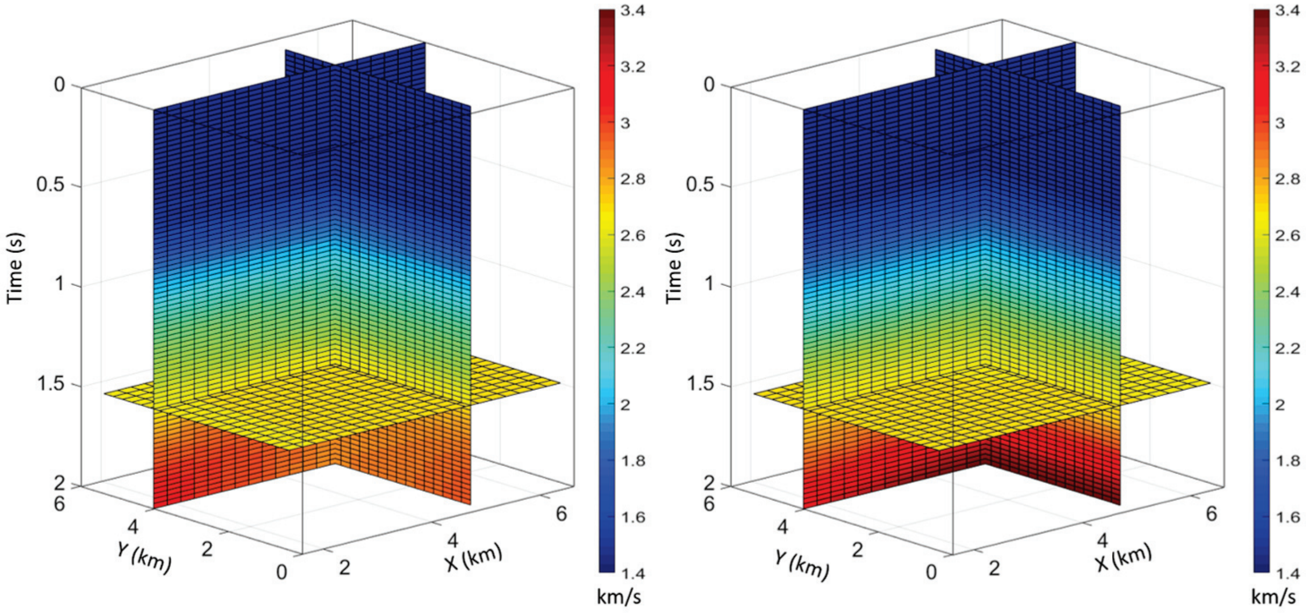

Figure 23: Comparison of 3D time-migration velocity fields derived from the kinematic time migration and demigration approach (left), and the conventional migration velocity analysis approach (right).

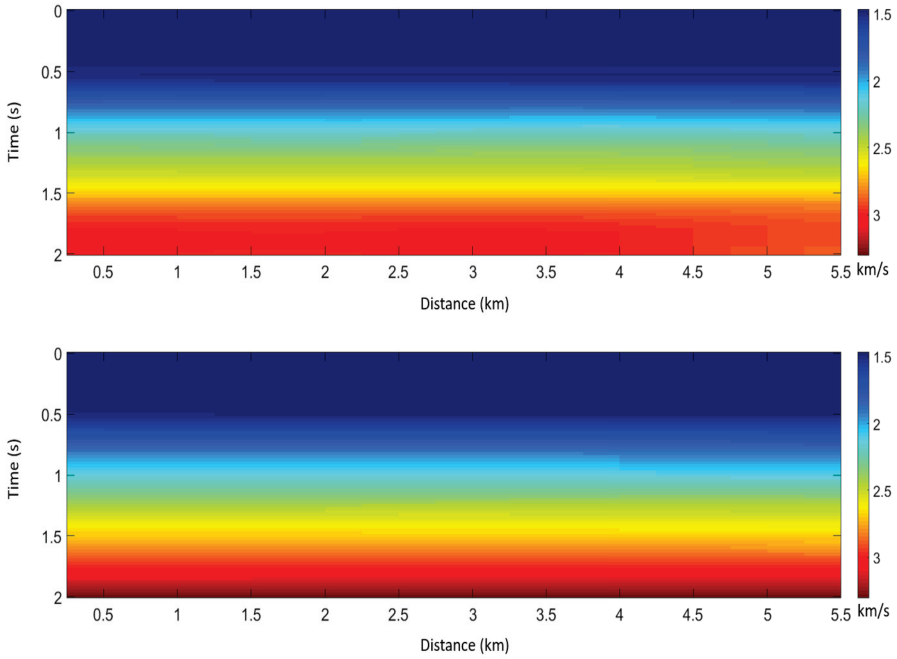

Figure 24: Comparison of the velocity-estimation derived time-migration velocity field (top) and the conventional migration-velocity-analysis-derived time-migration velocity field (bottom). The plot was selected from location x = 3 km

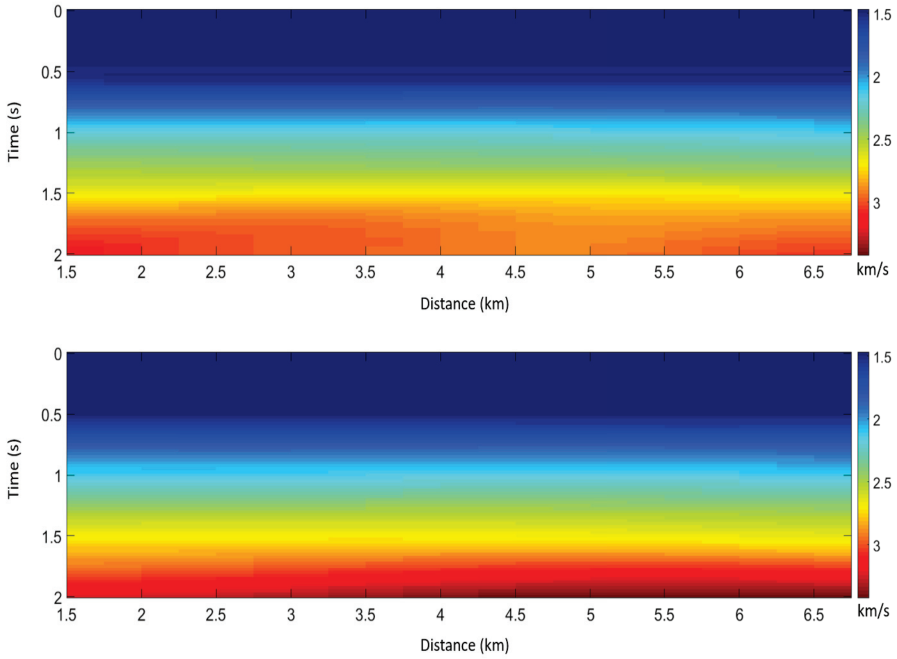

Figure 25: Comparison of the velocity-estimation derived time-migration velocity field (top) and conventional migration-velocity-analysis-derived time-migration velocity field (bottom). The plot was selected along from y = 1.65 km

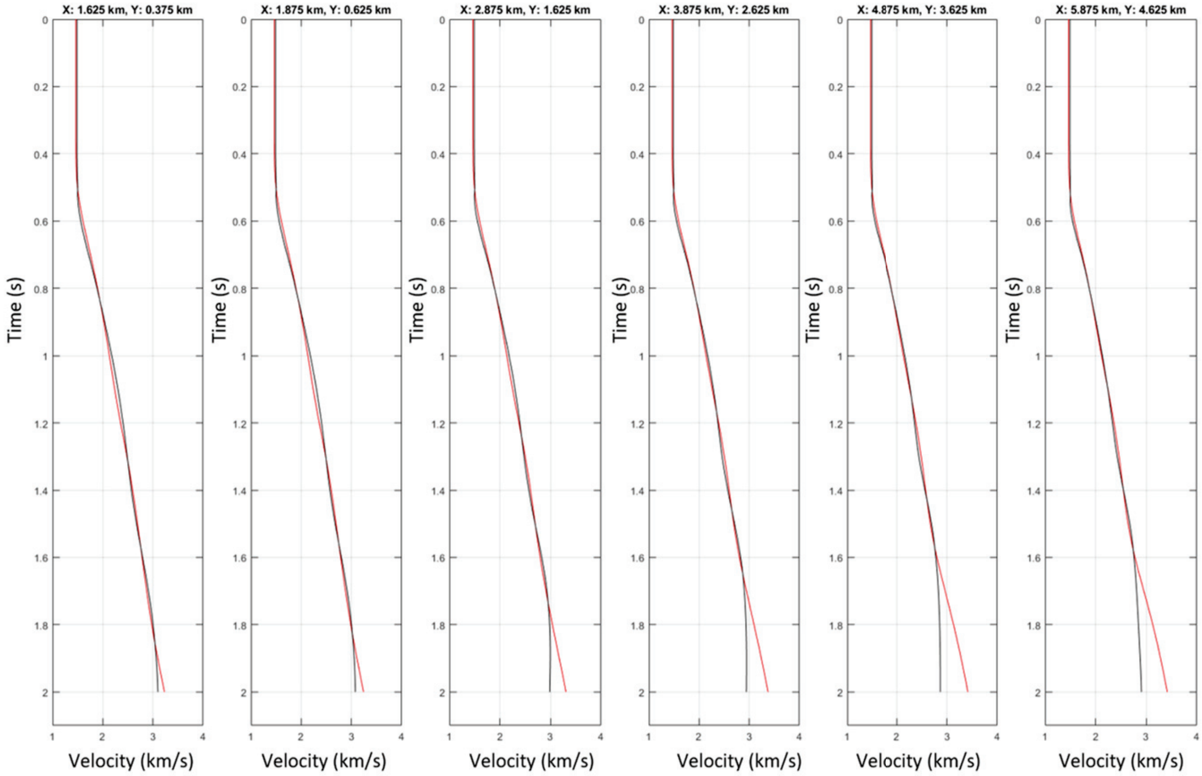

Figure 26: Comparison of velocity-estimation derived time-migration velocity field (black line) and the conventional migration-velocity-analysis- derived time-migration velocity field (red line) for randomly selected locations.

7 CONCLUSIONS

In this paper, we have presented a technique for time-migration velocity estimation, which is based on known reflection traveltimes and local slopes. We have generalised the time-migration velocity estimation using nonlinear mapping processes based on kinematic time migration and demigration, and derived, to a great detail, the involved Fréchet derivatives; that is, the partial derivatives of the local reflection slopes in the offset direction with respect to the time-migration velocity model. Ultimately, a system of linear equations was applied iteratively in order to solve the nonlinear velocity update.

Using the proposed scheme, we have generalised both the 2D and 3D homogeneous and heterogeneous seismic time-migration velocity estimation approaches based on reflection traveltimes and local slopes. The scheme is applied to both conventional narrow- and wide-azimuth acquisition geometries. The proposed time-migration velocity estimation approach is, in general, more accurate than conventional methods because it better honours the spatial variations of the diffraction time function. Through numerical examples, we have shown that the new approach is robust. The optimal migration velocity was obtained within the internal velocity estimation loop, and was subsequently used for final PSTM. Regarding reflection traveltime picking, we proposed extracting the local reflection slopes using the technique of gradient structure tensor and semi-automatic reflection horizon picking in the pre-stack migration domain in order to utilise the migrated pre-stack data with a higher resolution and signal-to-noise ratio.

In the numerical experiments, the theoretical formulations were tested using three examples. In the first example, we verified the Fréchet derivatives used for the time-migration velocity estimation. The presented examples of the comparison between the analytical and numerical derivatives of both the kinematic migration and Fréchet derivatives proved the accuracy of the theoretical derivation. In the next example, we demonstrated the time-migration velocity estimation on a 2D dataset. The experimental dataset was initially generated by Kirchhoff modelling. In the subsequent velocity estimation, the generated synthetic datasets were migrated by PSTM using an initial migration velocity model, and then the reflection traveltime picks and corresponding local slopes were derived. The following applied internal velocity updates showed a rapid convergence of the linear velocity iterations. The accuracy of the derived 2D time-migration velocity was also proved by the flatness of the final PSTM-migrated gather and the reasonable quality of the PSTM-migrated stack image. In the last numerical example, we demonstrated the feasibility of applying the derived scheme for the estimation of time-migration velocity to a 3D marine field dataset. In this example, as we were short of a PSTM-migrated prestack dataset, only obtaining the migrated stacked dataset, the corresponding integrated reflection horizons, and legacy PSTM migration-velocity field, we used a workaround scheme to derive the invariant reflection traveltimes and local slopes in the recording domain, and applied the velocity estimation using the input from selected finite-offset planes. Although we understand that the picking in the recording domain may have included artifacts from the complex geological region, the experiment-derived migration velocity volume still showed good consistency with the velocity derived from conventional migration-velocity analysis. This proved the feasibility of the 3D time-migration velocity estimation formulation.

In general, considering the initial depth-velocity model is still crucial for most of the depth-domain tomography algorithms, we believe that the proposed technique of time-migration velocity estimation, using nonlinear kinematic migration/demigration solvers based on Fréchet derivatives, will improve the accuracy of velocity model estimation and the resulting final image in both the time and depth domains.

ACKNOWLEDGMENTS

The authors acknowledge support from the Norwegian Research Council through the Petro-Maks 2 project (NFR/234019). We thank Lundin Norway AS for making the 3D field dataset available for this study. We also grateful to NORSAR for providing the software for the synthetic data generation.

REFERENCES

Adler, F., Baina, R., Soudani, M. A., Cardon, P., & Richard, J.-B., 2008. Nonlinear 3d tomographic least-squares inversion of residual moveout in kirchhoff prestack-depth-migration common-image gathers, *Geophysics*, **73**(5), VE13–VE23.

Aster, R. C., Borchers, B., & Thurber, C. H., 2013. *Parameter estimation and inverse problems*, Academic Press, Waltham, MA, 2nd edn.

Bakker, P., 2002. *Image structure analysis for seismic interpretation: Ph.D. thesis*, Ph.D. thesis, Technische Universiteit Delft.

Barros, T., Ferrari, R., Krummenauer, R., & Lopes, R., 2015. Differential evolution-based optimization procedure for automatic estimation of the common-reflection surface traveltime parameters, *Geophysics*, **80**(6), WD189–WD200.

Bartels, R. H., Beatty, J. C., & Barsky, B. A., 1987. *An Introduction to Splines for Use in Computer Graphics and Geometric Modeling.*, Morgan Kaufmann Publishers.

Bauer, A., Schwarz, B., & Gajewski, D., 2009. Enhancement of prestack diffraction data and attributes using a traveltime decomposition approach, *Studia Geophysica et Geodaetica*, **60**, 471–486.

Baykulov, M. & Gajewski, D., 2009. Prestack seismic data enhancement with partial common-reflection-surface (CRS) stack, *Geophysics*, **74**(3), V49–V58.

Bergler, S., Hubral, P., Marchetti, P., Cristini, A., & Cardone, G., 2002. 3D common-reflection-surface stack and kinematic wavefield attributes, *The Leading Edge*, **21**(10), 1010–1015.

Berkovitch, A., Belfer, I., & Landa, E., 2008. Multifocusing as a method of improving subsurface imaging, *The Leading Edge*, **27**(2), 250–256.

Berkovitch, A., Belfer, I., Hassin, Y., & Landa, E., 2009. Diffraction imaging by multifocusing, *Geophysics*, **74**(6), WCA75–WCA81.

Bigun, J., 1987. G.h.: Optimal orientation detection of linear symmetry, in *In: Proceedings of the IEEE First International Conference on Computer Vision, London, Great Britain*, pp. 433–438.

Billette, F. & Lambaré, G., 1998. Velocity macro-model estimation from seismic reflection data by stereotomography, *Geophysical Journal International*, **135**(2), 671–690.

Bloot, R., Coimbra, T. A., Faccipieri, J. H., & Tygel, M., 2018. Common-reflection-surface method in weakly anisotropic vertical transverse isotropic media, *Geophysics*, **83**(3), C99–C113.

Bóna, A., 2011. Shot-gather time migration of planar reflectors without velocity model, *Geophysics*, **76**(2), S93–S101.

Bonomi, E., Cristini, M., Theis, D., & Marchetti, P., 2009. 3D CRS analysis: a data-driven optimization for the simultaneous estimate of the eight parameters, in *SEG Houston 2009 International Exposition and Annual Meeting*.

Chauris, H., Noble, M. S., Lambaré, G., & Podvin, P., 2002a. Migration velocity analysis from locally coherent events in 2-d laterally heterogeneous media, part i: Theoretical aspects, *Geophysics*, **67**(4), 1202–1212.

Chauris, H., Noble, M. S., Lambaré, G., & Podvin, P., 2002b. Migration velocity analysis from locally coherent events in 2-d laterally heterogeneous media, part II: Applications on synthetic and real data, *Geophysics*, **67**(4), 1213–1224.

Coimbra, T. A., de Figueiredo, J. J. S., Schleicher, J., Novais, A., & Costa, J. C., 2013. Migration velocity analysis using residual diffraction moveout in the poststack depth domain, *Geophysics*, **78**(3), S125–S135.

Coimbra, T. A., Faccipieri, J. H., Rueda, D. S., & Tygel, M., 2016a. Common-reflection-point time migration, *Studia Geophysica et Geodaetica*, **60**(3), 500–530.

Coimbra, T. A., Novais, A., & Schleicher, J., 2016b. Offset-continuation stacking: Theory and proof of concept, *Geophysics*, **81**(5), V387–V401.

Cooke, D., Bóna, A., & Hansen, B., 2009. Simultaneous time imaging, velocity estimation, and multiple suppression using local event slopes, *Geophysics*, **74**(6), WCA65–WCA73.

Dell, S. & Gajewski, D., 2011. Common-reflection-surface-based workflow for diffraction imaging, *Geophysics*, **76**(5), S187–S195.

Dell, S., Gajewski, D., & Tygel, M., 2014. Image-ray tomography, *Geophysical Prospecting*, **62**(3), 413–426.

Douma, H. & de Hoop, M. V., 2006. Leading-order seismic imaging using curvelets, in *SEG Technical Program Expanded Abstracts 2006*, Society of Exploration Geophysicists.

Faccipieri, J. H., Serrano, D. R., Gelius, L. J., & Tygel, M., 2013. Recovering diffractions in CRS stacked sections, *First Break*, **31**(1973), 27–31.

Faccipieri, J. H., Coimbra, T. A., Gelius, L. J., & Tygel, M., 2016. Stacking apertures and estimation strategies for reflection and diffraction enhancement, *Geophysics*, **81**(4), V271–V282.

Fomel, S., 2002. Applications of plane-wave destruction filters, *Geophysics*, **67**(6), 1946–1960.

Fomel, S., 2007a. Velocity-independent time-domain seismic imaging using local event slopes, *Geophysics*, **72**(3), S139–S147.

Fomel, S., 2007b. Local seismic attributes, *Geophysics*, **72**(3), A29–A33.

Fomel, S. & Kazinnik, R., 2012. Non-hyperbolic common reflection surface, *Geophysical Prospecting*, **61**(1), 21–27.

Garabito, G., Cruz, J, C. R., & S´olner, W., 2017. Finite-offset common reflection surface stack using global optimisation for parameter estimation: a land data example, *Geophysical Prospecting*, **65**(5), 11231137.

Gelius, L.-J. & Tygel, M., 2015. Migration-velocity building in time and depth from 3D (2D) Common-Reflection-Surface (CRS) stacking - theoretical framework, *Studia Geophysica et Geodaetica*, **59**(2), 253–282.

Gjøystdal, H. & Ursin, B., 1981. Inversion of reflection times in three dimensions, *Geophysics*, **46**(7), 972–983.

Guillaume, P., Audebert, F., Berthet, P., David, B., Herrenschmidt, A., & Zhang, X., 2001. 3d finite-offset tomographic inversion of CRP-scan data, with or without anisotropy, in *SEG Technical Program Expanded Abstracts 2001*, Society of Exploration Geophysicists.

Guillaume, P., Lambare, G., Leblanc, O., Mitouard, P., Moigne, J. L., Montel, J.-P., Prescott, T., Siliqi, R., Vidal, N., Zhang, X., & Zimine, S., 2008. Kinematic invariants: an efficient and flexible approach for velocity model building, in *SEG Technical Program Expanded Abstracts 2008*, Society of Exploration Geophysicists.

Guillaume, P., Reinier, M., Lambaré, G., Cavalié, A., Adamsen, M. I., & Bruun, B. M., 2013. Dip constrained non-linear slope tomography: an application to shallow channels characterization, in *13th International Congress of the Brazilian Geophysical Society and EXPOGEF,Rio de Janeiro, Brazil, 26–29 August 2013*, Society of Exploration Geophysicists and Brazilian Geophysical Society.

Hertweck, T., Schleicher, J., & Mann, J., 2007. Data stacking beyond CMP, *The Leading Edge*, **26**(7), 818–827.

Hoecht, G., Ricarte, P., Bergler, S., & Landa, E., 2009. Operator-oriented CRS interpolation, *Geophysical Prospecting*, **57**(6), 957–979.

Hubral, P., 1999. Special issue: Macro model independent seismic imaging, *Journal of Applied Geophysics*, **42**(3-4).

Hubral, P. & Krey, T., 1980. *Interval Velocities from Seismic Reflection Time Measurements*, Society of Exploration Geophysicists (SEG), Tulsa, USA.

Iversen, E., 2004. The isochron ray in seismic modeling and imaging, *Geophysics*, **69**(4), 1053–1070.

Iversen, E. & Gjøystdal, H., 1996. Event-oriented velocity estimation based on prestack data in time or depth domain1, *Geophysical Prospecting*, **44**(4), 643–686.

Iversen, E., Tygel, M., Ursin, B., & Hoop, M. V., 2012. Kinematic time migration and demigration of reflections in pre-stack seismic data, *Geophysical Journal International*, **189**(3), 1635–1666.

Jäger, R., Mann, J., Höcht, G., & Hubral, P., 2001. Common-reflection-surface stack: Image and attributes, *Geophysics*, **66**(1), 97–109.

Khoshnavaz, M. J., 2017. Oriented time-domain dip moveout correction for planar reflectors in common-source domain, *Geophysics*, **82**(6), U87–U97.

Khoshnavaz, M. J., Bóna, A., Dzunic, A., Ung, K., & Urosevic, M., 2016a. Oriented prestack time migration using local slopes and predictive painting in the common-source domain for planar reflectors, *Geophysics*, **81**(6), S409–S418.

Khoshnavaz, M. J., Bóna, A., & Urosevic, M., 2016b. Velocity-independent estimation of kinematic attributes in vertical transverse isotropy media using local slopes and predictive painting, *Geophysics*, **81**(5), U73–U85.

Kleyn, A. H., 1977. On the migration of reflection time contour maps, *Geophysical Prospecting*, **25**(1), 125–140.

Klokov, A. & Fomel, S., 2012. Separation and imaging of seismic diffractions using migrated dip-angle gathers, *Geophysics*, **77**(6), S131–S143.

Knutsson, H., 1989. Representing local structure using tensors, in *Proceedings of 6th Scandinavian Conference on Image Analysis*, pp. 244–251.

Lambaré, G., Deladerrière, N., Traonmilin, Y., Touré, J. P., Moigne, J. L., & Herrmann, P., 2009. Non-linear tomography for time imaging, in *71st EAGE Conference and Exhibition incorporating SPE EUROPEC 2009*, EAGE Publications BV.

Landa, E., 2007. *Beyond Conventional Seismic Imaging*, EAGE, The Hague, Netherlands.

Landa, E., Gurevich, B., Keydar, S., & Trachtman, P., 1999. Application of multifocusing method for subsurface imaging, *Journal of Applied Geophysics*, **42**(3-4), 283–300.

Landa, E., Keydar, S., & Moser, T. J., 2010. Multifocusing revisited - inhomogeneous media and curved interfaces, *Geophysical Prospecting*, **58**(11), 925–938,.

Messud, J., Lambaré, G., Guillaume, P., & Rohel, C., 2015. Non-linear slope tomography for orthorhombic pre-stack time imaging, in *77th EAGE Conference and Exhibition 2015*, EAGE Publications BV.

Minato, S., Tsuji, T., Matsuoka, T., Nishizaka, N., & Ikeda, M., 2012. Global optimisation by simulated annealing for common reflection surface stacking and its application to low-fold marine data in southwest japan, *Exploration Geophysics*, **43**(2), 59–69.

Neidell, N. S. & Taner, M. T., 1971. Semblance and other coherency measures for multichannel data, *Geophysics*, **36**(3), 482–497.

Perroud, M., Hubral, P., & Höcht, G., 1999. Common-reflection-point stacking in laterally inhomogeneous media, *Geophysical Prospecting*, **47**, 1–24.

Rad, P. B., Schwarz, B., Gajewski, D., & Vanelle, C., 2018. Common-reflection-surface-based prestack diffraction separation and imaging, *Geophysics*, **83**(1), S47–S55.

Randen, T., Monsen, E., Signer, C., Abrahamsen, A., Hansen, J. O., Sæter, T., & Schlaf, J., 2000. Three-dimensional texture attributes for seismic data analysis, in *SEG Technical Program Expanded Abstracts 2000*, Society of Exploration Geophysicists.

Riabinkin, 1957. Fundamentals of resolving power of controlled directional reception (cdr) of seismic waves, **14**, 36–60.

Rieber, F., 1936. Visual presentation of elastic wave patterns under various structural conditions, *Geophysics*, **1**(2), 196–218.

Shah, P. M., 1973. use of wavefront curvature to relate seismic data with subsurface parameters, *Geophysics*, **38**(5), 812–825.

Söllner, W. & Andersen, E., 2005. Kinematic time migration and demigration in a 3d visualization system, *Journal of Seismic Exploration*, **14**(2-3), 255–270.

Söllner, W., Andersen, E., & Lima, J., 2004. Fast time-to-depth mapping by first-order ray transformation in a 3-d visualization system, in *SEG Technical Program Expanded Abstracts 2004*, Society of Exploration Geophysicists.

Spinner, M. & Mann, J., 2006. True-amplitude based Kirchhoff time migration for AVO/AVA analysis, *Geophysics*, **15**, 133–152.

Stolk, C. C., de Hoop, M. V., & Symes, W. W., 2009. Kinematics of shot-geophone migration, *Geophysics*, **74**(6), WCA19–WCA34.

Stovas, A. & Fomel, S., 2015. Mapping of moveout attributes using local slopes, *Geophysical Prospecting*, **64**(1), 31–37.

Sword, C. H., 1986. Tomographic determination of interval velocities from picked reflection seismic data, in *SEG Technical Program Expanded Abstracts 1986*, Society of Exploration Geophysicists.

Tygel, M. & Santos, L. T., 2007. Quadratic normal moveouts of symmetric reflections in elastic media: A quick tutorial, *Studia Geophysica et Geodaetica*, **51**(1), 185–206.

Ursin, P., 1982. Quadratic wavefront and traveltime approximations in inhomogeneous layered media with curved interfaces, *Geophysics*, **47**(7), 1012–1021.

van de Weijer, J., van Vliet, L., Verbeek, P., & van Ginkel, R., 2001. Curvature estimation in oriented patterns using curvilinear models applied to gradient vector fields, *IEEE Transactions on Pattern Analysis and Machine Intelligence*, **23**(9), 1035–1042.

Vanelle, C., Abakumov, I., & Gajewski, D., 2018. Wavefront attributes in anisotropic media, *Geophysical Journal International*, **214**(1), 430–443.

Walda, J. & Gajewski, D., 2017. Determination of wavefront attributes by differential evolution in the presence of conflicting dips, *Geophysics*, **82**(4), V229–V239.

Waldeland, A. U., Coimbra, T. A., Faccipieri, J. H., Solberg, A. H. S., & Gelius, L. J., 2019. Fast estimation of prestack common reflection surface parameters, *Geophysical Prospecting*, **67**(5), 1163–1183.

Whitcombe, D. N., Murray, E. H., Aubin, L. A. S., & Carroll, R. J., 1994. The application of 3-d depth migration to the development of an alaskan offshore oil field, *Geophysics*, **59**(10), 1551–1560.

Zhang, Y., Bergler, S., Tygel, M., & Hubral, P., 2002. Model-independent travel-time attributes for 2-d, finite-offset multicoverage reflections, *Pure and Applied Geophysics*, **159**, 1601–1616.

APPENDIX A: FIRST- AND SECOND-ORDER DERIVATIVES OF DIFFRACTION TIME WITH RESPECT TO MIGRATION-TIME COORDINATES AND APERTURE

The diffraction-time function relies on migration-time coordinates and aperture– totally seven independent variables. We specify the first- and second-order derivatives in these variables.

To simplify the formulations, define the coordinate vector $\boldsymbol{\xi} = (\xi_i)$ such that $\xi_1 = m_1$, $\xi_2 = m_2$, $\xi_3 = \tau$, and the coordinate vector $\boldsymbol{\gamma} = (\gamma_r)$, with $\gamma_1 = h_1$, $\gamma_2 = h_2$, $\gamma_3 = a_1$, $\gamma_4 = a_2$. We observe that the first-order relations between source- and receiver-offset components (h_I^S and h_I^R) and the γ_r-components (h_J and a_J) are given by

$$\frac{\partial h_I^S}{\partial h_J} = -\delta_{IJ}, \qquad \frac{\partial h_I^S}{\partial a_J} = \delta_{IJ}, \tag{A.1}$$

and

$$\frac{\partial h_I^R}{\partial h_J} = \delta_{IJ}, \qquad \frac{\partial h_I^R}{\partial a_J} = \delta_{IJ}. \tag{A.2}$$

Once we know the derivative of T^S and T^R with respect to ξ_i and/or γ_r, the corresponding derivative of T^D results by simple summation.

A1 Derivatives of one-way time

First, consider the one-way time function T^S. Straightforward differentiation of the first subequation in (7) yields the first-order derivatives

$$\frac{\partial T^S}{\partial \xi_m} = \frac{1}{2T^S}\left[\frac{\xi_3}{2}\,\delta_{3m} + \frac{\partial}{\partial \xi_m}\left(S_{IJ}^{M(2)}\right) h_I^S\, h_J^S + \frac{\partial}{\partial \xi_m}\left(S_{IJKL}^{M(4)}\right) h_I^S\, h_J^S\, h_K^S\, h_L^S\right], \tag{A.3}$$

$$\frac{\partial T^S}{\partial \gamma_r} = \frac{\partial T^S}{\partial h_M^S}\,\frac{\partial h_M^S}{\partial \gamma_r}, \qquad \frac{\partial T^S}{\partial h_M^S} = \frac{1}{T^S}\left(S_{IM}^{M(2)}\, h_I^S + 2S_{IJKM}^{M(4)}\, h_I^S\, h_J^S\, h_K^S\right), \tag{A.4}$$

with $\partial h_M^S/\partial \gamma_r$ given by equation (A.1).

For the second-order derivatives we find

$$\begin{aligned}\frac{\partial^2 T^S}{\partial \xi_m \partial \xi_n} &= \frac{1}{2T^S}\left[\frac{\partial^2}{\partial \xi_m \partial \xi_n}\left(S_{IJ}^{M(2)}\right) h_I^S\, h_J^S + \frac{\partial^2}{\partial \xi_m \partial \xi_n}\left(S_{IJKL}^{M(4)}\right) h_I^S\, h_J^S\, h_K^S\, h_L^S\right] \\ &\quad - \frac{1}{T^S}\,\frac{\partial T^S}{\partial \xi_m}\,\frac{\partial T^S}{\partial \xi_n},\end{aligned} \tag{A.5}$$

$$\frac{\partial^2 T^S}{\partial \gamma_r \partial \gamma_s} = \frac{1}{T^S}\left(S_{MN}^{M(2)} + 6\,S_{IJMN}^{M(4)}\, h_I^S\, h_J^S\right)\frac{\partial h_M^S}{\partial \gamma_r}\,\frac{\partial h_N^S}{\partial \gamma_s} - \frac{1}{T^S}\,\frac{\partial T^S}{\partial \gamma_r}\,\frac{\partial T^S}{\partial \gamma_s}, \tag{A.6}$$

$$\begin{aligned}\frac{\partial^2 T^S}{\partial \xi_m \partial \gamma_r} &= \frac{1}{T^S}\left[\frac{\partial}{\partial \xi_m}\left(S_{IN}^{M(2)}\right) h_I^S + 2\frac{\partial}{\partial \xi_m}\left(S_{IJKN}^{M(4)}\right) h_I^S\, h_J^S\, h_K^S\right]\frac{\partial h_N^S}{\partial \gamma_r} \\ &\quad - \frac{1}{T^S}\,\frac{\partial T^S}{\partial \xi_m}\,\frac{\partial T^S}{\partial \gamma_r}.\end{aligned} \tag{A.7}$$

To obtain formulas for the corresponding derivatives of the one-way time T^R, simply substitute the superscript label R for S in equations (A.3)–(A.7).

A2 Derivatives of one-way time for rotationally symmetric diffraction moveout

If the diffraction-time moveout is rotationally symmetric, equations (A.3)–(A.7) are recast as

$$\frac{\partial T^S}{\partial \xi_m} = \frac{1}{2T^S}\left[\frac{\xi_3}{2}\,\delta_{3m} + \frac{\partial S^{M(2)}}{\partial \xi_m}(h^S)^2 + \frac{\partial S^{M(4)}}{\partial \xi_m}(h^S)^4\right], \tag{A.8}$$

$$\frac{\partial T^S}{\partial \gamma_r} = \frac{\partial T^S}{\partial h^S_M}\,\frac{\partial h^S_M}{\partial \gamma_r}, \qquad \frac{\partial T^S}{\partial h^S_M} = \frac{1}{T^S}\left(S^{M(2)} + 2S^{M(4)}\,(h^S)^2\right) h^S_M, \tag{A.9}$$

$$\frac{\partial^2 T^S}{\partial \xi_m \partial \xi_n} = \frac{1}{2T^S}\left[\frac{\partial^2 S^{M(2)}}{\partial \xi_m \partial \xi_n}(h^S)^2 + \frac{\partial^2 S^{M(4)}}{\partial \xi_m \partial \xi_n}(h^S)^4\right] - \frac{1}{T^S}\,\frac{\partial T^S}{\partial \xi_m}\,\frac{\partial T^S}{\partial \xi_n}, \tag{A.10}$$

$$\frac{\partial^2 T^S}{\partial \gamma_r \partial \gamma_s} = \frac{1}{T^S}\left(S^{M(2)} + 6\,S^{M(4)}\,(h^S)^2\right)\frac{\partial h^S_M}{\partial \gamma_r}\,\frac{\partial h^S_M}{\partial \gamma_s} - \frac{1}{T^S}\,\frac{\partial T^S}{\partial \gamma_r}\,\frac{\partial T^S}{\partial \gamma_s}, \tag{A.11}$$

$$\frac{\partial^2 T^S}{\partial \xi_m \partial \gamma_r} = \frac{1}{T^S}\left[\frac{\partial S^{M(2)}}{\partial \xi_m} + 2\frac{\partial S^{M(4)}}{\partial \xi_m}(h^S)^2\right] h^S_N\,\frac{\partial h^S_N}{\partial \gamma_r} - \frac{1}{T^S}\,\frac{\partial T^S}{\partial \xi_m}\,\frac{\partial T^S}{\partial \gamma_r}. \tag{A.12}$$

APPENDIX B: FIRST-ORDER DERIVATIVES OF DIFFRACTION TIME WITH RESPECT TO PARAMETERS OF THE TIME-MIGRATION VELOCITY MODEL

We show how one can calculate first-order derivatives of diffraction time with respect to parameters of the time-migration velocity model.

The first-order derivative of diffraction time with respect to a parameter ν of the time-migration velocity model is given by

$$\frac{\partial T^D}{\partial \nu} = \frac{\partial T^S}{\partial \nu} + \frac{\partial T^R}{\partial \nu}. \tag{B.1}$$

Since the derivatives of T^S and T^R have the same form, we only specify derivatives with respect to T^S in the following.

Consider a model parameter $\nu = \nu^{(2)}$ associated with the diffraction-time coefficient $S_{IJ}^{M(2)}$. For this parameter differentiation of the first sub-equation of (7) yields

$$\frac{\partial T^S}{\partial \nu^{(2)}} = \frac{1}{2T^S}\frac{\partial}{\partial \nu^{(2)}}\left(S_{IJ}^{M(2)}\right) h_I^S\, h_J^S. \tag{B.2}$$

Likewise, for a model parameter $\nu = \nu^{(4)}$ associated with the diffraction-time coefficient $S_{IJKL}^{M(4)}$ we obtain

$$\frac{\partial T^S}{\partial \nu^{(4)}} = \frac{1}{2T^S}\frac{\partial}{\partial \nu^{(4)}}\left(S_{IJKL}^{M(2)}\right) h_I^S\, h_J^S\, h_K^S\, h_L^S. \tag{B.3}$$

B1 Derivatives of one-way time for rotationally symmetric diffraction moveout

In the special case where the diffraction-time moveout is rotationally symmetric, equations (B.2)–(B.3) are simplified to

$$\frac{\partial T^S}{\partial \nu^{(2)}} = \frac{1}{2T^S}\frac{\partial}{\partial \nu^{(2)}}\left(S^{M(2)}\right) (h^S)^2, \tag{B.4}$$

$$\frac{\partial T^S}{\partial \nu^{(4)}} = \frac{1}{2T^S}\frac{\partial}{\partial \nu^{(4)}}\left(S^{M(2)}\right) (h^S)^4. \tag{B.5}$$

APPENDIX C: REPRESENTATION OF A TRIVARIATE LOCAL FUNCTION IN TERMS OF B-SPLINE BASIS FUNCTIONS

We consider the representation of a trivariate function in terms of "B-spline" basis functions. The generality is trivially extended to yield a multicomponent function and a number of variables higher than three.

C1 A hierarchy of local functions for a grid cell

Without loss of generality, consider the grid cell for which $i = j = k = 1$. The normalized coordinates for this grid cell shall be denoted as u, v, and w. Each of these coordinates extends between 0 and 1 inside the cell. Generalizing the results of Bartels et al. (1987), we write the approximate value of a function $\mathcal{M}$ in a point inside the cell as

$$\mathcal{M}(u,v,w) = \sum_{k=k_{min}}^{k=k_{max}} b_k(w) \sum_{j=j_{min}}^{j=j_{max}} b_j(v) \sum_{i=i_{min}}^{i=i_{max}} b_i(u) M^{i,j,k} \; . \tag{C.1}$$

Here, $M^{i,j,k}$ is a known value of the global function $M(\boldsymbol{\xi})$ in the grid point $X_{i,j,k}$, and the functions $b_i(u)$, $i = i_{min}, ..., i_{max}$ are referred to as *basis functions*. Equation (C.1) may be used for all three local function representations discussed in section 1.5. The basis functions and/or the limits of the sums in equation (C.1) are however different for a locally constant function, a local trilinear interpolator, and a local tricubic spline function.

Assume now that an unknown parameter ν to be estimated by the iterative linearized process is a coefficient of the type $M^{r,s,t}$ included on the right-hand side of equation (C.1). In order to obtain Fréchet derivatives, we may need, as indicated by equation (56), the derivative $\partial T^D/\partial\nu$ and therefore also $\partial\mathcal{M}/\partial\nu$. Since equation (C.1) is linear in the coefficients $M^{i,j,k}$, we obtain

$$\frac{\partial\mathcal{M}}{\partial M^{r,s,t}}(u,v,w) = b_i(u)\, b_j(v)\, b_k(w)\; \delta_{ir}\, \delta_{js}\, \delta_{kt}.$$

Consequently we have

$$\frac{\partial\mathcal{M}}{\partial M^{r,s,t}}(u,v,w) \quad = \quad \begin{cases} b_r(u)\, b_s(v)\, b_t(w) & \\ & \text{if } r \in [i_{min}, i_{max}];\ s \in [j_{min}, j_{max}];\ t \in [k_{min}, k_{max}]; \\ 0 & \text{otherwise.} \end{cases} \tag{C.2}$$

Equation (C.2) is interesting in several respects. In particular, equation (C.2) shows that derivatives of the type $\partial\mathcal{M}_\lambda/\partial\nu$ are equal for functions $\mathcal{M}_\lambda$ that are evaluated in the same location *and* are defined with respect to the same grid. Careful implementation of equation (C.2) is therefore expected to be very beneficial with respect to the efficiency of the Fréchet derivative calculations.

C2 Taking the mean value

Taking the summation limits in equation (C.1) as $i_{min} = j_{min} = k_{min} = 0$ and $i_{max} = j_{max} = k_{max} = 1$, and defining the basis functions as

$$b_0(u) = \frac{1}{2} \qquad b_1(u) = \frac{1}{2} \ , \tag{C.3}$$

equation (C.1) is reduced to

$$\mathcal{M}(u,v,w) = \frac{1}{8}\sum_{i=0}^{i=1}\sum_{j=0}^{j=1}\sum_{k=0}^{k=1} M^{i,j,k} \ . \tag{C.4}$$

In other words, the constant local function may be obtained by taking the mean value of the values $M^{i,j,k}$ in the vertices bounding the grid cell. Moreover, equation (C.2) gets the simple form

$$\frac{\partial \mathcal{M}}{\partial M^{r,s,t}}(u,v,w) = \begin{cases} \frac{1}{8} & \text{if } r \in [0,1];\ s \in [0,1];\ t \in [0,1]; \\ 0 & \text{otherwise.} \end{cases} \tag{C.5}$$

C3 Trilinear interpolation

For trilinear interpolation we have the summation limits $i_{min} = j_{min} = k_{min} = 0$ and $i_{max} = j_{max} = k_{max} = 1$, and the basis functions are given by

$$b_0(u) = 1 - u \qquad b_1(u) = u \ . \tag{C.6}$$

Writing out the various terms in equation (C.1) we therefore obtain

$$\begin{aligned} \mathcal{M}(u,v,w) &= b_0(u)b_0(v)b_0(w)M^{000} \\ &+ b_1(u)b_0(v)b_0(w)M^{100} \\ &+ b_0(u)b_1(v)b_0(w)M^{010} \\ &+ b_1(u)b_1(v)b_0(w)M^{110} \\ &+ b_0(u)b_0(v)b_1(w)M^{001} \\ &+ b_1(u)b_0(v)b_1(w)M^{101} \\ &+ b_0(u)b_1(v)b_1(w)M^{011} \\ &+ b_1(u)b_1(v)b_1(w)M^{111} \ . \end{aligned}$$

(C.7)

C4 Tricubic spline evaluation

Considering tricubic spline evaluation, the summation limits in equation (C.1) become $i_{min} = j_{min} = k_{min} = -1$ and $i_{max} = j_{max} = k_{max} = 2$, and the basis functions are given by Bartels et al. (1987),

$$\begin{aligned}
b_{-1}(u) &= \frac{1}{6}(1 - 3u + 3u^2 - u^3) \ , \\
b_0(u) &= \frac{1}{6}(4 - 6u^2 + 3u^3) \ , \\
b_1(u) &= \frac{1}{6}(1 + 3u + 3u^2 - 3u^3) \ , \\
b_2(u) &= \frac{1}{6}u^3 \ .
\end{aligned} \tag{C.8}$$

APPENDIX D: CURVATURE ESTIMATION BY QUADRATIC GRADIENT STRUCTURE TENSOR (QST)

The quadratic gradient structure tensor (QST) (van de Weijer et al. 2001; Bakker 2002) is a method for estimating local curvature. The main assumption behind this method is that we are considering a locally quadratic surface on the form:

$$S(\mathbf{x}) \approx \mathbf{x}^T \mathbf{A}\mathbf{x} + \mathbf{b}\mathbf{x} + c = 0, \tag{D.1}$$

where $\mathbf{b}$ is the unit normal vector to the surface and $\mathbf{A}$ is a symmetric 3×3 matrix with at least two non-zero eigenvalues. When observing the surface in the reflector-oriented coordinate system (u, v, w) (the u-axis is normal to the surface) the surface becomes:

$$S(\mathbf{x}) \approx \frac{1}{2}\kappa_1 v + \frac{1}{2}\kappa_2 w + u \tag{D.2}$$

where κ_1 and κ_2 are the principal curvatures of the surface. Further, it is shown in Bakker (2002) that these curvatures can be estimated by considering the transform that deforms S into a plane. This results in the expressions for obtaining the curvatures in the reflector-oriented coordinate system:

$$\kappa_1 = \frac{\overline{v g_u g_v}}{\overline{v^2 g_u^2}}, \tag{D.3}$$

$$\kappa_2 = \frac{\overline{w g_u g_w}}{\overline{w^2 g_u^2}}, \tag{D.4}$$

where the g_u, g_v and g_w are the gradients along the axes in the reflector-oriented coordinate system.

In Bakker (2002), the vectors spanning this coordinate system are given by the eigenvectors of the GST:

$$\begin{aligned} \mathbf{u} &= [x_u, y_u, t_u]^T \,\widehat{=}\, \mathbf{v}_1, \\ \mathbf{v} &= [x_v, y_v, t_v]^T \,\widehat{=}\, \mathbf{v}_2, \\ \mathbf{w} &= [x_w, y_w, t_w]^T \,\widehat{=}\, \mathbf{v}_3. \end{aligned} \tag{D.5}$$

In that case, the extracted curvatures will be the principal curvatures of the surface. We are, however, seeking the derivatives with respect to x and y. Therefore, we do not use the eigenvectors to span this coordinate system but force $\mathbf{v}$ and $\mathbf{w}$ to be oriented along the x- and y- axes.

Further more, Bakker (2002) shows that estimates of the second order derivatives are obtained by accounting for the rotation of the reflector-oriented coordinate system. Assuming that the two approaches for defining the reflector-oriented coordinate system coincide (that the principal curvature is the same as the derivative with respect to x), the curvatures (estimates of the second order derivatives) are given as:

$$\kappa_x = \widehat{\frac{\partial t^2}{\partial^2 x}} = \kappa_1 \left(1 + \left(\frac{\partial t}{\partial x}\right)^2\right)^{\frac{3}{2}}, \tag{D.6}$$

$$\kappa_y = \widehat{\frac{\partial t^2}{\partial^2 y}} = \kappa_2 \left(1 + \left(\frac{\partial t}{\partial y}\right)^2\right)^{\frac{3}{2}}. \tag{D.7}$$

APPENDIX E: TIME-MIGRATION VELOCITY MODEL DEFINITION

We define the time-migration model on a 3D rectangular grid. The model parameters related to the cells and the corresponding vertices within the grid. As shown Figure A1, a rectangular grid cell (i, j, k) is defined in terms of eight vertices $X_{i-1,j-1,k-1}$, $X_{i,j-1,k-1}$, $X_{i-1,j,k-1}$, $X_{i,j,k-1}$, $X_{i-1,j-1,k}$, $X_{i,j-1,k}$, $X_{i-1,j,k}$, $X_{i,j,k}$. We assume that the values of the function M_λ is known in all relevant grid vertices $X_{i,j,k}$, and we denote these values as ${M_\lambda}^{i,j,k}$.

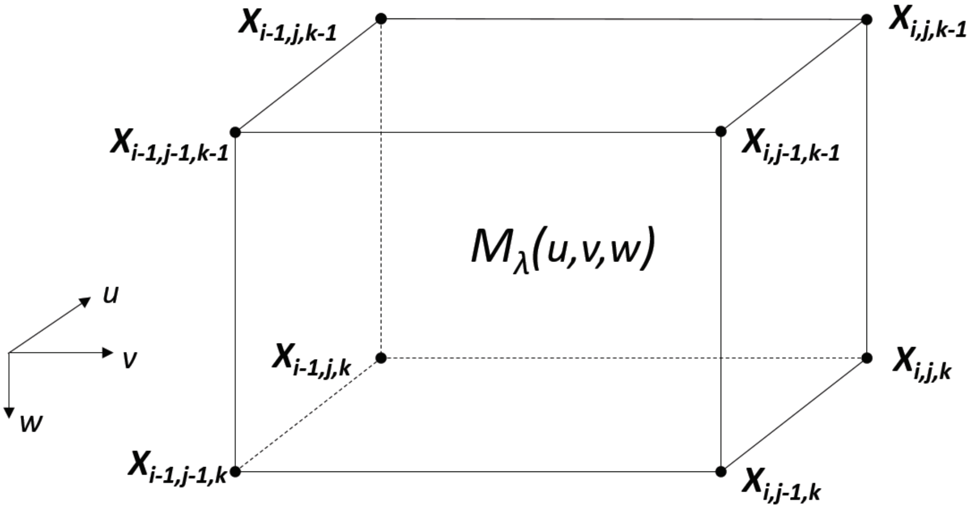

Figure A1: Grid cell and local dimensionless coordinates (u,v,w) used for describing the 3D time-migration velocity model.

As in (depth) tomography, we apply here a local function $\mathcal{M}_\lambda(u, v, w)$ which pertains only to one selected cell. The variables u, v, w are dimensionless and take values on the interval $[0, 1]$. At any point within the cell the global and local functions must yield the same output value,

$$M_\lambda(\xi_1, \xi_2, \xi_3) \quad = \quad \mathcal{M}_\lambda(u, v, w). \tag{E.1}$$

The evaluation of the function $\mathcal{M}_\lambda$ is based on the values ${M_\lambda}^{i,j,k}$ in the vertices forming the cell, and eventually also on values in grid vertices that are neighbors to the cell. In the following, we consider three ways of representing the local function $\mathcal{M}_\lambda$ in a specific grid cell (i, j, k).

E1 Constant local function

A common approach in tomography is to assume that the value of the function $\mathcal{M}_\lambda$ is constant within each grid cell. Using this approach, the medium within each cell is treated as homogeneous. Application of constant local functions will give rise to discontinuities in the function values across grid cell boundaries.

E2 Linear interpolation

Depending on whether the grid is 1D, 2D, or 3D, one may use linear, bilinear, or trilinear interpolation in order to obtain function values inside a grid cell. These interpolation approaches yield a continuous function value along and across the grid cell boundaries, while the first- and second-order derivatives with respect to the coordinate x_i are generally discontinuous. The number of grid vertices contributing to linear, bilinear, and trilinear interpolation are, respectively, two, four, and eight.

E3 Local spline approximation

In order to achieve continuity of zeroth-, first- and second-order derivatives, one may use a local spline function. For 1D, 2D, and 3D grids the spline function is referred to as cubic, bicubic and tricubic, respectively. The spline function does not interpolate exactly, meaning that the function value $\mathcal{M}_\lambda$ in the grid vertex $X_{i,j,k}$ is not necessarily equal to the input value $M_\lambda^{i,j,k}$. However, the local spline function possesses the so-called convex hull property, which prevents the function from fluctuating drastically between the grid vertices. As approximate coefficients of the function we take the input values to function generation given in the grid vertices. For cubic, bicubic, and tricubic spline evaluation, the number of contributing coefficients are, respectively, 4, 16, and 64.

APPENDIX F: PARTIAL DERIVATIVES RELATED TO THE TIME-MIGRATION VELOCITY MODEL

Our time-migration velocity model is described in terms of the vector function (M_λ), $\lambda = 1, \ldots, N^\lambda$. Within a given grid cell under consideration, the global function M_λ and the corresponding local function $\mathcal{M}_\lambda$ for the grid cell must be equal. Using equation (C.1) we can then write

$$M_\lambda(m_1, m_2, \tau) = \mathcal{M}_\lambda(u, v, w) = \sum_{k=k_{min}}^{k=k_{max}} b_k(w) \sum_{j=j_{min}}^{j=j_{max}} b_j(v) \sum_{i=i_{min}}^{i=i_{max}} b_i(u) M_\lambda^{i,j,k}. \tag{F.1}$$

When differentiating the function M_λ with respect to the variables m_1, m_2, and τ, we can utilize their one-to-one linear relationship with the corresponding dimensionless grid-cell variable,

$$m_1 \leftrightarrow u; \qquad m_2 \leftrightarrow v; \qquad \tau \leftrightarrow w. \tag{F.2}$$

For example, differentiation of equation (F.1) with respect to τ yields

$$\frac{\partial M_\lambda}{\partial \tau}(m_1, m_2, \tau) = \frac{1}{\Delta\tau} \sum_{k=k_{min}}^{k=k_{max}} \frac{\mathrm{d}b_k}{\mathrm{d}w}(w) \sum_{j=j_{min}}^{j=j_{max}} b_j(v) \sum_{i=i_{min}}^{i=i_{max}} b_i(u) M_\lambda^{i,j,k}, \tag{F.3}$$

where $\Delta\tau$ signifies the grid spacing in the τ direction. Likewise, a partial second derivative in, say, m_1 and τ is given by

$$\frac{\partial^2 M_\lambda}{\partial m_1 \partial \tau}(m_1, m_2, \tau) = \frac{1}{\Delta m_1\, \Delta\tau} \sum_{k=k_{min}}^{k=k_{max}} \frac{\mathrm{d}b_k}{\mathrm{d}w}(w) \sum_{j=j_{min}}^{j=j_{max}} b_j(v) \sum_{i=i_{min}}^{i=i_{max}} \frac{\mathrm{d}b_i}{\mathrm{d}u}(u)\, M_\lambda^{i,j,k}, \tag{F.4}$$

Equations (53) and (56) contain partial derivatives of the diffraction time T^D with respect to a given parameter of the time-migration velocity model, ν. Furthermore, the dependence of T^D on ν is channelled through the diffraction time coefficients, M_λ Now, let the parameter ν be defined as in equation (43). Differentiation of equation (F.1) with respect to ν yields, in view of equation (C.2),

$$\frac{\partial M_\lambda}{\partial \nu}(m_1, m_2, \tau) \quad = \quad \begin{cases} b_r(u)\, b_s(v)\, b_t(w) & \\ \qquad \text{if } r \in [i_{min}, i_{max}];\ s \in [j_{min}, j_{max}];\ t \in [k_{min}, k_{max}]; & \\ 0 \qquad \text{otherwise.} & \end{cases} \tag{F.5}$$

Equation (56) implies also computation of the second-order mixed partial derivative in the model parameter ν and the time variable τ. Differentiation of equation (F.5) with respect to τ yields

$$\frac{\partial^2 M_\lambda}{\partial \nu \partial \tau}(m_1, m_2, \tau) \quad = \quad \begin{cases} \frac{1}{\Delta \tau}\, b_r(u)\, b_s(v)\, \frac{\mathrm{d} b_t}{\mathrm{d} w}(w) \\ \qquad \text{if } r \in [i_{min}, i_{max}];\ s \in [j_{min}, j_{max}];\ t \in [k_{min}, k_{max}]; \\ 0 \qquad \text{otherwise.} \end{cases} \tag{F.6}$$